

AD-A101 513 PRINCETON UNIV NJ DEPT OF MECHANICAL AND AEROSPACE --ETC F/6 20/4  
AN EXPERIMENTAL INVESTIGATION OF TIP BLUNTNESSES EFFECTS ON THE T--ETC(U)  
MAY 81 W K GRAY, D S DOLLING, S M BOGDONOFF DAA629-77-6-0234  
UNCLASSIFIED MAE-1530 ARN-14254-3-F "

1 OF 2  
40 A  
101513

ADA101513

IIARO 14254.3-E

(12)

Princeton University



DTIC

JUL 17 1981

A

Department of  
Mechanical and  
Aerospace Engineering

DTIC FILE COPY

This document has been approved  
for public release or distribution  
distribution is unlimited.

31717-130

AN EXPERIMENTAL INVESTIGATION OF TIP  
BLUNTNESSES EFFECTS ON THE TURBULENT  
COMPRESSIBLE BOUNDARY LAYER ON  
AN AXISYMMETRIC BODY.

by

William K. Gray, David S. Dolling  
and Seymour M. Bogdonoff

Final Technical Report  
to the U. S. Army Research Office

Grant No. DAAG29-77-G-0234  
October 1, 1977 to May 31, 1981

Princeton University  
Mechanical and Aerospace Engineering Department  
Princeton, New Jersey 08544

May 1981

SPR  
S  
A

Approved for Public Release;  
Distribution Unlimited.

## UNCLASSIFIED

SECURITY CLASSIFICATION OF THIS PAGE (When Data Entered)

REPORT DOCUMENTATION PAGE		READ INSTRUCTIONS BEFORE COMPLETING FORM
1. REPORT NUMBER	2. GOVT ACCESSION NO.	3. RECIPIENT'S CATALOG NUMBER
4. TITLE (and Subtitle) AN EXPERIMENTAL INVESTIGATION OF TIP BLUNTNESSES EFFECTS ON THE TURBULENT COMPRESSIBLE BOUNDARY LAYER ON AN AXISYMMETRIC BODY		5. TYPE OF REPORT & PERIOD COVERED Final Technical Report 10/1/77 - 5/31/81
7. AUTHOR(s) William K. Gray David S. Dolling Seymour M. Bogdonoff	6. PERFORMING ORG. REPORT NUMBER 1530-MAE	
9. PERFORMING ORGANIZATION NAME AND ADDRESS Princeton University Mechanical & Aerospace Engrg. Department Princeton, NJ 08544	8. CONTRACT OR GRANT NUMBER(s) DAAG29-77-G-0234	
11. CONTROLLING OFFICE NAME AND ADDRESS U. S. Army Research Office Post Office Box 12211 Research Triangle Park, NC 27709	10. PROGRAM ELEMENT, PROJECT, TASK AREA & WORK UNIT NUMBERS Project No. P-14254-E	
14. MONITORING AGENCY NAME & ADDRESS (if different from Controlling Office)	12. REPORT DATE May 1981	
	13. NUMBER OF PAGES 186	
	15. SECURITY CLASS. (of this report) UNCLASSIFIED	
	15a. DECLASSIFICATION DOWNGRADING SCHEDULE	
16. DISTRIBUTION STATEMENT (of this Report) Approved for public release; distribution unlimited.		
17. DISTRIBUTION STATEMENT (of the abstract entered in Block 20, if different from Report) NA		
18. SUPPLEMENTARY NOTES The findings in this report are not to be construed as an official Department of the Army position, unless so designated by other authorized documents.		
19. KEY WORDS (Continue on reverse side if necessary and identify by block number)		
20. ABSTRACT (Continue on reverse side if necessary and identify by block number) An experimental study has been carried out in which the effect of tip bluntness on the turbulent boundary layer over an axisymmetric body was examined. The study was performed at a Mach number of 2.94 with a unit Reynolds number of roughly $6.34 \times 10^7$ per meter and a nearly adiabatic wall condition. A tangent ogive-cylinder was used with a nose fineness ratio of approximately 3. Six model tips were constructed with hemispherical and flat blunting of various dimensions. In addition,		

UNCLASSIFIED

SECURITY CLASSIFICATION OF THIS PAGE(When Data Entered)

to establish a reference baseline, tests were made using a model with a pointed tip.

Bow shock shapes and surface pressures were obtained at  $0^\circ$  and  $2.9^\circ$  angle of attack for each model tip. Boundary layer surveys were made along the windward and leeward meridians of the model for each tip.

The experimental results show that the boundary layer is influenced by the tip bluntness through the entropy wake, a region of hot gas next to the body. This high entropy region is caused by the strong shock section of the bow shock. The downstream development of boundary layer parameters, such as the displacement and momentum deficit thickness, form factor, and skin friction coefficient, was found to be strongly dependent on the geometry and size of the tip blunting.

UNCLASSIFIED

SECURITY CLASSIFICATION OF THIS PAGE(When Data Entered)

## TABLE OF CONTENTS

	<u>Page</u>
TITLE PAGE	
TABLE OF CONTENTS . . . . .	iii
ABSTRACT . . . . .	v
SYMBOLS . . . . .	vi
LIST OF FIGURES . . . . .	viii
1.0 INTRODUCTION . . . . .	1-1
2.0 REVIEW OF PREVIOUS STUDIES . . . . .	2-1
3.0 OUTLINE OF EXPERIMENTAL PROGRAM . . . . .	3-1
4.0 EXPERIMENTAL PROGRAM . . . . .	4-1
4.1 Wind Tunnel Facility . . . . .	4-1
4.2 Model Description . . . . .	4-2
4.2.1 Model Characteristics . . . . .	4-2
4.2.2 Model Construction . . . . .	4-3
4.2.2.1 Model A . . . . .	4-4
4.2.2.2 Model B . . . . .	4-5
4.2.3 Model Installation and Alignment . . . . .	4-6
4.3 Instrumentation . . . . .	4-7
4.3.1 Surface Pressures . . . . .	4-7
4.3.2 Pitot Surveys . . . . .	4-9
4.3.3 Optical Methods . . . . .	4-9
4.4 Estimation of Measurement Accuracy . . . . .	4-10
4.4.1 Components of the Data Acquisition System . . . . .	4-10
4.4.2 Model Angle of Attack . . . . .	4-11
4.4.3 Surface Pressure Measurements . . . . .	4-12
4.4.4 Pitot Surveys . . . . .	4-13
4.4.5 Other Measurements . . . . .	4-13
4.5 Data Reduction . . . . .	4-13
4.6 Probe Development . . . . .	4-14
5.0 RESULTS AND DISCUSSION . . . . .	5-1
5.1 General Flowfield Characteristics . . . . .	5-1
5.2 Bow Shock Shape and Structure . . . . .	5-5
5.2.1 Bow Shock Analysis . . . . .	5-6
5.2.2 Shock Detachment Distance . . . . .	5-12
5.3 Model Surface Pressures . . . . .	5-12
5.3.1 Ogive Nose . . . . .	5-12
5.3.2 Cylindrical Afterbody . . . . .	5-16
5.3.3 Comparison with Computational Results .	5-17
5.4 Boundary Layer Transition . . . . .	5-18

	<u>Page</u>
5.5 Boundary Layer Analysis . . . . .	5-21
5.5.1 Zero Angle of Attack . . . . .	5-24
5.5.2 Windside at Angle of Attack . . . . .	5-29
5.5.3 Leeside at Angle of Attack . . . . .	5-33
5.5.4 Boundary Layer Summary . . . . .	5-35
5.6 Scaling Parameter Development . . . . .	5-38
6.0 CONCLUSIONS . . . . .	6-1
7.0 PUBLICATIONS/DEGREES AWARDED . . . . .	7-1
REFERENCES . . . . .	R-1
TABLES . . . . .	T-1
FIGURES	
APPENDIX A Shadowgraph photographs . . . . .	A-1
APPENDIX B Velocity profile comparisons . . . . .	B-1
APPENDIX C Boundary layer parameter tabulations . . . . .	C-1

## ABSTRACT

An experimental study has been carried out in which the effect of tip bluntness on the turbulent boundary layer over an axisymmetric body was examined. The study was performed at a Mach number of 2.94 with a unit Reynolds number of roughly  $6.34 \times 10^7$  per meter and a nearly adiabatic wall condition.

A tangent ogive-cylinder was used with a nose fineness ratio of approximately 3. Six model tips were constructed with hemispherical and flat blunting of various dimensions. In addition, to establish a reference baseline, tests were made using a model with a pointed tip.

Bow shock shapes and surface pressures were obtained at  $0^\circ$  and  $2.9^\circ$  angle of attack for each model tip. Boundary layer surveys were made along the windward and leeward meridians of the model for each tip.

The experimental results show that the boundary layer is influenced by the tip bluntness through the entropy wake, a region of hot gas next to the body. This high entropy region is caused by the strong shock section of the bow shock. The downstream development of boundary layer parameters such as the displacement and momentum deficit thickness, form factor, and skin friction coefficient was found to be strongly dependent on the geometry and size of the tip blunting.

## SYMBOLS

$B_s$	Bow shock wave bluntness parameter (Eqtn. 1)
$\bar{B}$	Bluntness length (Eqtn. 7)
$C_{Dpb}$	Blunt pressure drag coefficient
$C_f$	Skin friction coefficient
$d$	Diameter
$D$	Diameter of cylinder
$D_{pb}$	Blunt pressure drag (Eqtn. 8)
$H$	Velocity profile form factor
$M$	Mach number
$n$	Power law exponent (Eqtn. 6)
$p, P$	Pressure
$r, R$	Radial distance from model ceterline
$r$	Recovery factor
$Re$	Reynolds number
$R_s$	Bow shock wave radius (Eqtn. 1)
$s$	Surface distance
$T$	Temperature
$u, U$	Velocity along $X$ coordinate
$x, X$	Axial distance along model centerline
$y$	Radial distance from model surface
$\alpha$	Angle of attack
$\delta$	Boundary layer thickness
$\xi^*$	Displacement thickness

$\Delta$	Shock standoff distance
$\theta$	Momentum deficit thickness
$\delta, \theta$	Surface inclination angles
$\kappa$	Curvature (Eqtn. 2, 4)
$\pi$	Wake strength parameter
$\rho$	Density
$\phi$	Azimuth angle measured from windward side

#### Subscripts

$b$	blunt tip
$c$	tip corner
$E$	boundary layer edge
$ew$	entropy wake impingement distance
$i$	shock inflection point
$r$	recovery conditions
$s$	bow shock wave
$t$	model tip
$w$	model wall
$\theta$	based on momentum deficit thickness
$o$	stagnation conditions
$\infty$	freestream conditions

## LIST OF FIGURES

### Title

Figure 1 Development of the Magnus force on a spinning axisymmetric body due to the crossflow-boundary layer interaction

Figure 2 Comparison of Computed and Experimental Velocity Profiles at  $X/D=4.925 \alpha=0^\circ$

Figure 3 Comparison of Computed and Experimental Velocity Profiles at  $X/D=4.925 \alpha=2.9 \phi=0^\circ$

Figure 4 Comparison of Computed and Experimental Velocity Profiles at  $X/D=4.925 \alpha=2.9 \phi=180^\circ$

Figure 5 Comparison of Computed and Experimental Displacement Surface Development

Figure 6 Diagram of the Wind Tunnel Layout

Figure 7 Diagram of the Coordinate System

Figure 8 Details of the Blunt Model Tips

Figure 9 Photograph of the Models and Tips

Figure 10 Tip measurements of the Flowfield Probes

Figure 11 Photograph of the Flowfield Probes

Figure 12 Drawing of the Entran Probe Design

Figure 13 Comparison of Pitot Profiles obtained with the Entran Probe at  $X/D=4.925 \alpha=2.9 \phi=180^\circ$

Figure 14 Sketch of the General Flowfield

Figure 15 Shock Curvature along the bow shock  
for the R2 tip

Figure 16 Position of the Shock inflection point  
versus Tip diameter

Figure 17 Position of the Shock inflection point  
versus Tip corner inclination

Figure 18 Shock standoff distance comparison for  
Blunt Model Tips

Figure 19 Surface Pressures on Model Tip P  
 $\alpha=0^\circ$

Figure 20 Surface Pressures on Model Tip P  
 $\alpha=2.9^\circ$

Figure 21 Surface Pressures on Model Tip R3  
 $\alpha=0^\circ$

Figure 22 Surface Pressures on Model Tip R3  
 $\alpha=2.9^\circ$

Figure 23 Surface Pressures on Model Tip R3  
 $\alpha=4.5^\circ$

Figure 24 Surface Pressures on Model Tip F3  
 $\alpha=0^\circ$

Figure 25 Surface Pressures on Model Tip F3  
 $\alpha=2.9^\circ$

Figure 26 Surface Pressures on Model Tip F3  
 $\alpha=4.5^\circ$

Figure 27 Surface Pressures on the Cylinder  
for all Model Tips with  $\alpha=0^\circ$

Figure 28 Surface Pressures on the Cylinder  
for all Model Tips with  $\alpha=2.9^\circ$   $\zeta=0^\circ$

Figure 29 Surface Pressures on the Cylinder  
for all Model Tips with  $\alpha=2.9^\circ$   $\zeta=180^\circ$

Figure 30 Comparison of Computed and Experimental  
Surface Pressures for the P Model Tip

Figure 31 Boundary Layer Transition Region versus  
Model Axial Distance

Figure 32 Boundary Layer Transition Region versus  
Model Surface Distance

Figure 33 Comparison of Pitot Profiles for Model  
Tips P and R2 at  $X/D=3.175$   $\alpha=2.9^\circ$   $\zeta=180^\circ$

Figure 34 Comparison of Velocity Profiles for Model  
Tips P and R2 at  $X/D=3.175$   $\alpha=2.9^\circ$   $\zeta=180^\circ$

Figure 35 Displacement thickness, Momentum thickness  
and Form factor versus  $X/D$   $\alpha=0^\circ$

Figure 36 Displacement thickness, Momentum thickness  
and Form factor versus  $R_b$   $\alpha=0^\circ$

Figure 37 Displacement and Momentum thickness growth  
versus  $R_b$   $\alpha=0^\circ$

Figure 38 Power Law Exponent,  $n$ , versus  $X/D$  and  $R_b$   
 $\alpha=0^\circ$

Figure 39 Wake Strength Parameter,  $\pi$ , versus  $X/D$  and  
 $R_b$   $\alpha=0^\circ$

Figure 40 Skin friction coefficient versus  $Re_\theta$   $\alpha=0^\circ$

Figure 41 Displacement thickness, Momentum thickness,  
and Form factor versus  $X/D$   $\alpha=2.9^\circ$   $\zeta=0^\circ$

Figure 42 Displacement thickness, Momentum thickness, and Form factor versus  $R_b$   $\alpha=2.9^\circ$   $\phi=0^\circ$

Figure 43 Displacement and Momentum thickness growth rates versus  $R_b$   $\alpha=2.9^\circ$   $\phi=0^\circ$

Figure 44 Power Law Exponent,  $n$ , versus  $X/D$  and  $R_b$   $\alpha=2.9^\circ$   $\phi=0^\circ$

Figure 45 Wake Strength Parameter,  $\pi$ , versus  $X/D$  and  $R_b$   $\alpha=2.9^\circ$   $\phi=0^\circ$

Figure 46 Skin friction coefficient versus  $Re_\theta$   $\alpha=2.9^\circ$   $\phi=0^\circ$

Figure 47 Displacement thickness, Momentum thickness, and Form factor versus  $X/D$   $\alpha=2.9^\circ$   $\phi=180^\circ$

Figure 48 Displacement thickness, Momentum thickness, and Form factor versus  $R_b$   $\alpha=2.9^\circ$   $\phi=180^\circ$

Figure 49 Displacement and Momentum thickness growth rates versus  $R_b$   $\alpha=2.9^\circ$   $\phi=180^\circ$

Figure 50 Power Law Exponent,  $n$ , versus  $X/D$  and  $R_b$   $\alpha=2.9^\circ$   $\phi=180^\circ$

Figure 51 Wake Strength Parameter,  $\pi$ , versus  $X/D$  and  $R_b$   $\alpha=2.9^\circ$   $\phi=180^\circ$

Figure 52 Skin friction coefficient versus  $Re_\theta$   $\alpha=2.9^\circ$   $\phi=180^\circ$

Figure 53 Bluntness length diagram

Figure 54 Bluntness length versus Shock bluntness parameter,  $B_s$   $\alpha=0^\circ$

Figure 55 Momentum deficit thickness versus Bluntness length  $\alpha=0^\circ$

Figure 56 Displacement and Momentum thickness growth rates versus Bluntness length  $\alpha=0^\circ$

Figure 57 Form factor and Power Law Exponent versus Bluntness length  $\alpha=0^\circ$

Figure 58 Momentum thickness and Wake Strength Parameter versus Bluntness length  $\alpha=2.9^\circ \phi=0^\circ$

Figure 59 Form factor versus Bluntness length  $\alpha=2.9^\circ \phi=180^\circ$

## INTRODUCTION

One of the many objectives of computational fluid dynamics in recent years has been the calculation of the flowfield around an axisymmetric body at angle of attack in a supersonic stream. The case of a spinning body is of particular practical interest. In such cases the interaction of the surface spin with the crossflow velocity modifies the three-dimensional boundary layer displacement surface giving rise to an assymmetric pressure distribution. The resultant side force, the Magnus force, is small (typically 1/10 to 1/100 of the normal force), but is important because its moment may be large enough to render the body dynamically unstable. Satisfactory prediction of the Magnus force clearly hinges on accurate modelling of the turbulent boundary layer development on the body.

To guide such computational procedures there is a need for detailed boundary layer profile data, both on spinning and non-spinning bodies, particularly at the high Reynolds numbers representative of flight. Only through comparison with a wide ranging, accurate series of experiments can the predictive capability and range of application of these codes be properly evaluated. Several studies have been made (1-9) comparing experimental and computational results, but further detailed investigations are needed.

Much of this early work has been done using cones (3,7,8,9). In many cases the Reynolds numbers have been rather low, necessitating the need for boundary layer trips to ensure a turbulent boundary layer. Almost all past tests were made with sharp tipped bodies and few investigations of the effects of tip blunting have been made in the supersonic regime.

The present experimental study, carried out using a non-spinning model, is similar to some earlier investigations, but is at much higher Reynolds numbers. Surface pressure distributions and boundary layer velocity profiles have been measured on a tangent ogive cylinder model at angle of attack in a high Reynolds number supersonic ( $M = 3$ ) flow. In all cases boundary layer transition occurred naturally and was close to the nose tip. As far as is known, no other similar data are available at such high Reynolds numbers. Measurements have been made using both sharp and hemi-spherical and flat blunted nose tips. The blunt tip produces a detached, curved bow shock wave and entropy wake resulting in a complex flowfield which poses a difficult computational problem. At the current time, computations are not available for this case. For the sharp tipped case, comparisons are made between the experimental data and predictions from a computational scheme developed by Sturek, et.al., at the U. S. Army Ballistic Research Laboratories.

## REVIEW OF PREVIOUS STUDIES

Only with the development of large, high speed computers has the prediction of complex viscous flowfields become a possibility. In the last ten years, great emphasis has been placed on the development of efficient, reliable methods to compute the flowfield and surface property characteristics for a given body in a specified flowfield. Great advances have been made, but significant improvements are needed before the accurate prediction of flowfield and surface properties are consistently achievable for arbitrary geometries.

Experimental and theoretical work on the flow over axisymmetric bodies prior to about 1960 was almost entirely devoted to developing reliable engineering methods to predict the aerodynamic force and moment coefficients of these bodies. Van Dyke (10,11) developed slender body approximations to the second order for subsonic and supersonic flowfields. Emphasis was placed on predicting shock shapes for blunt axisymmetric bodies and a large number of analytic and empirical methods were developed, all of which resulted in rather mediocre comparison with experimental results (12). Others, such as Lin and Shen (13) worked with a Taylor series expansion for the flow variables ( $\rho$ ,  $p$ ,  $v$ ) from the bow shock in the streamwise

direction to obtain surface pressures and aerodynamic coefficients. As Van Dyke (12) showed however, this method of analysis is inadequate. The radius of convergence of the Taylor series may not even extend to the body, making analysis there impossible. A large amount of work was also devoted to the development of relationships for the aerodynamic coefficients through careful experimentation and parameter variation (14-20). The engineering methods and theory developed were in very good agreement with experimental results, for small angles of attack ( $\alpha < 5^\circ$ ), but the accuracy degraded quickly with increasing incidence and the beginning of crossflow separation.

As large digital computing machines became available, computational efforts were first concentrated on inviscid problems. Van Dyke (11,21) developed an early shock location prediction program. While this program solved the inverse problem, where the shock shape is specified and the body shape is determined, it gave good results over a wide range of Mach numbers and body shapes. Many others have developed codes for use on high speed computers to give predictions of the pressure forces and moments on an axisymmetric body (3-9,21,22,23). These have shown good results in some areas but all have some deficiencies.

Rakich (23) developed a computational method which used characteristic and reference plane methods. The results were in very good agreement with experiments in

areas where viscous effects were small, but were not adequate in viscous interactions, such as the boundary layer development on the leeside of inclined bodies. While the codes employing the method of characteristics could predict pressure distributions, surface flow angles, and shock layer characteristics, they were completely incapable of including any viscous or heat transfer effects. These codes were also limited almost entirely to bodies which had pointed tips and attached shock waves.

The next major progression was made with the development of a single computer code consisting of two computational sections. The first was an inviscid flow calculation to give surface pressure distributions and the second was the calculation of the boundary layer development. When the first inviscid calculation was completed, the pressure gradients in the streamwise and crossflow directions,  $\partial p / \partial x$  and  $\partial p / \partial \phi$ , were used as the driver of the boundary layer calculation. With the completion of the boundary layer calculation, the displacement surface was computed and a second inviscid calculation was performed to give the resulting pressure distributions and force coefficients. Dwyers and Sanders (7,8) developed such a program and published results in 1975 with an emphasis placed on the calculation of the Magnus force on spinning supersonic cones. Their predictions showed good agreement and accuracy at small angles of attack, but results degraded

with increasing angle of attack. Predictions were largely in the form of normal force coefficients which are an integrated effect of the boundary layer. No comparison was made with an experiment to validate the computational results and the only comparison was with a computation made by Sedney (24). Specific boundary layer characteristics were not given or compared with experimental results.

The Magnus force is a side force which occurs when a spinning body is in flight at an angle of attack. It is caused by an asymmetry in the displacement surface of the boundary layer, which is distorted due to the interaction of the crossflow with the boundary layer on the spinning body. This is sketched in Figure 1. The spinning body will behave gyroscopically with the Magnus force producing a precession type rolling motion known as coning. This coning will tend to destabilize the body. In order to achieve the best combination of range and accuracy, the Magnus force should be minimized. Clearly, to give an accurate prediction of the Magnus force, a computational technique must be able to accurately predict the detailed boundary layer development. While progress has been made, most of the experimental work is confined to sharp tipped bodies with boundary layer tripping devices in the low Reynolds number regime (3,5,7,8). These conditions are not representative of real problems and so improvements are needed.

In 1979, both Rakich et al (9) and Schiff and Steger (4) developed new codes to model the viscous flowfield over inclined bodies of revolution. Both codes used a parabolized form of the Navier-Stokes equations which step through the flowfield in the streamwise direction. An initial data plane must be specified, and then the remaining downstream flowfield is computed. The equations are made parabolic, to allow streamwise marching, by neglecting the streamwise pressure gradient in the u-momentum Navier-Stokes equation. This assumption of the parabolized Navier-Stokes codes has not proved to be critical to results in nearly conical flows but, has yet to be shown as clearly valid in nonconical flowfields.

Schiff and Steger (4) applied a form of the parabolized Navier-Stokes code to the flow over a hemisphere-cylinder and found good agreement with experiment in both surface pressure distributions and velocity profiles. However, the Reynolds number of  $8.8 \times 10^4$  is rather low and the solution requires an initial data plane as a starting condition, as discussed above. This initial plane was selected at 3.5 nose radii downstream from the body tip. This comparison did not indicate the ability of the code to include tip effects, an important criterion of an effective code.

Rakich, Vigneron, and Agarwal (9) also used a parabolized Navier-Stokes code to compute the flow over various axisymmetric bodies. Reynolds numbers were higher,

on the order of  $10^7$  when based on body length. Results showed good agreement with experiments for a secant ogive-cylinder at  $M=3.0$  and  $4.2^\circ$  angle of attack and for cone configurations. A series of computations for a tangent ogive-cylinder at  $M=3.0$  were stated as being underway, but a caution was given. The results were stated as being very "transition" dependent. The location of the change from laminar to turbulent viscosity appears to affect the results far downstream. This would mean, that for this code to be useful, the location of transition on a body would have to be known before the computation was performed.

Lubard and Rakich performed a calculation of the flow over a blunted cone (3). The flowfield was computed by a form of the parabolized Navier-Stokes equations downstream of the hemispherical tip blunting. The tip bluntness was handled by assuming no separation was present and using a combined inviscid-viscous calculation. A time dependent blunt body technique was used to give the surface pressure distribution over the tip. An axisymmetric boundary layer code used this pressure distribution as a driver for the boundary layer calculation. Slightly downstream of the hemisphere-cone tangency point, the initial plane for the parabolized Navier-Stokes code was specified, and the remaining flowfield computed. The solution was for laminar flow in the hypersonic regime and a high angle of attack. The results for surface pressure and heat

transfer distributions agreed with the experimental results within experimental accuracy. Pressure profile trends were in basic agreement with experimental data, but the code did not predict the magnitude of the pressure values accurately through the entire flowfield. The assumptions involved in the starting mechanism were given as a partial cause of the problem and improvements would be needed in this area for a more widely applicable code.

The work at Princeton preceding this investigation (1,2) examined the flowfield around a pointed ogive-cylinder at  $M=3.0$ . A comparison of experimental results and computational predictions was made. Computations were performed by Dr. Walter Sturek at the Ballistics Research Laboratory, Aberdeen Proving Grounds. The Ballistics Research Laboratory has been working extensively over the past several years to model the flow over spinning projectiles and predict the Magnus and other forces acting on such a body in flight (5,6). Two sets of computations were made and, where applicable, results from each are shown in the figures of this report. The first, as mentioned above, was a combination of two codes, an inviscid flow computation and a boundary layer calculation using the static pressure as the compatibility condition. Results of this code are referred to as output from the BL code. The second program was a form of the parabolized Navier-Stokes equations which allows starting

at an initial data plane and stepping through the flow-field in the streamwise direction. These results are referred to as being from the PNS code.

The boundary layer calculation of the BL code used a single eddy viscosity turbulence model and assumed a turbulent Prandtl number of 0.90. The parabolized Navier-Stokes computation utilized a two layer Cebecchi type eddy viscosity model and assumed a turbulent Prandtl number of 0.80. Both programs handled transition from laminar to turbulent flow by a manual inputting of the turbulence model over a specified number of streamwise steps in the calculation.

Initial results from the first computation did not show particularly good results in the prediction of specific boundary layer characteristics over a large part of the body. Figure 2 shows one of the best comparisons of both computational results with experiment. This is for  $\alpha=0^\circ$  and  $X/D=4.925$ . Both codes give results that are not in good agreement with the experimental results through the entire boundary layer at this location. Figures 3 and 4 show a comparison at  $\alpha=2.9^\circ$ ,  $X/D=4.925$  on the wind and leeside. These results are worse than the predictions at  $\alpha=0^\circ$ . The parabolized Navier-Stokes code predictions were not significantly more accurate and showed no improvement over the BL code in the prediction of the velocity profile. Predictions of  $\delta^*$  along the body are shown in Figure 5. This allows comparison of  $\partial\delta^*/\partial x$ , which is

important to normal force predictions. Again, both computational results give only fair agreement. Sturek, however, found considerable improvement with the parabolized Navier-Stokes code when compared to experimental work he had completed at the Ballistics Research Laboratory. His work was done at a lower Reynolds number. His comparisons are shown in Schiff and Sturek (5) but, a close examination is difficult due to the manner in which they are presented.

## OUTLINE OF EXPERIMENTAL PROGRAM

This study was designed to provide a simple and basic test case for the prediction of the flow around blunt tipped axisymmetric bodies. It was also to repair some of the deficiencies of previous experiments including artificial transition, low Reynolds number, and no significant longitudinal pressure gradient. Test conditions were used which are representative of the actual full scale conditions for projectile flight. A good deal of computational work is concentrating in this area.

The model used was a tangent ogive-cylinder with a nose fineness ratio of approximately 3. Seven different model tips were used with varying amounts of bluntness and different geometries. Data was collected at zero angle of attack and a small angle of attack, selected as  $2.9^\circ$ . This was small enough to insure no separation was present.

This program documented the bow shock shape, surface pressure distributions, and boundary layer velocity profiles. This data would be compared with computational predictions made by Dr. Walter Sturek, Ballistics Research Laboratory. These computations have not been completed at this time.

## EXPERIMENTAL PROGRAM

### 4.1 WIND TUNNEL FACILITY

This experimental program was conducted at the Gas Dynamics Laboratory, Forrestal Campus, Princeton University. All tests were conducted in the variable density, high Reynolds number blowdown wind tunnel with a nominal freestream Mach number of 2.95. Stagnation pressures of  $4 \times 10^5$  N/m<sup>2</sup> to  $35 \times 10^5$  N/m<sup>2</sup> (60-500 psia) can be achieved and the desired stagnation pressure can be maintained constant to within about one percent during a test.

Four Worthington four-stage compressors are used to compress atmospheric air, which is then dried and stored in tanks having a capacity of 56.6 m<sup>3</sup> (2000 ft<sup>3</sup>). This supply capability provides run times varying from about fifteen seconds to several minutes depending on the stagnation pressure. The air supply is maintained at ambient temperature and the stagnation temperature varies with atmospheric temperature, Joule-Thompson losses through the laboratory valving, and piping heat transfer. No corrections were made for this and, therefore, stagnation temperature is variable during each run and between runs. This variation was very small and had no significant effect on the results as will be discussed in Section 4.2.2.1.

This investigation was conducted with a stagnation pressure of  $6.89 \times 10^5 \text{ N/m}^2$  (100 psia). Stagnation temperature varied from 290° K to 240° K giving a variation of unit Reynolds number from  $5.46 \times 10^7/\text{m}$  to  $7.27 \times 10^7/\text{m}$ . Values given in this report are taken from the average values of 260° K and  $6.34 \times 10^7/\text{m}$  respectively. Each run had a duration of approximately 30-40 seconds. Successive runs were separated roughly 15 minutes. This timing arrangement gave very nearly the same variation of model temperature during each test.

The tunnel had three test sections as shown in Figure 6. Each section has a 20 cm x 20 cm cross section and is 90 cm long. All tests in this investigation were conducted in Section 1 with the model mounted on a sting and drive housed in Section 2. A more complete description of the test facility is given by Vas and Bogdonoff (25).

#### 4.2 MODEL DESCRIPTION

##### 4.2.1. MODEL CHARACTERISTICS

The model used was a tangent ogive-cylinder with a body diameter of 4.95 cm (1.95 in) and a nose fineness ratio of 3. A caliber number of 9.25 was used to generate the nose shape. This is the ratio of the radius of the nose generating arc to the diameter of the swell or cylinder of the body. The overall length of the model was approximately ten calibers.

A cylindrical-polar coordinate system has been used for data presentation purposes and is illustrated in Figure 7. Axial distances were measured along the center-line of the body from the pointed tip of the ogive and were given as either  $X$  or  $X/D$ , where  $D$  is the diameter of the body. The polar coordinate,  $\phi$ , measured the azimuthal position around the body. It is measured in a plane perpendicular to the  $X$  axis. Standard convention was followed with  $\phi=0^\circ$  on the windward meridian and  $\phi=180^\circ$  on the leeward meridian. The normal coordinate,  $Y$ , was measured along a ray of fixed  $\phi$  perpendicular to the  $X$  axis with  $Y=0$  being designated at the surface of the model.

Model noses having flat and hemispherical surfaces of dimensions representative of actual geometries were used. Details of the tips are given in Figure 8. The flat tips were designed to have the same radial distance to the corner of the tip as the radial distance to the point of tangency between the hemisphere and the ogive for the hemispherical tips. It is important to note that axial distance measurements are made from the virtual pointed tip of the ogive and not the tip of the model for that test. In the discussion that follows, model tips will be referred to by the same designation given in Figure 8, i.e. P, R1, F3.

#### 4.2.2 MODEL CONSTRUCTION

Two models were built for use in this study. Model A was built to document the surface pressures over the cylin-

drical body and was used for all boundary layer measurements. Model B was built to allow examination of the surface pressures on the ogive section of the model. Due to the geometry and size of the available interior space in the model for pressure tubing and surface area for taps, two models were required. Both models were constructed in the Forrestal Machine Shop. Brass was used as the working material because machining was easier than with other material. A photograph of the models used is shown in Figure 9.

#### 4.2.2.1 MODEL A

Model A consisted of two main components, a cylindrical section and an ogive nose. The cylindrical section was constructed of tubing with a 5.04 cm outside diameter and a 3.8 cm inside diameter. The ogive nose section was machined and soldered into the cylindrical section. Model tips were fitted by installing a threaded mount in the nose section at a distance of 2.54 cm behind the pointed tip. The tips then screwed into the model nose for simplicity and ease of operation. A cylindrical guide section was used to insure proper alignment between the tip and the ogive. Each tip was machined while actually fitted in the ogive section, giving a very smooth junction and minimizing any step at this location to less than 5  $\mu\text{m}$  (2 mils).

Model A was instrumented with seven rows of pressure taps located at  $\phi=0^\circ$  (windside) to  $\phi=180^\circ$  (leeside) in increments of  $30^\circ$ . Each row contained 20 taps, beginning at  $X/D=2.925$ ,

0.075 calibers upstream of the ogive shoulder, and spaced every 1.27 cm. This allowed measurements at X/D locations from 2.925 to 6.425. Additional taps were located at X/D=2.925  $\phi=270^\circ$  and X/D=7.925  $\phi=0^\circ, 90^\circ, 180^\circ, 270^\circ$  to be used in model alignment and adjustment.

To monitor the temperature history of the model, three Chromel-Alumel thermocouples were also installed, flush with the model surface, at  $\phi=45^\circ$ , X/D=3.75, 5.5, and 7.5. All model temperatures in this study were obtained from the thermocouple at X/D=3.75 as previous tests showed little temperature variation with position. As mentioned in Section 4.1, stagnation temperature varied during each run and, therefore, so did the model temperature. An average run would last approximately thirty seconds and the stagnation temperature would drop approximately 3.0° K giving  $dT_o/dt \approx -0.1 \text{ }^\circ\text{K/s}$ . The model temperature would decrease in a constant effort to reach recovery temperature. Though this approach is asymptotic, the model would quickly cool and the ratio of the wall temperature to the recovery temperature would reach a fairly constant value. The ratio of  $T_w/T_r$  would vary, but was always between 1.00 and 1.06 with an average value being 1.03. With this ratio of  $T_w/T_r$  very close to 1.0, the model was assumed to be adiabatic.

#### 4.2.2.2 MODEL B

Model B was constructed in three major sections, a cylindrical body, a nose section and a tip section. The three sections were fitted together with cylindrical guides

and were held firmly in place with set screws. Only three model tips were used with Model B, the P, F3, and R3 tips. This allowed the most static pressure taps to be placed in the tip without excessive cost or time. The outside surface was machined with all three sections assembled and steps at section junctions were less than 5  $\mu\text{m}$  (2 mils). All set screws were placed well back on the model to prevent any wave interference on the pressure readings.

Model B was instrumented with 37 taps arranged along the nose in one axial plane. The nose could then be rotated so the taps were positioned in any desired axial plane. The taps would then give readings on opposing azimuth angles, i.e.  $0^\circ$ - $180^\circ$ ,  $30^\circ$ - $210^\circ$ . Pressure taps were concentrated near the tip and especially in the area where the tip shape faired into the original ogive shape. This provided the best possible documentation of the expansion of the flow through the transonic region. From experience with Model A, no thermocouples were installed as it was felt the model could be assumed adiabatic.

#### 4.2.3 MODEL INSTALLATION AND ALIGNMENT

The models were mounted on a sting and initially aligned geometrically on the centerline of the tunnel. A ball joint type mount was designed to allow movement of the models in the vertical plane only and could be adjusted to any desired angle of attack in the range of  $0^\circ$  to  $\pm 4.5^\circ$ . The sting could be moved from outside the tunnel, allowing the models to be

positioned in the same section of the tunnel and allowing easy adjustment of the model's position between runs.

To determine the zero angle of attack position, the pointed tip was installed on the models and a series of tests were made. Surface pressures were measured along the length of the model at azimuth angles of  $0^\circ$ ,  $90^\circ$ , and  $180^\circ$ . These pressure distributions were compared and the models were adjusted to locate the zero incidence position. Coarse adjustments were made using the ball joint mount and fine adjustments were made with six small set screws positioned circumferentially around the base of the cylinder. Adjustments were continued until surface pressures at the three azimuth locations fell within 2% of one another consistently along the length of the body.

All further adjustments from this zero position to the desired angle of attack were made geometrically. Using the distance from the pivot point of the ball joint mount to the model tip and the desired angle of attack, the displacement of the model tip was computed. The models were then adjusted to the desired incidence using a vernier height gauge.

#### **4.3 INSTRUMENTATION**

##### **4.3.1 SURFACE PRESSURES**

A total of 140 pressure taps were used to document the surface pressure distributions on Model A and 39 taps were used on Model B.

To measure the surface pressures on Model A, two groups of taps were formed with 60 taps in the first and 80 taps in the second. They were both, in turn, connected to two 48 port male Scanivalve connectors. Two Scanivalves were used, and therefore, two runs were required to totally document the surface pressures. Data collected in separate tests was compared to insure no discrepancies were present. Each Scanivalve was fitted with a  $1.034 \times 10^5 \text{ N/m}^2$  (15 psia) Druck differential pressure transducer.

Model B, with 39 taps, only required one 48 port Scanivalve. However, a larger Druck differential transducer with a range of  $0-3.45 \times 10^5 \text{ N/m}^2$  (0-50 psia) was used to measure the much higher surface pressures expected near the stagnation point.

During all runs, a vacuum of less than 100 microns was maintained on the reference side of the transducers. The Scanivalves were computer controlled. The results were recorded by the HP 1000 minicomputer described in Section 4.5. The pressure in the tubing to the Scanivalve was monitored to insure equilibration before data acquisition was initiated. This was done by observing the output voltage of a differential pressure transducer on a digital voltmeter. This transducer was attached to the Scanivalve tubing. When the voltmeter displayed a steady output voltage, indicating pressure equilibration, data acquisition was initiated.

#### **4.3.2 PITOT SURVEYS**

Boundary layer surveys were made along the windside ( $\phi=0^\circ$ ) and leeside ( $\phi=180^\circ$ ) meridians of the model for each model tip at Stations 2, 9, and 14 (values of  $X/D=3.175$ , 4.925, and 6.175 respectively).

Pitot probe tips were made from flattened tubing with a probe tip height of 0.18 mm (0.007 in). A sketch is shown in Figure 10 and a photograph of the probes is shown in Figure 11. Pressures were measured with a Pace differential pressure transducer with a  $0-3.45 \times 10^5 \text{ N/m}^2$  (0-50 psia) range referenced to vacuum. Probe displacements were measured using a linear reluctance type transducer mounted on the drive mechanism which was calibrated with a dial indicator gauge. The probe was traversed by hand, taking care to allow the transducer enough time to measure the pressure accurately at each displacement height before the probe was moved. This required slow movement in areas of steep pressure gradients, i.e. the lower 20% of the boundary layer. Data reduction is discussed in Section 4.5.

#### **4.3.3 OPTICAL METHODS**

Shadowgraph photographs were taken for all seven model tips at both  $0^\circ$  and  $2.9^\circ$  angle of attack. This gave a very good record of the bow shock wave shape. The boundary layer and any shock structure behind the bow shock were also clearly visible. Due to the difference in density profiles, a laminar boundary layer appears as a fine white line slightly off the

surface of the model, while a turbulent layer appears as a thicker, blurred region extending to the model surface. This gave an approximate location of the transition region of the boundary layer on the body. Standoff distances were determined by measuring forward from a point of known body diameter to the leading edge of the bow shock.

#### 4.4 ESTIMATION OF MEASUREMENT ACCURACY

##### 4.4.1 COMPONENTS OF THE DATA ACQUISITION SYSTEM

Individual components of the data acquisition system will be discussed and an overall accuracy assigned to each type of measurement. These accuracies will be given in both absolute dimensions and a percentage of a given reference.

Stagnation and pitot pressure measurements were made using Pace strain gauge differential pressure transducers with a vacuum used as a reference pressure. The Pace transducers have a nonlinearity of  $\pm 0.5\%$  of full scale deflection. This means an absolute error of  $\pm 6.9 \times 10^3 \text{ N/m}^2$  (1.0 psia) for stagnation pressure and  $\pm 1.7 \times 10^3 \text{ N/m}^2$  (0.25 psia) for pitot pressures. The transducers were calibrated with Wallace and Tiernan gauges accurate to  $\pm 0.066\%$  of full scale deflection. The accuracy of the calibration input pressures is limited to  $\pm 138 \text{ N/m}^2$  (0.02 psia) for stagnation pressure calibrations and  $\pm 69 \text{ N/m}^2$  (0.01 psia) for all other pressures measurements. Scanivalve measurements on the cylindrical body using Model A used a  $1.034 \times 10^5 \text{ N/m}^2$  (15 psia) Druck transducer with a maximum nonlinearity of  $\pm 0.06\%$  of full scale

or less than  $\pm 2.07 \times 10^2$  N/m<sup>2</sup> (0.03 psia). These transducers were also calibrated with the Wallace and Tiernan gauges.

Displacement measurements of probes were made using linear reluctance type transducers with a maximum non-linearity of  $\pm 0.025\%$  of full scale or  $\pm 12.7 \mu\text{m}$  (0.0005 in). These transducers were calibrated with dial indicators, which were accurate to  $\pm 12.7 \mu\text{m}$  (0.0005 in).

Temperature measurements were made with Chromel-Alumel thermocouples referenced to an ice bath. Calibration was performed by inputting voltages from the N.B.S. Tables using an accurate millivolt source as an input reference. The reference source was no more than 0.001 volt different from the specified input calibration voltage.

All measurements were fed into high impedance amplifiers where zero and gain adjustments could be made. A Preston GMAD-4 analog-to-digital converter was used to digitize all measurements for input to the HP-1000 minicomputer system, discussed in Section 4.5.

#### 4.4.2 MODEL ANGLE OF ATTACK

The model was geometrically set at the desired angle of attack by measuring the displacement distance of the tip from the zero angle of attack position. Determination of the zero angle of attack position was discussed in Section 4.2.3. Final measurements showed the agreement in pressure between the wind and leeside to be within 500 N/m<sup>2</sup>. Comparison of experimental measurements with

inviscid predictions of  $\Delta p/p^\infty$  between the wind and leeside shows that the zero angle of attack position is within  $0.25^\circ$  for all surface pressure measurements on the cylindrical body and pitot surveys. With Model B used to obtain the surface pressures on the ogive nose, the zero position is within  $0.25^\circ$ . Additional errors due to subsequent adjustment by geometric means are no more than  $\pm 0.05^\circ$ . To check that no movement of the model occurred during a test due to aerodynamic loading, a telescopic sight was used to observe the model's motion. The model experienced vibration upon tunnel startup and shutdown but this lasted only a few seconds. During the test the model was steady at the same position as before tunnel startup.

#### 4.4.3 SURFACE PRESSURE MEASUREMENTS

Surface pressure taps were drilled to be 0.4 mm (15 mils) in diameter and great care was taken during machining, installation, and operation to insure taps were not blocked by dust or burrs. To prevent any inaccuracy in the measurements due to the delay of pressure equilization in tubing to the Scanivalve, a monitor was used to insure steady pressures throughout the system. This was discussed more fully in Section 4.3.1. Readings were taken at a rate of three per second to insure the Scanivalve transducer had reached equilibrium. Calibrations were obtained with a possible error of less than  $\pm 200 \text{ N/m}^2$  (0.03 psia). Combining possible calibration

and transducer errors, the overall accuracy of the surface pressure measurements is within  $\pm 200 \text{ N/m}^2$  (0.03 psia) or  $\pm 1.0\%$  of freestream static pressure.

#### **4.4.4 PITOT SURVEYS**

Pitot probe details were discussed in Section 4.3.2. Pressure and displacement measurements were made at the rate of three per second while the probe was being traversed and, in most cases, approximately one hundred readings could be obtained in the boundary layer region. Probe interference was determined to exist within a distance of 1.5 probe heights from the model surface. This was determined by placing the pitot probe tip above a static pressure tap and observing the static pressure as the probe was moved toward the wall. Any points within this interference region were deleted from all boundary layer surveys before analysis. Calibration procedures and equipment specifications combine to give pitot pressures within  $\pm 1.72 \times 10^3 \text{ N/m}^2$  (0.25 psia) and probe displacement measurements an accuracy of within  $38 \mu\text{m}$  (0.0015 in).

#### **4.4.5 OTHER MEASUREMENTS**

All measurements of stagnation pressure are within  $\pm 6.9 \times 10^3 \text{ N/m}^2$  (1.0 psia). Temperatures are accurate to within  $\pm 1.0^\circ \text{ K}$ .

### **4.5 DATA REDUCTION**

All data acquisition, storage, and subsequent reduction was carried out using the HP-1000 Minicomputer Facility at

the Gas Dynamics Laboratory. Programs developed at the Gas Dynamics Laboratory were used in conjunction with a Preston GMAD-4 analog-to-digital converter to control Scanivalve movements and readings, pitot survey pressure and height measurements, as well as temperature and stagnation pressure readings.

#### **4.6 PROBE DEVELOPMENT**

Pitot surveys were made with a standard pitot probe connected to a strain gauge transducer by a length of tubing about one meter long. The time required for the pressure to equalize throughout the system was relatively long and caused the careful measurement of one survey to require a long tunnel run time. Even more important, the long run time consumes a large portion of the air supply and, in turn, reduces the number of tests available from a given amount of compressed air.

With the development of modern miniature pressure transducers, an attempt was made to improve survey efficiency by developing a probe with the transducer mounted internally as near to the probe tip as possible. This reduced the ratio of pressure tubing length to tubing inside diameter, indicative of the equilibration time, from roughly 1500 to 250, or about one order of magnitude. The internal volume of the pressure transducer would also be reduced with a smaller transducer.

The transducer should be as small as possible and have an operating range of roughly  $0-3.45 \times 10^5 \text{ N/m}^2$  (0-50 psia).

Several transducers were available that meet these requirements. The Entran EPI-093-50 was selected because of economic and scheduling factors. It is a differential transducer, 0.093 inches in diameter, with a range of  $0-3.45 \times 10^5 \text{ N/m}^2$  (0-50 psia). A special reference tube was mounted to extend out of the probe shaft. Due to its small size, the transducer had inherently high frequency response, but the output voltage was passed through a low pass filter with a corner frequency of 10 Hz to filter out any high frequency readings due to the tunnel fluctuating pressures.

A probe shaft was designed and constructed in the Forrestal Machine Shop. The transducer was internally mounted with the reference pressure tube and output wires extending out of the top. The probe is pictured in Figure 11 and a detailed sketch is shown in Figure 12. The probe tips were fitted into the probe shaft with a threaded fitting to allow different tips to be used for different applications.

The probe was tested to insure no leaks were present and then used in the wind tunnel. The boundary layer on the model was surveyed slowly with the Entran probe to give a base line survey. In succeeding tests, the probe speed was increased and the equilibration delay in the data acquisition system decreased. The surveys obtained were compared and typical results are shown in Figure 13. Points in both surveys were taken at a rate of four per

second with a total test time for Test 4 of about 40 second compared to 10-12 seconds for Test 7. No real discrepancy can be seen in the boundary layer region,  $Y < 3$  mm, though above 16 mm there is some discrepancy. This is due to a slight variation in the position of the reflected bow shock.

Results indicated survey times could be reduced by a factor of three to four which provided a large savings in the air used for a given test. Combined with the additional supply air that was compressed between tests, the loss of supply pressure for each test was reduced to between  $3.45 \times 10^5$ - $5.17 \times 10^5$  N/m<sup>2</sup> (50-75 psia). This provided a capability for nearly 40 runs from a full supply capacity. This is a significant improvement over the previous techniques where each test reduced the supply pressure by about  $1.20 \times 10^6$  N/m<sup>2</sup> (175 psia). Though actual improvements will vary with the application and method, savings of this magnitude have been achieved with several other experiments and tunnel configurations where this probe has been used at the Gas Dynamics Laboratory.

## RESULTS AND DISCUSSION

### 5.1 GENERAL FLOWFIELD CHARACTERISTICS

A brief discussion of the general flowfield is given to provide an overview of the present study. Figure 14 shows a sketch of the general flowfield. The numbered areas in the figure will be referred to in the text.

A sharp tipped body of revolution travelling at supersonic speeds is shown in Figure 14a. The tip is assumed infinitely sharp. The shock wave is attached and, very near the tip, the shock angle can be well predicted by conical theory. The flow expands gradually over the ogive nose as it passes through region 4 and returns to the freestream flow direction, within allowances for the displacement surface effect. As the expansion waves from the ogive nose reach the bow shock, the shock strength is decreased and a gentle shock curvature results. The curvature of the shock is proportional to the curvature of the body. Far from the body, the flow direction is unchanged, so the shock must approach zero strength, i.e. a Mach wave. If this did not occur, the body would have an infinite wave drag and flight would be impossible. The flow over the cylindrical afterbody (region 5) continues to experience the normal viscosity effects and, at zero angle of attack when the boundary layer

thickness is small compared to the body diameter the boundary layer parameters can be correlated with the flat plate case.

As the shock from 1 to 3 is only slightly curved, flow properties directly behind the shock do not vary substantially along its length. As the fluid expands over the shoulder it will have thermodynamic properties ( $\rho$ ,  $p$ ,  $T$ ) which are fairly constant in the direction normal to the body surface. This will be true for a distance from the body surface which is large compared to the boundary layer thickness. The boundary layer will develop in a region that has very small shock curvature effects, i.e. rotationality and thermodynamic property gradients. It is clear, when Figure 2 is examined, that the rotationality effect outside of the boundary layer region is small in comparison to the boundary layer.

For the blunted case, Figure 14b, a radically different situation is present. In this case, a detached, curved bow shock exists ahead of the body. Near the center of the bow shock, region 1', a portion of the shock wave is effectively normal. A subsonic flow region is produced behind the shock, here shown as region 3'. A sonic line exists as the flow accelerates around the corner of the blunt tip. The location of the ends of the sonic line may be determined from the shock relations and the turning angle to give sonic flow behind the shock. The shape of the sonic line is not easily determined and

is discussed in Hayes and Probstein (26). The shape of the sonic line will determine the effect that body shape may have on the transonic region of the flow. If the characteristics from the body in the transonic region reach the sonic line, these characteristics will exert an influence on the sonic line and, therefore, the entire subsonic region. Any disturbance to body shape, such as ablation in a real flow, will be reflected as a change in the subsonic region of the flow.

As the fluid in the subsonic region accelerates, it will turn to pass around the model tip and follow the surface of the body. This turning of the flow generates very large expansions in region 4', depending on the body shape. The sharp corner shown here is the most extreme case. Inviscid theory would predict an infinite pressure gradient at this point as the radius of curvature of the fluid streamlines near the surface is almost zero. The bow shock ahead of the body, prior to the interaction of the expansion fan in region 4', will be slightly curved. In region 4' the interaction of the expansion with the bow shock will decrease the bow shock strength more rapidly than before the interaction. The turning angle of the flow through the shock will be zero on the centerline, increase along the shock to reach a maximum near the end of the sonic line, and decrease to zero far from the body. As in the pointed body case, the bow shock must decrease in strength and become a Mach

wave far from the body.

The region 5', near the tip following the expansion at the corner, is a region where the flow may adapt in various ways to the expansion through region 4'. For the radical flow direction changes that occur around the tip corner, the fluid may overexpand in turning the corner. A recompression shock, 5', will occur in this region to adjust the flow to the proper conditions. Some investigators have observed that the flow separates because it cannot follow the body surface around the corner. In reattaching, the flow must turn through a small, but nonnegligible angle, producing a reattachment shock. Another possible cause of a recompression shock is a complicated wave pattern formed by the reflection of the expansion fan from the sonic line and bow shock as a series of compression waves which coalesce to form a compression shock. This is discussed by Perkins et al (27). Experimental results show these mechanisms are both very geometry dependent, and either may be the cause of a recompression shock for a given geometry with different flow conditions.

The expansion region 6' is again present as the flow turns to follow the body, and the pressure decreases. In region 7', the flow direction has returned to roughly the original direction.

The layer of fluid close to the body is not only rotational, but has gradients in the thermodynamic

properties due to the shock curvature. As the boundary layer develops next to the body it will lie at the bottom of this region and, may eventually, totally contain the region. The shock curvature is highest in the region where the bow shock and expansion in region 4' interact and approaches zero at an infinite distance from the body. The shock angle is a maximum at the stagnation streamline and decreases to the Mach angle at infinity. The fluid near the stagnation streamline, which will be at the bottom of the boundary layer, will have an entropy rise due to the strong shock and a velocity gradient will exist across the streamlines due to the shock curvature. As each streamline is entrained into the boundary layer, it will be in a unique state and have a different history. This region is discussed by Hayes and Probstein (26) as the entropy wake, a region where the flow has markedly higher entropy due to passing through a strong shock wave.

### 5.2 BOW SHOCK SHAPE AND STRUCTURE

The flowfield around the model was visualized with a shadowgraph optical system. Since the shadowgraph visualization system is sensitive to the second derivative of density, it provides a good record of the bow shock shape. It has the disadvantage that little quantitative information can be obtained.

Shadowgraphs were taken of all seven model tips at  $0^\circ$  and  $2.9^\circ$  angle of attack (Appendix A). Several

general features of the flow structure may be noted quickly. All blunt noses give a detached, curved bow shock. The pointed tip produces an attached shock wave which is slightly curved due to the expansion around the ogive nose of the body. Some cases of bluntness produce interior shocks (shocks behind the bow shock), e.g. A-7. These may be due to an overexpansion of the flow around the tip corner or a complicated wave pattern as discussed in Section 4.1. This shock can be seen just behind the corner of the flat tips. Its strength seems to increase with bluntness. A complex series of interior shocks is seen on the windside of the model at angle of attack, e.g. A-10. These shocks appear to increase in strength with increasing hemispherical bluntness at a fixed angle of attack. The same shock system is strongest for the small flat tip and disappears in the two larger flat cases. It will be shown later, however, that all these shocks are actually very weak and that the shock strength cannot be judged from the photographs. The weak wave which appears at roughly  $X/D=0.5$  for the pointed tip (e.g. A-1), and in a corresponding position for the other tips, is due to the small junction step where the tip screwed into the model.

#### 5.2.1 BOW SHOCK ANALYSIS

Following the analysis of Van Dyke and Gordon (21) bow shock shapes were fitted to the equation

$$r^2 = 2R_s X - B_s X^2 \quad (1)$$

where  $r$  and  $X$  are the coordinates of the shock position in a cylindrical polar system originating at the shock vertex. This equation may define any conic section and gives some basic insight into the interaction of the body and the shock it produces.

The nose radius of the shock,  $R_s$ , is the radius at its vertex and is indicative of the vorticity in the fluid near the stagnation streamline. This fluid will be the first to be affected by the body and is important in the early development of the boundary layer. The bluntness parameter,  $B_s$ , is a measure of the eccentricity of the shock.  $B_s = -1$  for a hyperbolic section and  $B_s$  is 0 for a parabolic section. A hyperbola eventually approaches an asymptote and the curvature of the shock therefore decreases. It decreases for a parabolic shock as well, but much more slowly. The bluntness parameter,  $B_s$ , may be used to indicate the amount of the fluid that has passed through a curved shock wave. As  $B_s$  becomes more positive from the hyperbolic value of -1, a larger portion of the downstream flowfield will have passed through the curved shock wave with the associated entropy gradient.

Shock wave shapes were transferred from the photographs to graph paper by optical means and coordinates of the shock position were taken from the graph. A least squares polynomial fit was used to obtain the

coefficient values. The curve fits obtained were accurate to within 5-10%. The choice of the coordinate system poses a problem. The X axis was aligned with the model axis for this comparison. It was also placed along the undisturbed freestream flow direction and the results were roughly comparable. This is due to the small angle of attack present, and not indicative of the independence of the proper choice of the axis system.

Table 1 presents the values of  $R_s$  and  $B_s$  obtained from the shock curve fits. Examination of Table 1 reveals several clear patterns.  $R_s$ , at zero angle of attack, increases with the bluntness of the nose. When the values of  $R_s$  are placed in order of increasing magnitude, the round and flat tip values alternate. Although the round and flat tips present roughly the same blunted cross sectional area, a strong difference in the shock structure exists causing this behavior. This is understandable from the aspect of blast wave theory (28). Here, a blast wave or piston-wave analogy is made for the blunted tip. The factor which typifies the tip is the energy imparted to the fluid in the unsteady analogy. This energy may also be interpreted as the drag due to the tip blunting. Clearly the variation of drag with tip blunting would give a pattern of roughly this alternating type. This pattern is repeated in  $B_s$  but is not exactly the same, as the values of  $B_s$  for both the F2 and F3 tips are more positive than the value of

$B_s$  for the R3 tip. With angle of attack  $B_s$  decreases on the windside for a given tip and increases on the leeside. No clear trend is seen in the changes in  $R_s$  at an angle of attack.

The quantities  $R_s$  and  $B_s$  can be translated into shock curvature,  $\kappa$ . With the basic equation of curvature

$$\kappa = \frac{r''}{\{1 + (r')^2\}^{3/2}} \quad (2)$$

where

$$r = f(x) \quad (3)$$

the equation for curvature for these conic sections can be derived as

$$\frac{-B_s(2R_sX - B_sX^2)^{-1/2} - (R_s - B_sX)^2(2R_sX - B_sX^2)^{-3/2}}{\left[ \frac{X^2(B_s^2 - B_s) + X(2R_s - 2R_sB_s) - R_s^2}{2R_sX - B_sX^2} \right]} \quad (4)$$

When the values of  $R_s$  and  $B_s$  are substituted and the values of  $\kappa$  compared for model tips the results are much clearer.

Table 2 presents the curvature at  $X/D=0.5$  for all seven tips. The pattern of increasing  $R_s$  is again seen at zero angle of attack, but is now also present at angle of attack. A small angle of attack should not produce a marked change in the shock shape. Figure 15 shows a comparison of  $\kappa$  along the shock for the R2 tip at  $0^\circ$  and  $2.9^\circ$  angle of attack. The curvature of the shock wave is increased on the windside and decreased on the leeside of the body at an angle of attack. This can be paralleled

This contrasts with the present study where the inflection point location is not at a fixed number of tip diameters. Results of this study are shown in Figure 16. Further analysis showed that the location of the inflection point was not dependent on the tip bluntness but, rather on the shock strength and the local surface inclination at the point on the body where the shock originates. Since with this model the surface inclination varies monotonically along the axis, tip bluntness and the local inclination angle can be correlated. If the inflection point is plotted versus  $\theta_c$ , the local inclination at the corner of the flat tip, the results shown in Figure 17 are obtained. The three points obtained from this study show an approximate linear trend and are compared with the results of Geise and Bergholdt for 15° half angle truncated cones. Present results give a higher value of  $x_i/d_t$  at  $\theta_c=15^\circ$ , but it is felt that this is due to a Mach number effect as the recompression shock would have a larger inclination at  $M=2.45$  than at  $M=3.0$  for an equal shock strength. This would in turn give a lower value of  $x_i/d_t$ . No similar observation can be made for the hemispherical tips. This is in agreement with the findings of Perkins et al (27) who found this recompression phenomenon was very geometry dependent. This discussion must be qualified as no information on shock strength was available. This discussion does however give a good insight into this recompression and bow shock phenomenon,

in blast wave theory as well since less energy would have to be imparted to the fluid around the nose on the leeside and more would be required on the windside. This is also seen in Table 2 for all the model tips except the F2 and F3 tips.

Insight into these trends and other features of the flowfield is gained through the discussion given by Bennet (29). The features of the bow shock can be related to the interaction between the bow shock on the centerline and the expansion fan originating as the fluid turns to follow the surface. As the expansion fan interacts with the bow shock, the shock strength decreases and a decrease in the bow shock angle is present. This fan is clearly visible in the photographs of the flow near the tip, e.g. A-11. The flat tips have a noticeable shock emanating from the tip corner. This is due to a recompression following an overexpansion of the flow around the corner (Section 5.3.1). The shock is produced as the expansions reflected off the sonic line and bow shock as compression waves coalesce. The recompression shock can be seen to produce a small sharp increase and inflection point in the bow shock angle for the flat tipped models. This is due to the increase in shock strength as the two compression waves interact. Geise and Bergholdt (30) noted this in a study of truncated cones at  $M=2.45$ . They noted the inflection or interaction of the two shocks occurred between 13 and 16 tip diameters behind the shock vertex.

but does not deal with the many difficult points involved.

### 5.2.2 SHOCK DETACHMENT DISTANCE

Predictions of detachment distance were made using the methods proposed by Leipman and Roshko (31), Love (32), Kaatari (33), and Guy (34). These predictions are plotted in Figure 18. All show a similar trend and are in fair agreement.

Experimental determination of the actual standoff distance from the shadow photographs available was discussed in Section 4.3.3. For the small blunting, where  $\Delta$  is also very small, inaccuracies in the measurements resulted in a negative standoff distance. This is, of course, physically impossible.

With the geometry involved, the standoff distance would be small for most of the cases examined. Measurements of these distances is not possible with the accuracy necessary to obtain reliable values. The F3 tip, which has a geometry large enough to allow accurate measurement, does give a standoff distance in good agreement with Love (33) and Leipmann and Roshko (31).

## 5.3 MODEL SURFACE PRESSURES

### 5.3.1 OGIVE NOSE

Figures 19 and 20 show the surface pressure distributions on the ogive nose obtained with Model B for the pointed tip. Pressure taps were only available from  $X/D=1.25$  to 2.75.

As expected with the pointed tip, the pressure decreases monotonically along the ogive nose in a smooth curve. When compared with theoretical methods, the tangent cone method is seen to give the better prediction of the surface pressures but even this method is not good over the forward portion of the tip. The tangent cone method gives fairly good agreement at  $0^\circ$  angle of attack but is slightly less accurate at  $\alpha=2.9^\circ$ . At angle of attack, the pressure is higher on the windside than the leeside. The discrepancy in readings at  $X/D=1.275$  is due to an impinging wave from the tunnel section junction. These results are in agreement with expectations and show no unexpected behavior.

Pressure distributions on the R3 tip are shown in Figures 21, 22, and 23. Note that the measurements of  $X/D$  are taken from the virtual pointed tip of the ogive. The model tip is located at  $X/D=0.309$  for this case. The figures show both the pressure along the entire nose for the R3 tip and a comparison of the pressures for the R3 and P tips on an expanded scale. The pressure is a maximum at the stagnation point and decreases very rapidly around the tip as the flow expands through the transonic region. The pressure gradient exceeds  $1.85 \times 10^7 \text{ N/m}^2/\text{m}$  ( $6.83 \times 10^1 \text{ psi/in}$ ) around the tip corner for zero angle of attack. The pressure relaxes to the ogive surface pressures almost instantaneously after passing the tangency point between the hemisphere and the ogive. Again, at angle of attack, pressures are

higher on the windside and lower on the leeside as expected. The pressure gradient at the tip is decreased on the windside and increased on the leeside at incidence. The results compare well with Perkins et al (27) who examined the surface pressures on blunted cones. They found that at lower Mach numbers an overexpansion and recompression occurred near the sonic point or tip corner. Their results show this overexpansion is very small at Mach numbers near 3.0 for hemispherically blunted tips and present results confirm this. The pressure distributions show that the series of interior shocks on the windside of the model at angle of attack are of very low strength (see Section 5.2). These are felt to be due to the wave system discussed in Section 5.1 and by Perkins et al (27). The geometry dependence of this wave system is confirmed by these results. They produce no noticeable effect on the surface pressures. This shows that the strength of these interior shocks cannot be judged from the shadowgraphs that were taken. When theoretical pressure coefficients are compared, the modified Newtonian theory predicts the pressures on the hemisphere quite well. The tangent cone method remains more accurate on the ogive section. This is valid at all angles of attack examined.

Surface pressure distributions for the F3 tip are plotted in Figures 24, 25, and 26. The model tip is at  $X/D=0.404$  and the first three points were all taken on

the flat face. The first was on the centerline, the second halfway to the tip corner, and the third was about 2 mm from the tip corner. They are spaced apart for clarity. Again a comparison with the pressures for the P tip is shown on an expanded scale. The most striking feature is the series of pressure changes near the tip corner. The flow around the corner experiences a very large pressure gradient and overexpands around the tip. A recompression shock raises the pressure again and then a slight relaxation to the normal ogive values is present. This behavior is validated by the shadowgraphs as discussed in Section 5.2. The minimum pressure seems to be unaffected by model angle of attack or azimuthal position. The recompression is stronger on the windside and the recompression shock strength increases with increasing incidence. The converse is true on the leeside with a smaller recompression than on the windside and a decrease in recompression shock strength with increasing incidence. The location of the compression shock measured from the shadowgraphs is shown in the figures to verify the position of the compression.

When compared to theoretical methods, it is clear that neither Newtonian or modified Newtonian pressure coefficients are completely adequate as the pressure is not constant across the tip face as would be predicted. The surface pressure decreases at the edge of the tip due to the beginning of the corner expansion. However,

near the center of the blunt face, modified Newtonian theory again predicts the pressure fairly accurately.

For both the R3 and F3 tips, the pressure distributions returned to the normal ogive nose values very quickly following the immediate area of the blunted tip. The distance required for the pressure to normalize to the ogive values will be designated as  $x_{ew}$  or the entropy impingement distance (36). Downstream of this point, the entropy wake no longer has any influence on the surface pressures on the model except through its influence on the displacement surface to be discussed later.

### 5.3.2 CYLINDRICAL AFTERBODY

Surface pressures on the cylindrical afterbody were measured as described in Section 4.4.3. Figures 27, 28, and 29 show surface pressures along the body for  $\alpha=0^\circ$  and  $\alpha=2.9^\circ$  for all seven model configurations. Within experimental accuracy, model tip geometry has no effect on the surface pressures over the cylinder. This is valid at the angle of attack examined. Pressures at the last two locations have been affected by the reflected bow shock. The scatter at the first data point in Figure 27 and  $X/D=3.5$  in Figure 28 is due to an impinging wave from the tunnel junction.

This lack of dependence on tip shape is explained in the following way. If the problem is considered as

totally inviscid, all tip bluntness effects on the surface pressures are concentrated near the tip and are due to the change in the shock wave and expansion structure. It may be stated that once the flow has passed  $x_{ew}$  all shocks and expansions associated with the tip bluntness are upstream. The inviscid features of the flow are the same downstream of  $x_{ew}$ , whether the tip is pointed or blunted.

With the inclusion of viscous effects, the same arguments are valid for any shock structure present. Displacement surface effects being the only major difference between the inviscid and viscous cases, it may be concluded that displacement surface effects are very insensitive to tip bluntness as well. The change in the growth of the displacement surface may be significant, but will produce only a small change in the effective body shape. This will produce surface pressure changes, but the change may be too small to be seen at this small angle of attack. The tip bluntness has no major effect on the surface pressure distribution on the cylindrical body at small angles of attack.

### 5.3.3 COMPARISON WITH COMPUTATIONAL RESULTS

Computational results for surface pressure distributions are only available for the pointed tip. Results of the PNS code have not been received and so only the BL code results will be used.

Figure 30 shows a comparison of model surface pressures at zero angle of attack with the computational results. The

lower solid line shows the results of an inviscid calculation. The upper solid line shows the results of a viscous calculation which included displacement surface effects as described for the BL code. Both codes predict the pressure distribution trends well and the displacement surface effects seem to make very little difference in the computation except very near the ogive cylinder junction. However, the computational results tend to be lower than the experimental results along the total length of the body. Comparisons at 2°, 4°, and 5° angle of attack have also been made (1,2). All showed the BL code was capable of predicting the surface pressure trends in both the streamwise and circumferential directions, but did not predict the surface pressure correctly. Displacement surface effects produced little variation in the surface pressures and do not appear to be critical within the range of angle of attack examined.

#### 5.4 BOUNDARY LAYER TRANSITION

An examination of the shadowgraph photographs was made to determine the transition region. Over the ogive nose, the boundary layer was generally less than one millimeter in thickness which makes observation difficult.

Figure 31 shows the location of the transition region in terms of the centerline distance  $X$ , with the origin at the virtual point of the ogive. Results are shown for both  $\phi=0^\circ$  and  $\phi=180^\circ$  at  $\alpha=0^\circ$  to give an estimate of accuracy.

At zero angle of attack, transition seems to move downstream slowly with increasing tip bluntness. The flat tip blunting seems to cause transition upstream of both the pointed and hemispherical tips. As the model is moved to an angle of attack, transition appears to move upstream on the leeside and be shifted downstream on the windside.

Another comparison was made using the surface distance,  $s$ , or the distance the fluid has travelled along the surface of the body from the stagnation point. Figure 32 shows the transition region, where plotted in terms of the surface distance,  $s$ , is rather insensitive to hemispherical blunting at  $\alpha=0^\circ$ . Flat blunting causes a small forward movement of the transition region with increasing bluntness. With angle of attack, transition again moves forward on the leeside and rearward on the windside.

Ericsson (36) presented a very complete discussion and outline of the importance of the entropy swallowing process on transition. Entropy swallowing is the process of entraining all of the fluid with higher entropy due to the strong portion of the bow shock into the boundary layer. Ericsson finds that windside transition is guided by entropy wake swallowing very strongly and this is supported by the present data. At angle of attack, more distance will be required to complete the entropy swallowing and consequently transition is retarded. On the leeside

Ericsson found that transition is dominated by crossflow effects. Comparison with his results is not possible as his tests were made at hypersonic speeds. He concluded that transition moved forward (as it does in this case) because of the increasing crossflow effect at angle of attack.

Transition on blunted bodies is influenced by two main factors, as discussed by Stetson and Rushton (35). These factors are a reduction in the Reynolds number due to the blunting and the variation of the transition Reynolds number with tip blunting. With tip blunting, the Reynolds number decreases tending to move transition aft while the variation in transition Reynolds number with tip blunting tends to move the transition location forward. They found that increasing bluntness delayed transition initially but that a reversal occurred eventually and the transition location would move forward again. This is because the decrease in the transition Reynolds number with tip blunting is much larger than the reduction in Reynolds number due to tip blunting. This is seen in the present study as increasing hemispherical blunting delays transition while increasing the bluntness to a flat tip brings the transition region forward again.

No comparison of the present experimental data with others is possible with any confidence because of the inaccurate determination of the transition region and the small amount of data on the entropy wake effects for the

cases considered.

### 5.5 BOUNDARY LAYER ANALYSIS

To obtain boundary layer velocity and Mach number profiles, the static pressure was taken to be constant in the normal direction and equal to the wall pressure and a total temperature profile, suggested by Settles, 1975, was assumed with

$$T_o = T_{o\infty} [1.0 + 0.05(1 - \frac{y}{\delta})] \quad (5)$$

While this is an approximation to the actual total temperature distribution, the profiles that are obtained are very insensitive to the temperature distribution.

Figure 33 shows typical pitot pressure profiles for a case of moderate blunting and the pointed tip. The edge of the boundary layer is not well defined for the K2 tip. For the blunted case, the strong shock curvature effect present produces normal derivatives of the flow properties much larger than those encountered with a pointed tip. These flow property gradients tend to make the boundary layer region more difficult to distinguish. Using the wall static pressure, the assumed total temperature profile, and a first estimate of the boundary layer edge made from the pitot profile, these surveys were reduced to give the velocity profiles shown in Figure 34. Now the edge of the boundary layer is more definite in both cases. The P tip has no velocity gradient outside the boundary layer, while a small

velocity gradient is present outside the boundary layer for the R2 tip. This problem was encountered in the reduction of many of the surveys made. The problem became more pronounced with increasing tip bluntness, at forward survey locations, and on the leeside at angle of attack. An iterative process was used until the selected boundary layer thickness was judged to be near the true value. Only the integrated values of displacement and momentum thickness can be presented with any real confidence. Velocity profiles for all model tips at Stations 2, 9, and 14 are graphed in Appendix B for  $0^\circ$  and  $2.9^\circ$  angle of attack.

Analysis was also performed by using an "in house" program to fit the experimental data to the Law of the Wall-Law of the Wake profile. This program was based on a code developed by Sun and Childs (37). It uses an iterative technique to vary the parameters of the Wall-Wake Law until the deviation of the experimental data from the Wall-Wake Law is minimized. While the Wall-Wake Law was developed for the flat plate turbulent boundary layer and may not be technically correct for the analysis of these profiles, it was utilized as it was felt to provide a good method to show the boundary layer development. This method of locating the boundary layer edge is the least arbitrary so it is felt to be the best indication of the boundary layer development.

All surveys examined were analyzed with this program and good Wall-Wake curve fits were obtained. The values

of the boundary layer parameters were then computed from the fitted Wall-Wake Law velocity profile. They are accurate to within  $\pm 10\%$ . These values are more accurate as the lower portion of the boundary layer was included in their computation. This region had to be deleted from experimental surveys due to probe interference and, for some cases at Station 2, the deleted section constituted a major portion of the boundary layer.

To provide a comparison of the fullness of the boundary layer, the power law

$$\frac{u}{U_e} = \left(\frac{y}{\delta}\right)^{1/n} \quad (6)$$

was utilized. Though only valid over the central portion of the layer for the turbulent compressible boundary layer, it provides a simple estimate of profile fullness. The values of  $n$  were obtained by taking the logarithms of the  $y/\delta$  and  $u/U_e$  profiles and then obtaining a least squares linear curve fit to obtain the slope which then gives the value of  $n$ . This method is felt to be more accurate than the graphical analysis of Beck (1). Values of  $n$  are estimated to be within  $\pm 0.15$ .

Tables of the most important boundary layer characteristics are contained in Appendix C for future comparison and use. The source of all values and an estimated accuracy is given.

The boundary layer development will be examined first at zero angle of attack in an attempt to understand the

effect of tip bluntness. Then a discussion of the windside and leeside boundary layers will follow. Finally a summation of the observed trends and effects will be made.

#### 5.5.1 ZERO ANGLE OF ATTACK

Boundary layer surveys at zero angle of attack were analyzed as discussed above. A favorable gradient is present over the nose. A very slight adverse pressure gradient is present along the body after the ogive cylinder junction. The boundary layer must undergo some deceleration near Station 2. These pressure gradients are shown in Figures 19 and 27, and are discussed in Section 5.3.

A plot of displacement and momentum thickness along the body is shown in Figure 35. Both  $\delta^*$  and  $\theta$  increase with  $X$  as would be expected. This increase is very nearly linear for the momentum thickness and is generally linear for the displacement thickness but some cases of tip bluntness exhibit a different behavior. The two most blunt tips, F3 and R3, produce a much more rapid increase in  $\delta^*$  and  $\theta$  than the other tips. While this appears to be linear it is probably some power function of the Reynolds number. However, in this range of Reynolds number it is effectively linear. Figure 36 shows a plot of  $\delta^*$  and  $\theta$  versus the tip radius for each station. It is seen that the values of  $\theta$  increase with increasing tip bluntness at each station. Displacement thickness does not correlate well with tip bluntness at Stations 2 and 9,

but tends to exhibit a scaling effect at Station 14. This will be discussed later. The values of  $\theta$  increase with increasing tip radius more rapidly for the flat tips than the hemispherical tips. At larger values of  $X$  momentum thickness increases more rapidly for both the flat and hemispherical tips. The values of  $\partial\theta/\partial x$  therefore seem to be dependent on both station or  $X$  and tip geometry. The values of  $\delta^*$  are believed to behave in a similar manner though a linear behavior is not necessarily supported. At Station 9, the hemispherical tip values of  $\delta^*$  scale fairly well on  $R_b$ , but this is not true for the flat tips or at Station 2.

If the plot of  $\theta$  versus station is examined, the values of  $\theta$  increase with increasing bluntness. The values of  $\theta$  at Station 2 are about the same for all model tips and vary by only 40-50% from the pointed case. Knowing from the physical standpoint that  $\theta=0$  at the pointed model tip, the variation of  $\theta$  at Station 14 tends to show that the value of  $\partial\theta/\partial x$  is dependent on tip geometry. If the values of  $\partial\theta/\partial x$  are plotted versus  $R_b$ , a clear trend is seen. For each geometry of the model tip (hemispherical or flat),  $\partial\theta/\partial x$  increases approximately linearly with  $R_b$  as shown in Figure 37. Also shown is a plot of  $\partial\delta^*/\partial x$  versus  $R_b$ . A fairly clear scaling trend is seen here as well. There seems to be a clear dependence on  $R_b$ , but the functional form is not obvious.

Figure 35 shows a plot of  $H$  versus station for each model tip. If the value of 5.1 is assumed as the asymptotic value of  $H$  from the pointed tip behavior then the R3 and F3 model tips produce a boundary layer that takes more time to adjust to the conditions present. The boundary layer seems to be in a different condition, dependent on the model tip, and not all cases of model tips produce a boundary layer that has reached a constant condition at the stations examined. It is also seen that  $H$  generally decreases with increasing tip bluntness as shown in Figure 36. This reflects the fact that the boundary layer profile is less full and can be thought of as having had a shorter history due to the unit Reynolds number reduction caused by the tip bluntness. The form factor of the boundary layer seems to be retarded by tip bluntness.

The results of the power law analysis are plotted versus station and tip bluntness in Figure 38. The boundary layer is still strongly influenced by the strong favorable pressure gradient over the nose at Station 2 and this is evidenced by a relaxation of the boundary layer from Station 2 to 9. The boundary layer when subjected to the favorable pressure gradient over the nose develops in a fuller form and then must decelerate as it is affected by the adverse gradient along the body. The fullness, as indicated by  $n$ , then increases again at Station 14. This reflects the general increase in  $n$  with increasing  $Re_\theta$ . This is in agreement with the results that

Settles (38) and Beck (1) obtained with the same model. The plot of  $n$  versus  $R_b$  shows the decreasing pattern of  $n$  with tip bluntness at Station 14. This same pattern is not clear at the other stations but the influence of the relaxation is felt to be strongly involved here. A pattern which reflects the actual behavior of  $n$  with tip bluntness may not reveal itself until well after the boundary layer has readjusted to the adverse pressure gradient over the cylinder.

Figure 39 shows a plot of  $\pi$ , the wake strength parameter versus station and  $R_b$ . The consistent pattern seems to be an increase in  $\pi$  from Station 2 to 9 and a decrease from Station 9 to 14. Only the F3 tip does not follow this pattern. It is also seen that  $\pi$  scales with  $R_b$  at Station 14 but this is not true at Stations 2 and 9. This is again believed to be because of the relaxation at the forward stations discussed in connection with the power law exponent,  $n$ , which exhibits a similar behavior.

The values of skin friction coefficient are plotted versus  $Re_6$  in Figure 40. The skin friction coefficient was computed as a part of the Wall-Wake Law analysis. Comparison of the computed values from the Wall-Wake program with experimental values for the floor of the tunnel is good. The trends indicate that  $C_f$  decreases with increasing distance along the body, as would be expected. The variation of  $C_f$  for different model tips at a specific station also becomes less with an increasing

axial distance. The reduction in the scatter of values at a specific station is due to the dissipation of the tip bluntness effects as the boundary layer continues to develop. Also plotted is a comparison with the skin friction coefficient predicted by the Van Driest II method with a recovery factor of 0.897. The general trend is well predicted but the slope is generally steeper for the experimental data. The discrepancy is due to the fact that the Van Driest II method was developed for flat plate boundary layers. In this layer, where an adverse gradient is present, the values of  $C_f$  would decrease more rapidly as the layer decelerates due to the pressure gradient. As well, the value of skin friction coefficient increases with increasing tip bluntness and is always markedly higher for the cases of large tip blunting. This is due to the fact that the large tip blunting gives a reduction in Reynolds number and effectively shortens the wetted length.

The results for Station 2 are felt to be affected not only by the tip bluntness but also the pressure gradient. At Station 2, the boundary layer is just leaving the ogive nose where it is affected by a strong favorable pressure gradient. It must now readjust to a slight adverse gradient. This nonequilibrium is reflected in the values of  $H$  at Station 2 and the change in  $n$  and  $\pi$  from Station 2 to 9. The boundary layer parameters at Station 2 may not give a result that is indicative of the

patterns which will be present at the downstream stations.

In general, the following trends are exhibited by the results. At a given station, the displacement and momentum thickness increase with increasing bluntness while the form factor decreases. A longer distance is required for the tip bluntness effects to dissipate with increasing bluntness. Boundary layer growth rates scale on tip bluntness, but different curves are obtained for each tip geometry. With tip bluntness, the momentum deficit in the lower boundary layer is increased. The unit Reynolds number reduction due to the normal shock tends to decrease the effective wetted length. This is reflected in the reduction of the form factor,  $H$ , and power law coefficient,  $n$ . Increasing bluntness generally increases the skin friction coefficient, again reflecting the unit Reynolds number reduction due to tip blunting.

#### 5.5.2 WINDSIDE AT ANGLE OF ATTACK

When the model is inclined at an angle of attack, the windside boundary layer presents a more complicated problem. If the flow is considered as consisting of an axial component and a cross flow component, the boundary layer can be thought of as a combination of a flat plate boundary layer and the boundary layer at the stagnation point of a circular cylinder normal to the flow. A favorable pressure gradient is present on the model nose followed by a near zero pressure gradient along the body downstream of the ogive-cylinder junction.

These gradients are shown in Figures 20 and 28.

Figure 41 shows the displacement and momentum thicknesses plotted versus the axial distance along the model. Both parameters increase along the body and, at a fixed axial station, both increase with increasing bluntness. In comparison with zero angle of attack, the values found here are lower. Their variation with  $R_b$  is shown in Figure 42. As in the zero angle of attack case, both parameters increase with increasing tip bluntness in a manner which is roughly linear over this range but is probably a complicated function of Reynolds number. The displacement and momentum thickness again increase at higher rates for the blunter model tips. An attempt was made to correlate  $\partial\delta^*/\partial x$  and  $\partial\theta/\partial x$  with tip bluntness. The results are shown in Figure 43. The trends are not as clear as they were in the  $0^\circ$  angle of attack case.

Figure 41 shows a comparison of  $H$  for each model tip at the stations surveyed. A trend similar to that found at zero angle of attack is seen. The asymptotic value of  $H$  is about 5.1, based on the behavior of  $H$  for the pointed tip and for the  $0^\circ$  angle of attack case. For large tip blunting, the boundary layer form factor is closer to the asymptotic value at the forward stations than at  $0^\circ$  angle of attack. While  $H$  increases much more quickly along the body, it still approaches the value of 5.1 at Station 14. The rate of approach is, however, much more rapid than in the zero angle of attack case.

A comparison of  $H$  versus  $R_b$  is shown in Figure 42. Again it is seen that  $H$  decreases with increasing bluntness at a given station, reflecting the increase in the momentum deficit in the lower boundary layer with tip bluntness. However, this decrease is much smaller for a given tip radius than at  $\alpha=0^\circ$ .

The power law parameter,  $n$ , is plotted versus station and  $R_b$  in Figure 44. The value of  $n$  increases slowly along the body and the rate of increase seems to be very tip dependent. The value of  $\partial n / \partial x$  is highest for the pointed tip and is roughly zero for the F3 tip. At the same time, the values of  $n$  seem to scale with  $R_b$  at Stations 9 and 14. The slow increase in  $n$  for large blunting is probably due to the unit Reynolds number reduction for the blunted tip, but also indicates that it requires more distance for the effects of this reduction in Reynolds number to be dissipated. In other words, the entropy wake effects are very slow to dissipate from the boundary layer as seen in the behavior of  $H$  discussed above. Also different from the zero angle of attack case is the behavior in  $n$  from Stations 2 to 9. The decrease found at zero angle of attack is not seen here. This is due to the decrease in the adverse pressure gradient until a nearly flat plate condition is obtained.

Figure 45 shows a plot of  $\pi$  versus station and tip bluntness. Here again the prevalent pattern has changed from the zero angle of attack case. The wake strength

parameter decreases monotonically along the body in all cases except for the F3 tip. No peak is exhibited at Station 9 as for the  $0^\circ$  angle of attack case. Again  $\pi$  does increase with increasing bluntness as seen at zero angle of attack. In general, the values of  $\pi$  obtained are also lower than those found at zero angle of attack and are closer to the value of 0.62, the value of  $\pi$  for an equilibrium flat plate boundary layer.

When skin friction coefficients were compared, in Figure 46, with the Van Driest II values with  $r=0.897$ , a much better comparison is obtained than at zero angle of attack. The improvement is probably due to the fact that the boundary layer is more nearly a flat plate case which the Van Driest II method was developed to predict. Again,  $C_f$  decreases along the body and the variation with tip bluntness at each station decreases at higher values of  $X$ . It is believed that increasing bluntness gives a higher skin friction coefficient because of the Reynolds number reduction.

The following conclusions can be made concerning the windside boundary layer development. The boundary layer parameters,  $\delta^*$  and  $\theta$ , scale on tip bluntness though overall values are lower than at zero angle of attack. The decreased pressure gradient is reflected in the values of  $H$  and  $\pi$ , both of which approach the asymptotic value, determined from the behavior for the pointed tip, more rapidly. Values of  $H$  approach the asymptotic value of 5.1

more quickly than at zero angle of attack and again scale on  $R_b$  with the larger  $R_b$  giving a smaller  $H$ . The power law coefficient behavior is very bluntness dependent. The rate of increase of  $n$ , along the body, decreases with increasing  $R_b$ . At each station, an increase in  $R_b$  gives a decrease in the value of  $n$ . The wake strength parameter,  $\pi$ , is generally lower on the windside and again increasing bluntness gives increasing values of  $\pi$ . However,  $\pi$  decreases monotonically along the body in this case. These results are all felt to be indicative of the unit Reynolds number reduction and decrease of the density of the fluid in the boundary layer associated with the tip blunting.

#### 5.5.3 LEESIDE AT ANGLE OF ATTACK

The boundary layer on the leeside of an inclined body is subjected to a favorable gradient over the model nose. Downstream of the ogive-cylinder junction an adverse gradient, larger than the one at zero angle of attack, is present. The pressure gradients present are shown in Figures 20 and 29.

When displacement and momentum thickness are examined with increasing axial distance or tip bluntness (Figures 47 and 48), trends similar to those found at  $\alpha=0^\circ$  and on the windside at angle of attack are seen. Displacement and momentum thickness increase along the body in a fairly linear manner and the values are larger than at  $\alpha=0^\circ$  for a

given tip and station. When compared at each station with increasing tip bluntness, a peak in the values is present at  $R_b=0.25$ . This is a reversal of all previous patterns. When  $\partial\delta^*/\partial x$  and  $\partial\theta/\partial x$  were compared with tip bluntness in Figure 49 a similar trend was found with a peak present at  $R_b=0.25$ .

When  $H$  was examined, the values were seen to be much more dispersed around the value of approximately 5.4. This is shown in Figure 47. The asymptotic value appears to be about 5.4 in this case. The approach to 5.4 with distance along the model is even more gradual than in the previous cases. When plotted against  $R_b$ , the same trend is seen as before. With increasing bluntness,  $H$  decreases as shown in Figure 48. This decrease in  $H$  is sharper and drops farther than in the other cases examined.

The power law coefficient is compared in Figure 50 with axial distance and tip bluntness. It behaves like the zero angle of attack case with a decrease from Station 2 to 9 and an increase at Station 14. The band of values is much narrower however and very little variation with  $R_b$  is present. This indicates that the fullness of the boundary layer is relatively insensitive to tip bluntness on the leeside of the body.

The comparison of  $\pi$ , the wake strength parameter, is shown in Figure 51. The value of  $\pi$  increases from Station 2 to 9 and is fairly constant from 9 to 14. When plotted against  $R_b$ , a peak is again present at  $R_b=0.25$ . This peak

will be discussed later. It is clear though, that the boundary layer is in a fairly constant state as soon as it relaxes from the favorable gradient over the nose.

A comparison of  $C_f$  is shown in Figure 52 along with the values predicted by the Van Driest method. Here the Van Driest II method gives results which are poorer than for the windside and zero angle of attack cases examined. The scatter of values at each station is increased over that present at  $\alpha=0^\circ$ . As well,  $C_f$  drops much more rapidly along the body. These observations can be attributed to the increase in the adverse pressure gradient and the piling up of the boundary layer crossflow.

Overall results on the leeside of the body show that the boundary layer equilibrates very shortly after the ogive cylinder junction and then changes its form very little along the body. The state of the boundary layer in terms of the parameters  $H$  and  $\pi$  can be scaled well on tip bluntness. The power law coefficient,  $n$ , experiences little variation with tip bluntness. Skin friction seems to be very sensitive to tip bluntness and axial distance.

#### 5.5.4 BOUNDARY LAYER SUMMARY

While the boundary layer is affected by both the tip bluntness and pressure gradients on the body, these may be seen to affect different aspects of the boundary layer. For example, the values of  $\partial\theta/\partial x$  scale on  $R_b$  for each case while the magnitudes of  $\partial\theta/\partial x$  for a specific tip are different for the three situations examined i.e.  $\alpha=0^\circ$ ,  $\alpha=2.9^\circ$ ,  $\theta=0^\circ$ ,

$\theta=180^\circ$ . The value of  $\partial\theta/\partial x$  is always largest on the leeside and smallest on the windside at a small angle of attack with the zero angle of attack case falling between the high and low values. This is indicative of the pressure gradient difference and may partly be a crossflow effect.

The following observations can be made concerning the boundary layer parameters and the effects produced by both tip bluntness and pressure gradient.

Displacement and momentum thickness both increase with increasing  $X$ . At a specific station, increasing tip bluntness also causes an increase in these parameters. A clear scaling behavior with tip bluntness is seen at the downstream stations. The values of  $\delta^*$  and  $\theta$  are greatest with the largest adverse pressure gradient reflecting the pressure gradient, though the crossflow may also be involved.

The asymptotic value of  $H$ , judged from the pointed tip behavior, is approached by all cases of tip blunting. The form factor scales with tip bluntness at any specific station with increasing bluntness giving a lower  $H$ , reflecting the reduction in the fullness of the velocity profile and unit Reynolds number due to the tip bluntness. The rate of approach to the asymptotic value for the blunt tip is different in the cases of  $0^\circ$  and  $2.9^\circ$  angle of attack. The return to the value of 5.1 is achieved much more quickly for the smaller adverse gradient on the windside at angle of attack. This is felt to reflect an interaction of the entropy wake, which causes the initial variation with tip

bluntness, and the pressure gradient, which does not allow the entropy wake effects to dissipate.

The fullness of the boundary layer, as reflected in  $n$ , is affected by both the entropy wake and pressure gradient. The power law exponent scales on tip bluntness at any given station for the  $0^\circ$  and  $2.9^\circ$  angle of attack case on the windside. Very little variation of  $n$  with tip bluntness takes place on the leeside at angle of attack. This is felt to be due to the fact that, with the smaller pressure gradients, the value of  $n$  is more affected by tip bluntness than the gradient. The pressure gradient does influence the magnitude of  $n$  with the lowest pressure gradient giving the largest values of  $n$ .

Skin friction is reflective of the pressure gradient when its rate of decrease with distance is examined but, at a given station, it also reflects the tip bluntness. The values of  $C_f$  drop more rapidly for the higher adverse gradient but a variation with tip bluntness is present at each station at a given condition. The variation of  $C_f$  with  $R_b$  is also influenced by the pressure gradient. When the adverse gradient is smaller, the entropy wake effects dissipate more rapidly and the variation of  $C_f$  with  $R_b$  is much smaller.

The wake strength parameter is affected by the tip bluntness at all stations. The overall values of  $\pi$  and its behavior with distance, is more dominated by the pressure gradient. The largest absolute values of  $\pi$  and

$\partial\pi/\partial x$  are found with the largest adverse pressure gradients. This is in good agreement with the behavior of  $\pi$  for a two dimensional turbulent boundary layer in an adverse pressure gradient.

In general, the parameter variation with the combination of tip bluntness and pressure gradient may be explained in the following way. The entropy wake affects the parameters at the early stations in a manner analogous to a decrease in the unit Reynolds number or wetted length and a decrease in the mass and momentum contained in the boundary layer. The pressure gradient affects the boundary layer by controlling the rate of dissipation of the entropy wake effects. For a larger adverse gradient, the entropy wake effects dissipate more slowly.

### 5.6 SCALING PARAMETER DEVELOPMENT

From previous analysis it was obvious that a scaling on tip bluntness was present in some functional form. The flat and hemispherical tips each scaled in basically the same manner when using tip radius,  $R_b$ . The tip geometry, flat or hemispherical, was also involved in some functional way as the scaling rate was different for the two geometries. A parameter which would be an indication of the severity and area of the blunting of the tip would collapse the data onto a single curve. The geometry of the blunting would be included and only a single curve would result for hemispherical, flat, and other tip shapes.

A parameter called the bluntness length and labelled  $\text{IB}$  was developed.  $\text{IB}$  is obtained by integrating the surface angle of the tip along one meridian. This integration is carried out from the stagnation point to the point on the tip where the surface angle is the angle necessary for shock detachment at that freestream Mach number. The detachment angle was determined from the graphs given in NACA Report 1135. Referring to Figure 53,  $\text{IB}$  may be written as

$$\text{IB} = \int_0^d \delta ds \quad (7)$$

where  $d$  is the detachment angle point. This gives the pattern of  $\text{IB}$  as shown in Table 3. A good indication that the effect of geometry had been removed was given by the pattern that appeared and that has been seen earlier in the bow shock analysis, Section 5.2.1. A small change would be present in this parameter at angle of attack. This was recomputed for both the windside and leeside at  $2.9^\circ$  angle of attack. These values of  $\text{IB}$  obtained are all given in Table 3.

The additional pressure drag due to the tip bluntness,  $D_{pb}$ , was also computed. The computational method proposed by Krasnov (39) was utilized. Krasnov used a series of formulas for the pressure distribution over the blunted region of the tip. The formulas used were compared with experimental results by Krasnov and showed good agreement. The drag coefficients are then computed by integrating the pressure distribution over the blunt tip region. The value

of the drag coefficient is equal for all the tips of a given geometry or for the hemispherical tips  $C_{Dpb} = 0.869$  and for the flat tips  $C_{Dpb} = 1.655$ . The additional drag is then computed using the formula

$$D_{pb} = C_{Dpb} \frac{1}{2} \rho V_\infty^2 r_b^2 \quad (8)$$

This gives the values of  $D_{pb}$  shown in Table 4. This clearly removes the effect of tip geometry and gives the same pattern found with the bluntness length above.

When the parameters  $\bar{B}$  and  $D_{pb}$  were used instead of  $R_b$ , a very good correlation of the data is obtained. Each parameter gave a very similar correlation of the data. The remaining plots will be made with  $\bar{B}$  as the blunting parameter, though nearly equivalent plots could be obtained with  $D_{pb}$ . Only the cases that scaled well with  $R_b$  will be shown to illustrate the improved correlation. Cases which did not scale well with  $R_b$  are felt to be affected by other factors (i.e., entropy wake entrainment, pressure gradient changes) so that no real scaling can take place with tip bluntness.

Figure 54 shows a comparison of  $\bar{B}$  versus the shock bluntness parameter,  $B_s$ , at zero angle of attack. The results give trends that are physically understandable. Increasing  $\bar{B}$  gives a less negative  $B_s$  or a bow shock that has a larger portion which is strong and curved. As  $\bar{B}$  approaches zero,  $B_s$  tends to approach large negative values indicating a decrease in the bluntness and the approach to

the straight or only slightly curved conical shock that would be obtained with a sharp tip. Figure 55 shows a comparison of  $\theta$  at Stations 2, 9, and 14 with  $\beta$ . The parameter provides a good correlation of the data. Figure 56 shows a plot of  $\partial\delta^*/\partial x$  and  $\partial\theta/\partial x$  versus  $\beta$  and, again, an excellent correlation of the data is obtained. A single curve is produced in each case. A plot of  $H$  and  $n$  versus  $\beta$  was also made for  $\alpha=0^\circ$  at Station 14 and is shown in Figure 57.

At angle of attack, similar results can be obtained as shown in Figure 58 where  $\theta$ , and  $\pi$  are plotted versus  $\beta$  for selected stations on the windside. Figure 59 shows a plot of  $H$  versus  $\beta$  on the leeside and again the data correlates well.

The bluntness length parameter,  $\beta$ , or the additional pressure drag,  $C_{Dpb}$ , give a good correlation of the data and removes tip geometry effects from the results. Either bluntness parameter is effective in correlating all the parameters which can be scaled with  $R_b$  and provides a correlation which is as good as the one obtained with  $R_b$ .

In attempting to explain the significance of the bluntness length an argument phrased in terms of unsteady piston theory is helpful. Here the outline of the body may be thought of as a time history of the position of a piston and the slope of the surface of the body as the velocity of the piston. The parameter,  $\beta$ , may be interpreted as the path weighted by the velocity of

the piston. It is an indication of the distance the piston travelled and the speed at which it travelled that distance. This is to say that the bluntness length would give a rough idea of the work exerted on the piston to move it or the additional drag incurred by a blunted body tip.

## CONCLUSIONS

An examination of the turbulent boundary layer over an axisymmetric body was made at  $M=2.94$  with a unit Reynolds number of  $6.3 \times 10^7$  per meter. Results of the surface pressure and boundary layer measurements may be summarized as follows.

- 1) Tip bluntness produces a detached, curved bow shock and an associated entropy wake (a region of fluid with increased entropy due to the strong shock portion of the bow shock). The shock shape is affected by the size and type of the tip blunting. For a given blunting geometry, the size of the entropy wake increases with increasing tip size. At an angle of attack, the radial extent of the entropy wake is increased on the windside and decreased on the leeside.
- 2) Tip bluntness has a significant effect on the surface pressure distributions only very near the model tip. Surface pressures return to the values obtained for the sharp tipped body very quickly following the blunted tip.
- 3) The interaction of the entropy wake with the boundary layer has a significant effect on its

streamwise development. The effects are thus strongly dependent on tip geometry and size. In the simplest sense, the entropy wake may be thought of as influencing the boundary layer by reducing the Reynolds number based on length at a given point. This results in a reduction in the fullness of the boundary layer velocity profile and increase in the skin friction coefficient. The pressure gradient, in combination with the entropy wake, also influences the boundary layer. The following statements briefly summarize the influence of the entropy wake and pressure gradient on the boundary layer.

- a) On the windside, where the boundary layer is subjected to a near zero streamwise pressure gradient, the effects of the entropy wake dissipate more quickly than for a more adverse gradient.
- b) On the leeside of the body, the entropy wake effects dissipate very slowly due to the larger adverse pressure gradient.
- c) Transition is affected by the interaction of the entropy wake and the developing boundary layer. The trends are correctly predicted by theory.

4) A correlation of the boundary layer parameters in terms of tip bluntness was developed by using either the blunt tip pressure drag or the bluntness length,  $\overline{B}$ , as a scaling parameter. The bluntness length obtained by

$$\overline{B} = \int_0^d \delta ds$$

provides an indication of the actual area and severity of the tip blunting. When parameters which scale on tip radius are plotted versus  $\overline{B}$  or  $D_{pb}$ , the effect of tip geometry is removed, and a single curve is obtained for all cases.

## PUBLICATIONS

In addition to the required semi-annual reports, an Interim Technical Report entitled "Supersonic, High Reynolds Number Flow Over a Tangent Ogive Cylinder at Small Angles of Attack: An Experimental Study and Comparison with Theory," was submitted to the Army Research Office in January 1979 (MAE Rept.#1421).

## DEGREES AWARDED

Two M.S.E. Degrees were awarded during the Grant period: Alain Beck, August 1978  
William Gray, May 1981

## REFERENCES

- 1) Beck, A., "An Experimental Study of a Tangent Ogive-Cylinder at Small Angles of Attack in Supersonic Flows," M.S.E. Thesis, Princeton University, 1978.
- 2) Dolling, D.S. and Bogdonoff, S.M., "Supersonic, High Reynolds Number Flow over a Tangent Ogive-Cylinder at Small Angles of Attack: An Experimental Study and Comparison with Theory," Interim Technical Report, U.S. Army Research Grant DAAG29-77-G-0234, January, 1979.
- 3) Lubard, S.C. and Rakich, J.V., "Calculation of the Flow on a Blunted Cone at a High Angle of Attack," AIAA Paper 75-149.
- 4) Schiff L.B. and Steger, J.L., "Numerical Simulation of Steady Supersonic Viscous Flow," AIAA Paper 79-0130.
- 5) Schiff, L.B. and Sturek, W.B., "Numerical Simulation of Steady Supersonic Flow over an Ogive-Cylinder-Boattail Body," AIAA Paper 80-0066.
- 6) Sturek, W.B., Reklis, R.P., Kayser, L.D., and Opalka, K.C., "Three Dimensional Boundary Layer Studies as Applied to the Magnus Effect on Spinning Projectiles," U.S. Army Ballistics Research Laboratories, Aberdeen Proving Grounds, Maryland, 21005.
- 7) Dwyer, H.A. and Sanders, B.R., "Magnus Forces on Spinning Supersonic Cones - Part I: The Boundary Layer," AIAA Paper 75-193.
- 8) Sanders, B.R. and Dwyer, H.A., "Magnus Forces on Spinning Supersonic Cones - Part II: Inviscid Flow," AIAA Journal, Volume 14, Number 3, pp. 576-582.
- 9) Rakich, J.V., Vigneron, Y.C., and Agarwal, R., "Computation of Supersonic Viscous Flow over Ogive-Cylinders at Angle of Attack," AIAA Paper 79-0131.
- 10) Van Dyke, M.D., "The Similarity Rules for Second-Order Subsonic and Supersonic Flows," NACA TN 3875, 1957.
- 11) Van Dyke, M.D., "Second Order Slender-Body Theory--Axisymmetric Flow," NASA TN R-47, 1959.
- 12) Van Dyke, M.D., "The Supersonic Blunt Body Problem--Review and Extension," Journal of the Aero/Space Sciences, August, 1958, pp. 485-496.

- 13) Lin, C.C. and Shen, S.F., "An Analytic Determination of the Flow Behind a Symmetrical Curved Bow Shock in a Uniform Stream," NACA TN 2506, 1951.
- 14) Allen, H.J., "Estimation of the Forces and Moments Acting on Inclined Bodies of Revolution of High Fineness Ratio," NACA RM A9I26, 1949.
- 15) Allen, H.J., "Pressure Distributions and some Effects of Viscosity on Slender Inclined Bodies of Revolution," NACA TN 2044, 1950.
- 16) Cooper, R.D. and Robinson, R.A., "An Investigation of the Aerodynamic Characteristics of a Series of Cone-Cylinder Configurations at a Mach Number of 6.86," NACA RM L51J09, 1951.
- 17) Allen, H.J. and Perkins, E.W., "Characteristics of Flow over Inclined Bodies of Revolution," NACA RM A50L07, 1951.
- 18) Syvertson, C.A. and Dennis, D.H., "A Second-Order Shock-Expansion Method Applicable to Bodies of Revolution Near Zero Lift," NACA TN 3527, 1956.
- 19) Perkins, E.W. and Kuehn, D.M., "Comparison of Experimental and Theoretical Distributions of Lift on a Slender Inclined Body of Revolution at  $M=2$ ," NACA TN 3715, 1956.
- 20) Perkins, E.W. and Jorgensen, L.H., "Comparison of Experimental and Theoretical Normal-Force Distributions (Including Reynolds Number Effects) on an Ogive-Cylinder Body at Mach Number 1.98," NACA TN 3716, 1956.
- 21) Van Dyke, M.D. and Gordon, H.D., "Supersonic Flow Past a Family of Blunt Axisymmetric Bodies," NASA Report 1, 1959.
- 22) Sherer, A.D., "Analysis of the Linearized Supersonic Flow About Pointed Bodies of Revolution by the Method of Characteristics," NASA TN D-3578, 1966.
- 23) Rakich, J.V. and Cleary, J.W., "Theoretical and Experimental Study of Supersonic Steady Flow Around Inclined Bodies of Revolution," AIAA Paper 69-187.
- 24) Sedney, R., "Laminar Boundary Layer on a Spinning Cone at Small Angles of Attack in a Supersonic Flow," Journal of Aero. Science, Volume 24, Number 6 June, 1957.

- 25) Vas, I.E. and Bogdonoff, S.M., "A Preliminary Report on the Princeton University High Reynolds Number 8" x 8" Supersonic Tunnel," Internal Memorandum No. 39, Gas Dynamics Laboratory, Dept. of Mechanical and Aerospace Engineering, Princeton University.
- 26) Hayes, W.D. and Probstien, R.F., Hypersonic Flow Theory, Academic Press, New York, 1966.
- 27) Perkins, E.W., Jorgensen, L.H., and Sommer, S.C., "Investigation of the Drag of Various Axially Symmetric Nose Shapes of Fineness Ratio 3 for Mach Numbers from 1.24 to 7.4," NACA Report 1386, 1958.
- 28) Cheryni, G.C., Introduction to Hypersonic Flow, Trans. and Edited by R.F. Probstien, Academic Press, New York, 1961.
- 29) Bennet, F.D., "Note on Tip-Bluntness Effects in the Supersonic and Hypersonic Regimes," Journal of the Aeronautical Sciences, April, 1957, pp. 314-315.
- 30) Geise, J.H. and Bergholdt, V.E., "Interferometric Studies of Supersonic Flow about Truncated Cones," Journal of Applied Physics, November, 1953, pp. 1389-1396.
- 31) Liepmann, H.W. and Roshko, A., Elements of Gas Dynamics, Wiley, New York, 1957.
- 32) Love, E.S., "A Reexamination of the Use of Simple Concepts for Predicting the Shape and Location of Detached Shock Waves," NACA TN 4170, 1957.
- 33) Kaattari, G.E., "A Method for Predicting Shock Shapes and Pressure Distributions for a Wide Variety of Blunt Bodies at Zero Angle of Attack," NASA TN D-4539, 1968.
- 34) Guy, T.B., "A Note on the Standoff Distance for Spherical Bodies in Supersonic Flow," AIAA Journal, Volume 12, Number 3, pp. 380-381.
- 35) Stetson, K.F. and Rushton, G.H., "Shock Tunnel Investigation of Boundary Layer Transition at M=5.5," AIAA Journal, Volume 5, Number 5, pp 899-905.
- 36) Ericsson, L.E., "Correlation of Attitude Effects on Slender Vehicle Transition," AIAA Journal, Volume 12, Number 4, pp. 523-529.
- 37) Sun, C. and Childs, M.E., "Flowfield Analysis for Oblique Shock Wave-Turbulent Boundary Layer Interactions," NASA CR-2656.

- 38) Settles, G.S., "An Experimental Study of Compressible Turbulent Boundary Layer Separation at High Reynolds Numbers," Ph. D. Dissertation, Princeton University, 1975.
- 39) Krasnov, N.F., Aerodynamics of Bodies of Revolution, Edited and Annotated by Dean M. Morris, American Elsevier Publishing Company, Inc., New York, 1970.

Table 1: Shock Shape Parameters  
Shock Radius,  $R_s$  (mm)

	Tip R1	Tip R2	Tip R3	Tip F1	Tip F2	Tip F3
$\alpha=0^\circ$	2.08	4.19	8.89	2.18	5.99	12.01
$\alpha=2.9^\circ$	2.44	4.39	8.18	3.02	4.52	11.66
W/S						
$\alpha=2.9^\circ$	0.91	4.37	9.02	1.78	6.60	13.64
L/S						

Shock Bluntness,  $B_s$

	Tip R1	Tip R2	Tip R3	Tip F1	Tip F2	Tip F3
$\alpha=0^\circ$	-0.22	-0.20	-0.17	-0.22	-0.17	-0.16
$\alpha=2.9^\circ$	-0.18	-0.16	-0.14	-0.18	-0.17	-0.10
W/S						
$\alpha=2.9^\circ$	-0.30	-0.25	-0.24	-0.27	-0.22	-0.21
L/S						

Table 2: Shock Curvature,  $\kappa \times 10^3$  (mm $^{-1}$ )

	Tip R1	Tip R2	Tip R3	Tip F1	Tip F2	Tip F3
$\alpha=0^\circ$	-0.92	-2.38	-5.75	-1.00	-3.93	-7.87
$\alpha=2.9^\circ$	-1.37	-2.94	-5.91	-1.83	-2.96	-9.09
W/S						
$\alpha=2.9^\circ$	-1.71	-2.13	-4.76	-0.58	-3.72	-8.03
L/S						

Table 3: Bluntness Length Parameter,  $B$  (mm)

	Tip R1	Tip R2	Tip R3	Tip F1	Tip F2	Tip F3
$\alpha=0^\circ$	1.34	3.33	6.58	1.99	4.99	9.97
$\alpha=2.9^\circ$	1.29	3.20	6.33	2.06	5.15	10.30
W/S						
$\alpha=2.9^\circ$	1.31	3.26	6.46	1.93	4.83	9.65
L/S						

Table 4: Pressure Drag on Blunt Tip,  $D_{pb}$  (N)

	<u>Tip R1</u>	<u>Tip R2</u>	<u>Tip R3</u>	<u>Tip F1</u>	<u>Tip F2</u>	<u>Tip F3</u>
$\alpha = 0^\circ, 2.9^\circ$	0.56	3.60	13.95	0.98	6.14	25.57

## FIGURES

A list of figures is given on page viii.

Experimental data points are connected by straight lines in some figures to aid the reader in observing trends. These lines do not necessarily give the true values between data points.

The following symbol key is for Figures 35-59 where data points are presented for all seven model tips.

<u>Symbol</u>	<u>Tip</u>
○	P
△	R1
▲	R2
▽	R3
◊	F1
◆	F2
□	F3

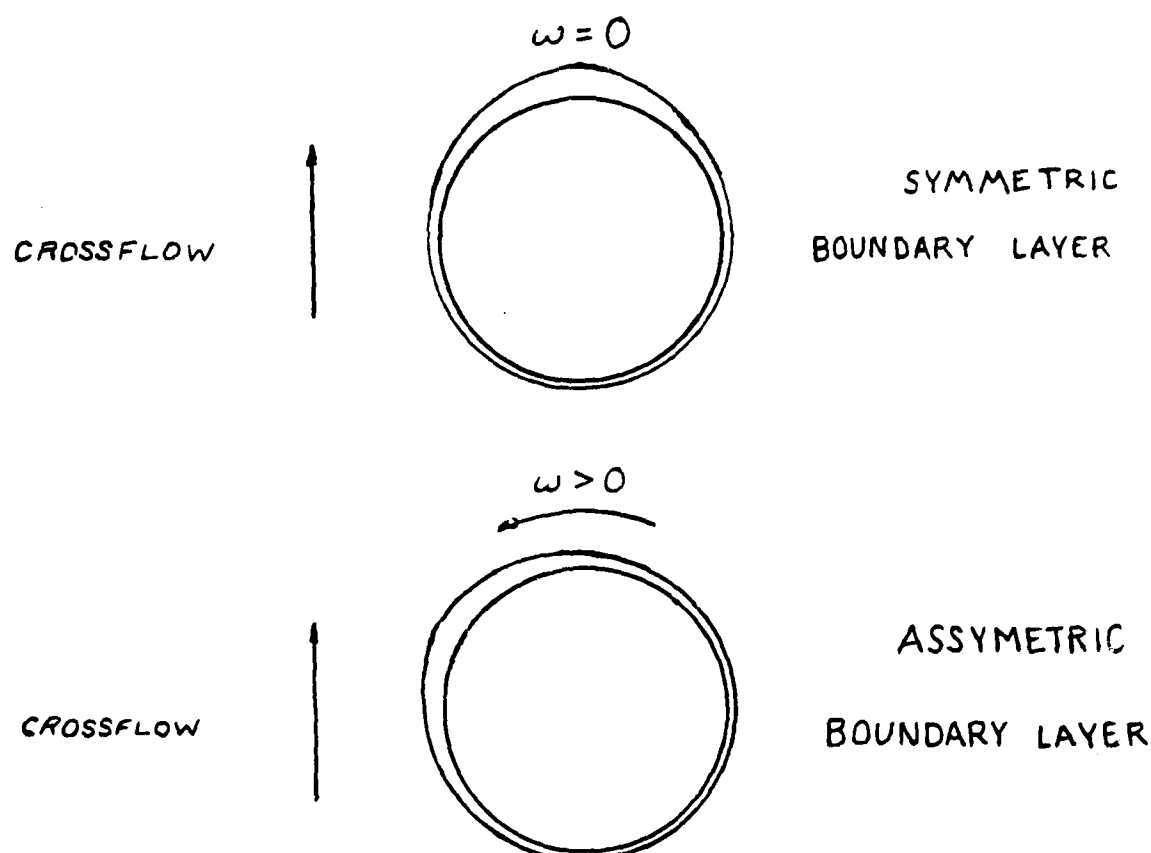
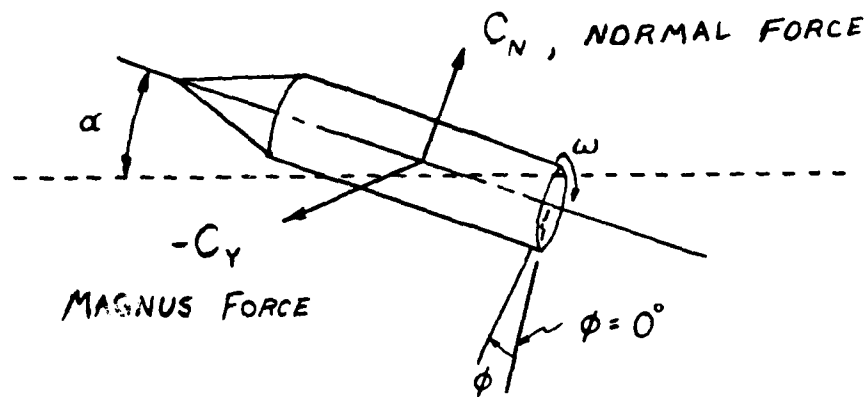


Figure 1. Development of the Magnus force on a Spinning Axisymmetric Body Due to the Crossflow-Boundary Layer Interaction.

AD-A101 513

PRINCETON UNIV NJ DEPT OF MECHANICAL AND AEROSPACE --ETC F/6 20/4  
AN EXPERIMENTAL INVESTIGATION OF TIP BLUNTNESSES EFFECTS ON THE T-ETC(U)  
MAY 81 W K GRAY, D S DOLLING, S M BOGDONOFF DAA629-77-6-0234

UNCLASSIFIED

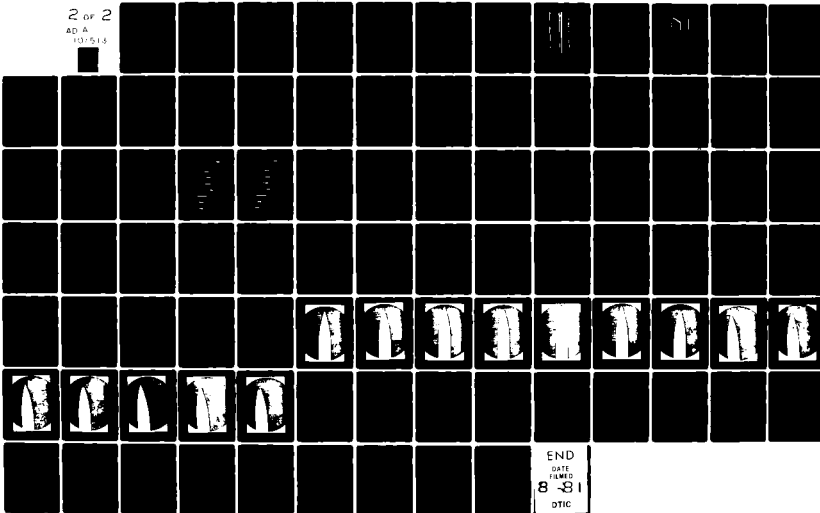
MAE-1530

ARO-1425A.3-F

AM

2 OF 2

AD A  
10-513



END  
DRAFT  
FACSIMILE  
8-81  
DTIC

TGT. OGIVE CYLINDER STUDY

$M=2.95$   $RE=6.3 \times 10^7$  /M

INCIDENCE= 0.0

X/D=4.925

PHI=0.0

□ EXPERIMENT

+ BL CODE

◊ PNS CODE

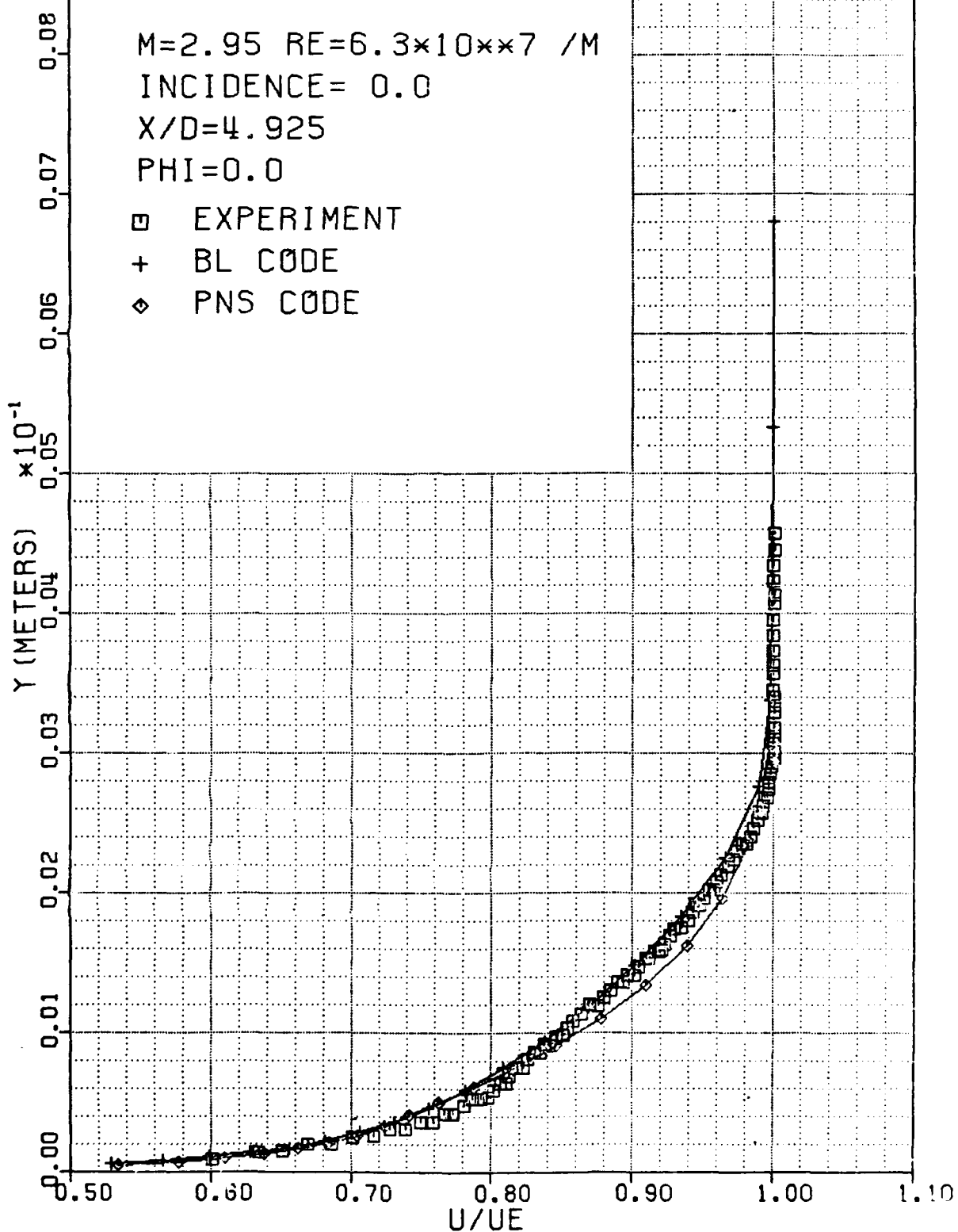


Figure 2. Comparison of Computed and Experimental Velocity Profiles at  $X/D = 4.925$ ,  $\alpha = 0^\circ$ .

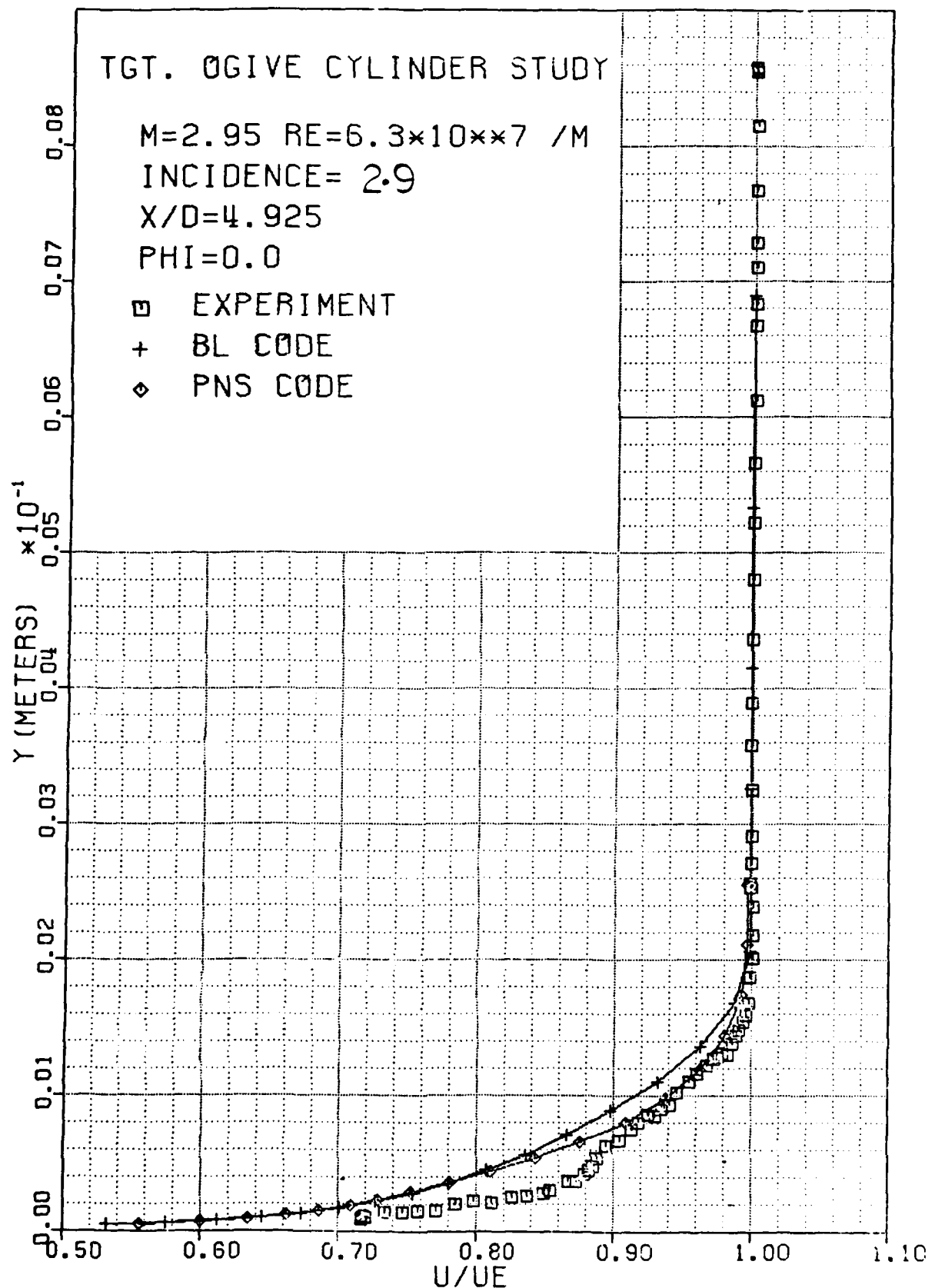


Figure 3. Comparison of Computed and Experimental Velocity Profiles at  $X/D = 4.925$ ,  $\alpha = 2.9$ ,  $\phi = 0^\circ$ .

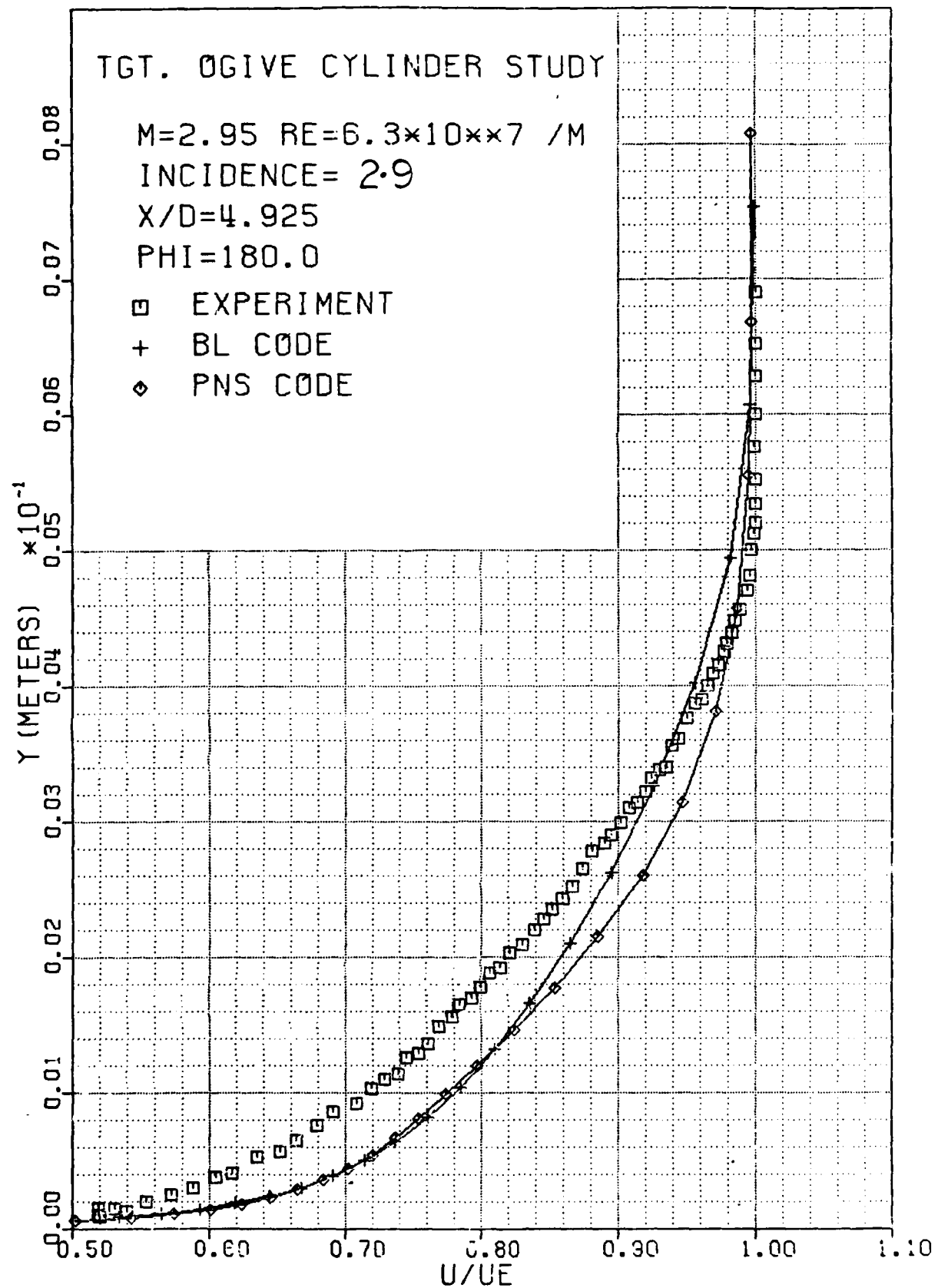


Figure 4. Comparison of Computed and Experimental Velocity Profiles at  $X/D = 4.925$ ,  $\alpha = 2.9$ ,  $\phi = 180^\circ$ .

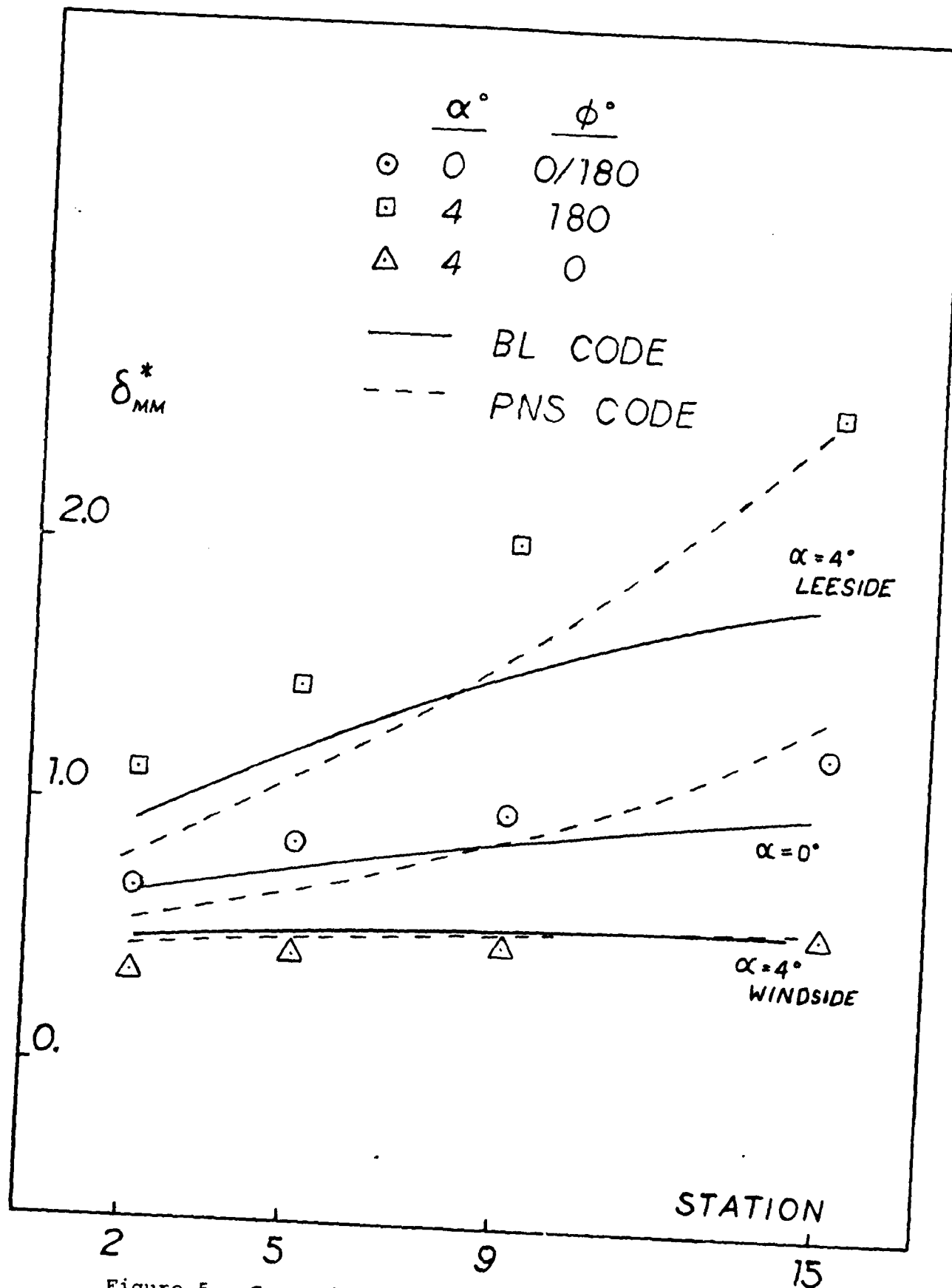


Figure 5. Comparison of Computed and Experimental Displacement Surface Development.

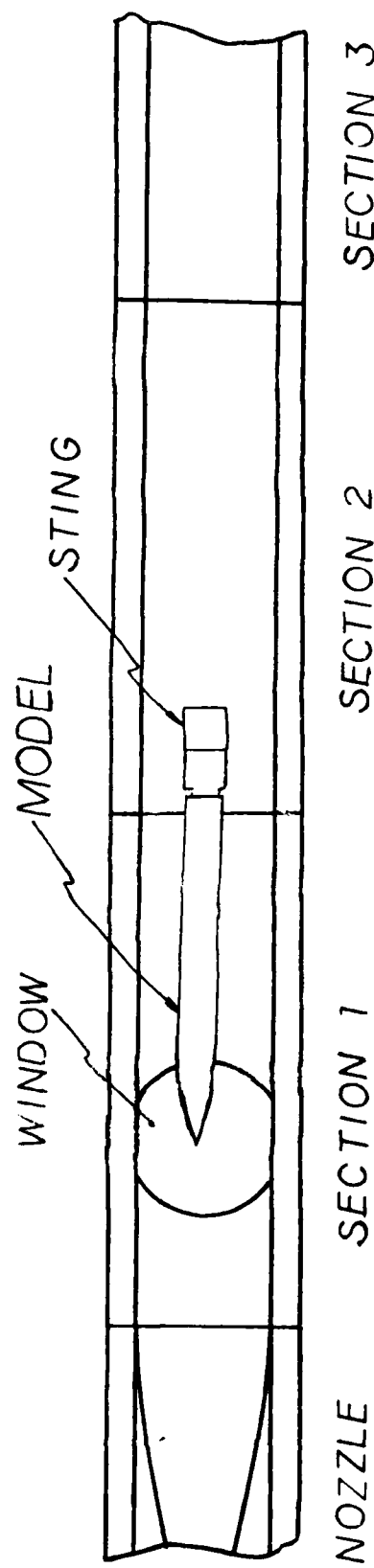


Figure 6. Diagram of the Wind Tunnel Layout.

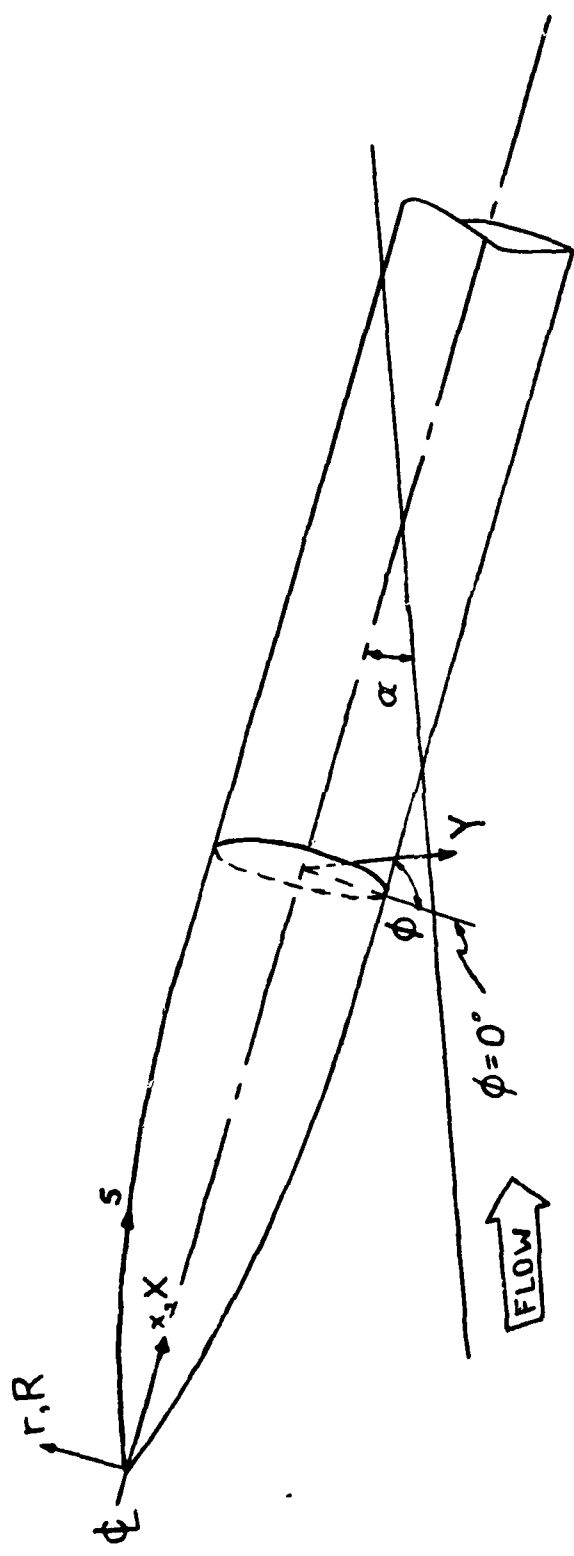
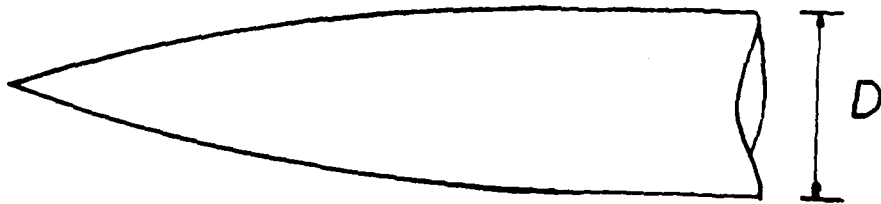
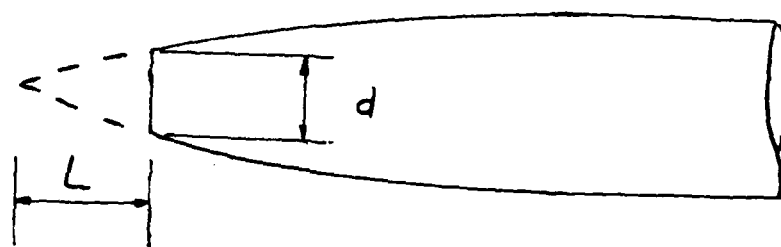


Figure 7. Diagram of the Coordinate System.

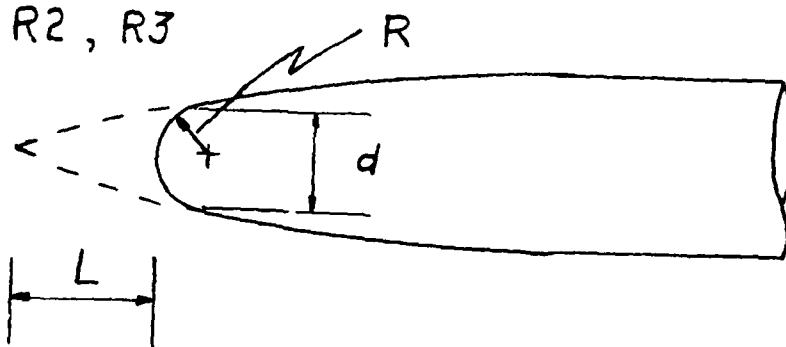
TIP P



TIP F1, F2, F3



TIP R1, R2, R3



<u>TIP</u>	<u>d</u>	<u>L</u>	<u>R</u>
F1	0.05D	0.076D	-
F2	0.125D	0.191D	-
F3	0.250D	0.404D	-
R1	0.05D	0.057D	0.026D
R2	0.125D	0.144D	0.066D
R3	0.250D	0.309D	0.130D

Figure 8. Details of the Blunt Model Tips.

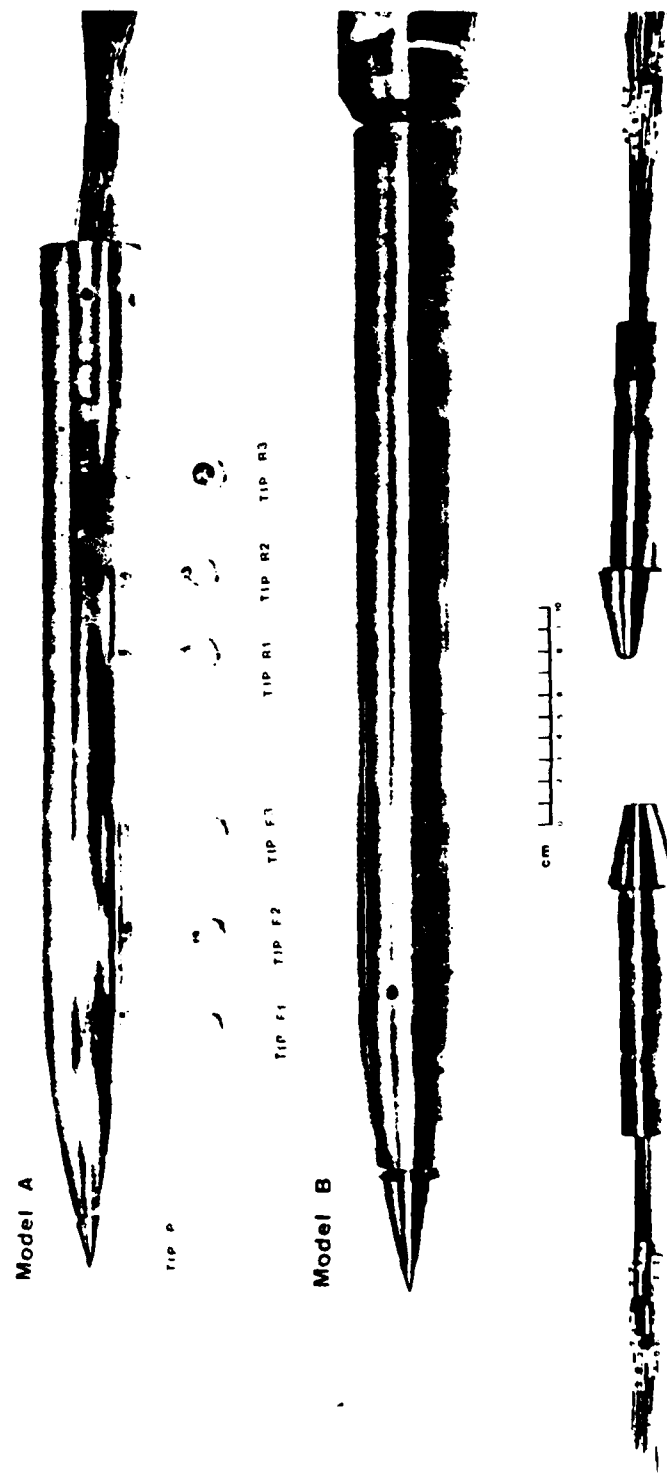
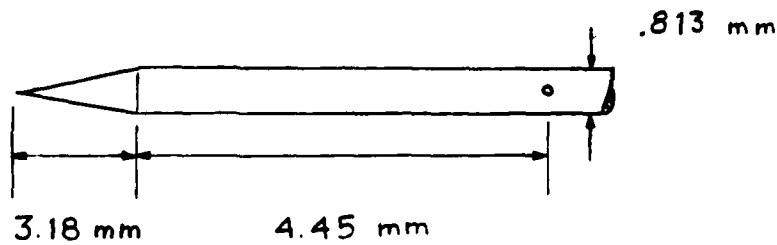


Figure 9. Photograph of the Models and tips.

## STATIC PROBE TIP



## PITOT PROBE TIP

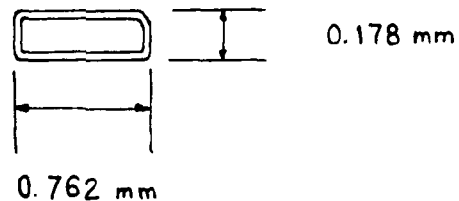


Figure 10. Tip Measurements of the Flowfield Probes.

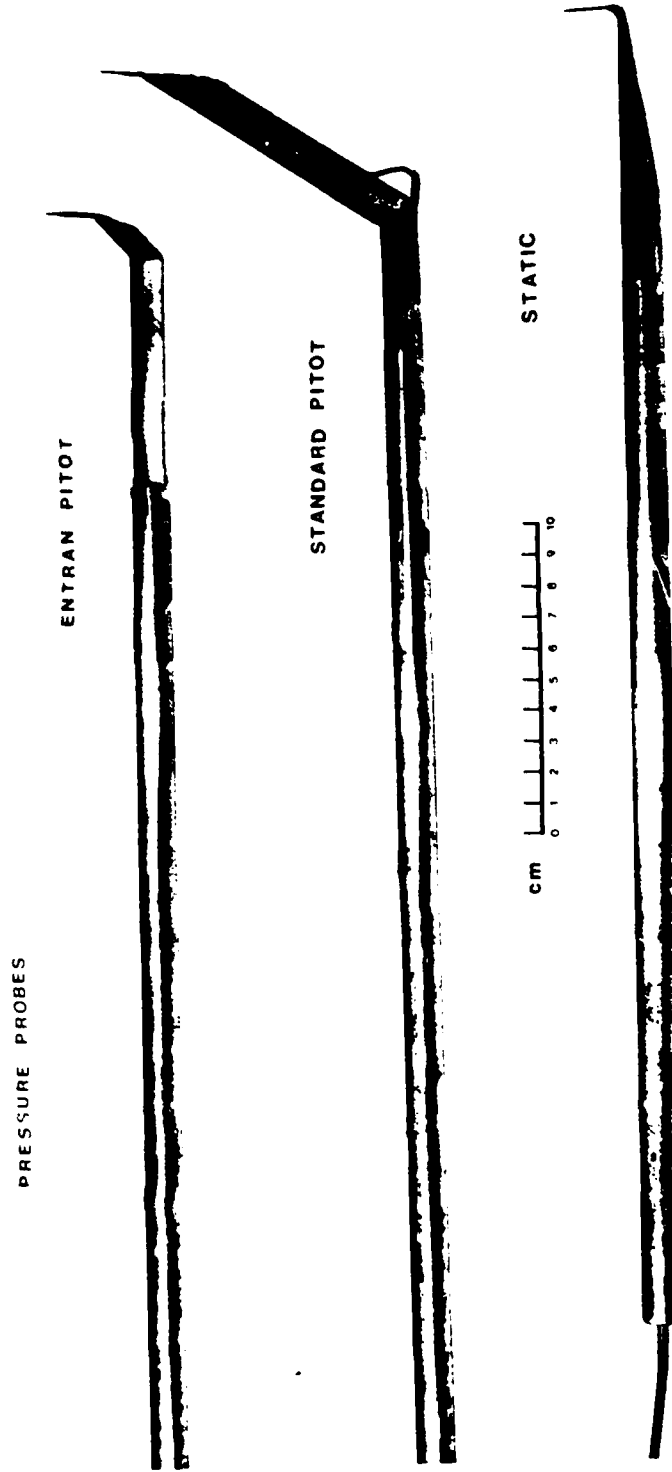


Figure 11. Photograph of the flowfield probes.

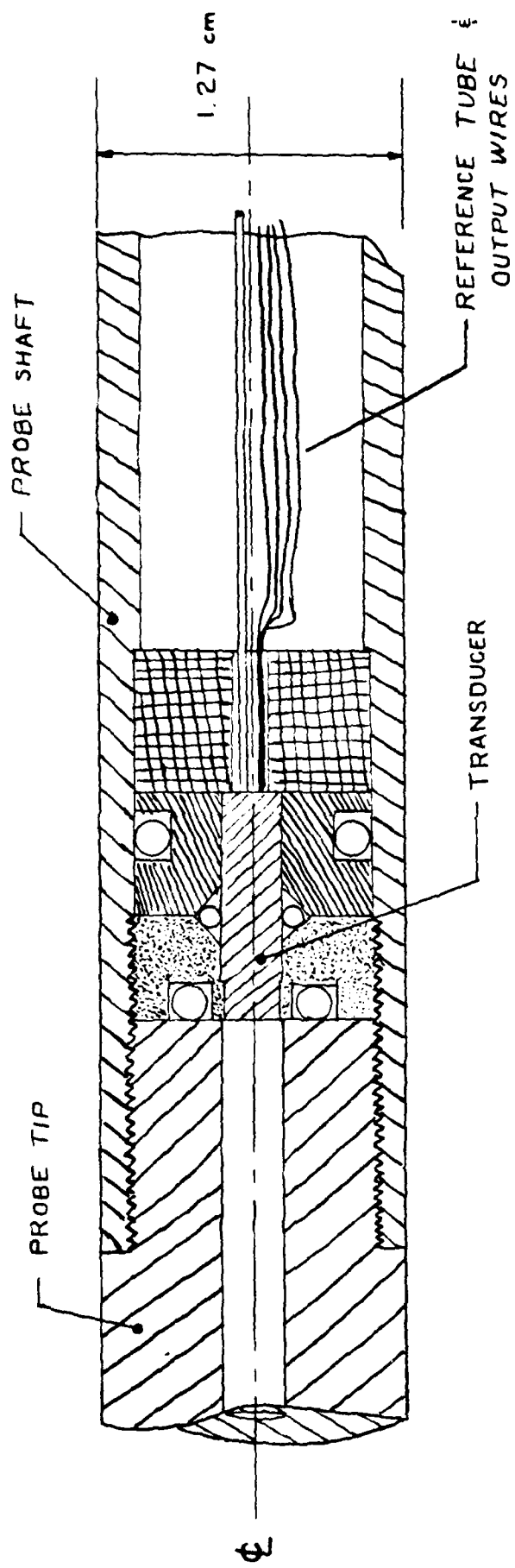


Figure 12. Drawing of the entrainment probe design.

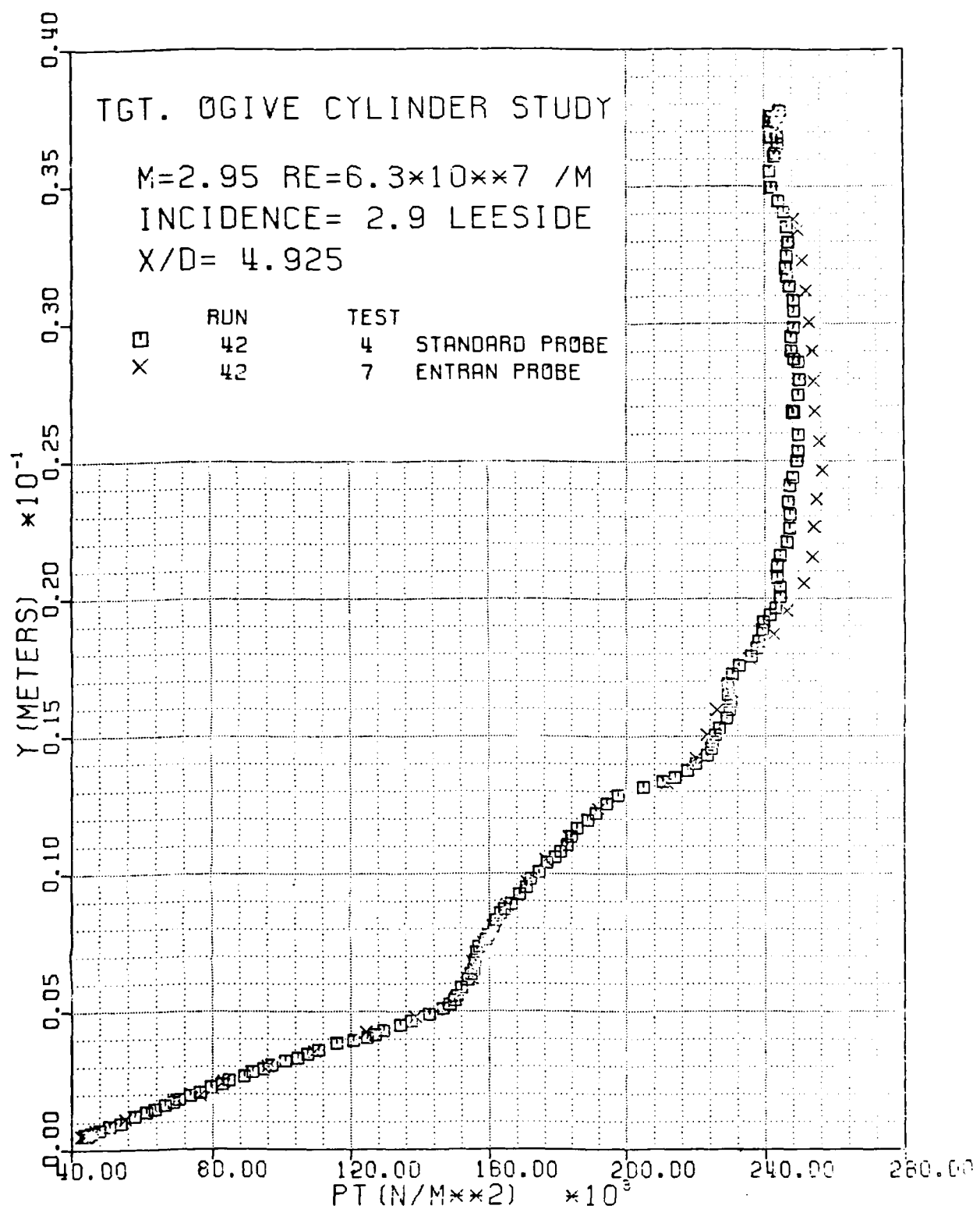


Figure 13. Comparison of Pitot Profiles Obtained with the Entran Probe at  $X/D = 4.925$ ,  $\alpha = 2.9$ ,  $\phi = 180^\circ$ .

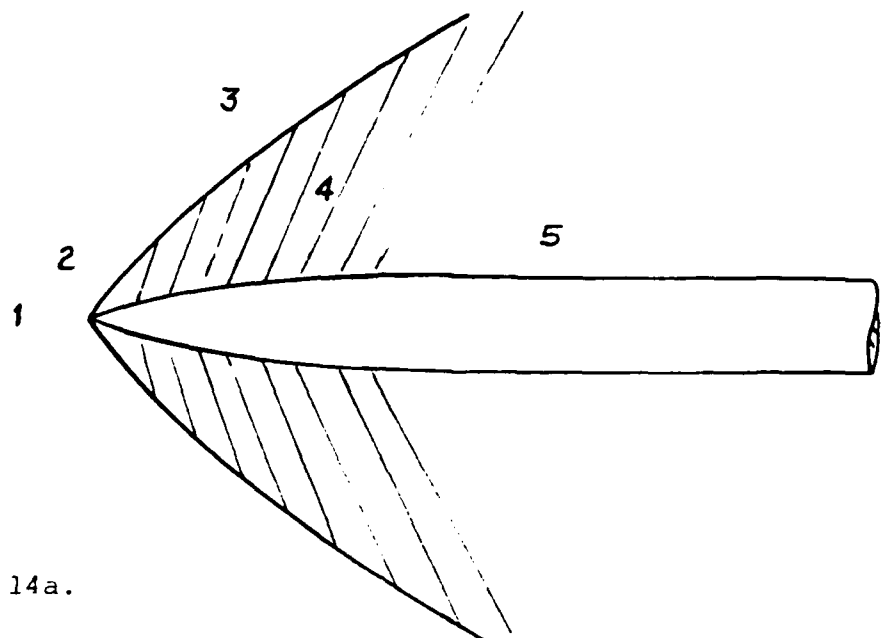


Fig. 14a.

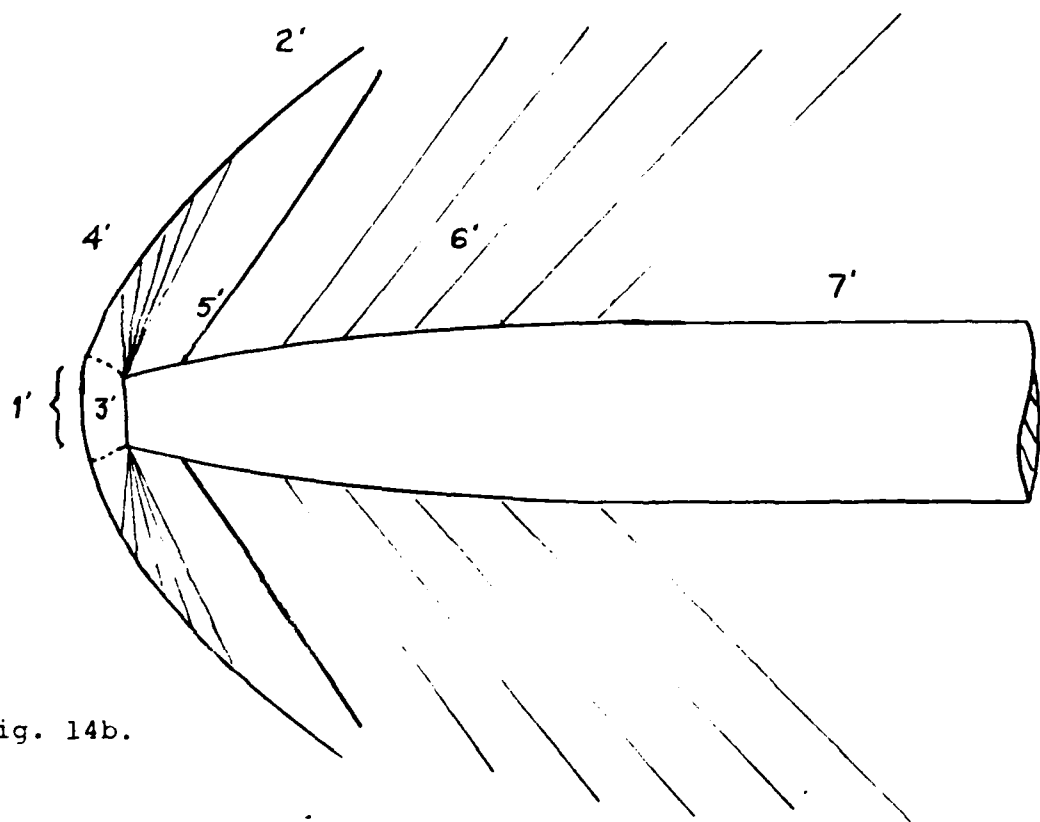


Fig. 14b.

Figure 14. Sketch of the General Flowfield.

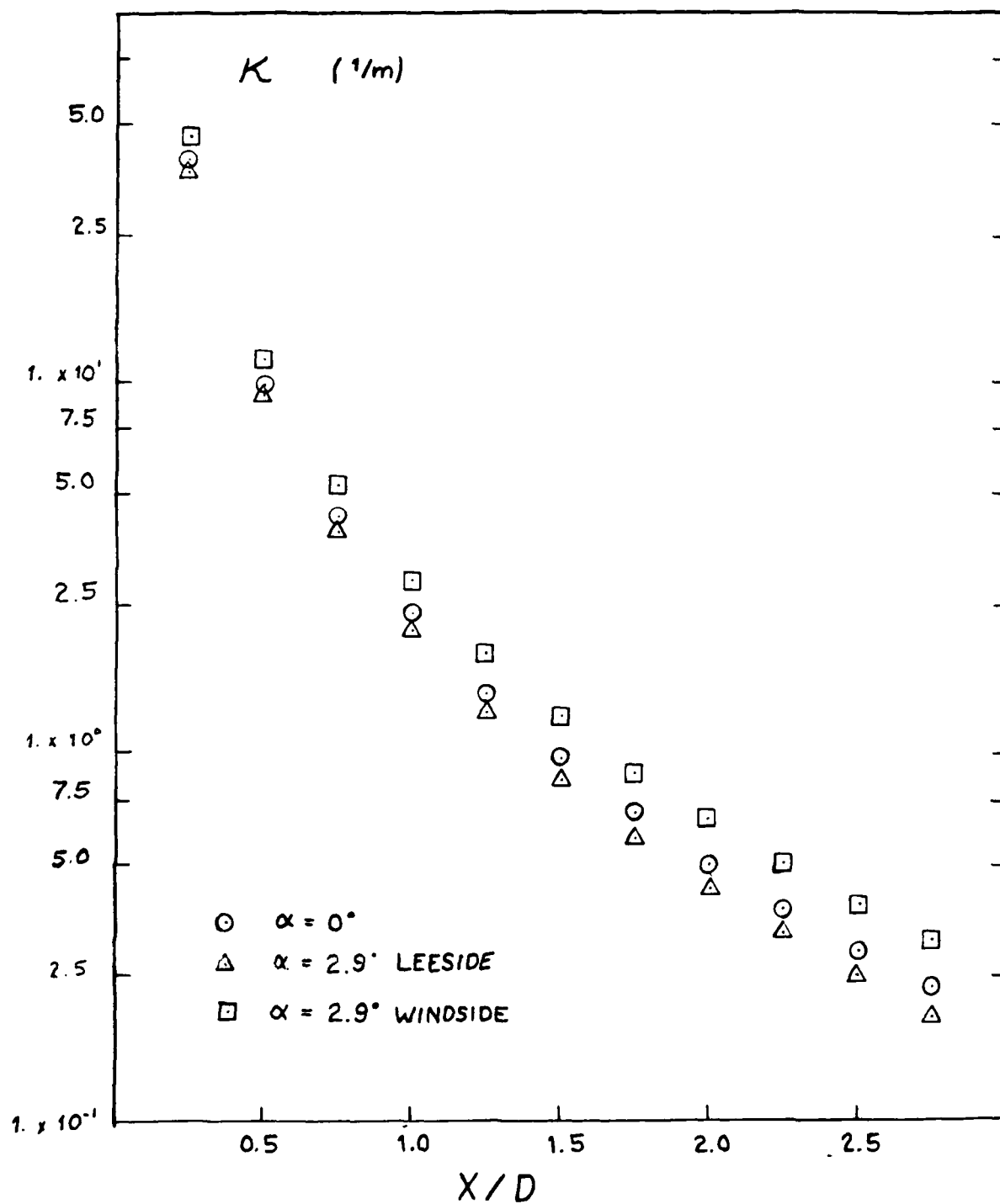


Figure 15. Shock Curvature Along the Bow Shock for the R2 Tip.

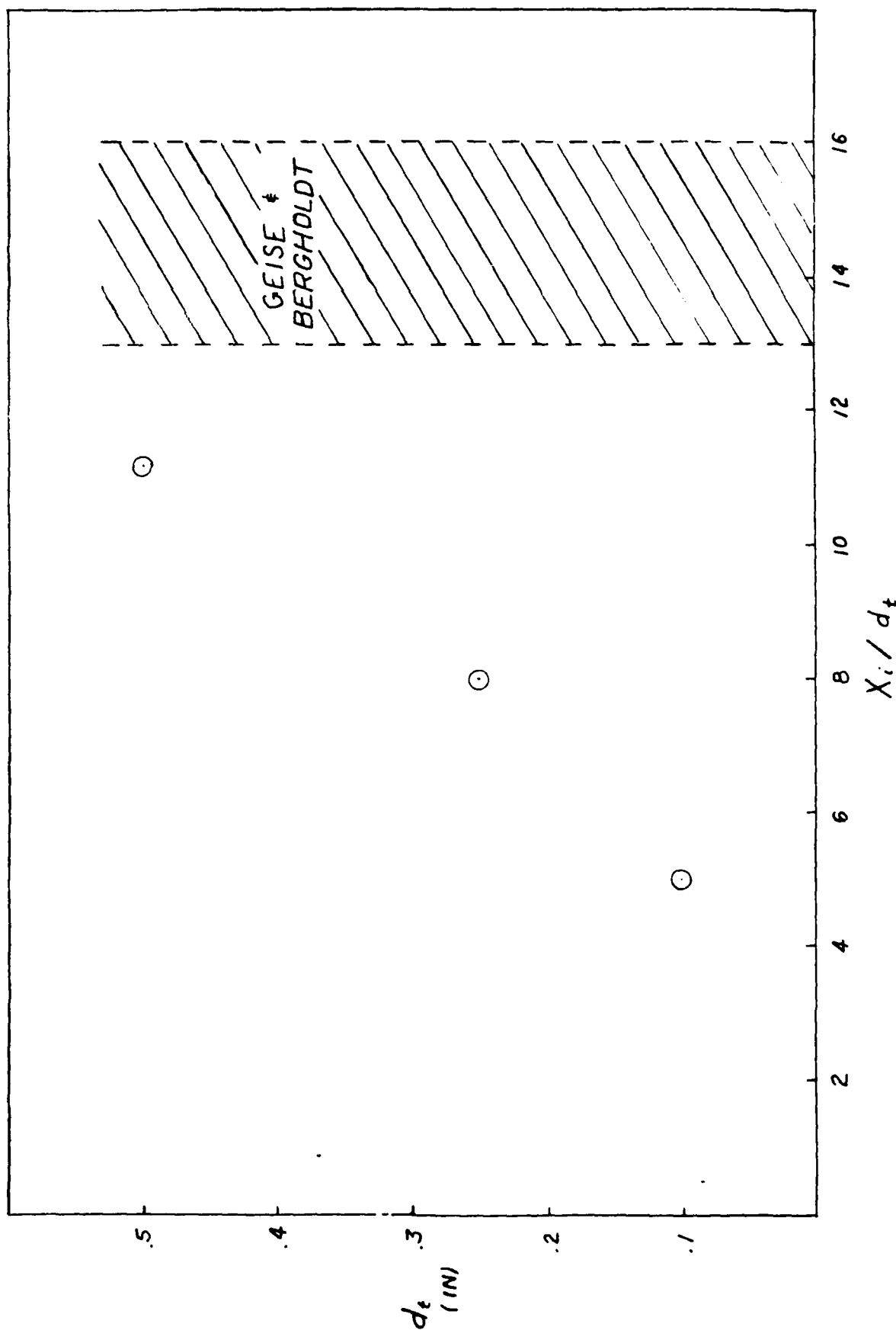


Figure 16. Position of the shock inflection point versus tip diameter.

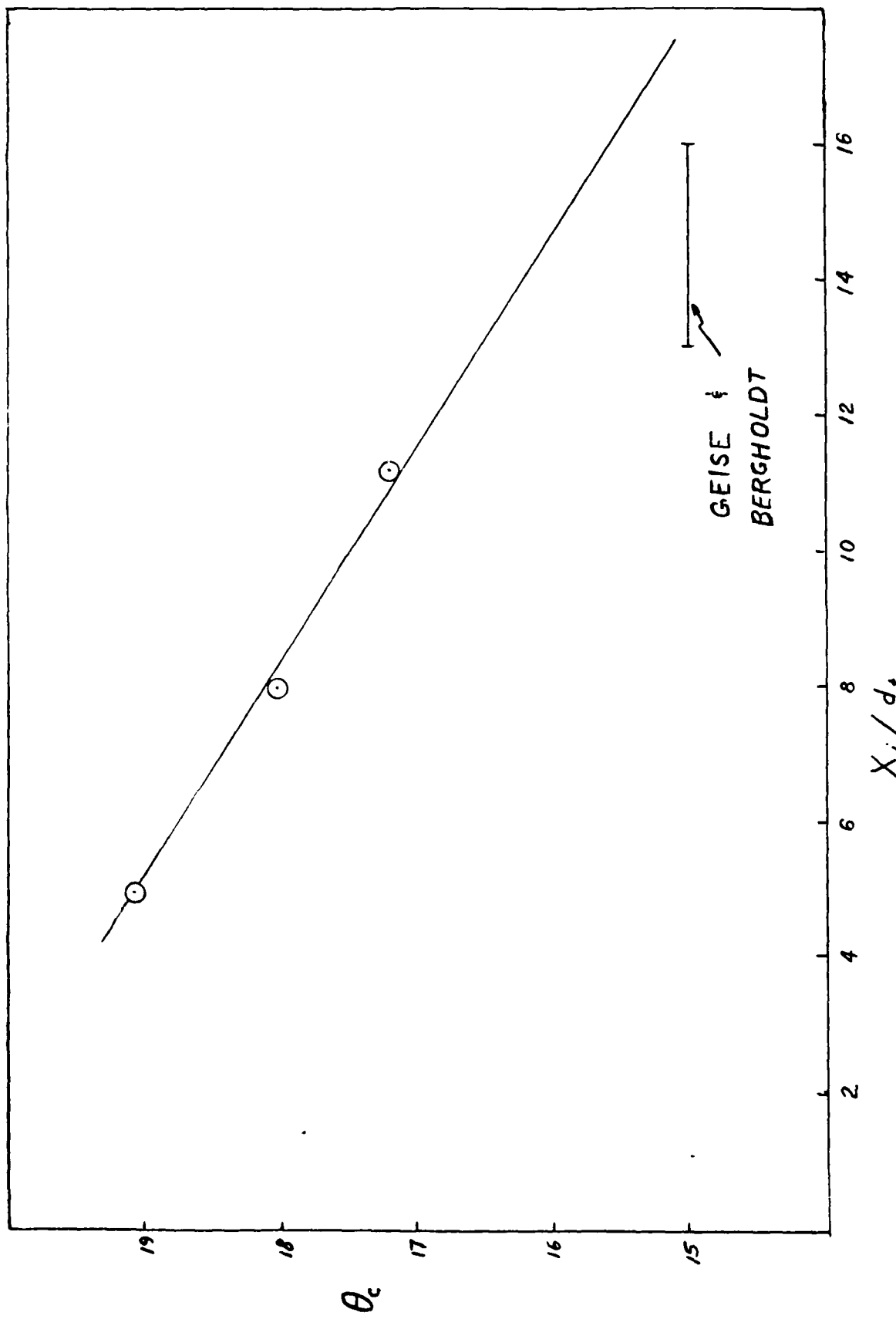


Figure 17. position of the shock inflection point versus tip corner inclination.

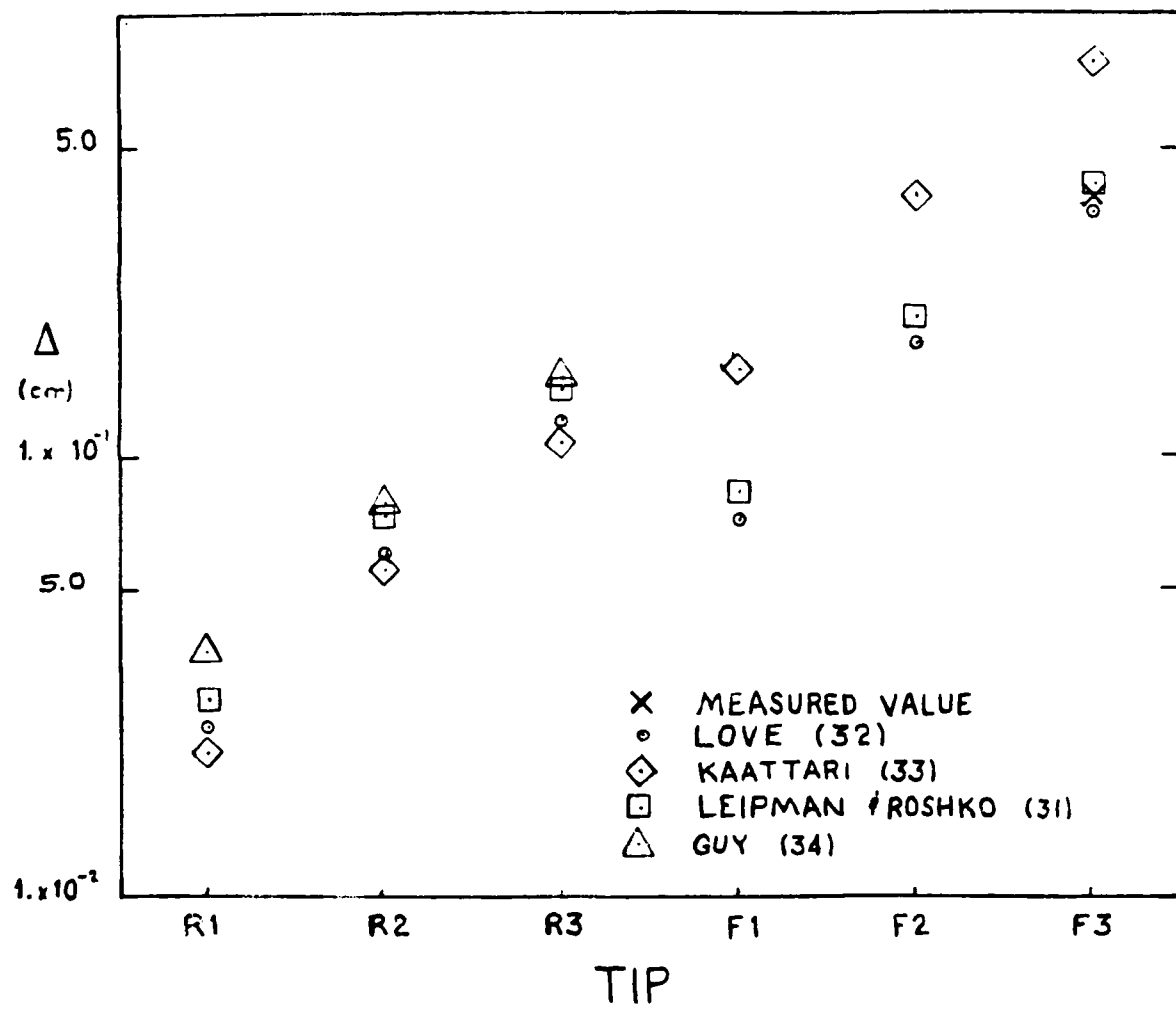


Figure 18. Shock Standoff Distance Comparison for Blunt Model Tips.

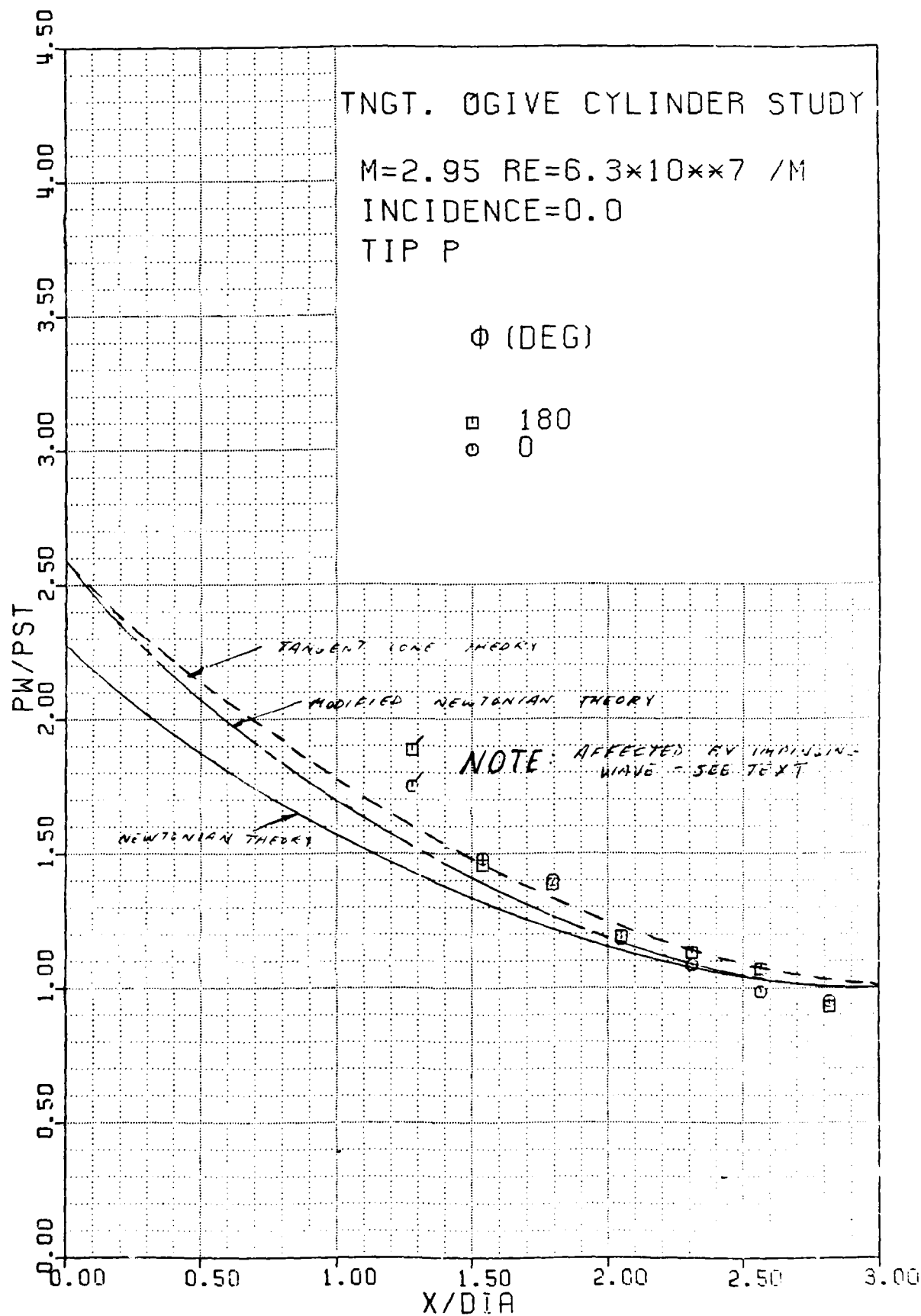


Figure 19. Surface Pressures on Model Tip P,  $\alpha = 0^\circ$ .

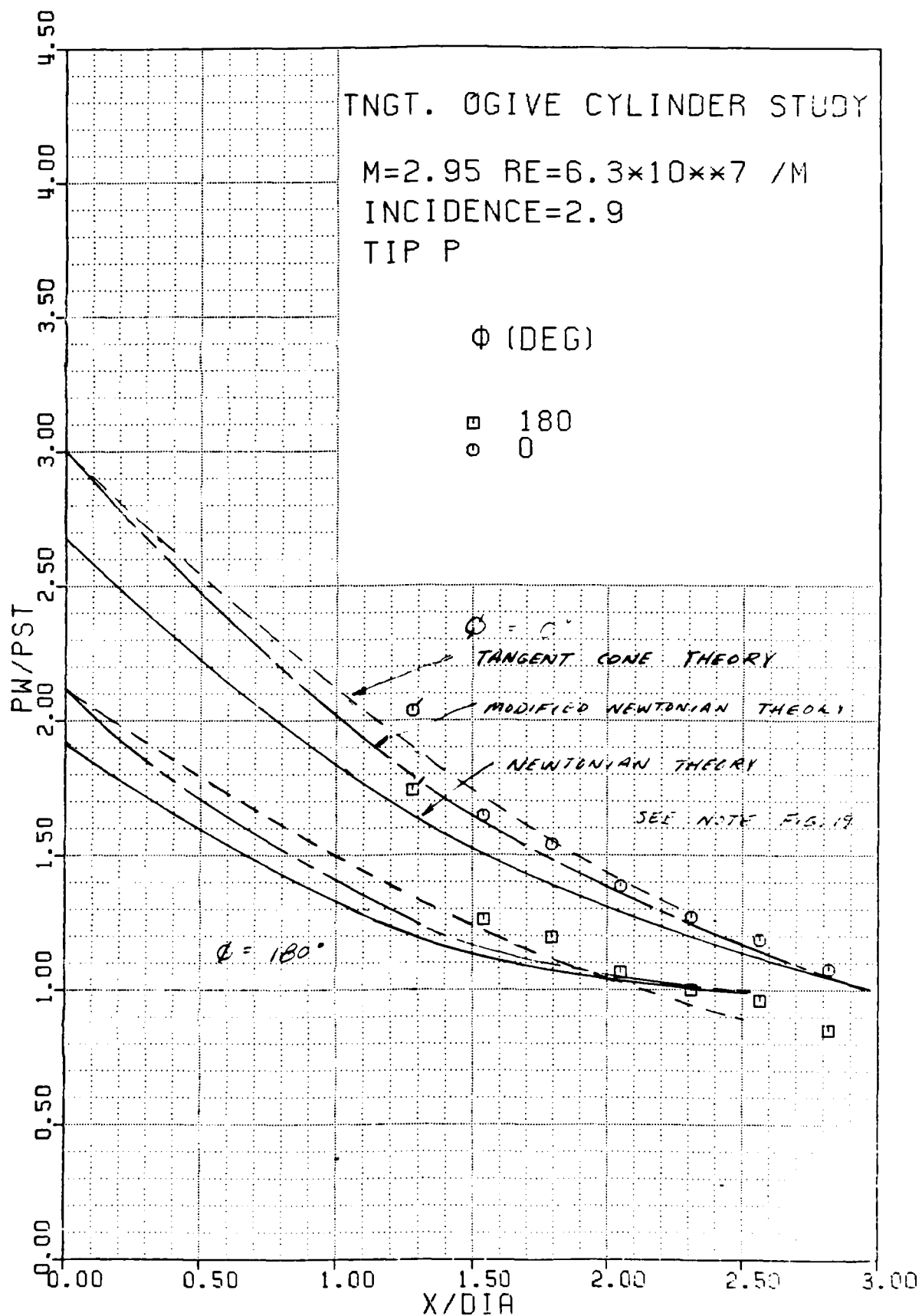


Figure 20. Surface Pressures on Model Tip P,  $\alpha = 2.9^\circ$ .

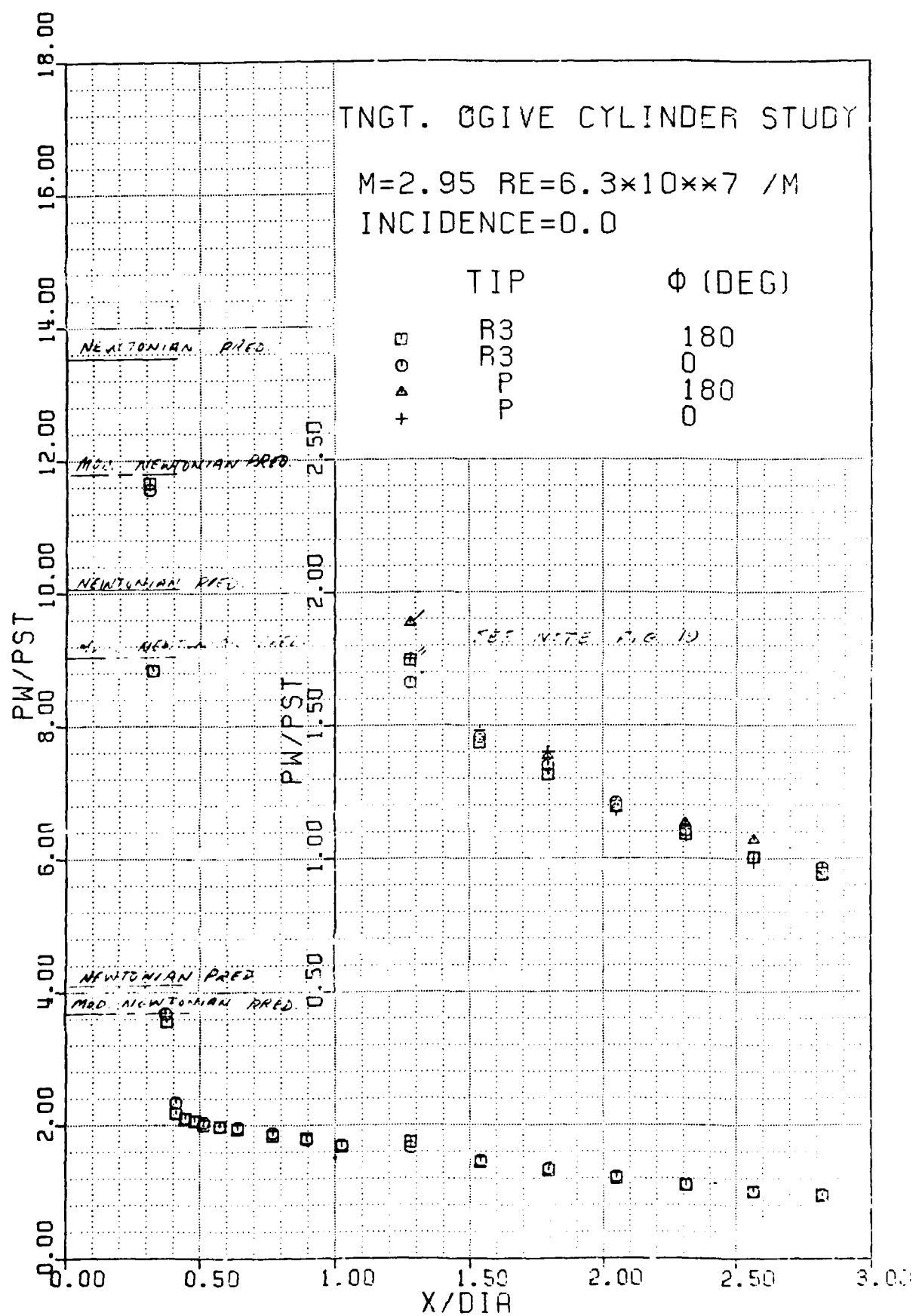


Figure 21. Surface Pressures on Model Tip R3,  $\alpha = 0^\circ$ .

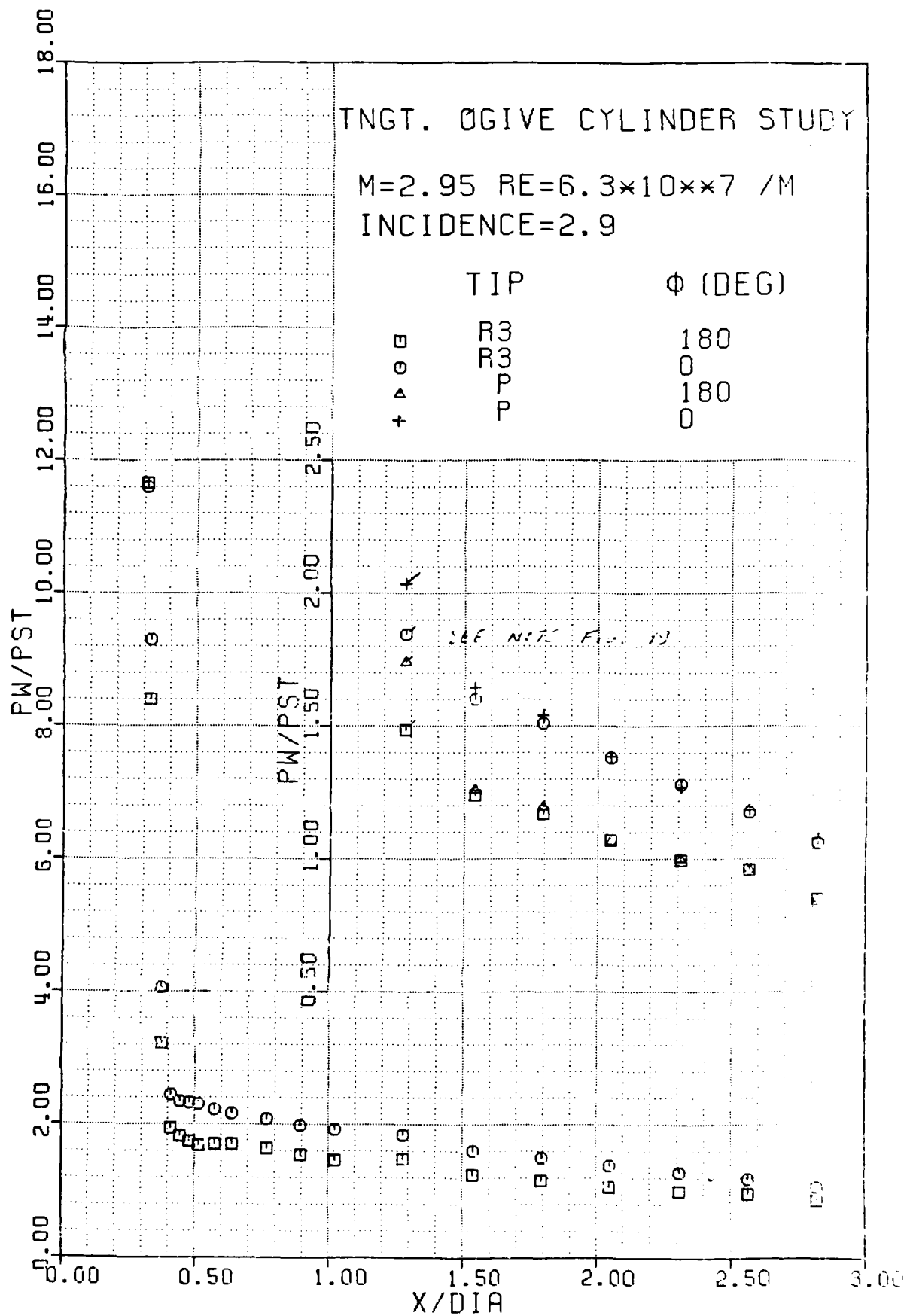


Figure 22. Surface Pressures on Model Tip R3,  $\alpha = 2.9^\circ$ .

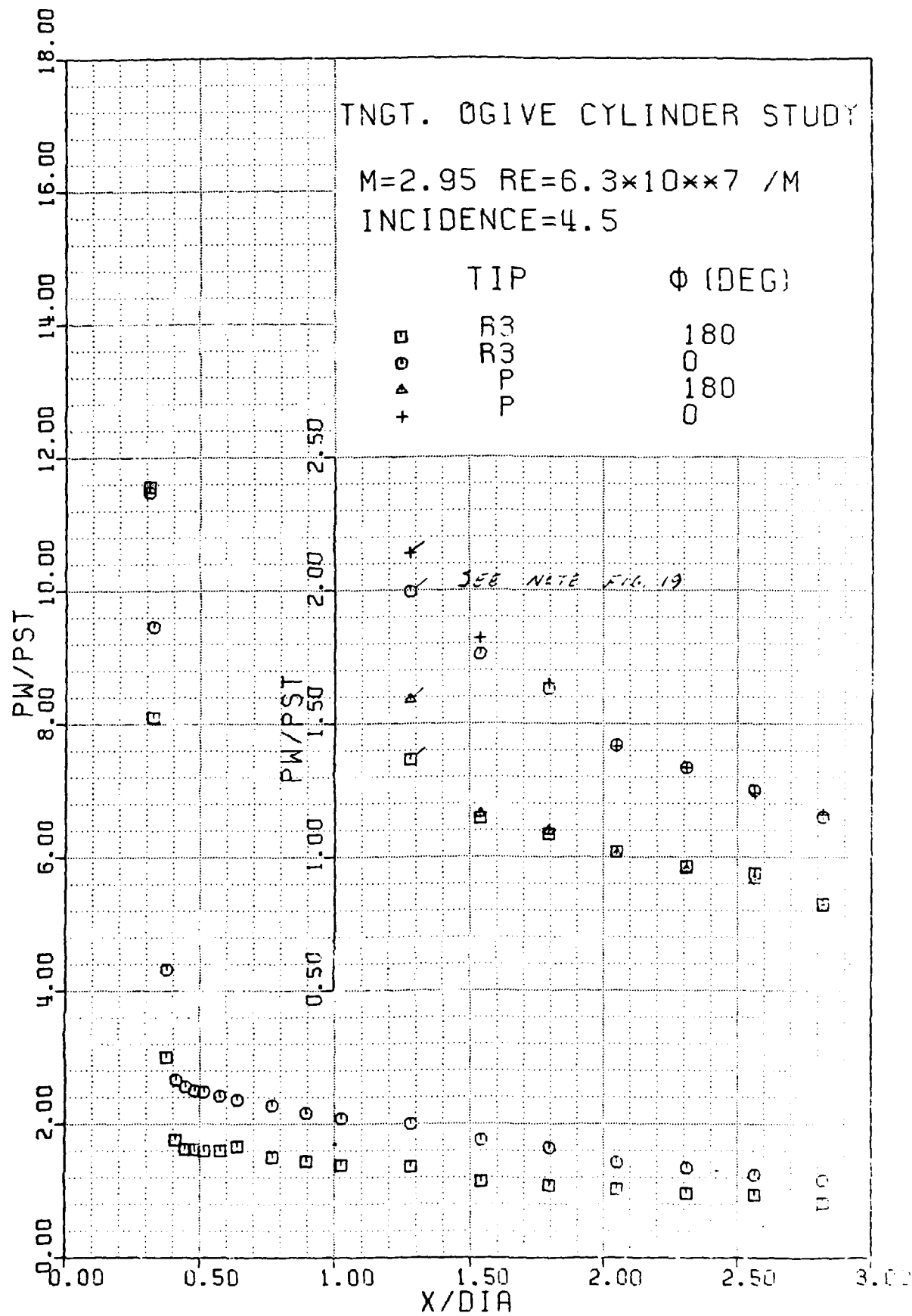


Figure 23. Surface Pressures on Model Tip R3,  $\alpha = 4.5^\circ$ .

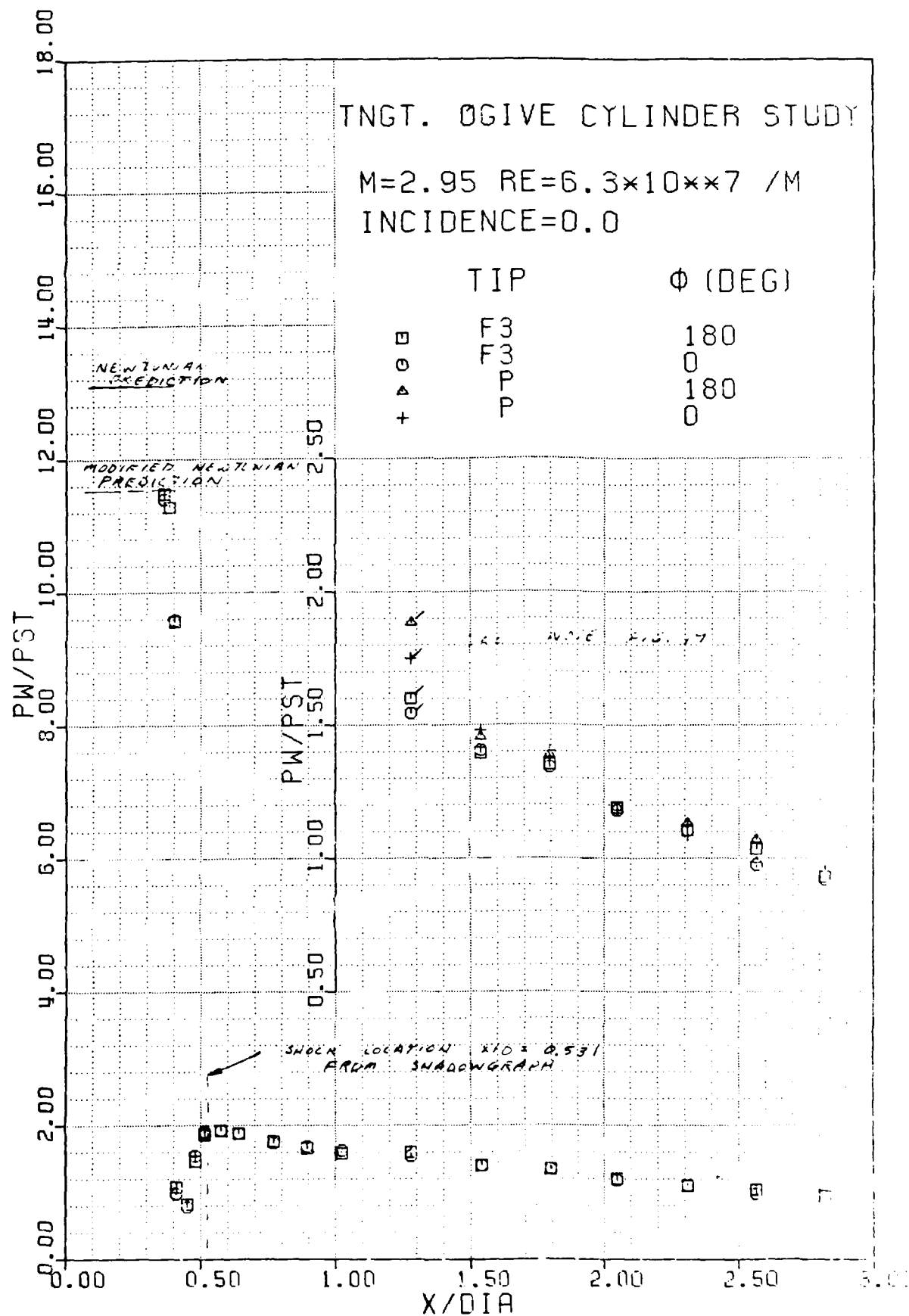


Figure 24. Surface Pressures on Model Tip F3,  $\alpha = 0^\circ$ .

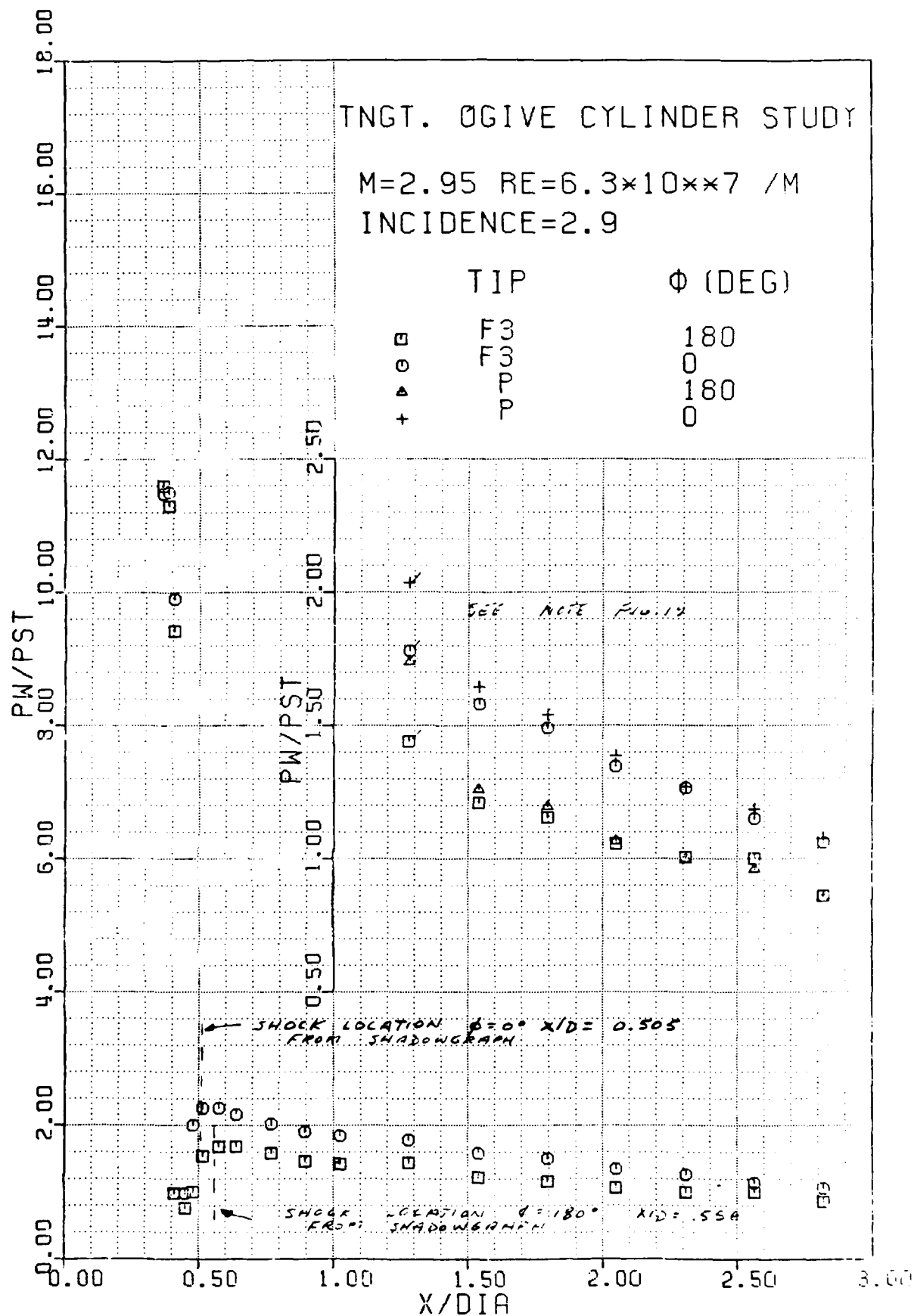


Figure 25. Surface Pressures on Model Tip F3,  $\alpha = 2.9^\circ$ .

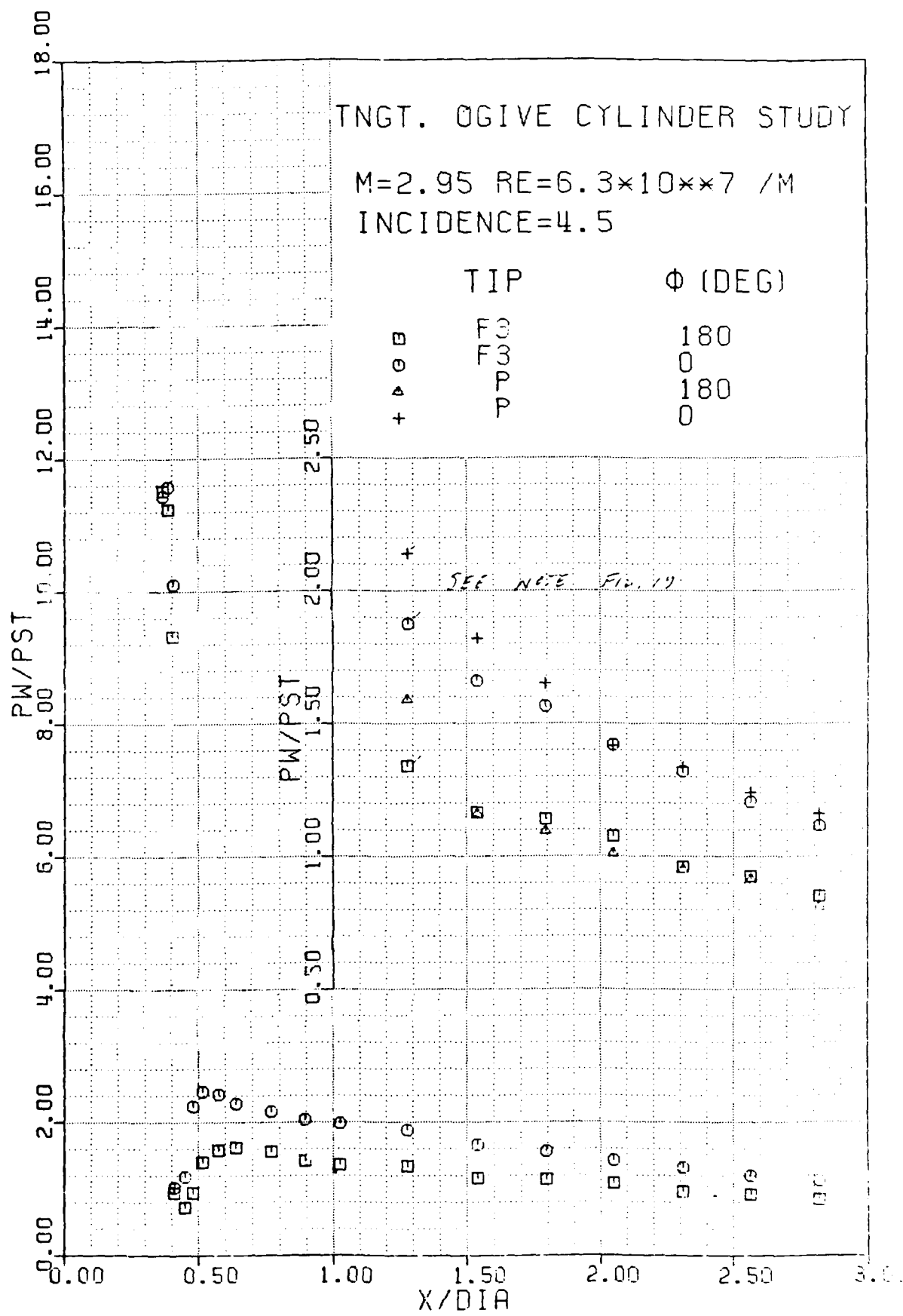


Figure 26. Surface Pressures on Model Tip F3,  $\alpha = 4.5^\circ$ .

TNGT. OGIVE CYLINDER STUDY

M=2.95 RE=6.3\*10\*\*7 /M

INCIDENCE=0.0  $\phi = 0$

TIP

P  
R1  
R2  
R3  
R4  
R5  
R6  
R7  
R8

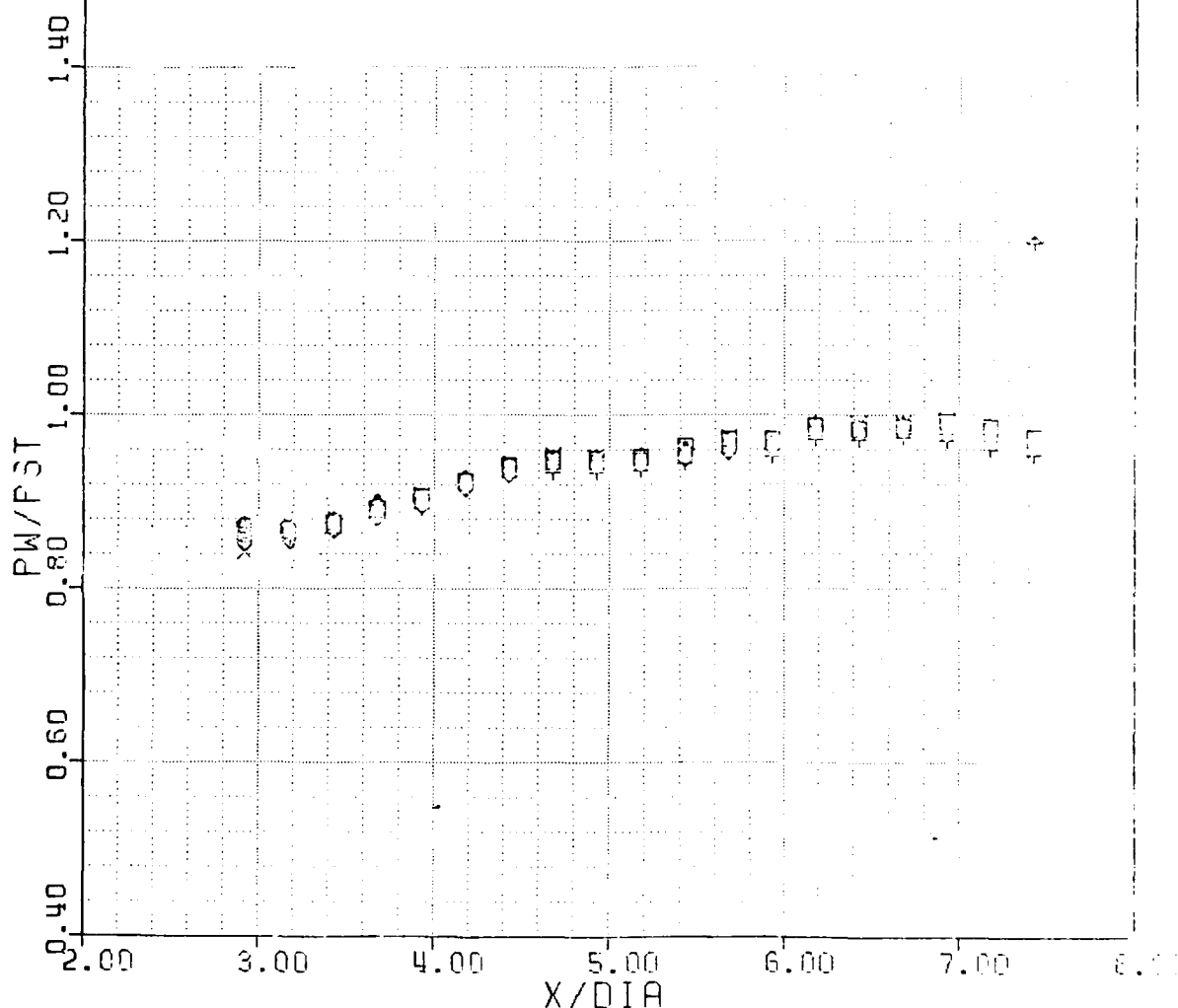


Figure 27. Surface Pressures on the Cylinder for all Model Tips with  $\alpha = 0^\circ$ .

TNGT. OGIVE CYLINDER STUDY

$M=2.95$   $RE=6.3 \times 10^7$  /M  
INCIDENCE=2.9  $\phi = 0$

TIP

P  
R1  
R2  
R3  
F1  
F2  
F3

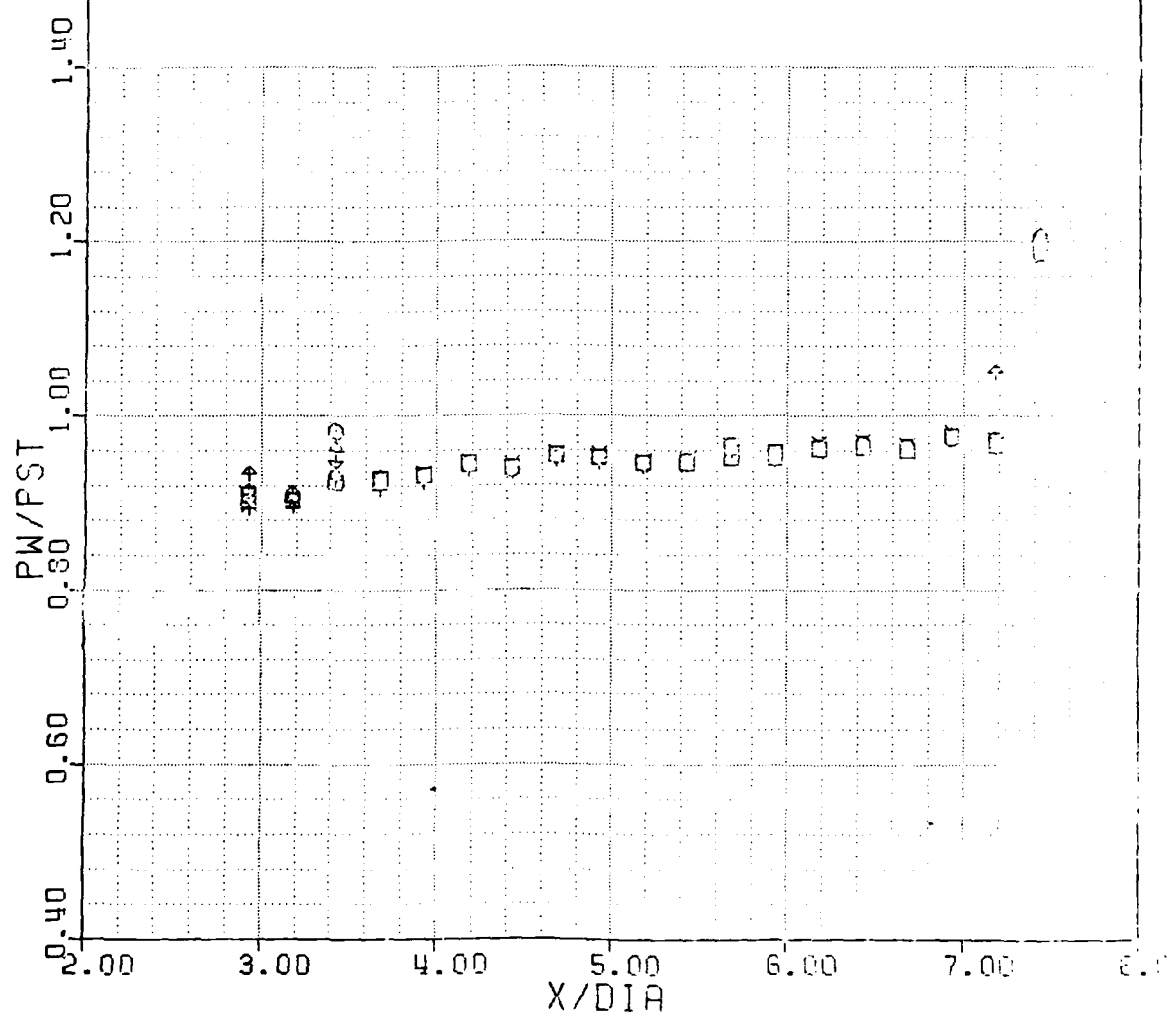


Figure 28. Surface Pressures on the Cylinder for all Model Tips with  $\alpha = 2.9^\circ$ ,  $\phi = 0^\circ$ .

TNGT. OGIVE CYLINDER STUDY

$M=2.95$   $RE=6.3 \times 10^7$  /M

INCIDENCE=2.9  $\phi=180$

TIP

P  
R2  
R3  
F3

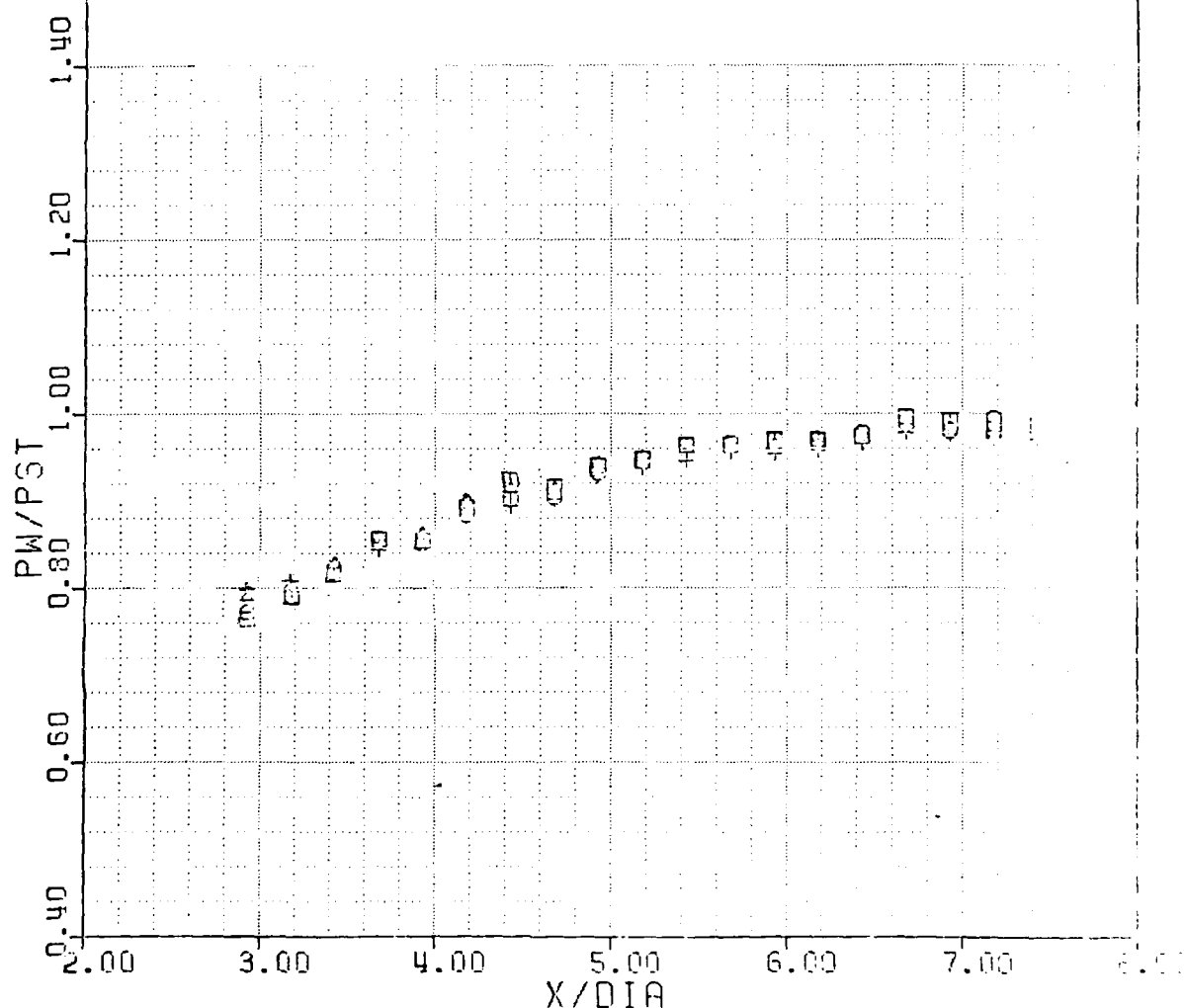


Figure 29. Surface Pressures on the Cylinder for all Model Tips with  $\alpha = 2.9^\circ$ ,  $\phi = 180^\circ$ .

TNGT. OGIVE CYLINDER STUDY

M=2.95 RE=6.3\*10\*\*7 /M  
INCIDENCE=0.0 TIP P

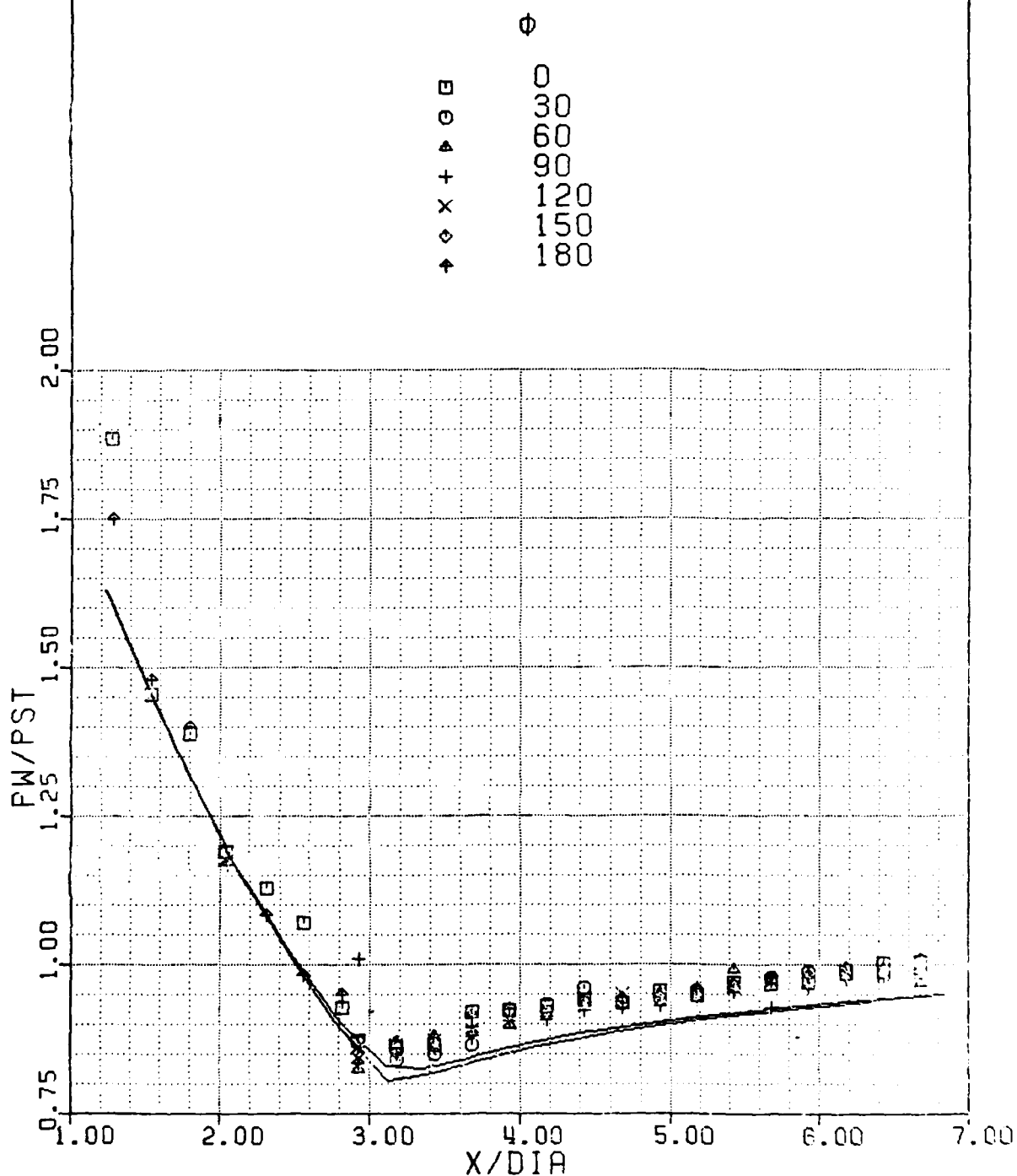


Figure 30. Comparison of Computed and Experimental Surface Pressures for the P Model Tip.

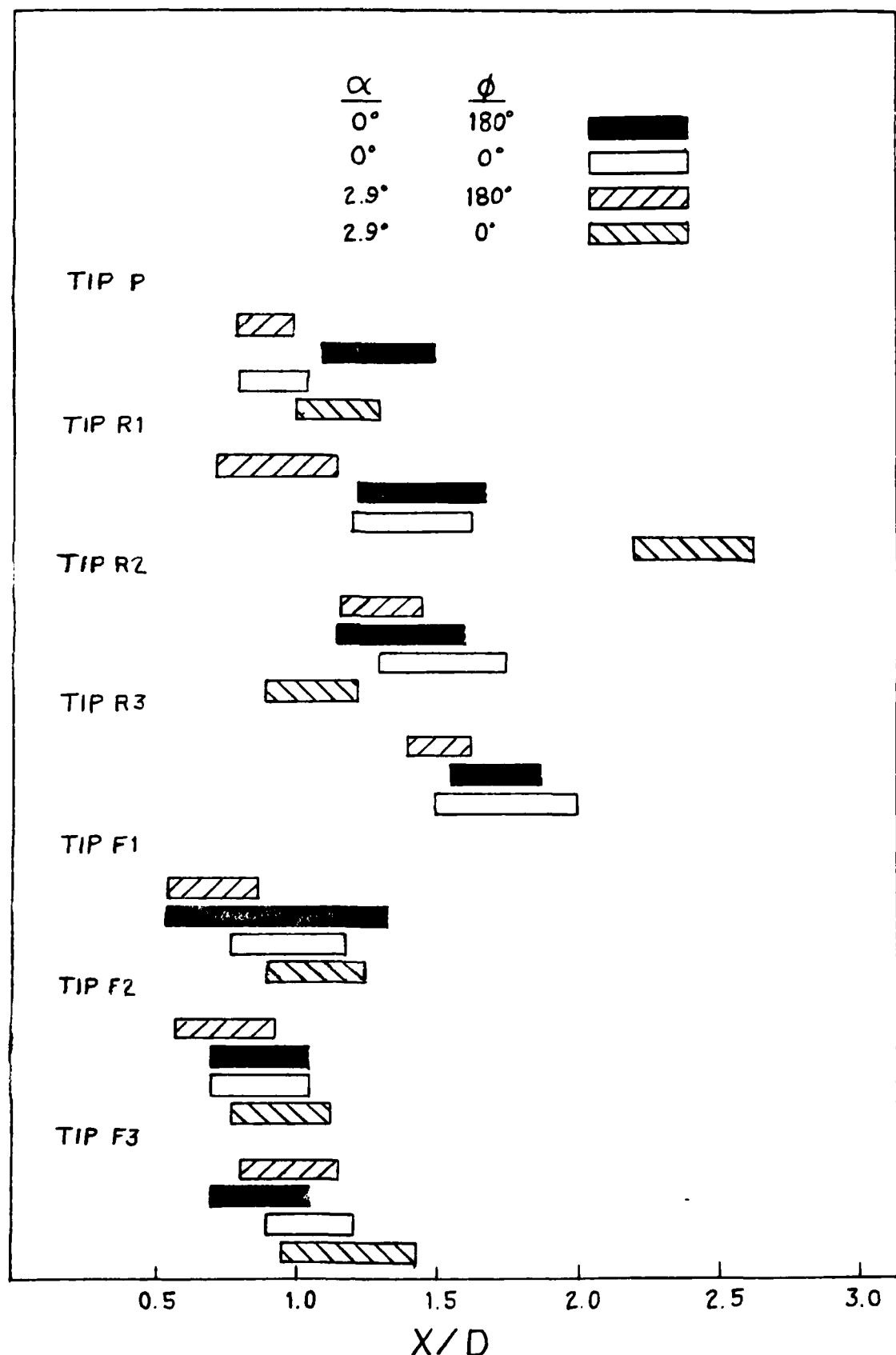


Figure 31. Boundary Layer Transition Region Versus Model Axial Distance.

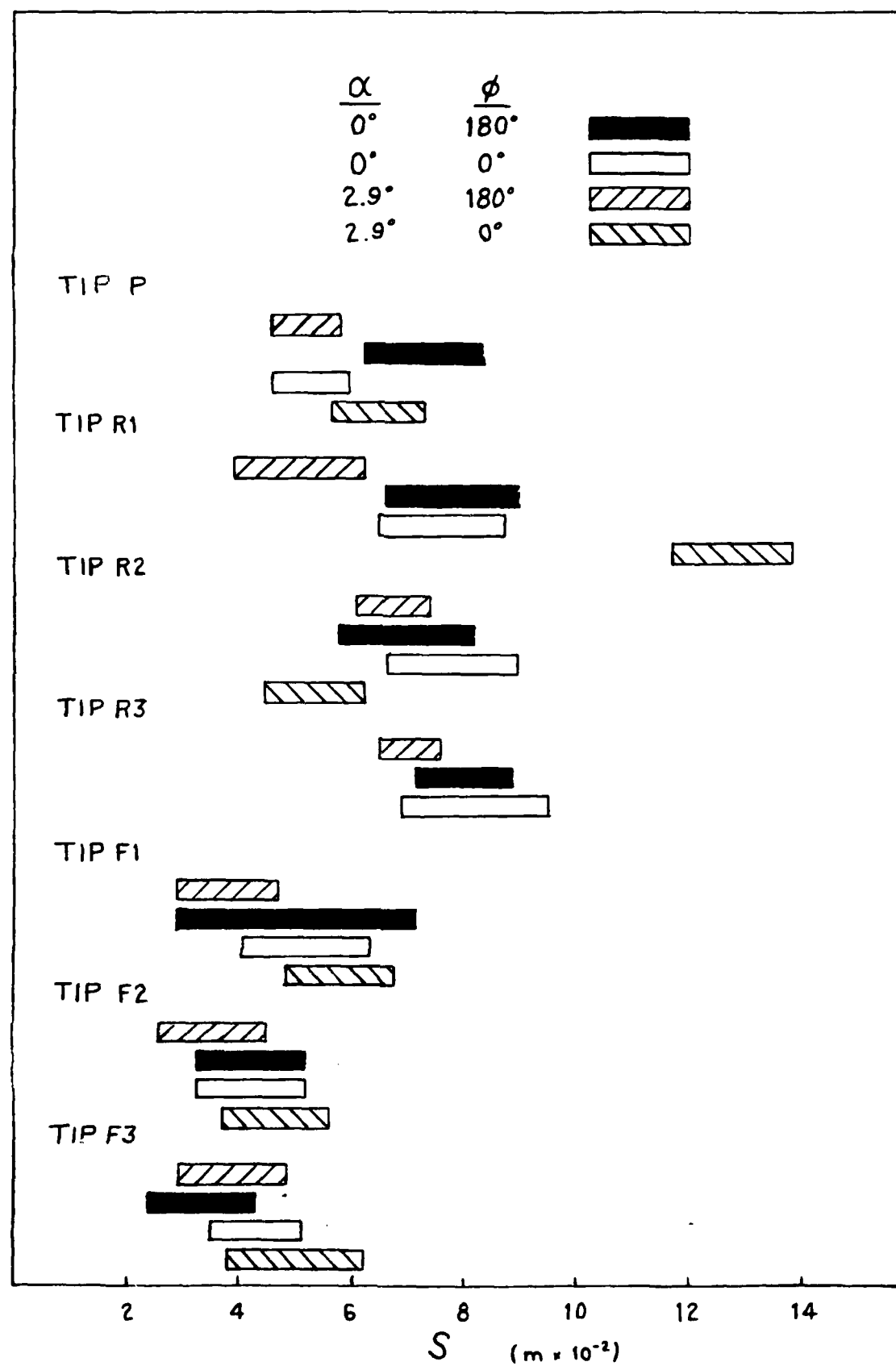


Figure 32. Boundary Layer Transition Region Versus Model Surface Distance.

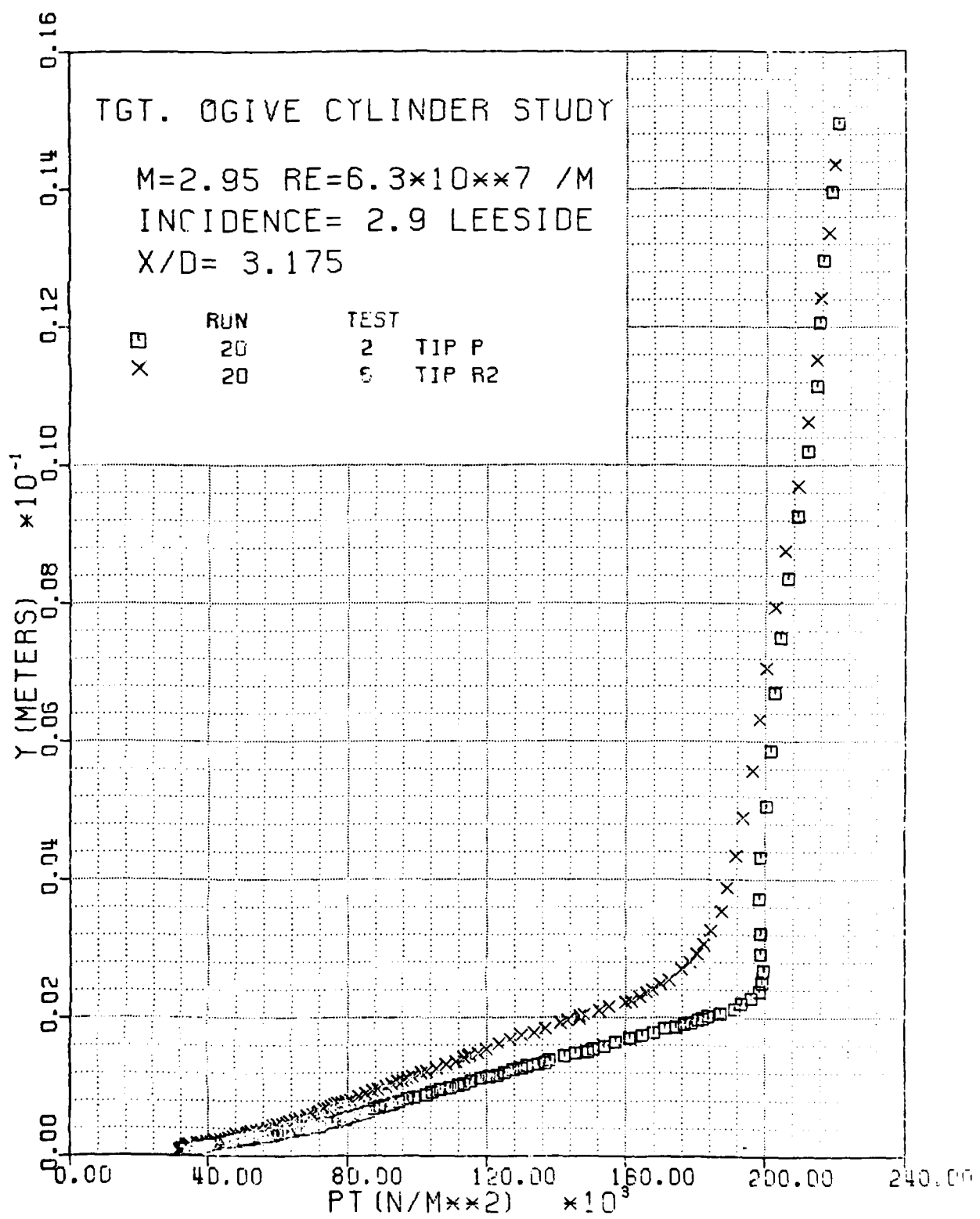


Figure 33. Comparison of Pitot Profiles for Model Tips P and R2 at  $X/D = 3.175$ ,  $\alpha = 2.9^\circ$ ,  $\Delta = 180^\circ$

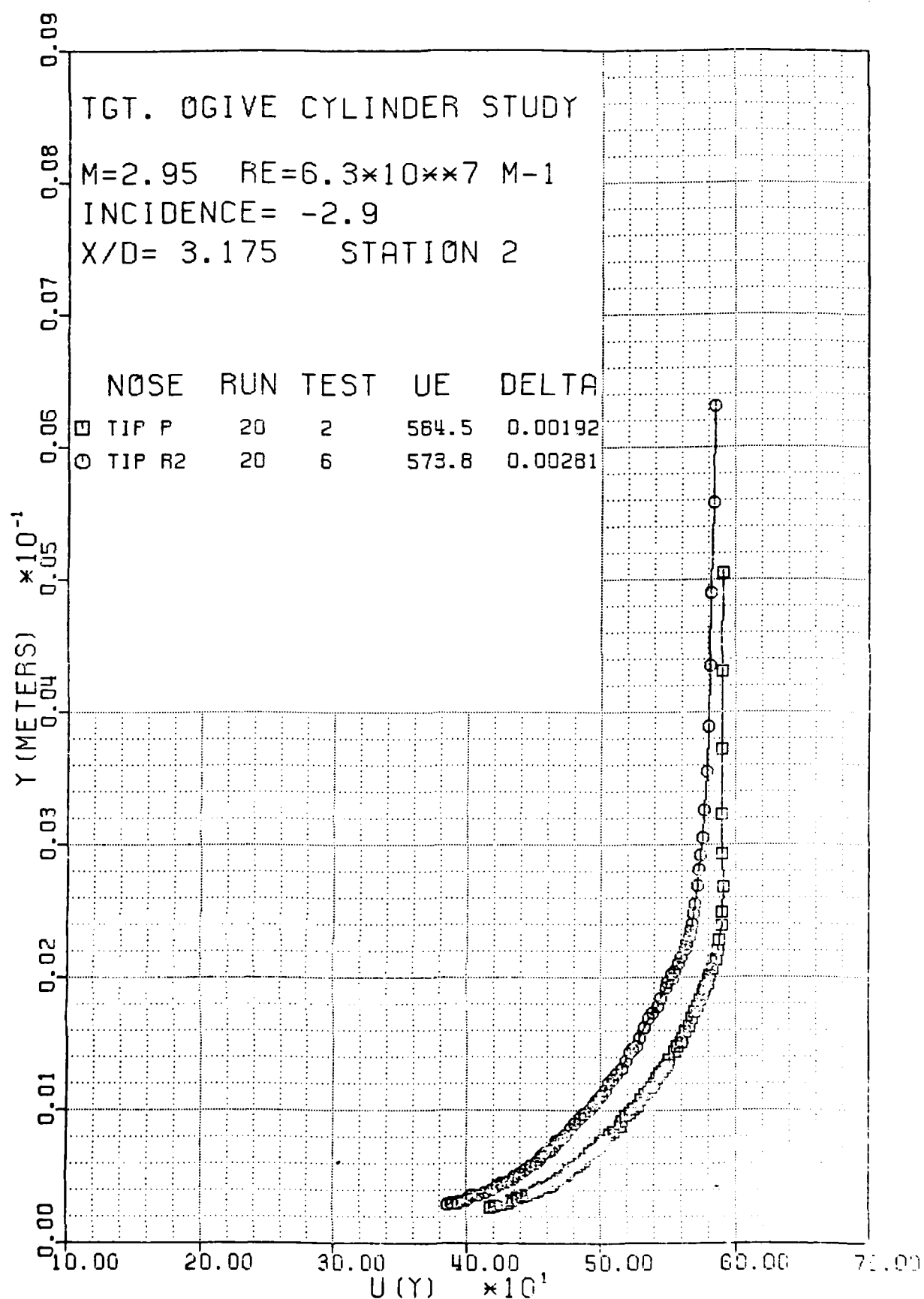


Figure 34. Comparison of Velocity Profiles for Model Tips P and R2 at  $X/D = 3.175$ ,  $\alpha = 2.9^\circ$ ,  $\phi = 180^\circ$ .

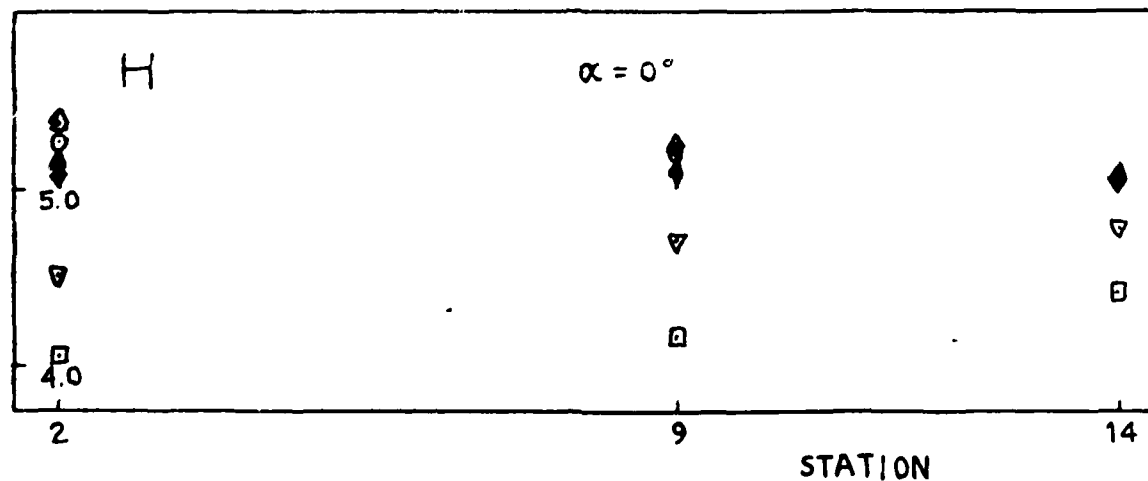
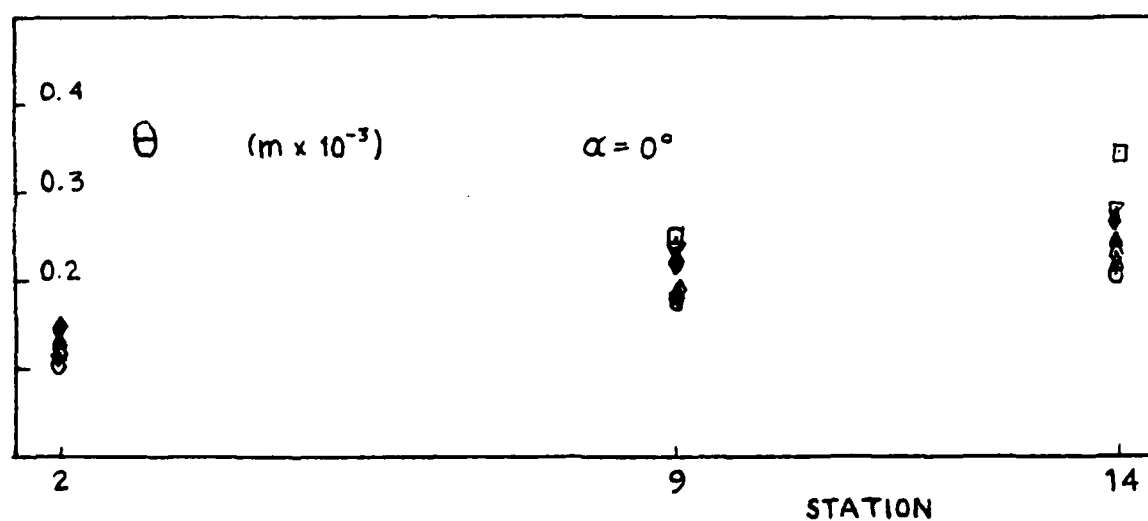
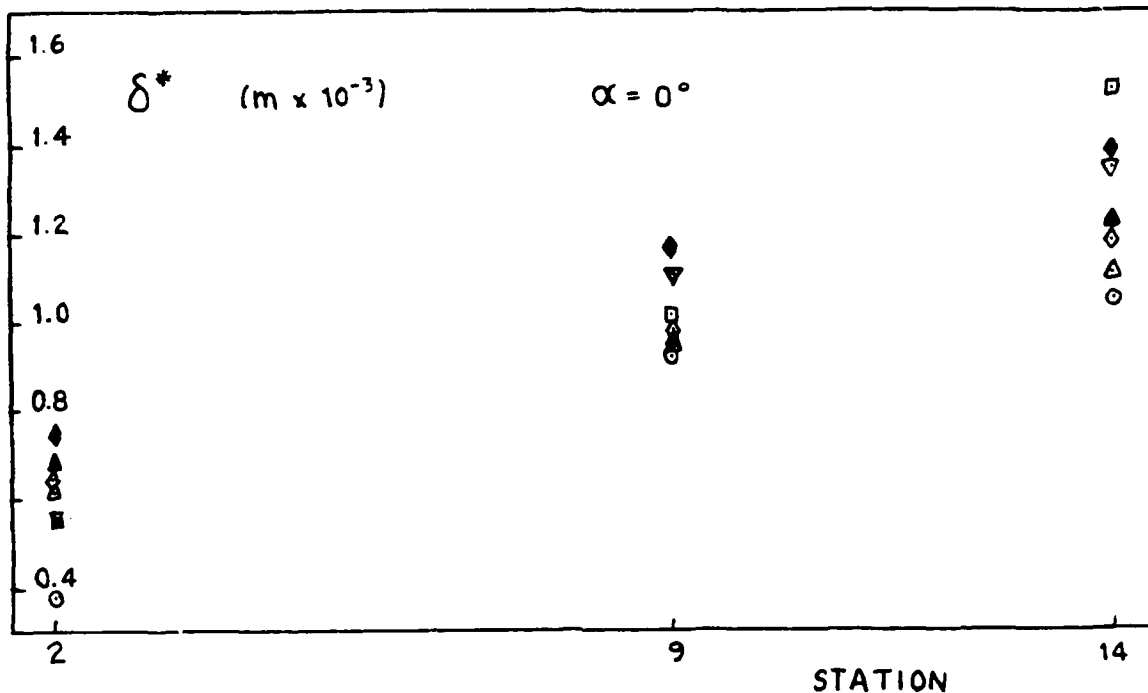


Figure 35. Displacement Thickness, Momentum Thickness and Form Factor Versus X/D,  $\alpha = 0^\circ$ .

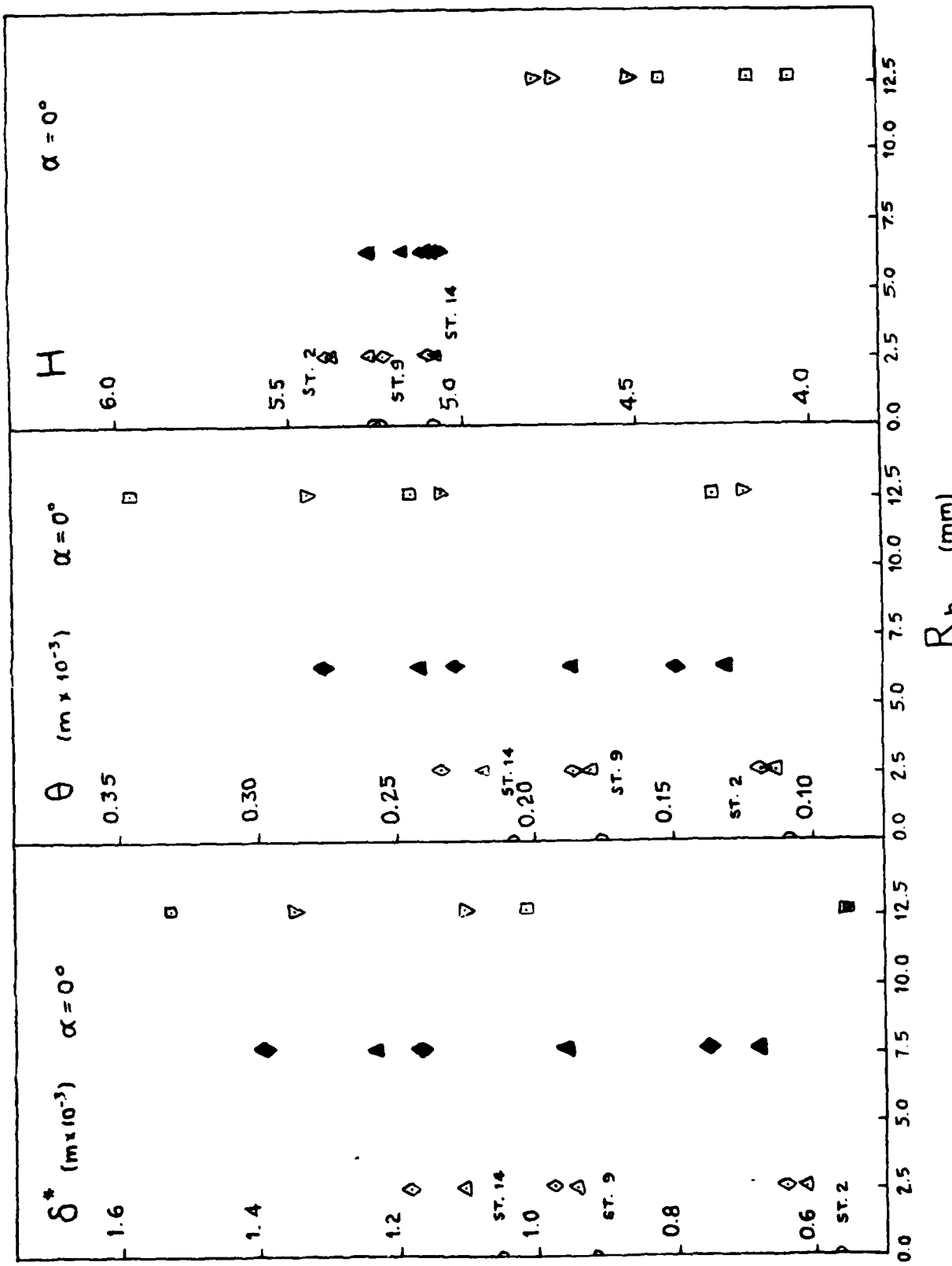


Figure 36. Displacement Thickness, Momentum Thickness and Form Factor versus  $R_b$ ,  $\alpha = 0^\circ$ .

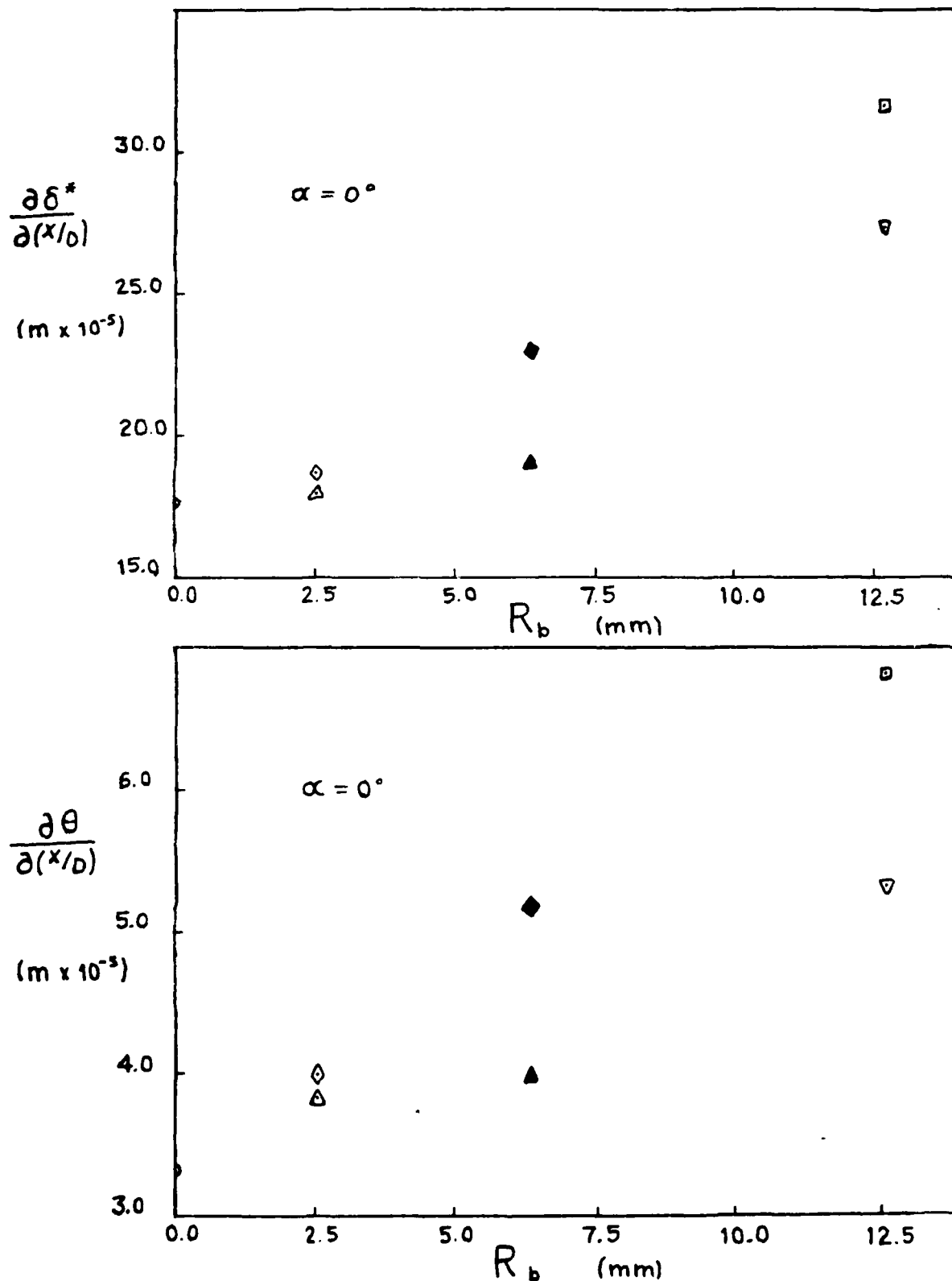


Figure 37. Displacement and Momentum Thickness Growth Versus  $R_b$ ,  $\alpha = 0^\circ$ .

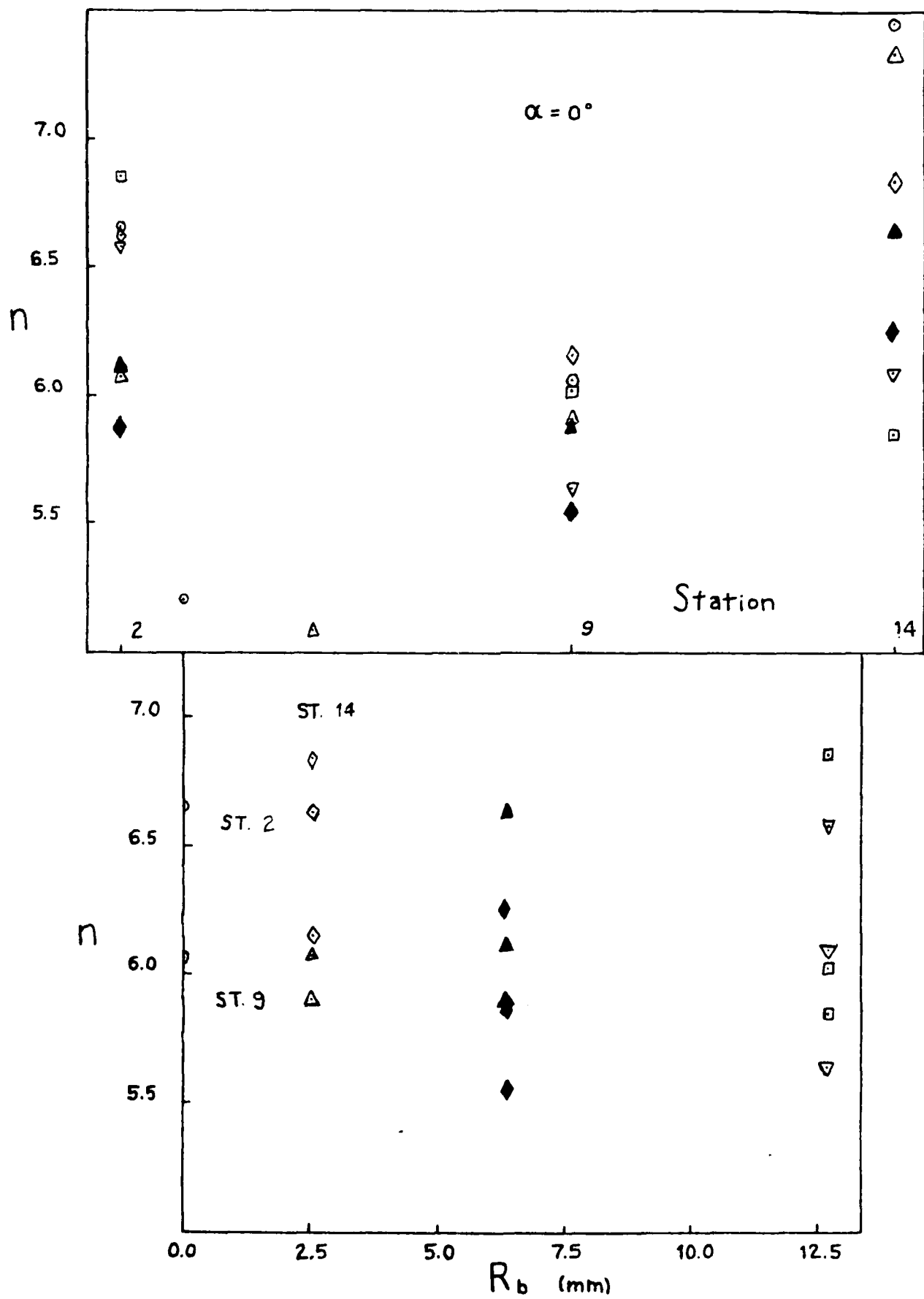


Figure 38. Power Law Exponent,  $n$ , Versus  $X/D$  and  $R_b$ ,  $\alpha = 0^\circ$ .

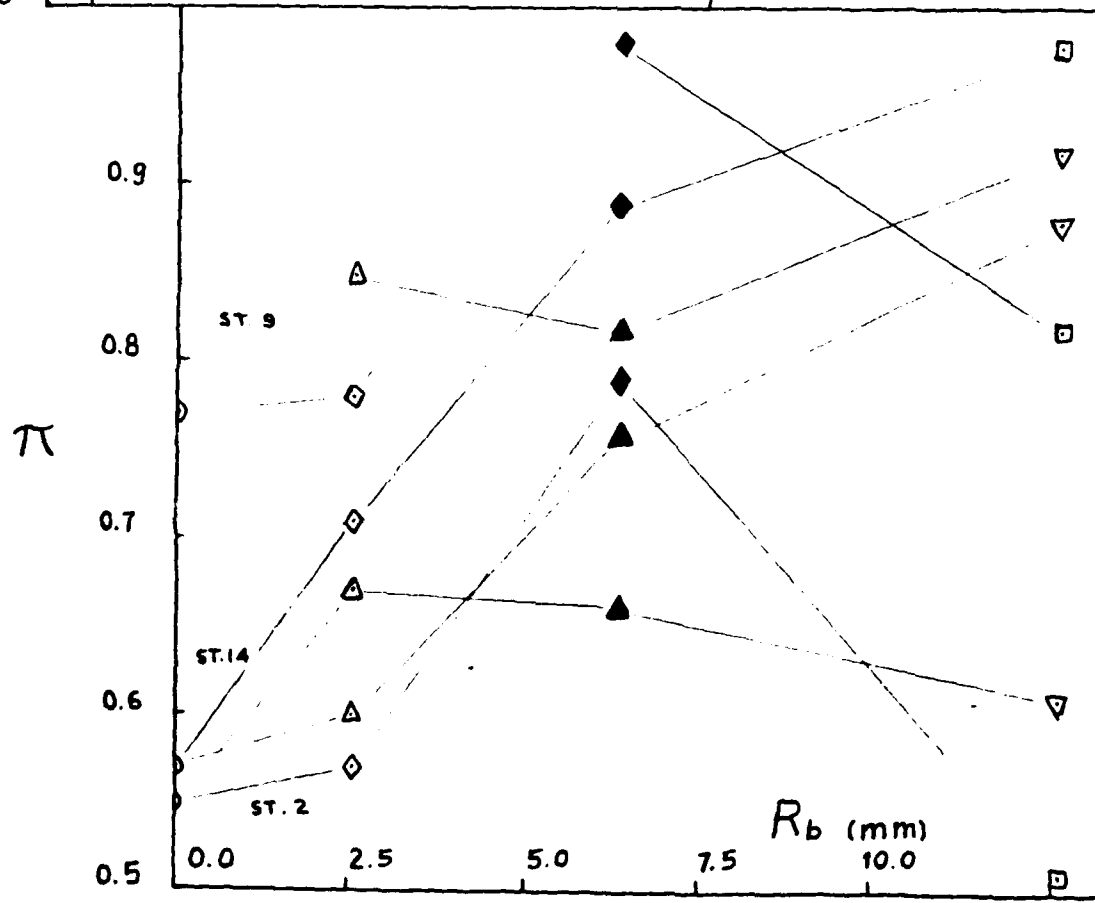
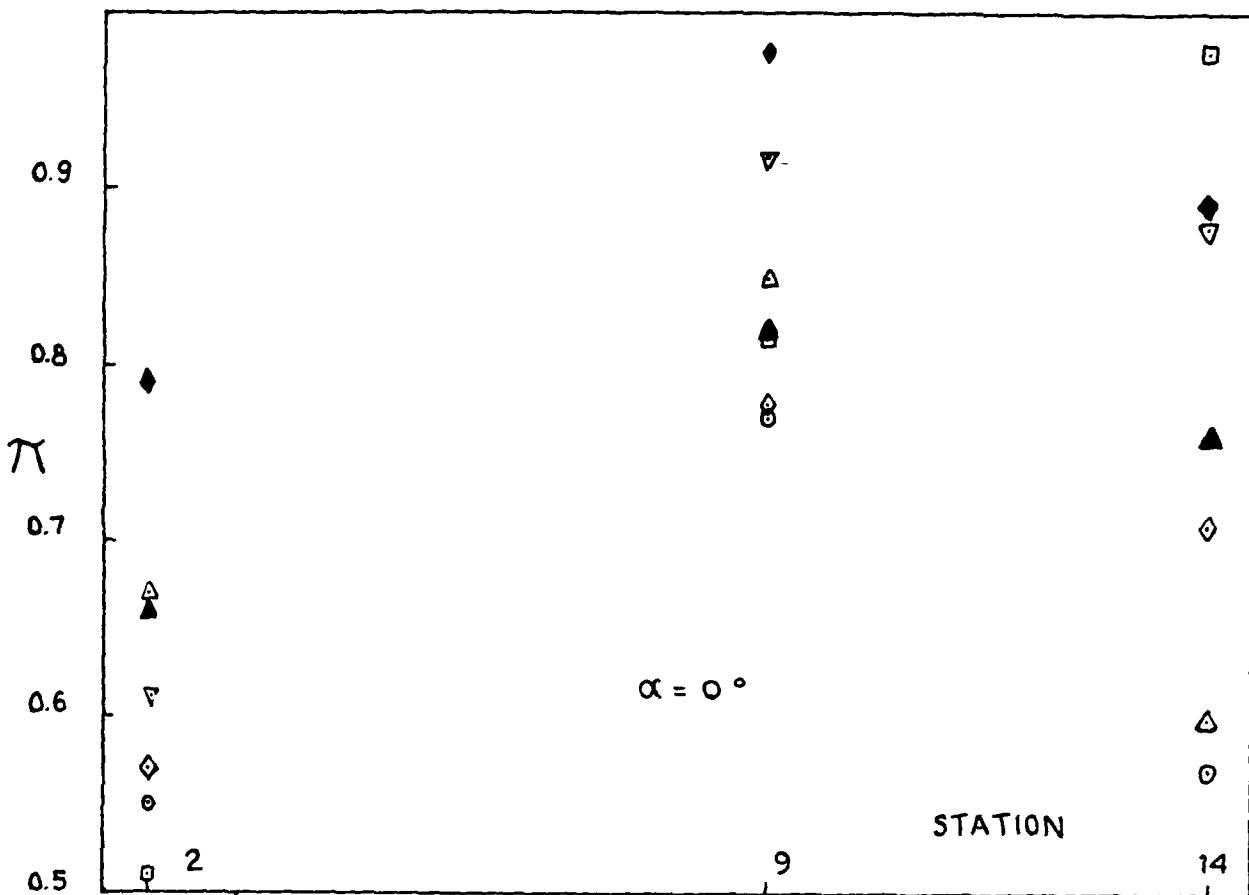


Figure 39. Wake Strength Parameter,  $\Pi$ , Versus  $X/D$  and  $R_b$ ,  $\alpha = 0^\circ$ .

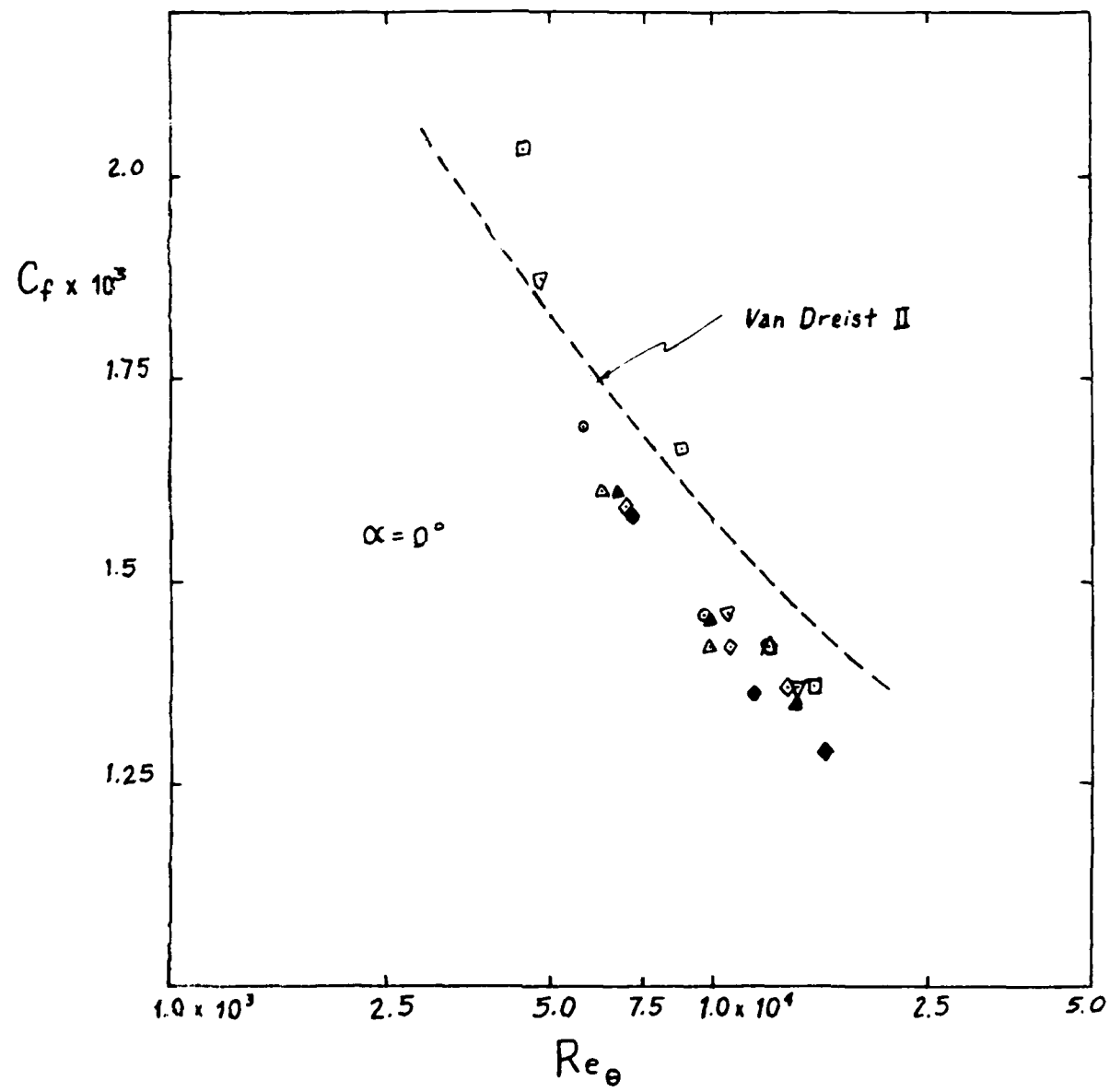


Figure 40. Skin Friction Coefficient Versus  $Re_\theta$ ,  $\alpha = 0^\circ$ .

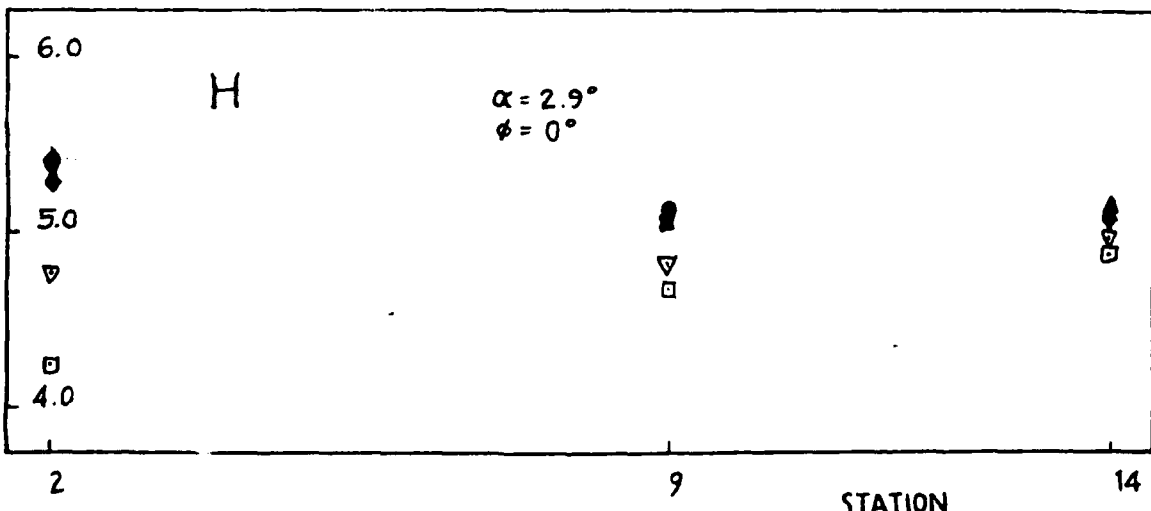
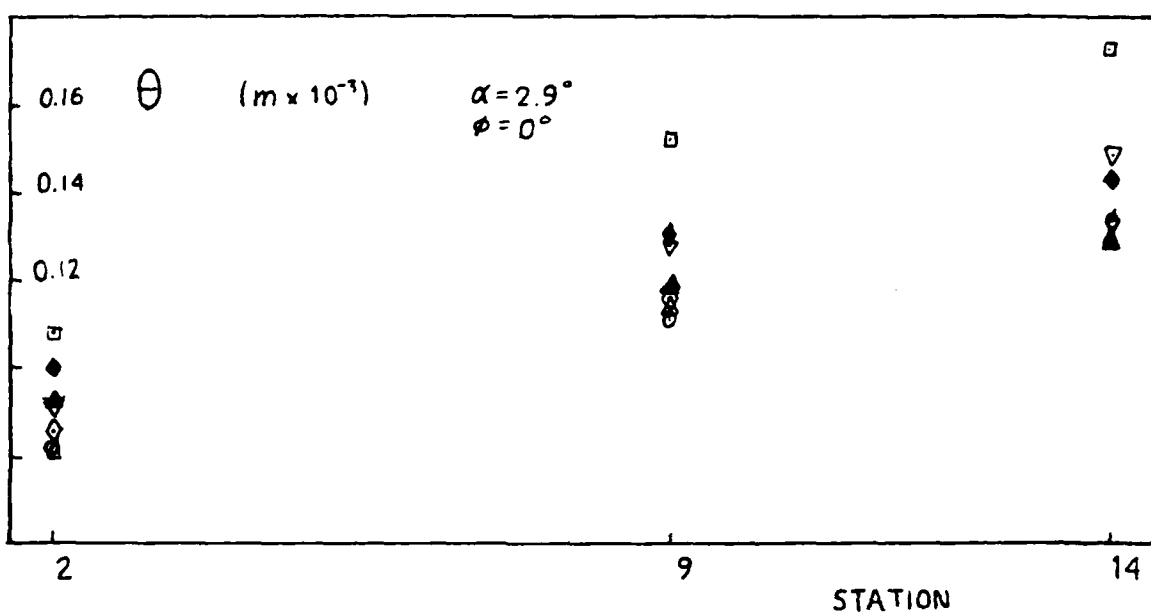
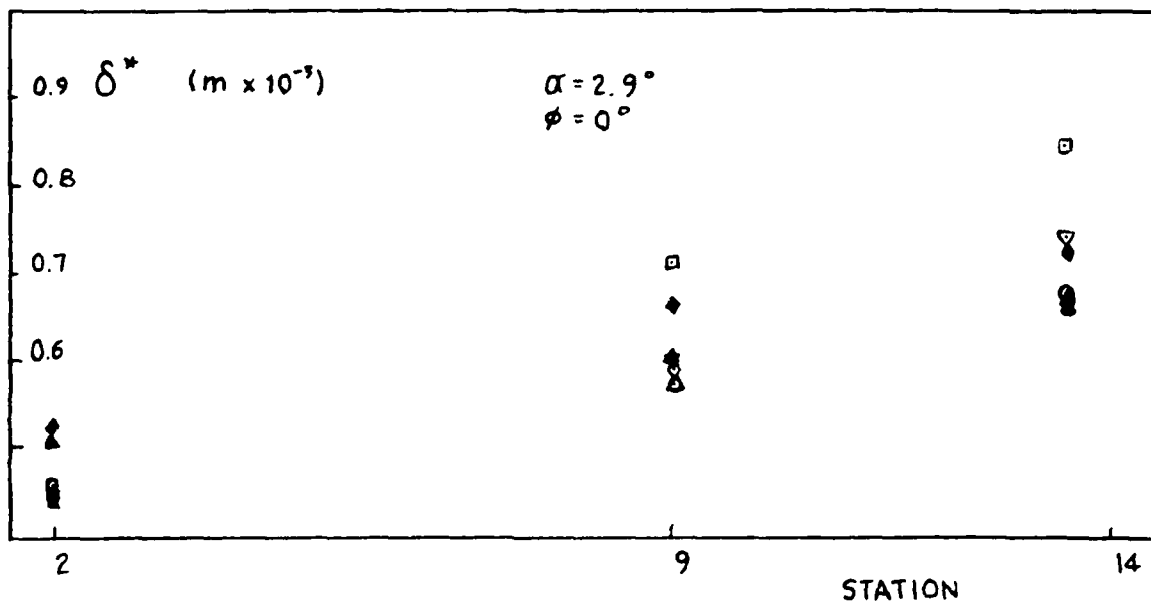


Figure 41. Displacement Thickness, Momentum Thickness, and Form Factor Versus X/D,  $\alpha = 2.9^\circ$ ,  $\phi = 0^\circ$ .

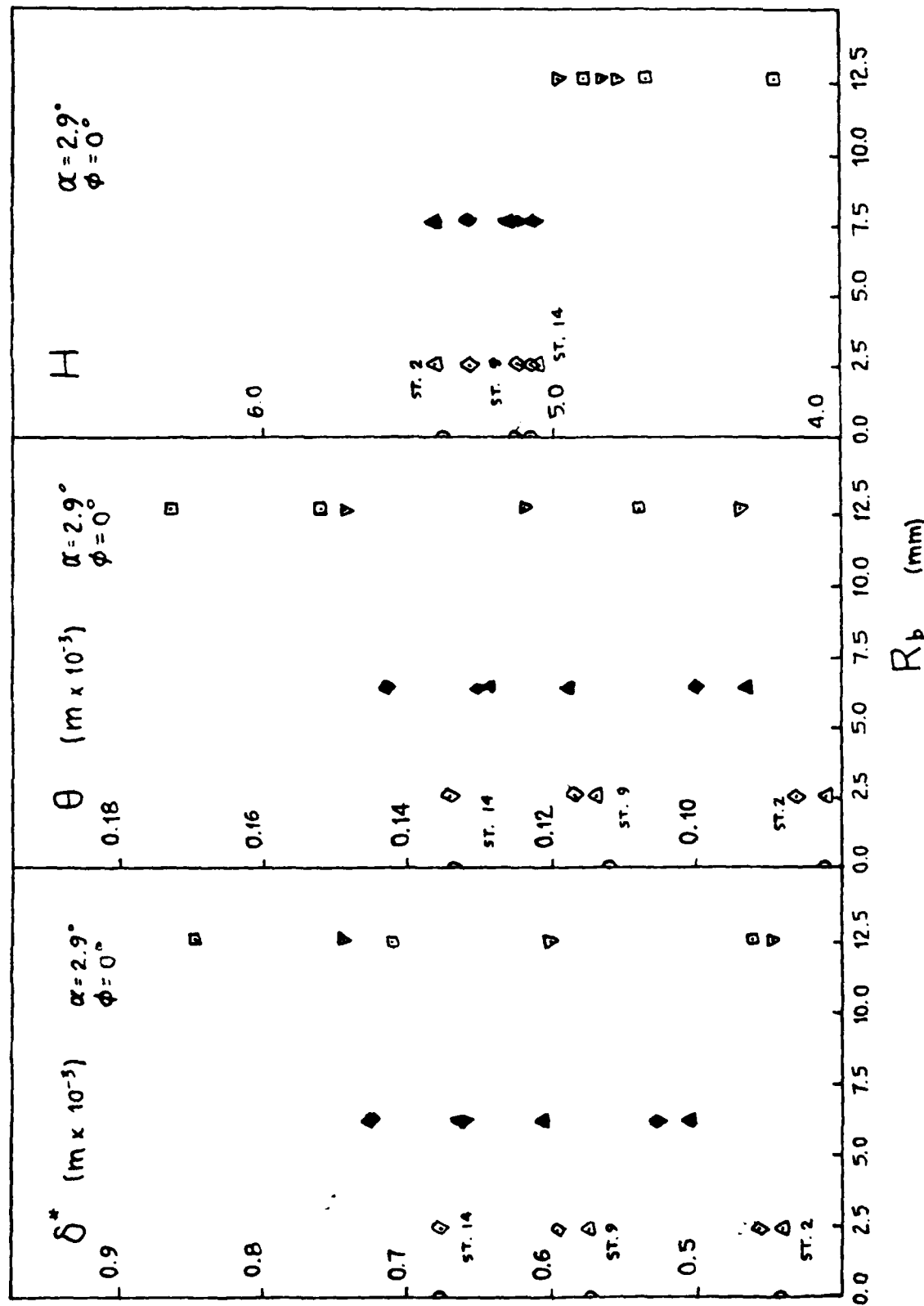


Figure 42. Displacement, Thickness, Momentum Thickness, and Form Factor Versus  $R_b$ ,  $\alpha = 2.9^\circ$ ,  $\phi = 0^\circ$ .

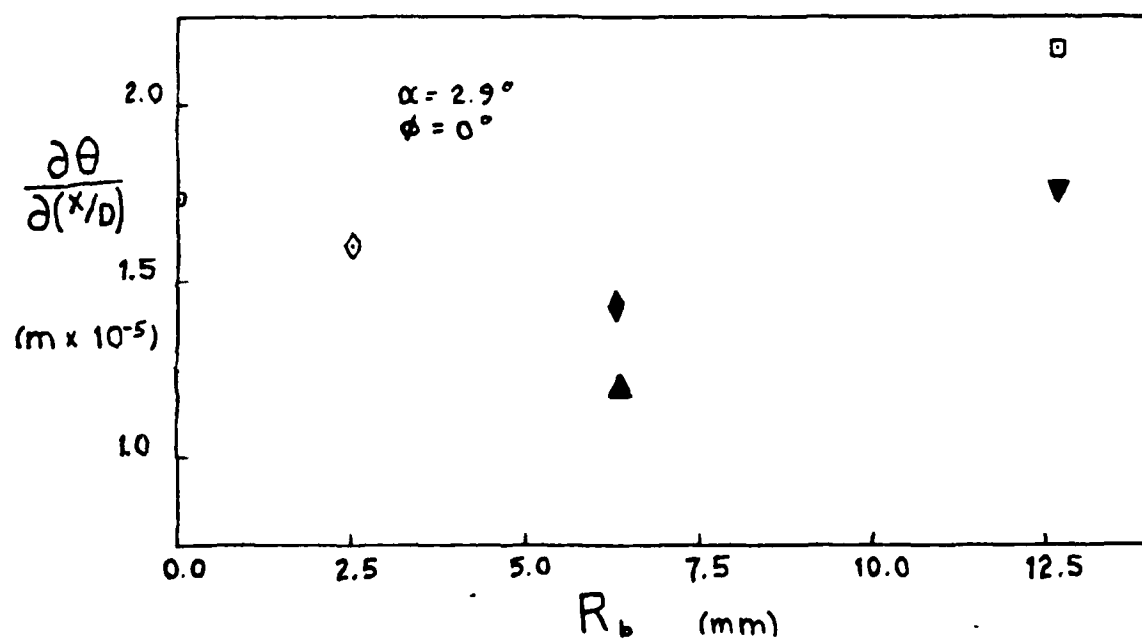
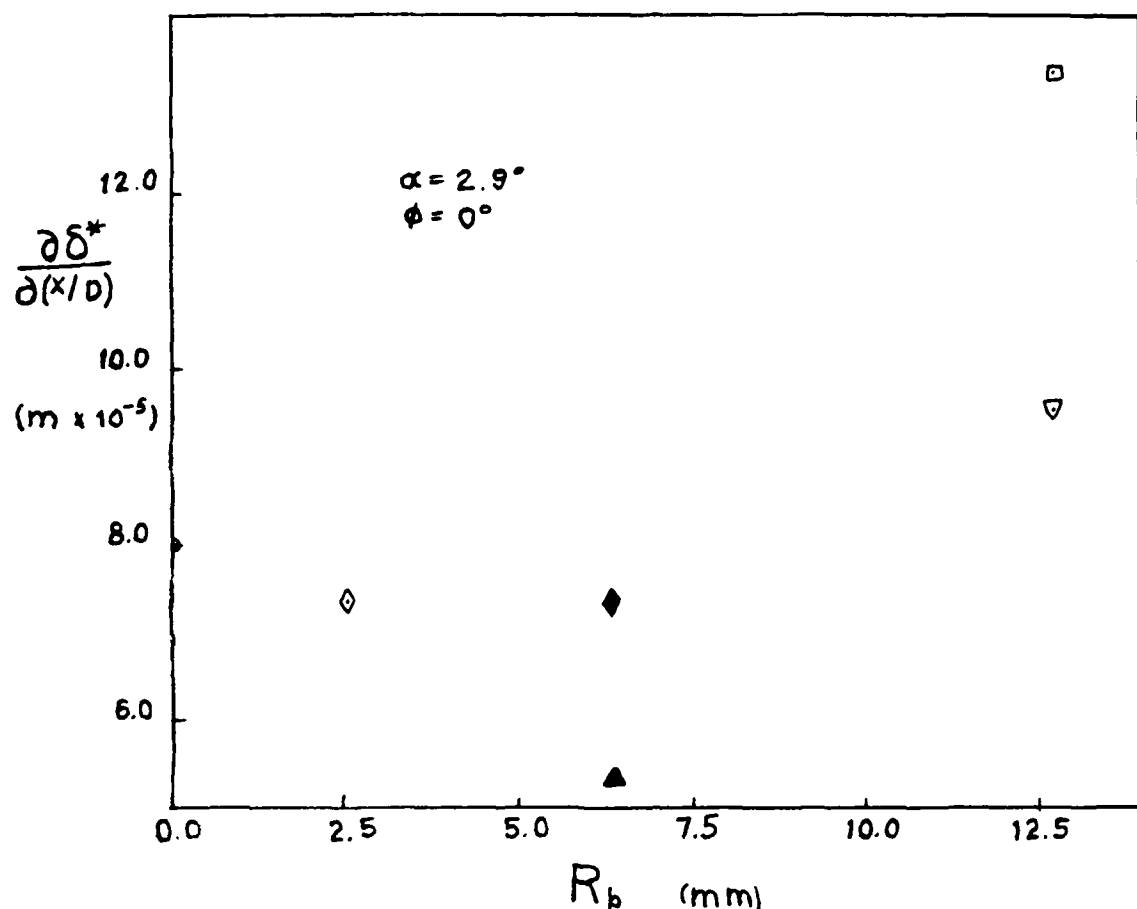


Figure 43. Displacement and Momentum Thickness Growth Rates Versus  $R_b$ ,  $\alpha = 2.9^\circ$ ,  $\phi = 0^\circ$ .

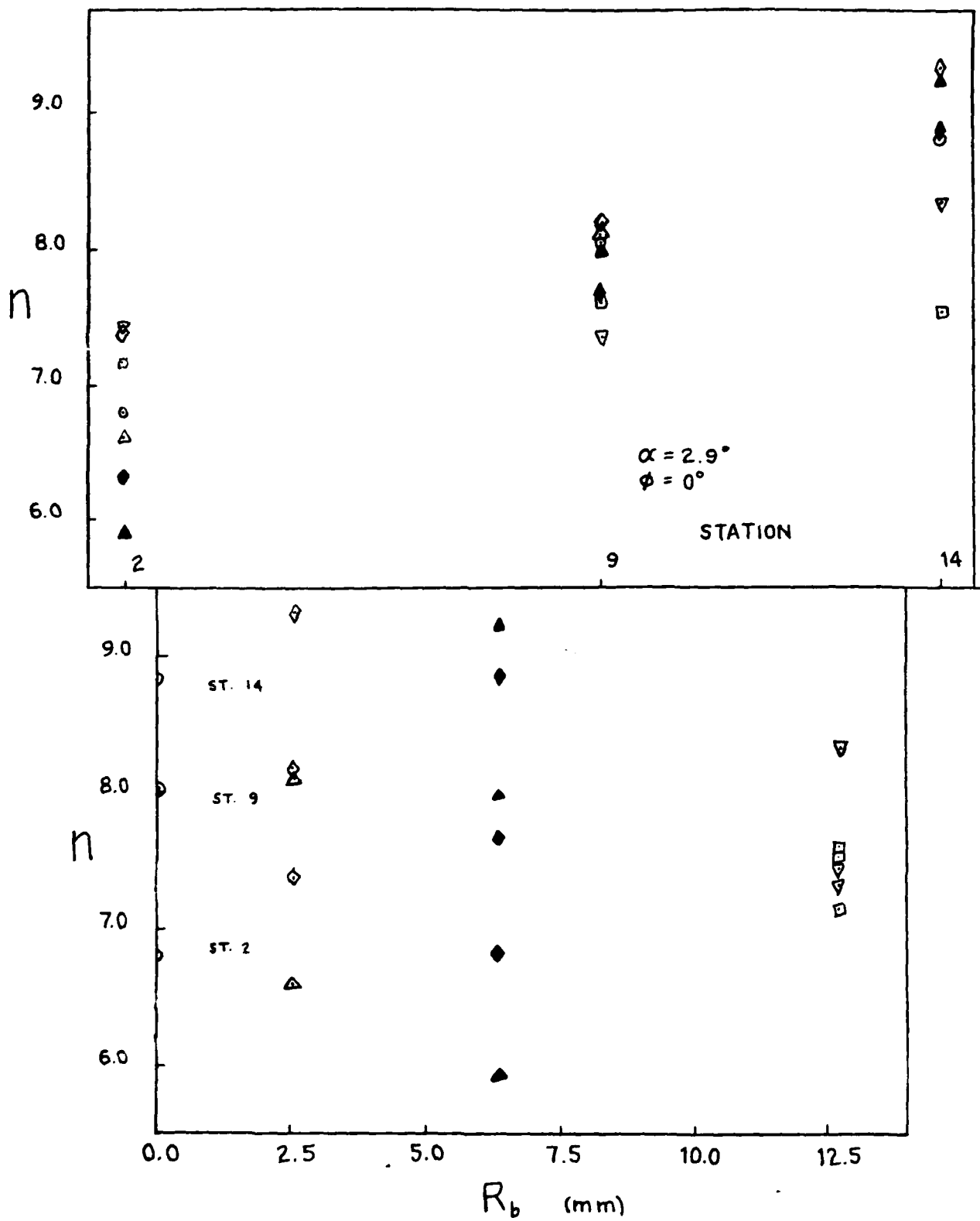


Figure 44. Power Law Exponent,  $n$ , Versus  $X/D$  and  $R_b$ ,  
 $\alpha = 2.9^\circ$ ,  $\phi = 0^\circ$ .

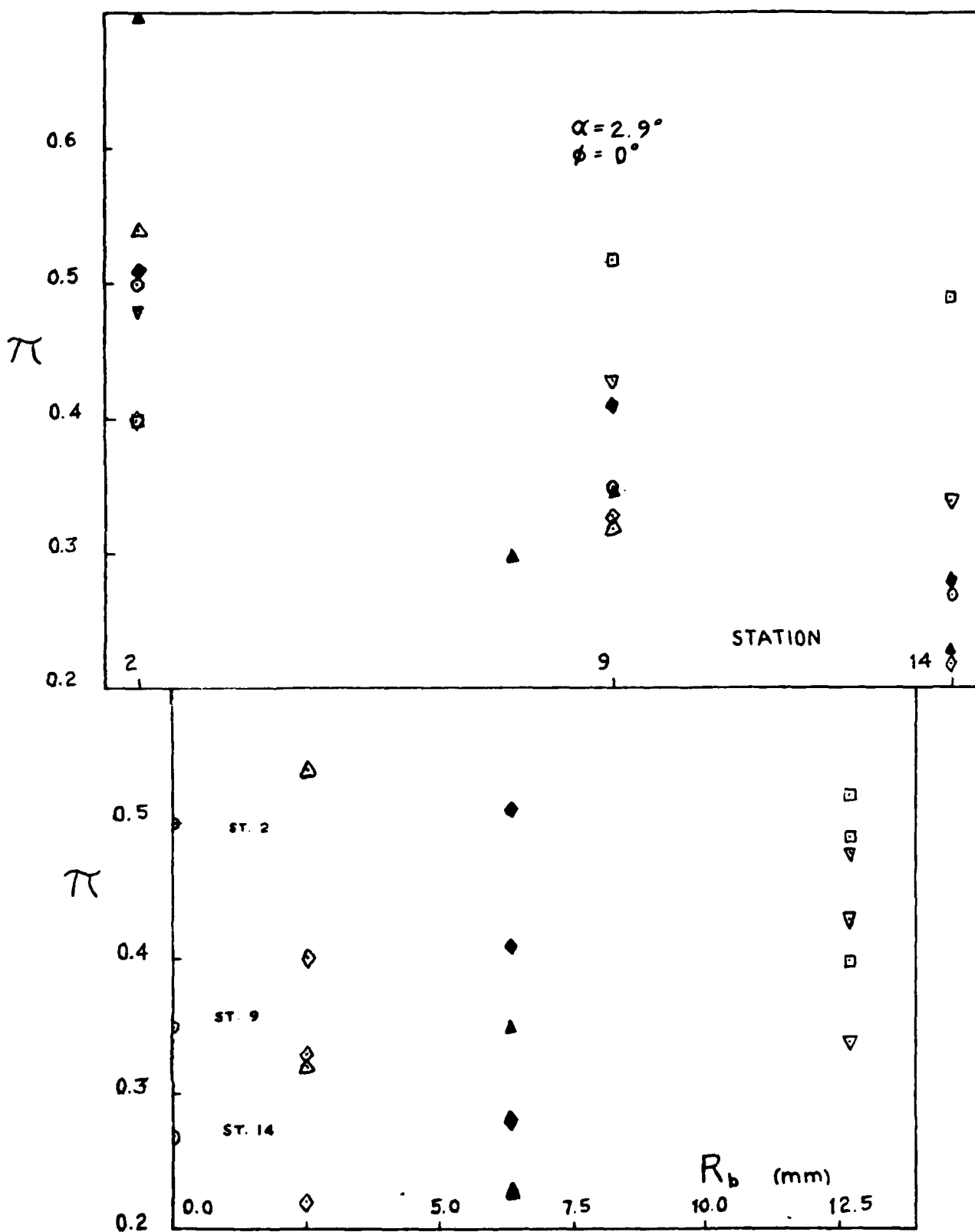


Figure 45. Wake Strength Parameter,  $\pi$ , Versus X/D and  $R_b$ ,  $\alpha = 2.9^\circ$ ,  $\phi = 0^\circ$ .

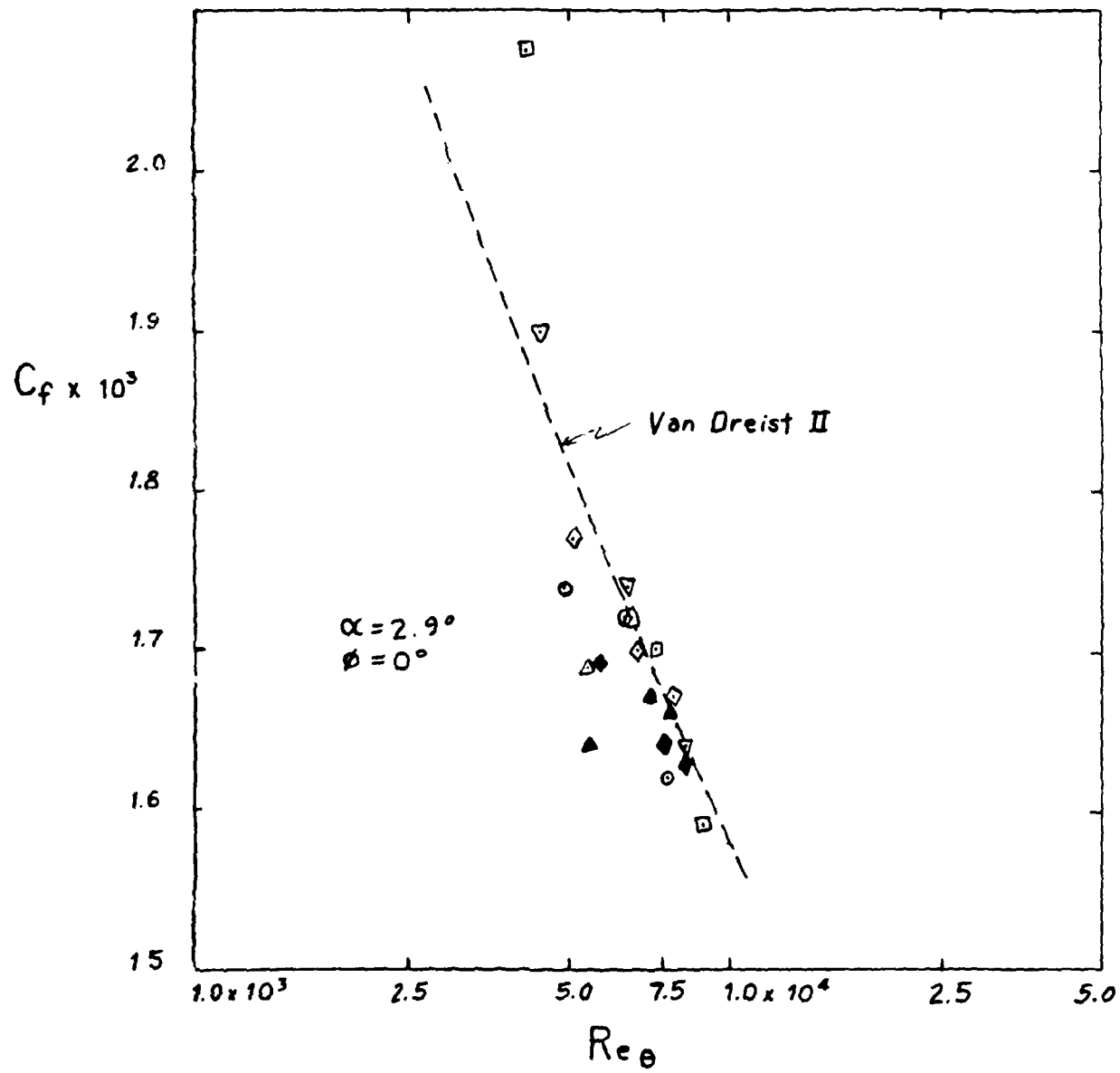


Figure 46. Skin Friction Coefficient Versus  $Re_\theta$ ,  $\alpha = 2.9^\circ$ ,  
 $\phi = 0^\circ$ .

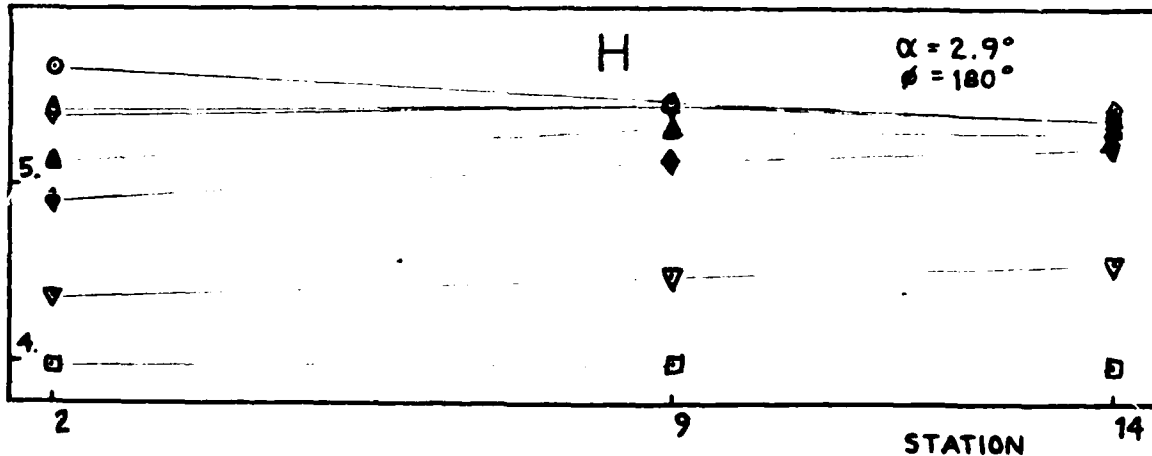
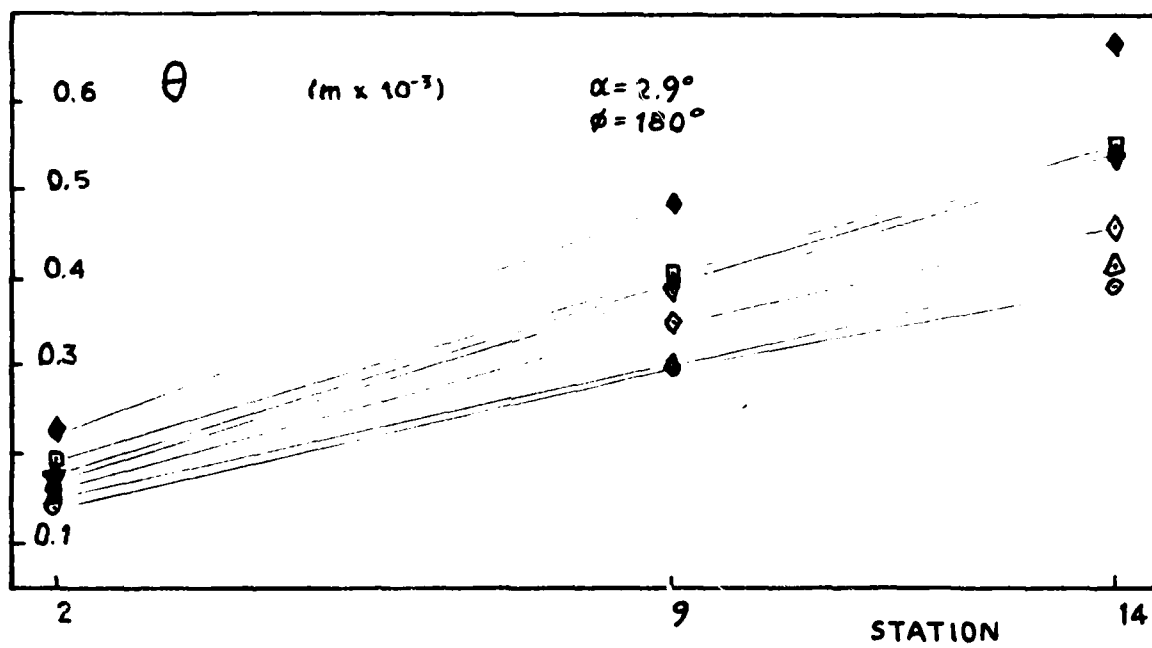
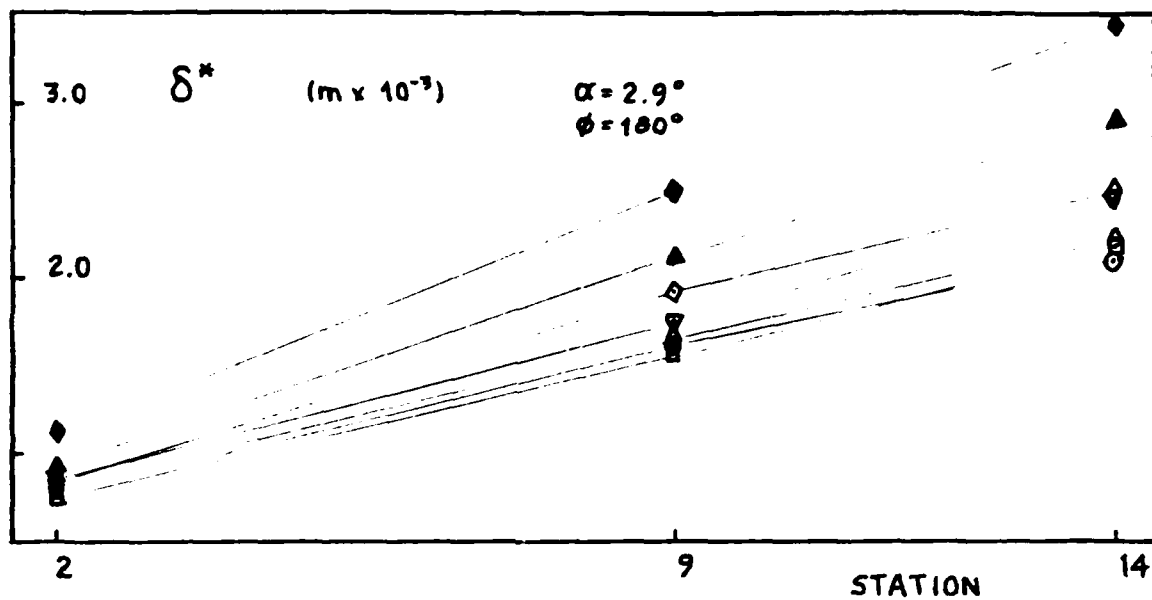


Figure 47. Displacement Thickness, Momentum Thickness, and Form Factor Versus  $X/D$ ,  $\alpha = 2.9^\circ$ ,  $\phi = 180^\circ$ .

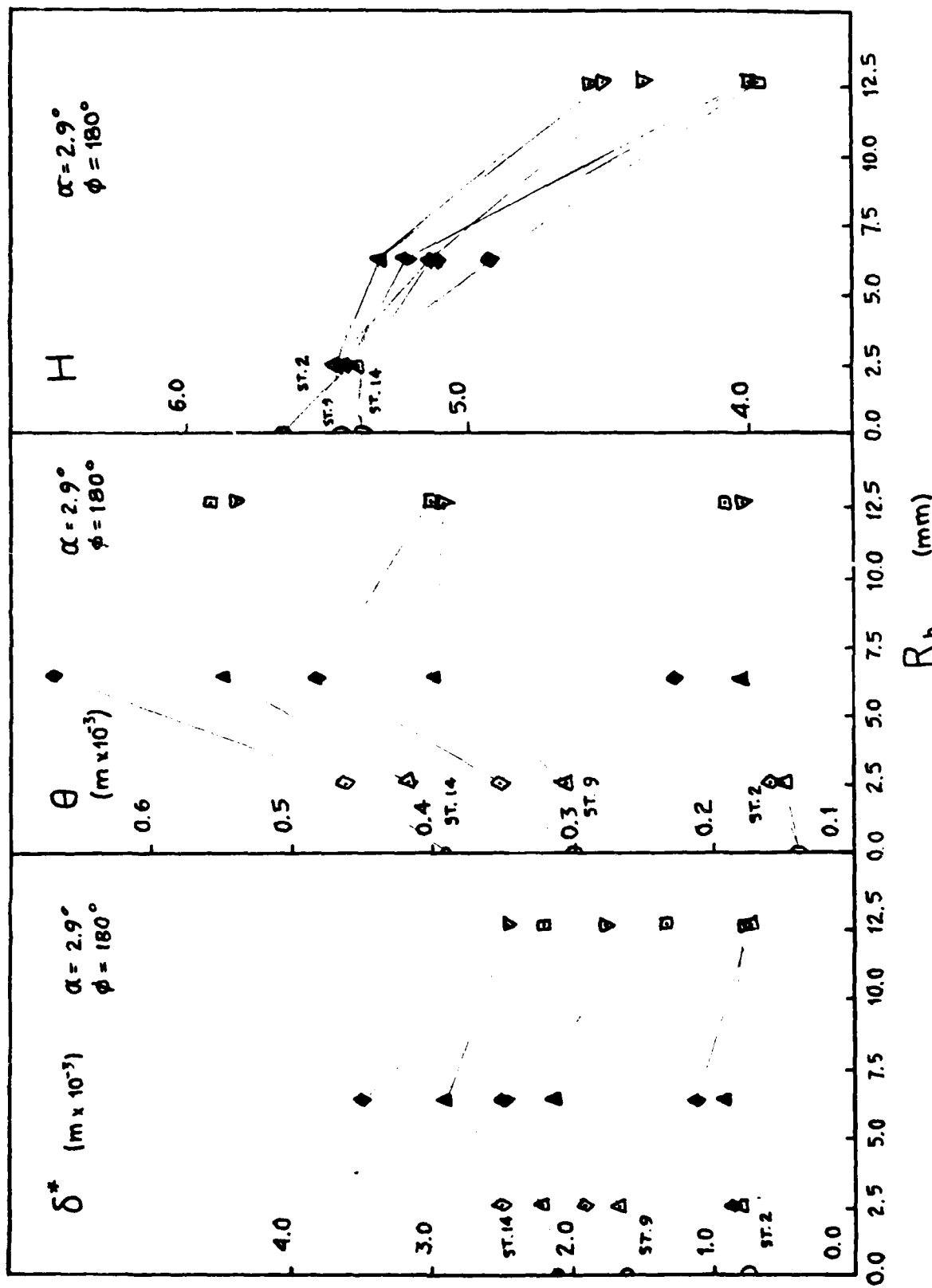


Figure 48. Displacement Thickness, Momentum Thickness, and Form Factor Versus  $R_b$ ,  $\alpha = 2.9^\circ$ ,  $\phi = 180^\circ$ .

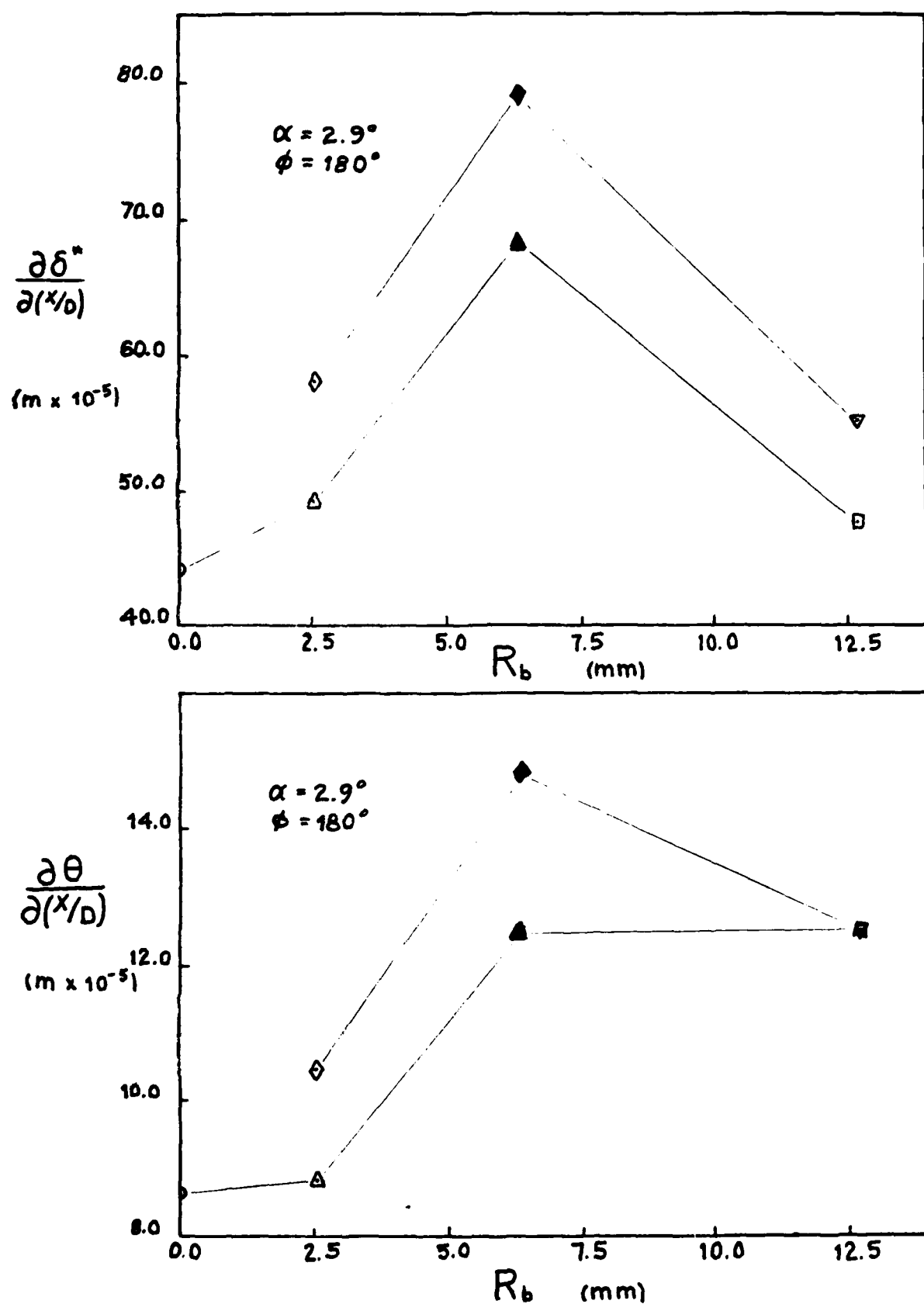


Figure 49. Displacement and Momentum Thickness Growth Rates Versus  $R_b$ ,  $\alpha = 2.9^\circ$ ,  $\phi = 180^\circ$ .

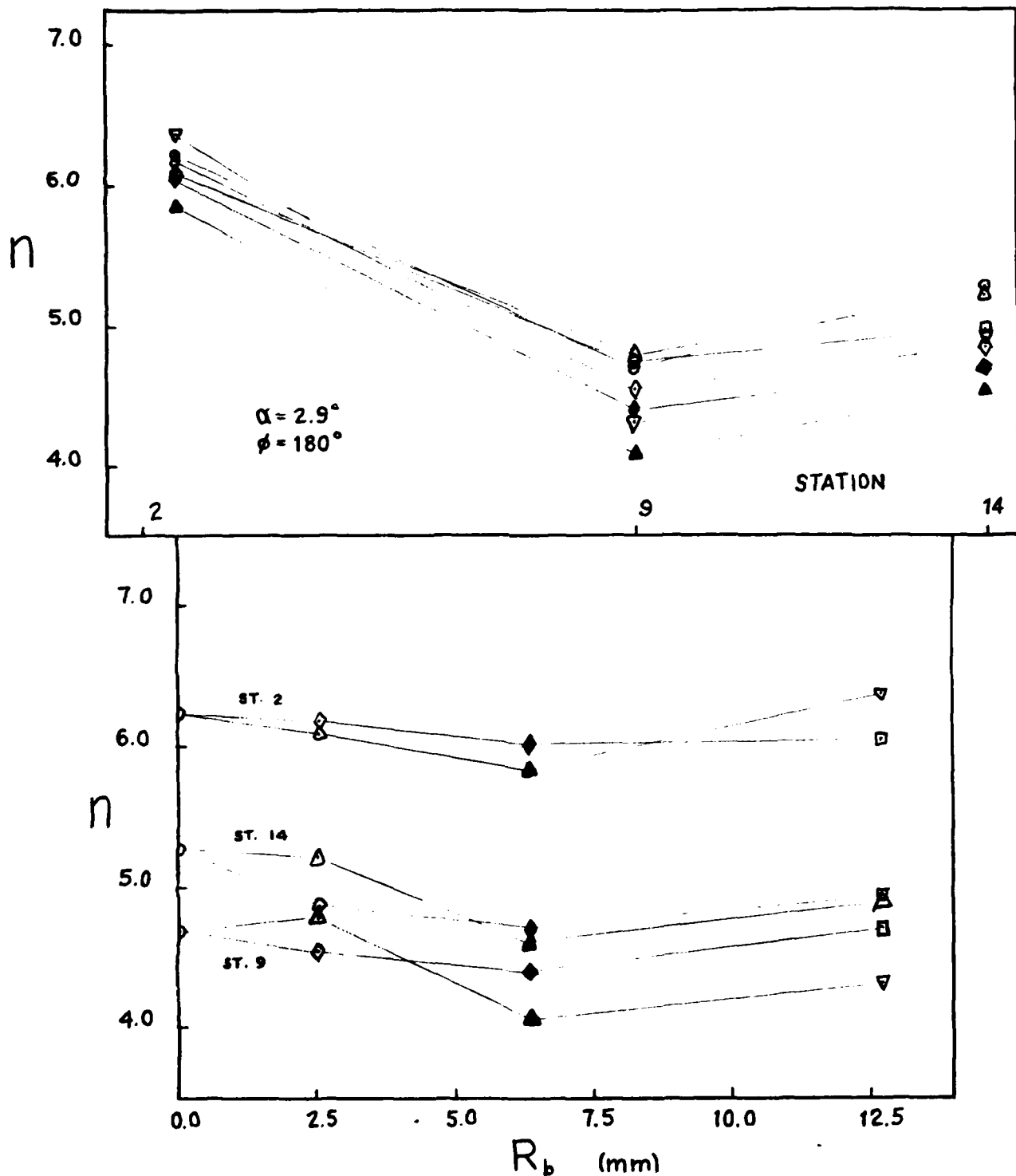


Figure 50. Power Law Exponent,  $n$ , Versus  $X/D$  and  $R_b$ ,  
 $\alpha = 2.9^\circ$ ,  $\phi = 180^\circ$ .

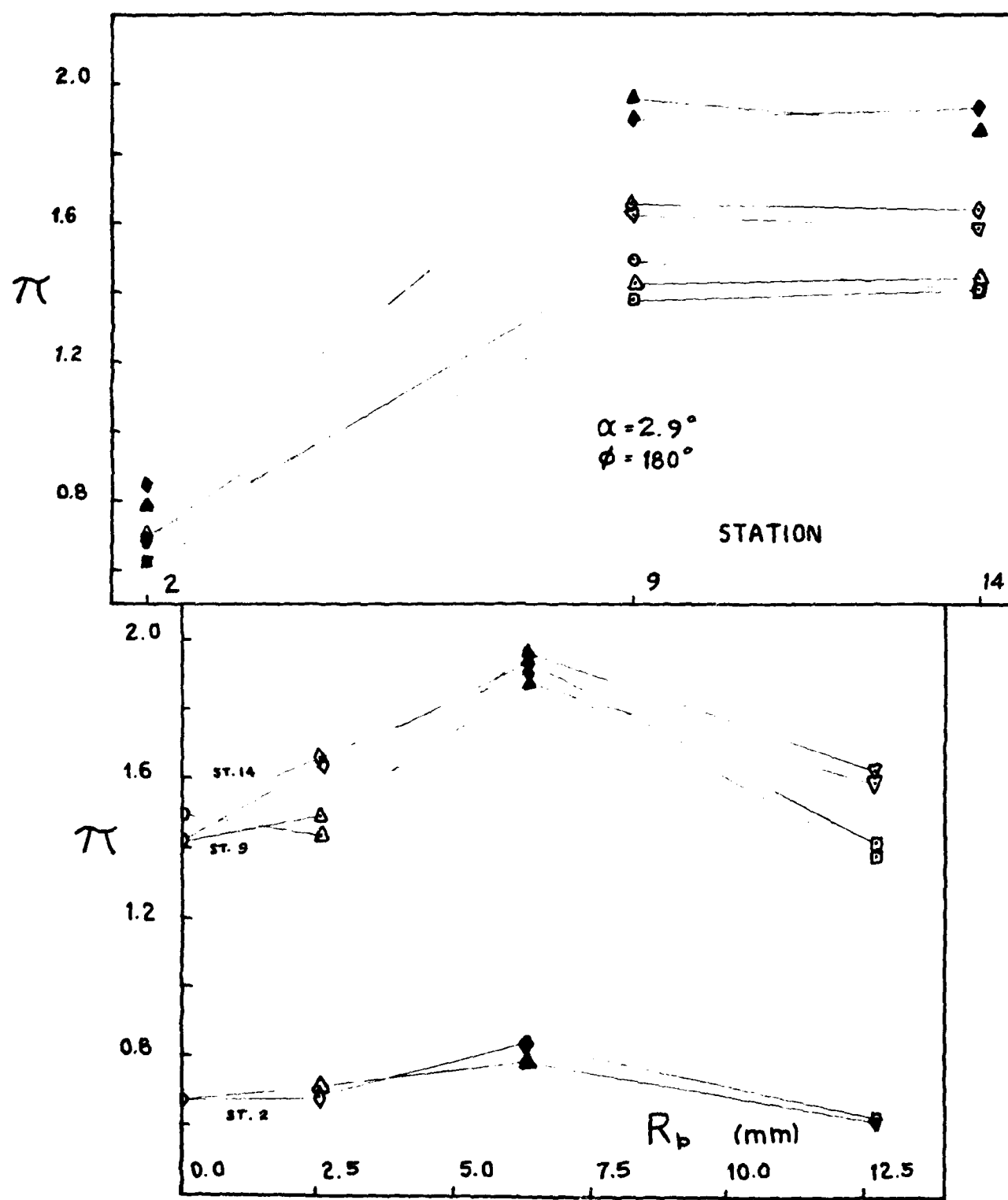


Figure 51. Wake Strength Parameter,  $\pi$ , Versus  $X/D$  and  $R_b$ ,  
 $\alpha = 2.9^\circ$ ,  $\phi = 180^\circ$ .

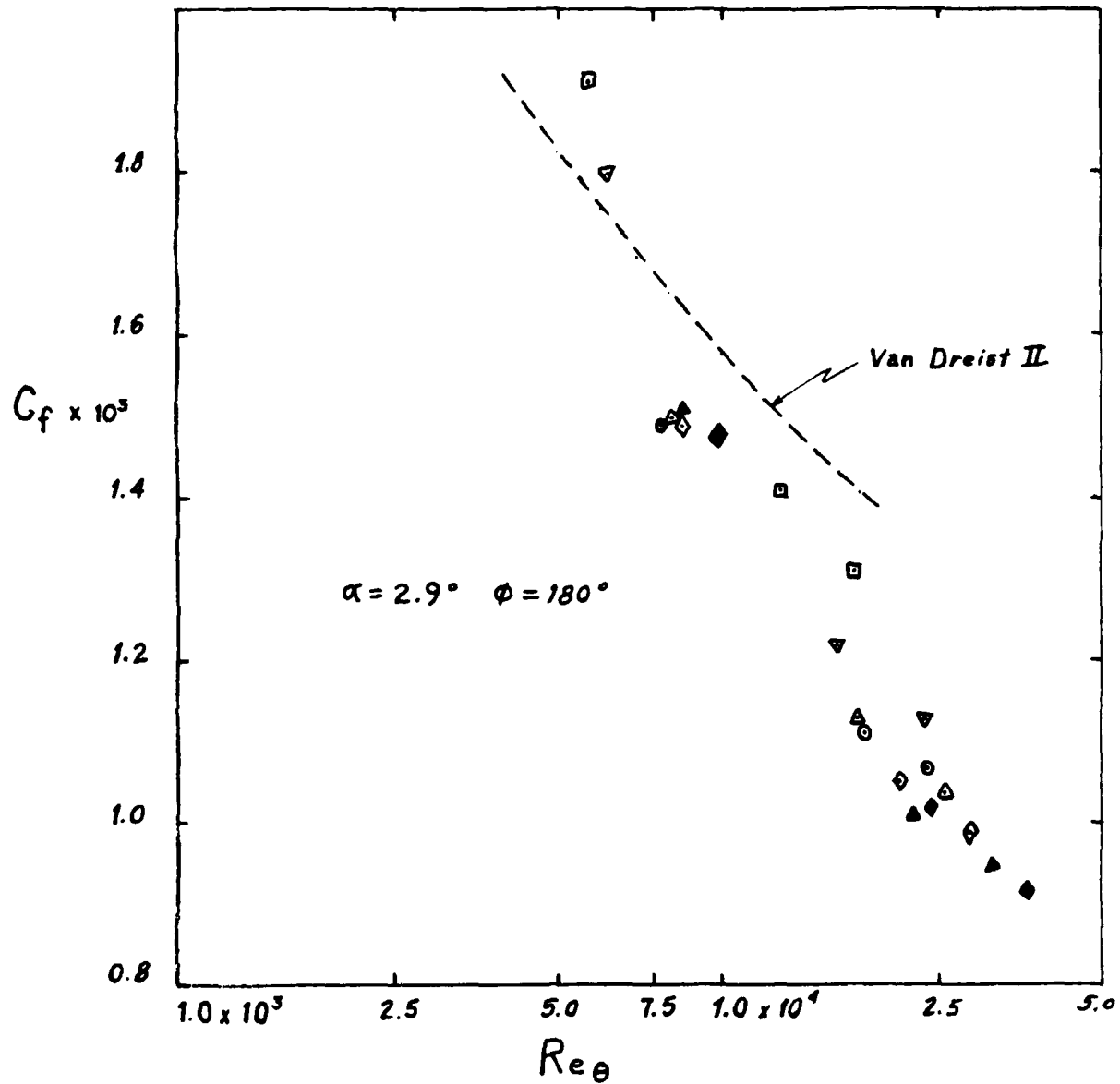


Figure 52. Skin Friction Coefficient Versus  $Re_\theta$ ,  $\alpha = 2.9^\circ$ ,  $\phi = 180^\circ$ .

$$B = \int_0^d \delta \, ds$$

where

$\delta$  = turning angle

$o$  = stagnation point

$d$  = point where  $\delta = \delta$  for shock

detachment at  $M_\infty$

$s$  = surface distance

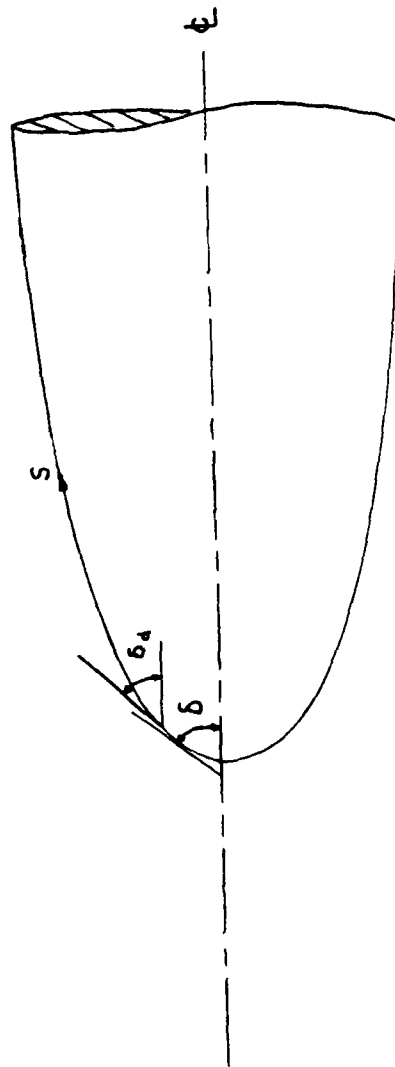


Figure 53. Bluntness Length Diagram.

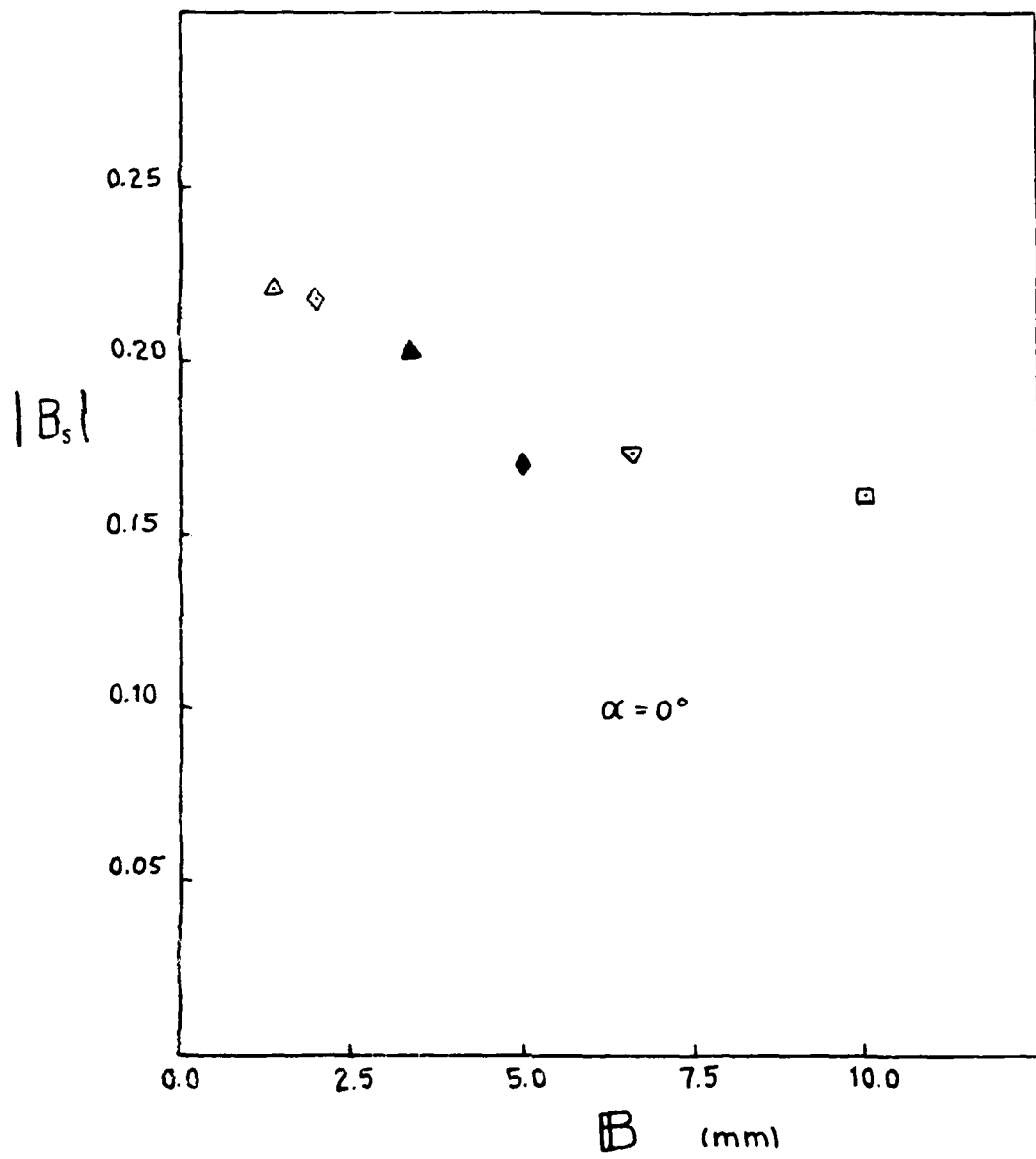


Figure 54. Bluntness Length Versus Shock Bluntness Parameter,  $B_s$ ,  $\alpha = 0^\circ$ .

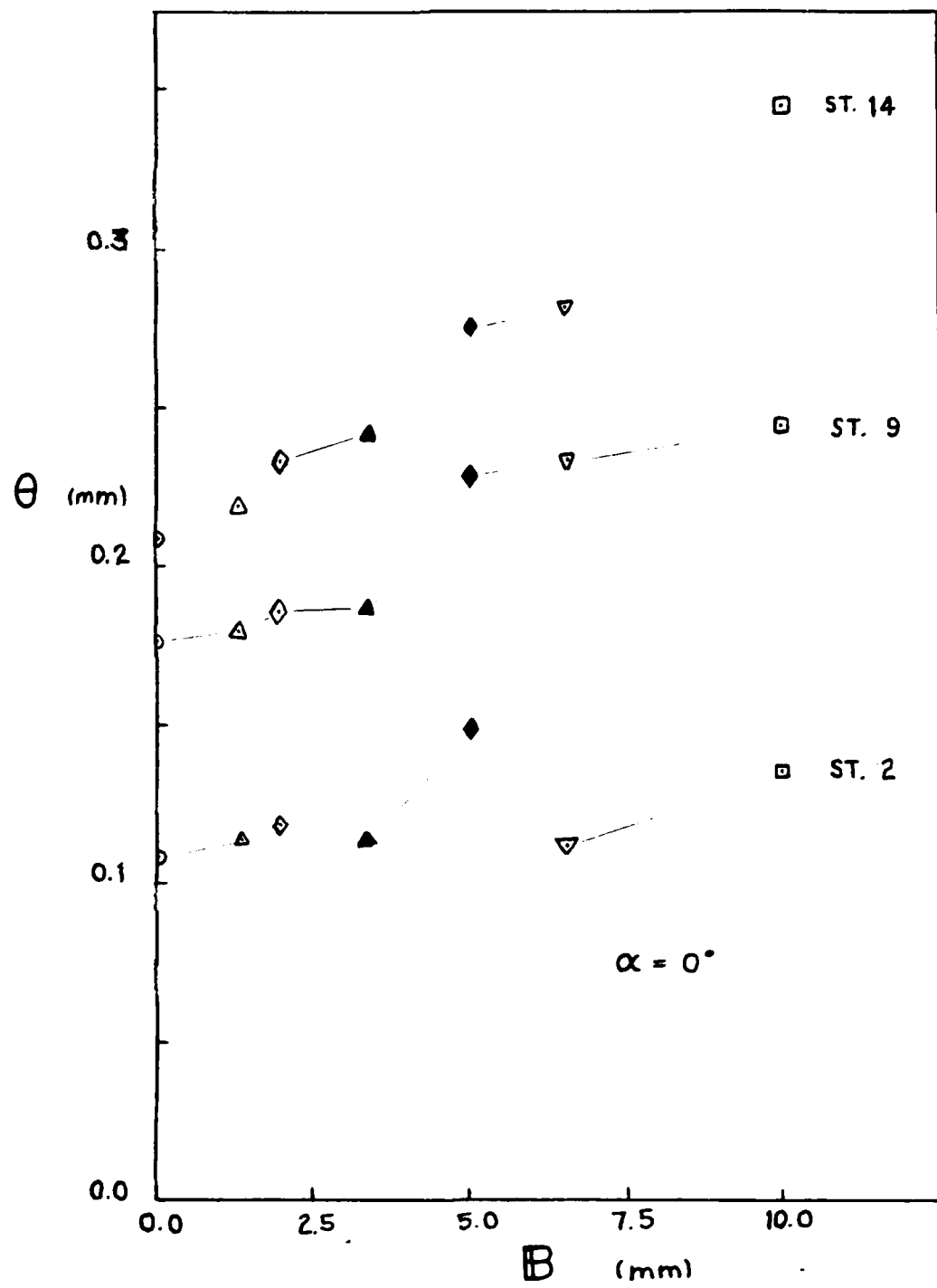


Figure 55. Momentum Deficit Thickness Versus Bluntness Length,  $\alpha = 0^\circ$ .

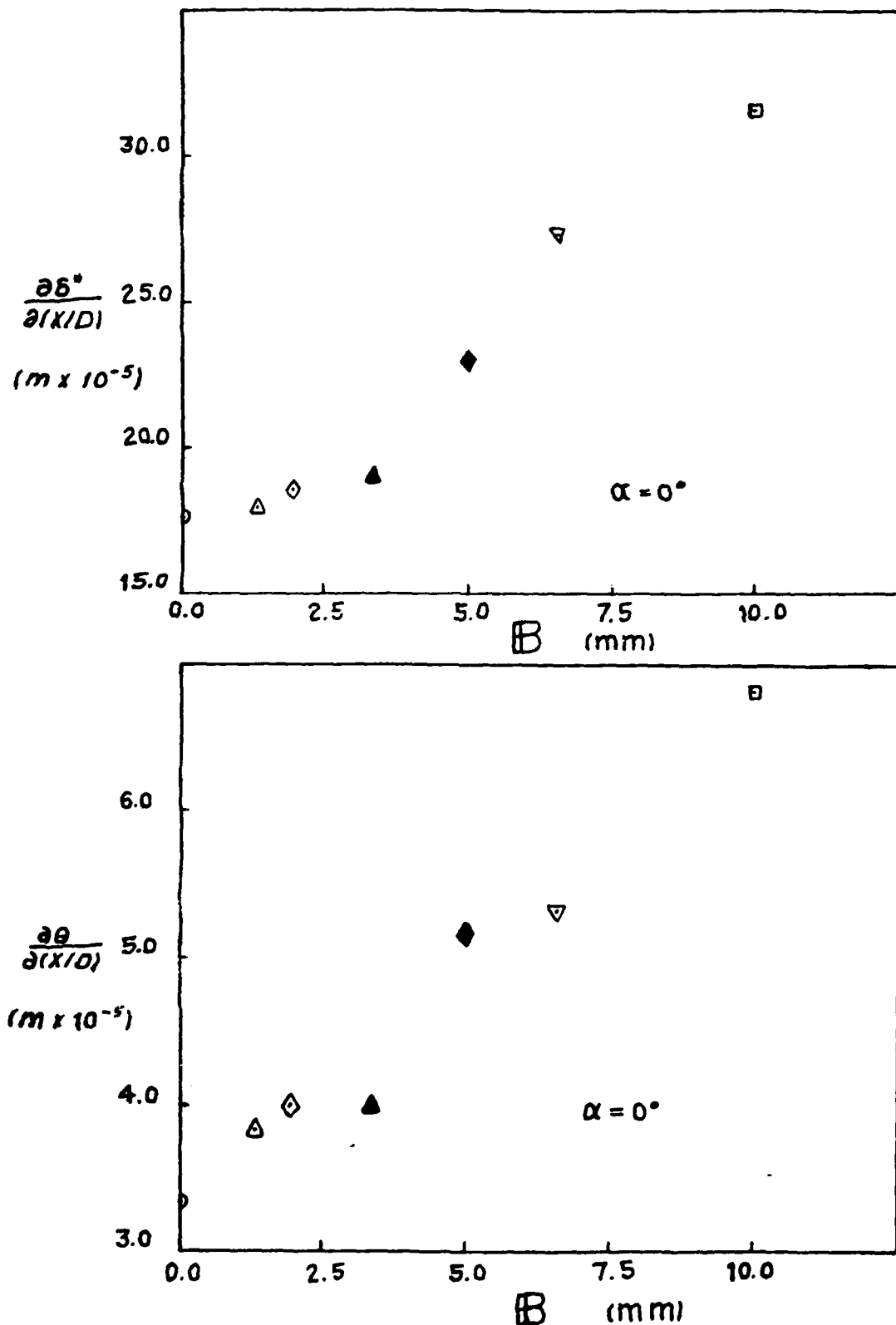


Figure 56. Displacement and Momentum Thickness Growth Rates Versus Bluntness Length  $\alpha = 0^\circ$ .

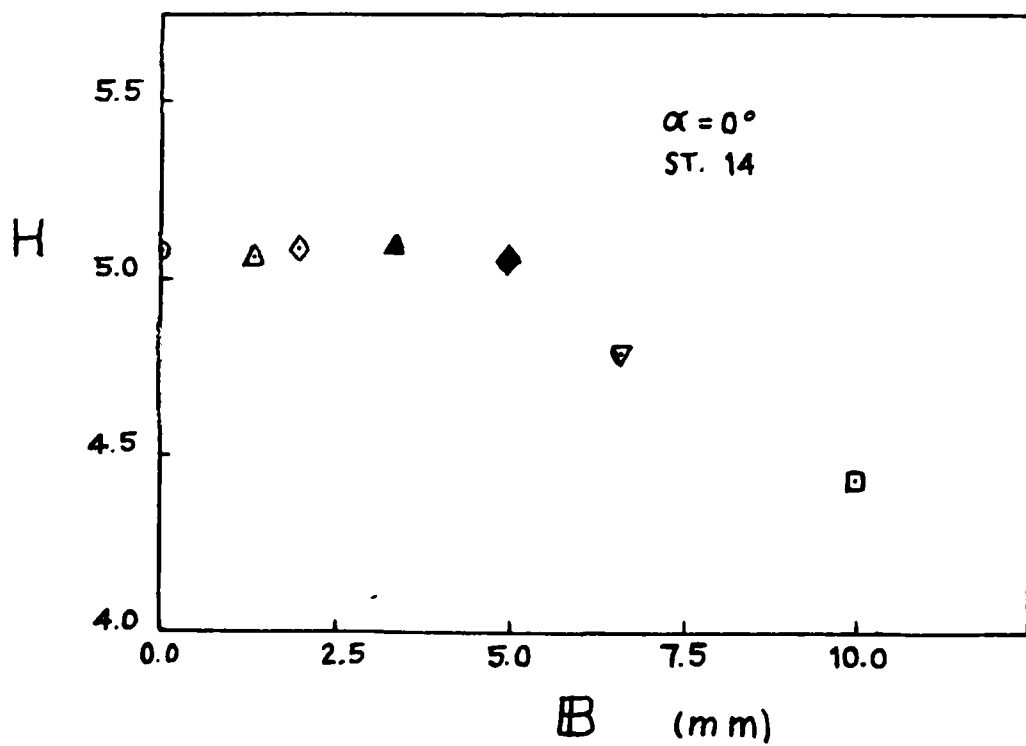
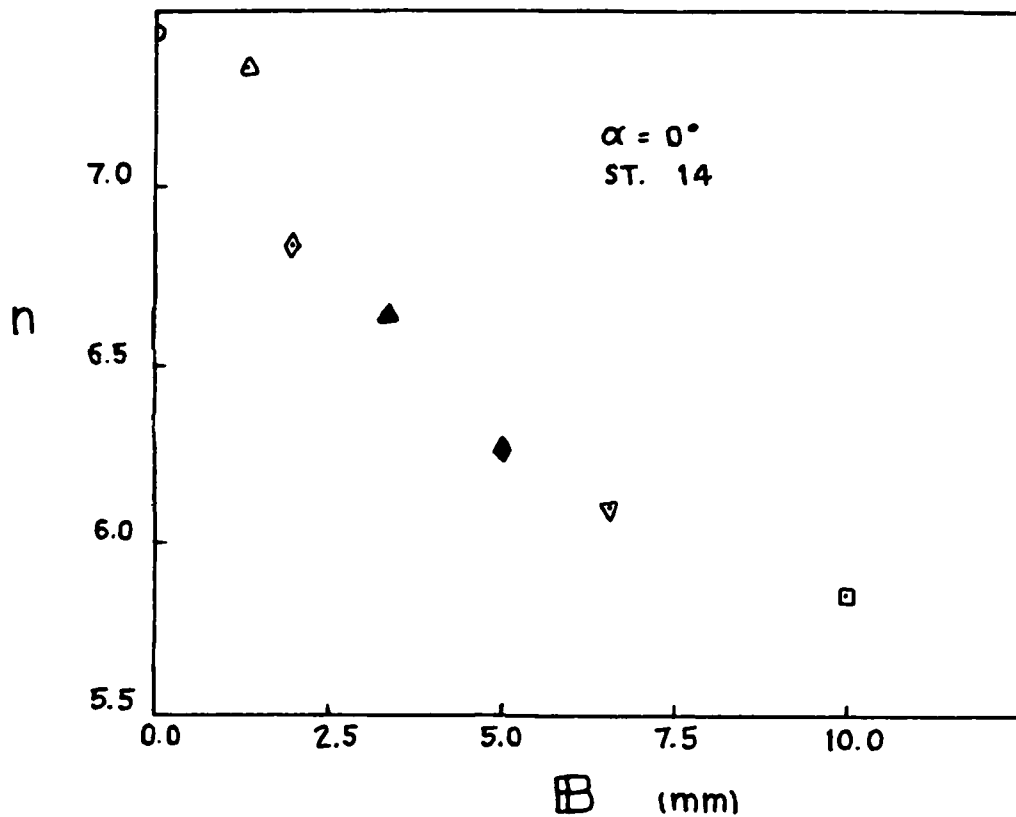


Figure 57. Form Factor and Power Law Exponent Versus Bluntness Length  $\alpha = 0^\circ$ .

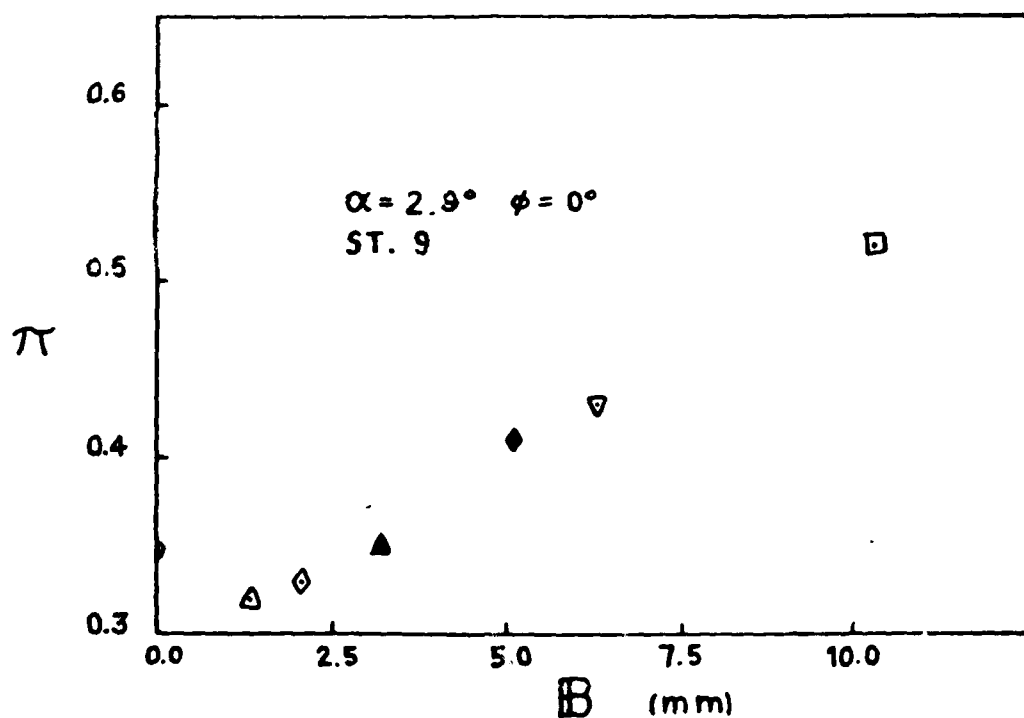
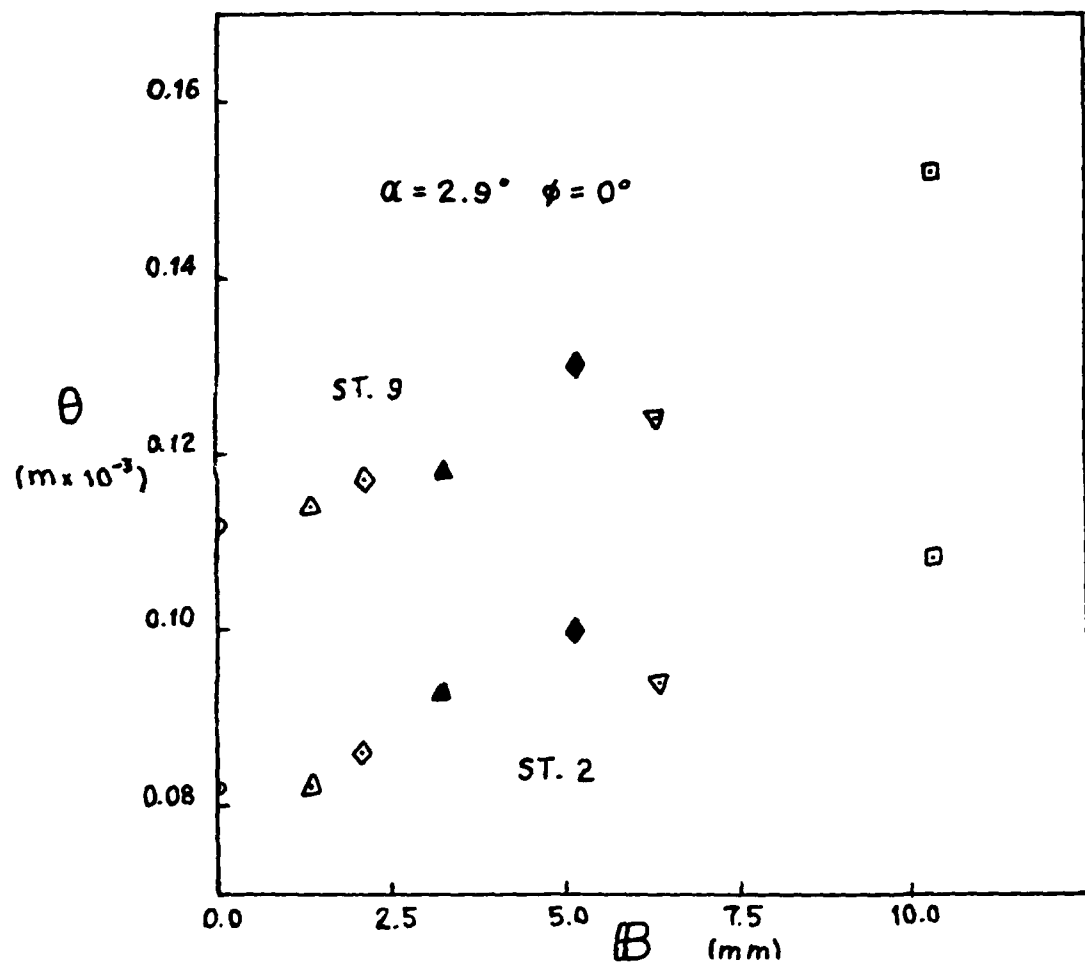


Figure 58. Momentum Thickness and Wake Strength Parameter Versus Bluntness Length  $\alpha = 2.9^\circ$ ,  $\phi = 0^\circ$ .

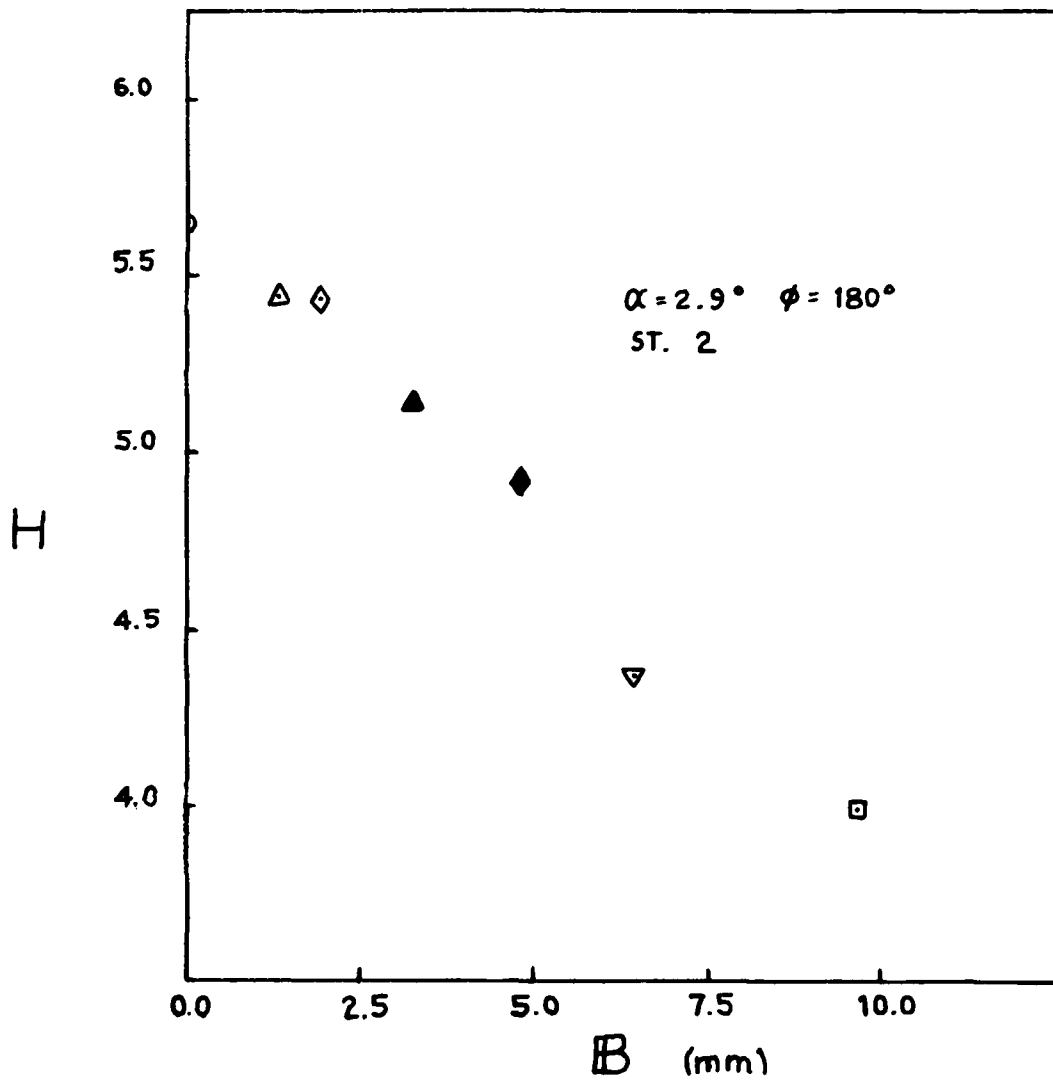
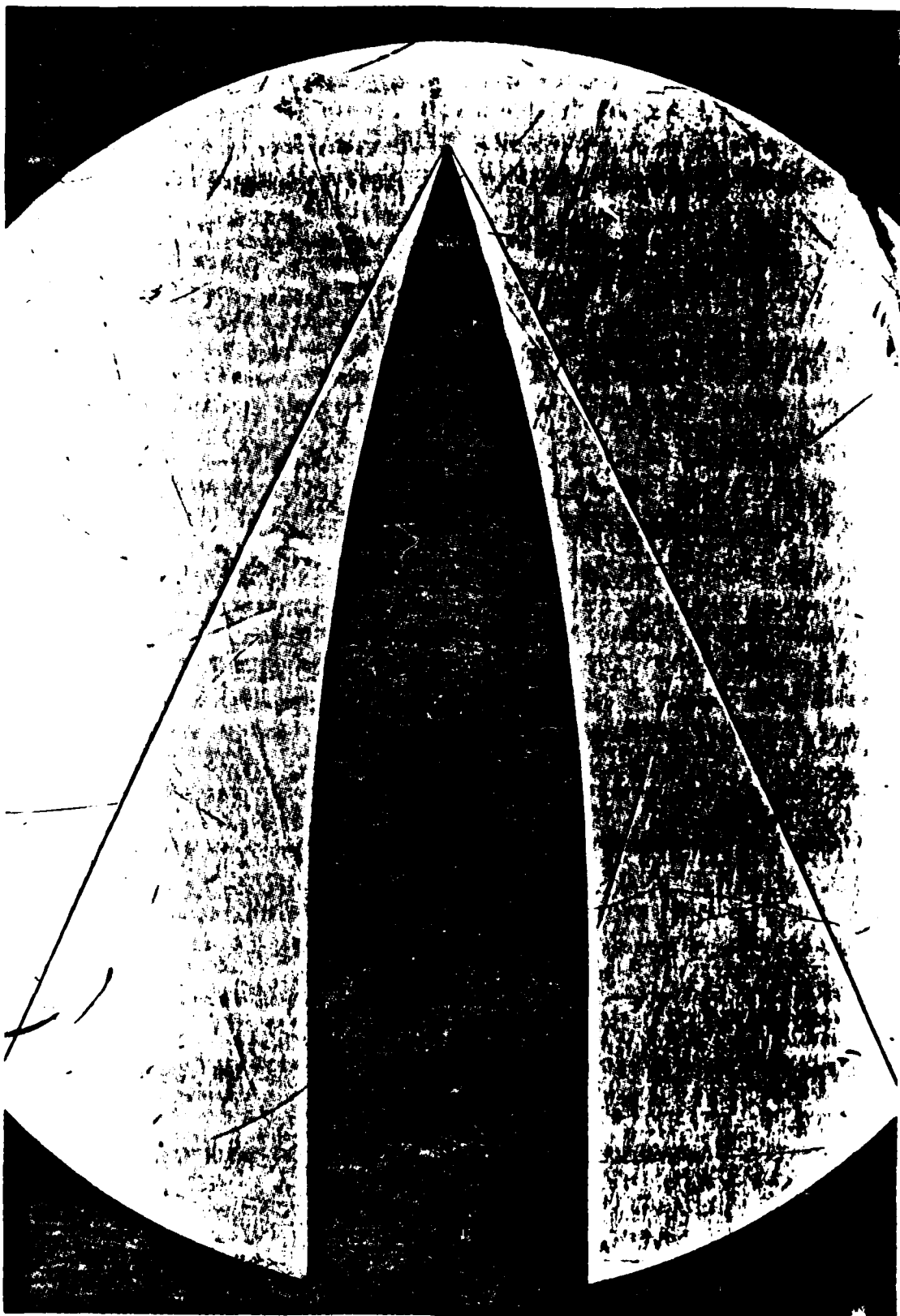


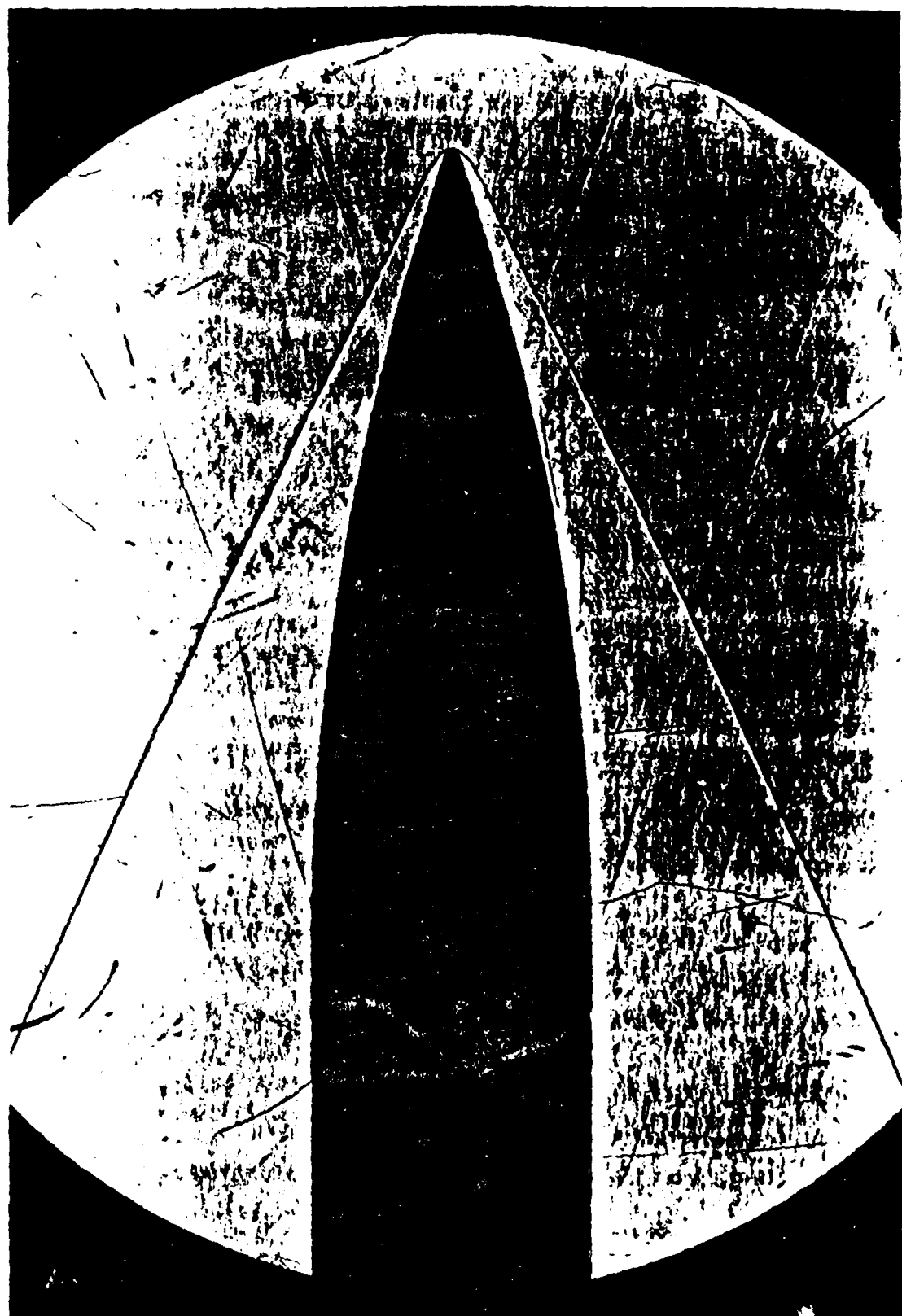
Figure 59. Form Factor Versus Bluntness Length  
 $\alpha = 2.9^\circ$ ,  $\phi = 180^\circ$ .

APPENDIX A Shadowgraph Photographs

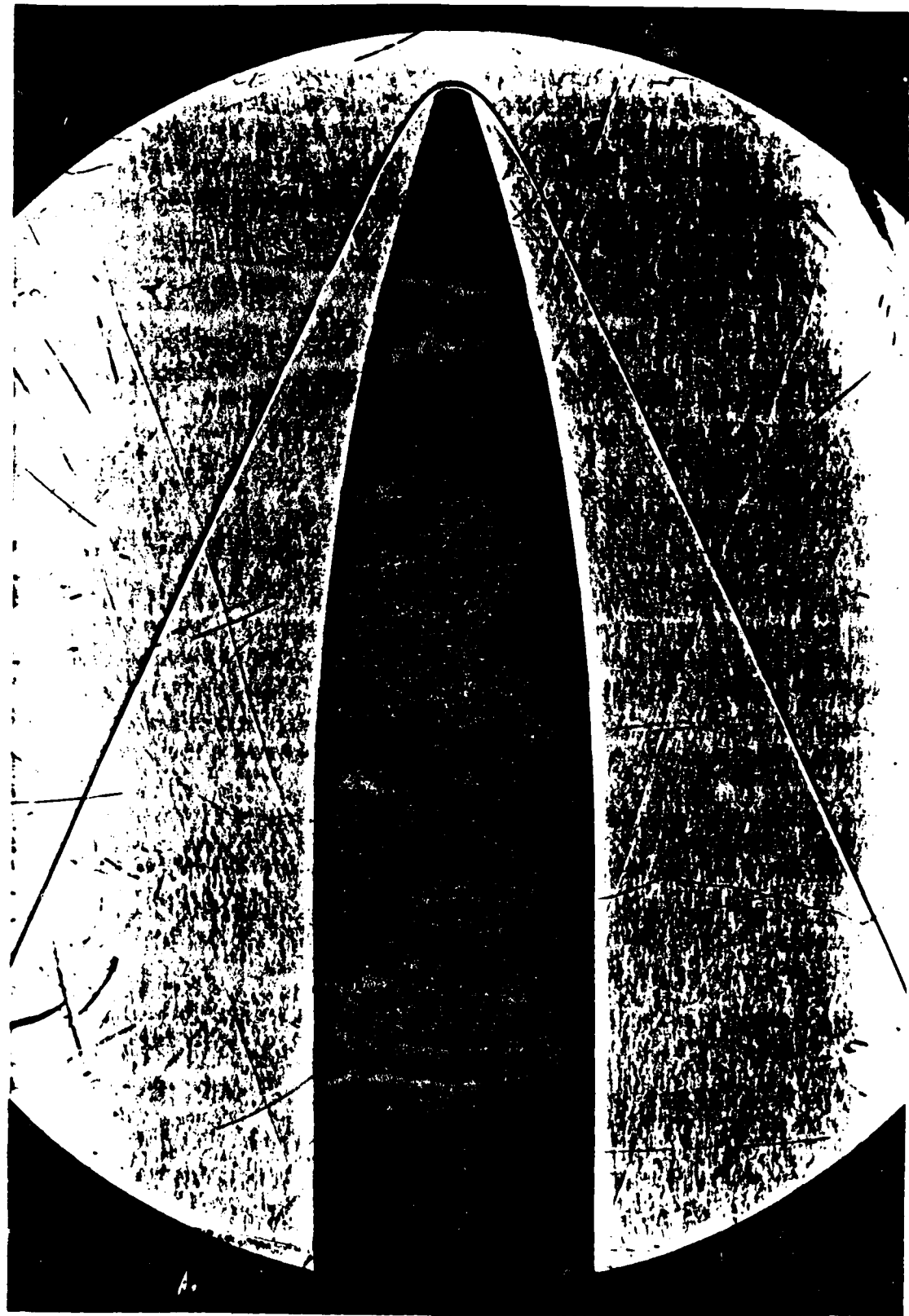
<u>Photograph</u>	<u>Subject</u>
A1	Tip P $\alpha=0^\circ$
A2	Tip R1 $\alpha=0^\circ$
A3	Tip R2 $\alpha=0^\circ$
A4	Tip R3 $\alpha=0^\circ$
A5	Tip F1 $\alpha=0^\circ$
A6	Tip F2 $\alpha=0^\circ$
A7	Tip F3 $\alpha=0^\circ$
A8	Tip P $\alpha=2.9^\circ$
A9	Tip R1 $\alpha=2.9^\circ$
A10	Tip R2 $\alpha=2.9^\circ$
A11	Tip R3 $\alpha=2.9^\circ$
A12	Tip F1 $\alpha=2.9^\circ$
A13	Tip F2 $\alpha=2.9^\circ$
A14	Tip F3 $\alpha=2.9^\circ$



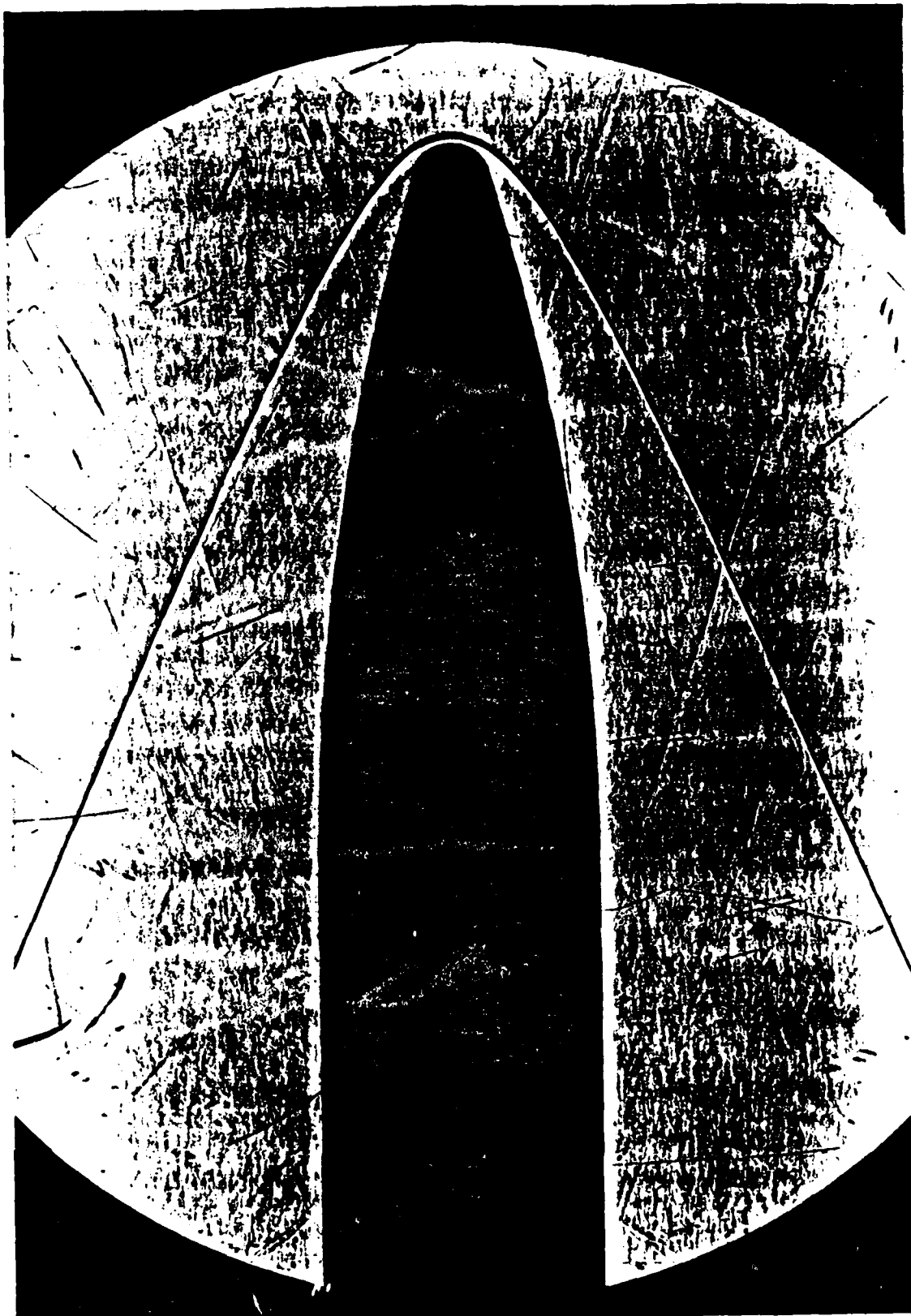
Photograph A1: Tip P,  $\alpha = 0^\circ$ .



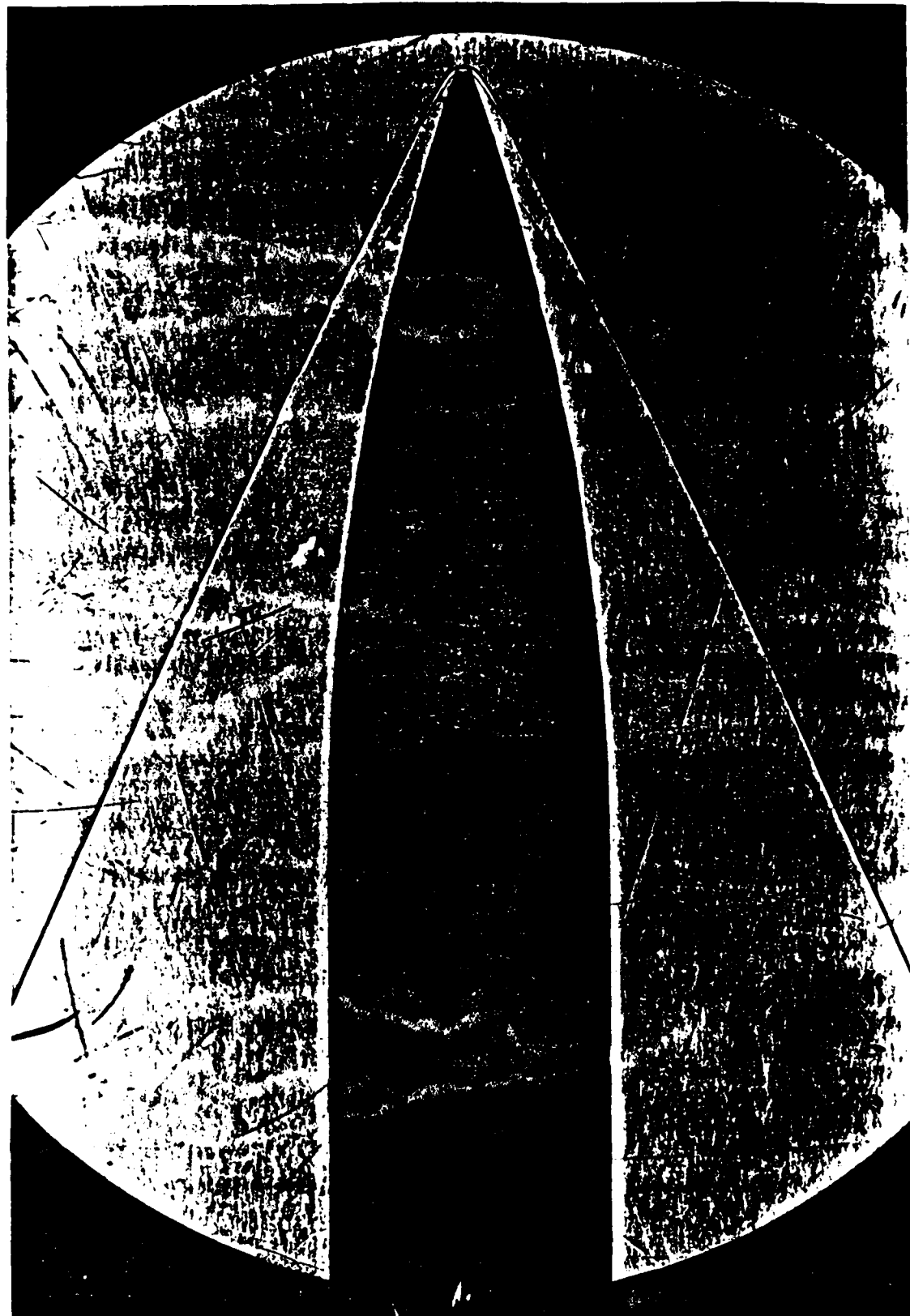
Photograph A2: Tip R1,  $\alpha \approx 0^\circ$ .



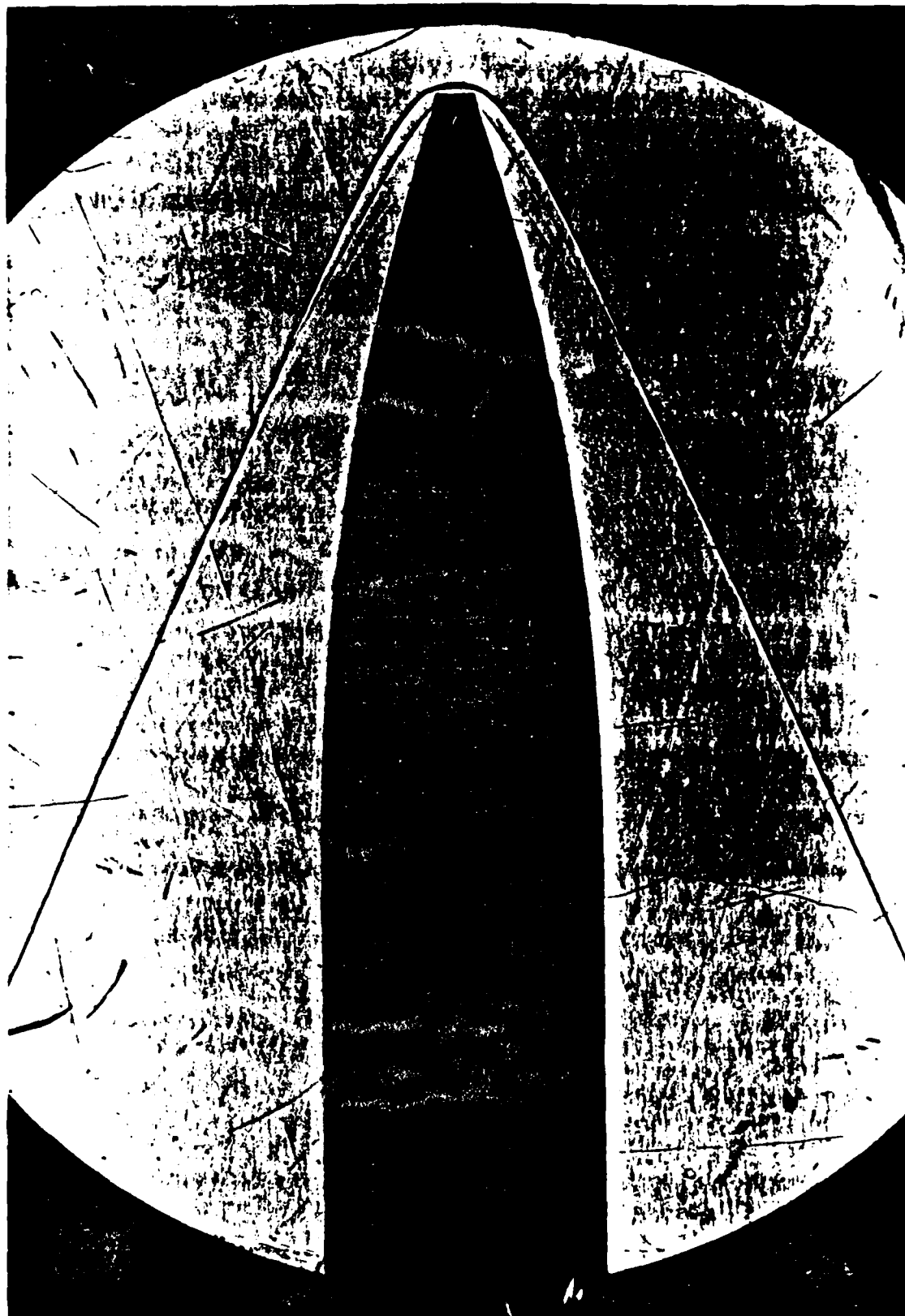
Photograph A3: Tip R2,  $\alpha = 0^\circ$ .



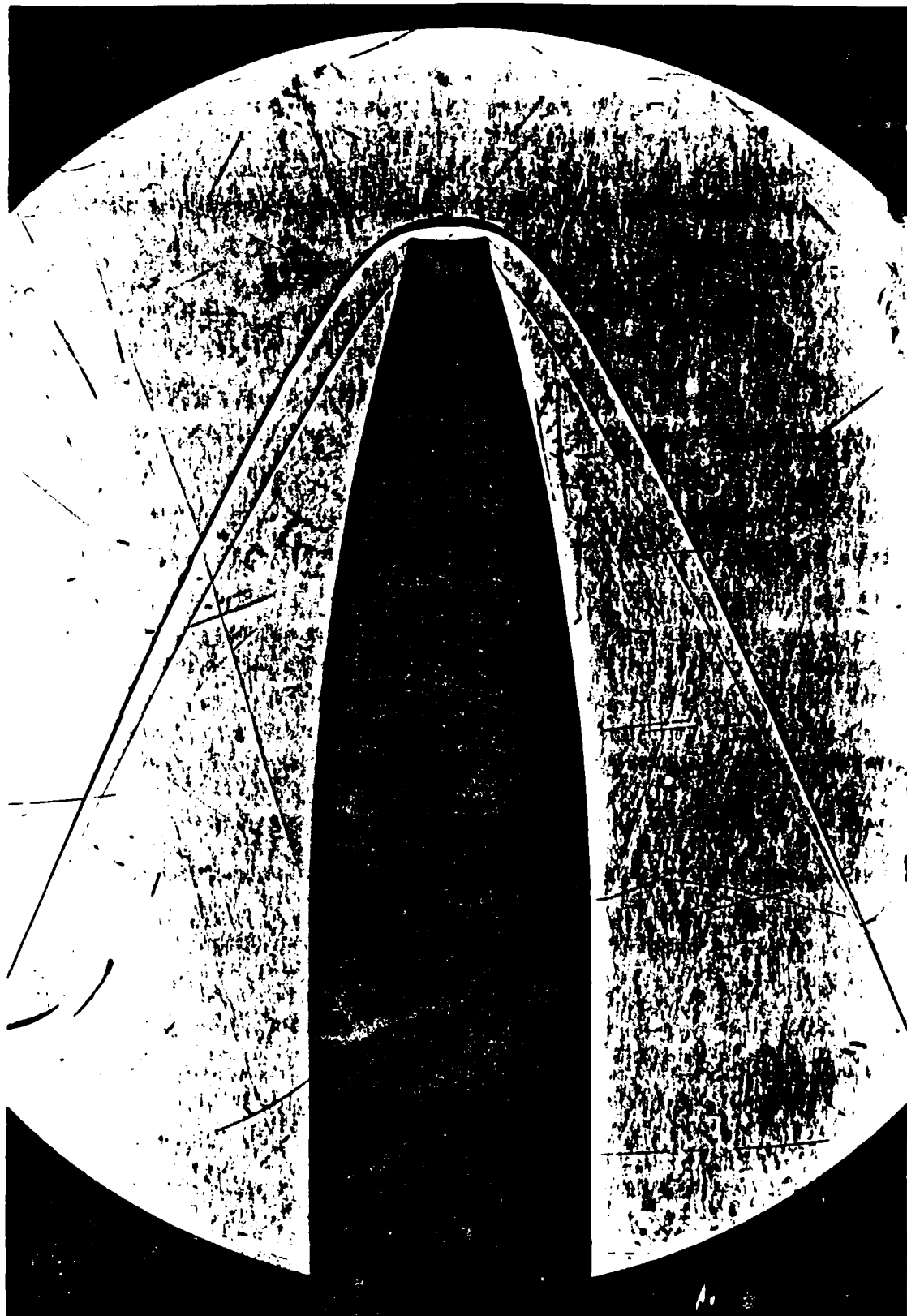
Photograph A4: Tip R3,  $\alpha = 0^\circ$ .



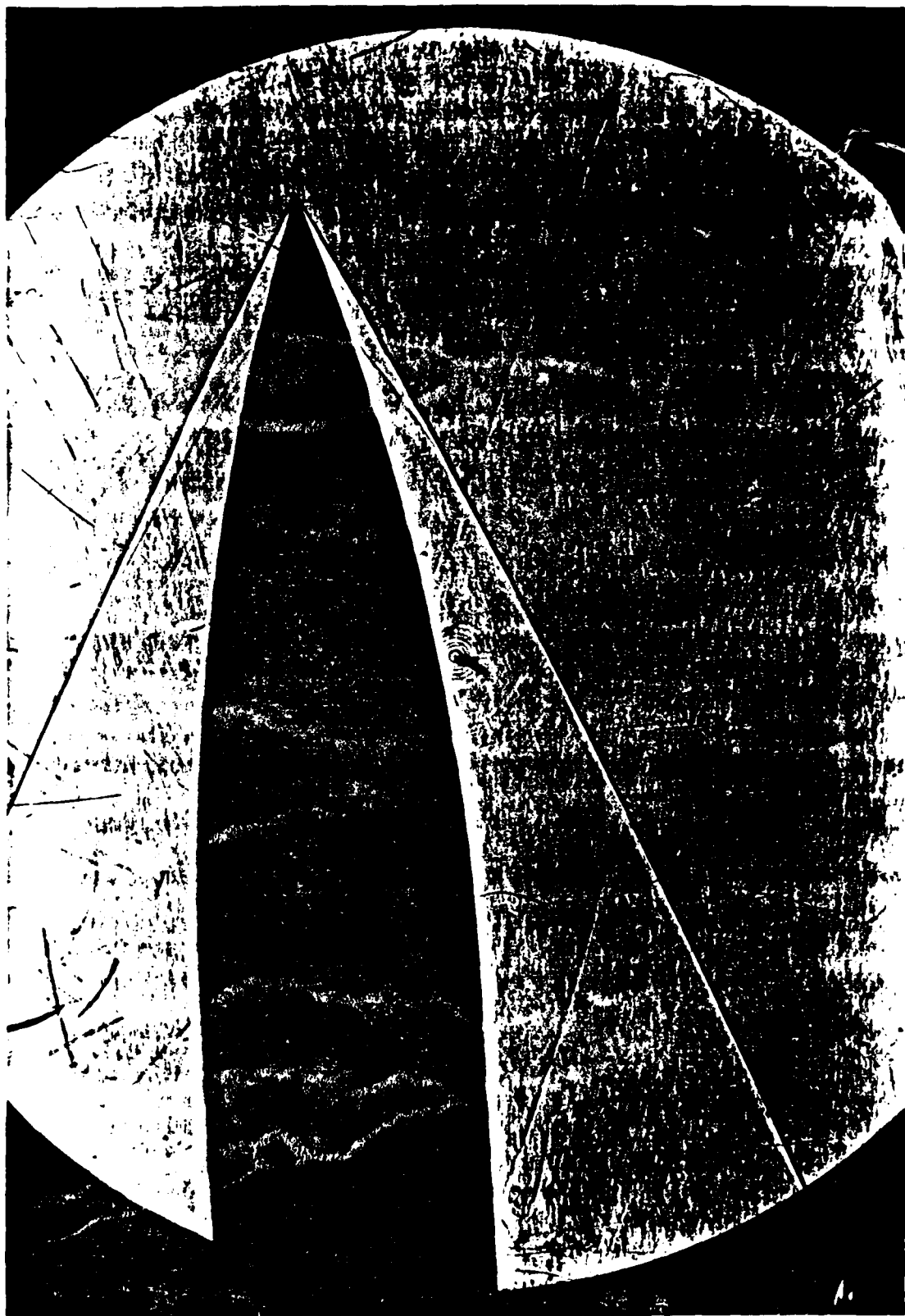
Photograph A5: Tip F1,  $\alpha = 0^\circ$ .



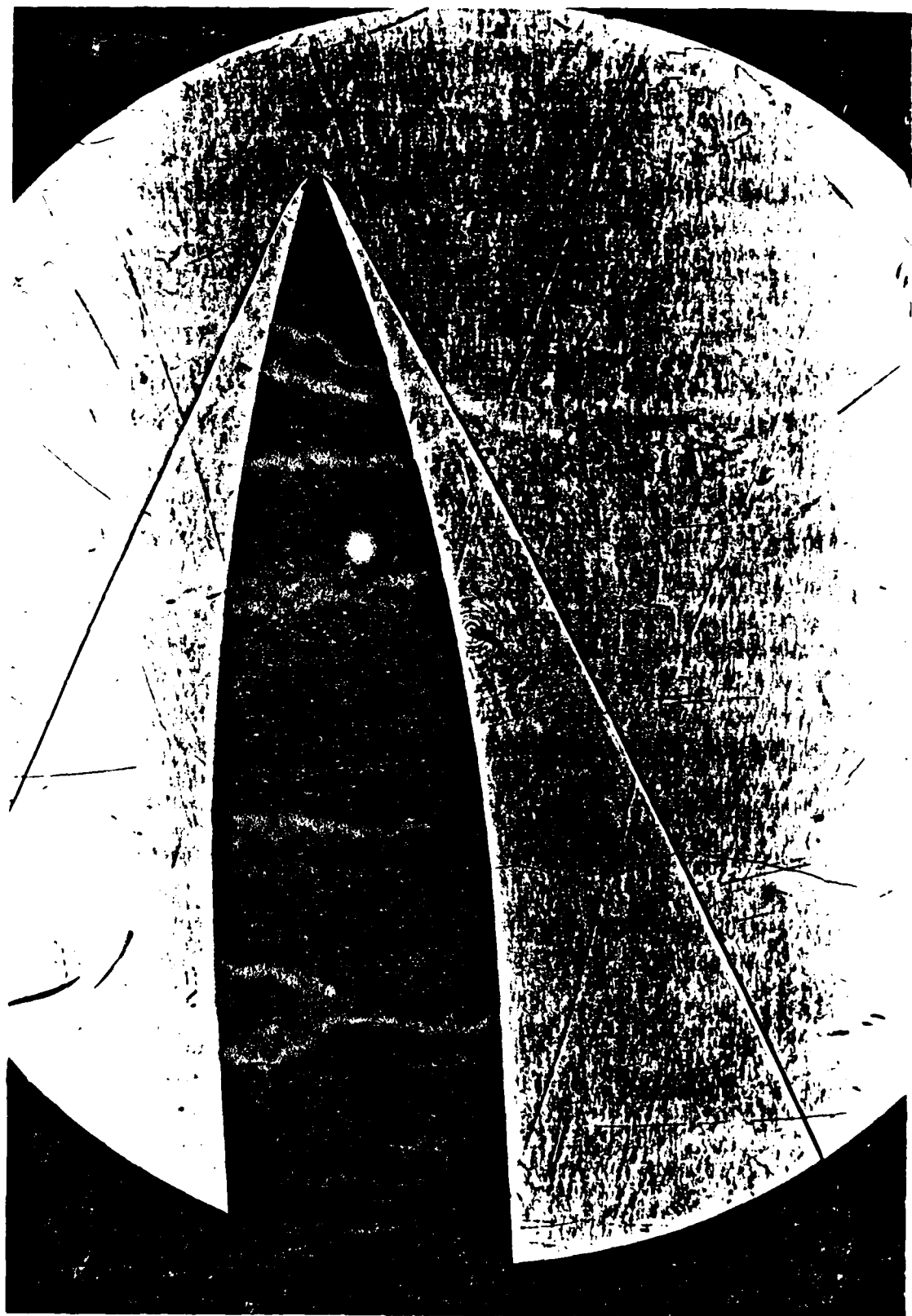
Photograph A6: Tip F2,  $\alpha = 0^\circ$ .



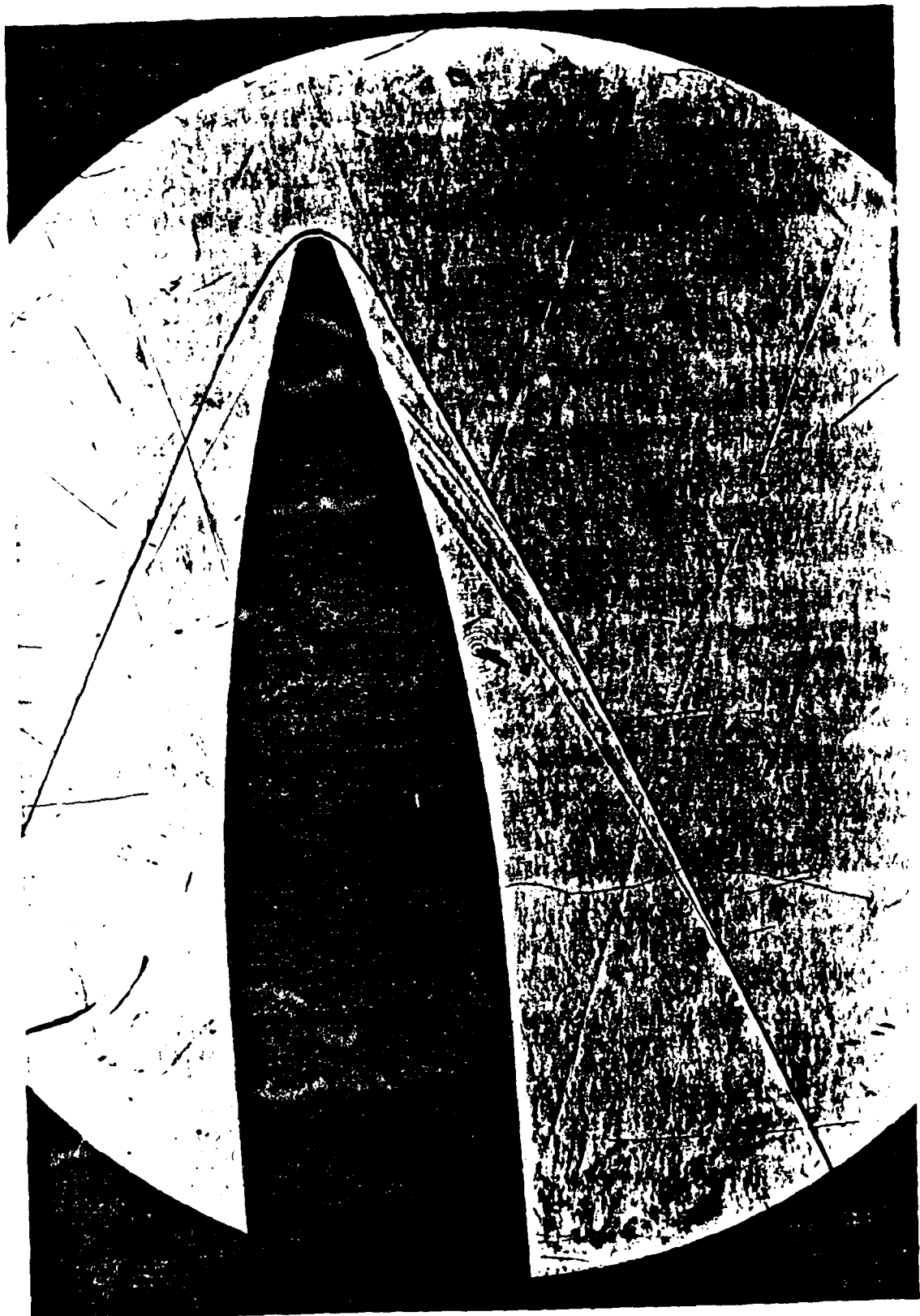
Photograph A7: Tip F3,  $\alpha = 0^\circ$ .



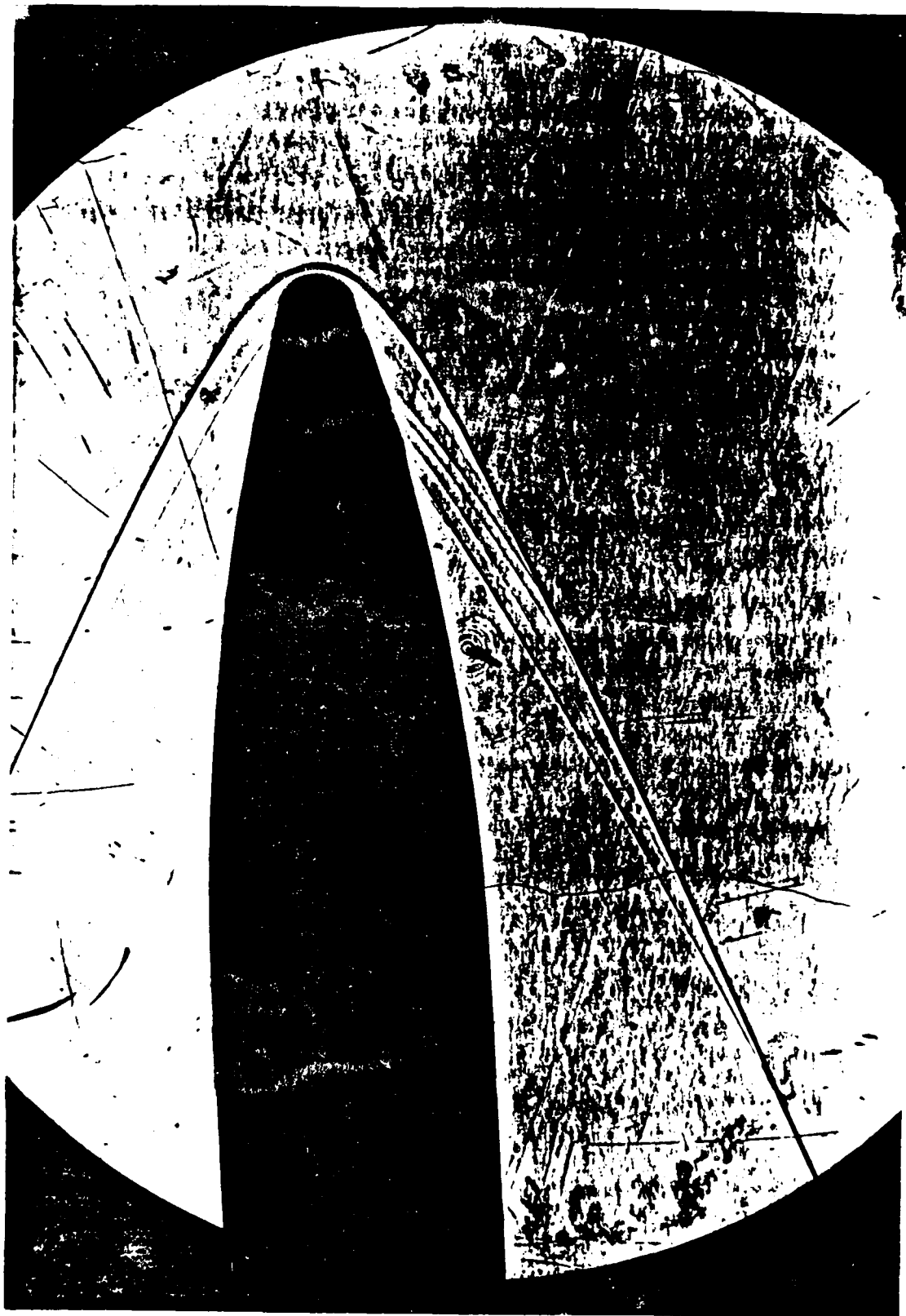
Photograph A8: Tip P,  $\alpha = 2.9^\circ$ .



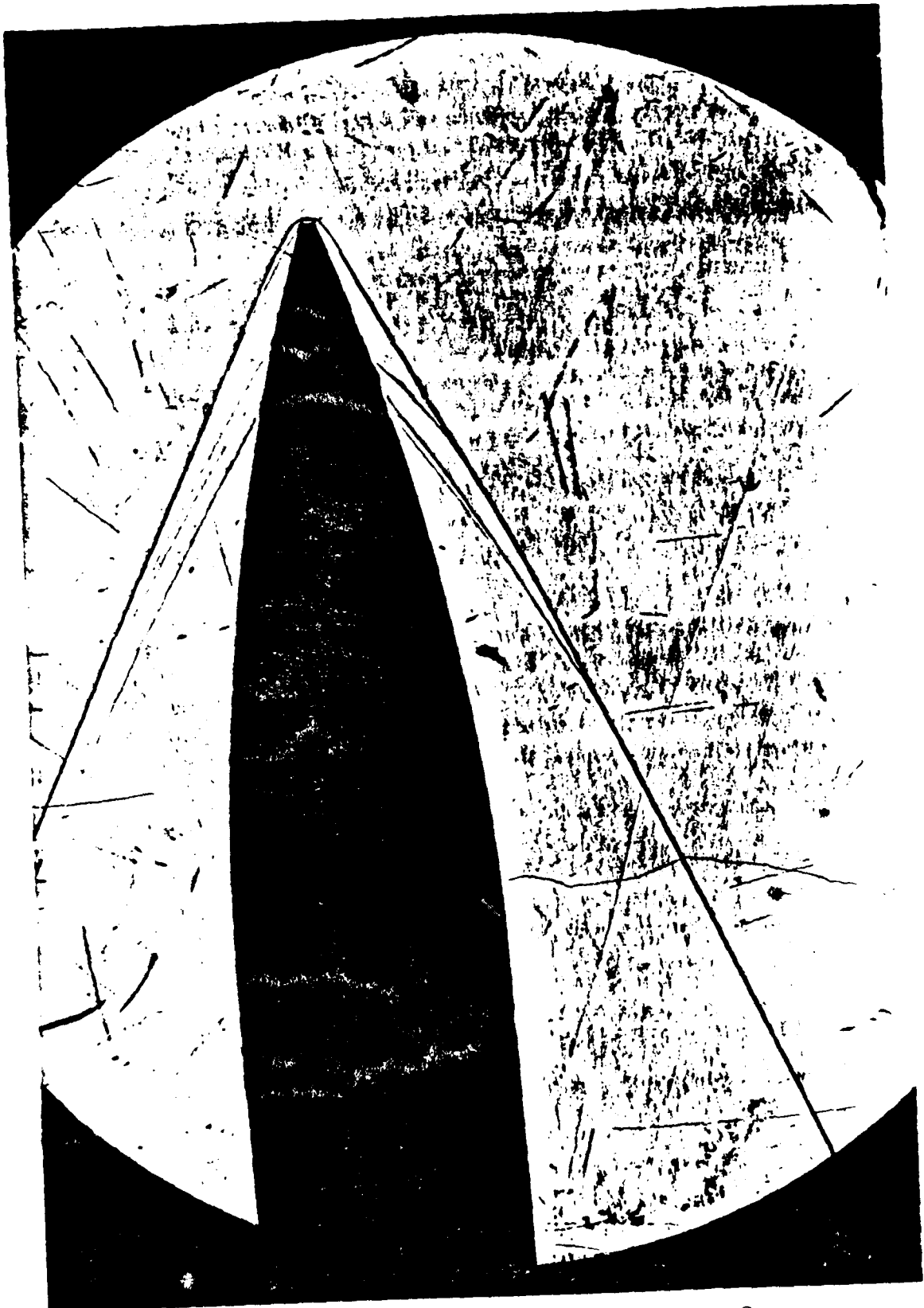
Photograph A9: Tip R1,  $\alpha = 2.9^\circ$ .



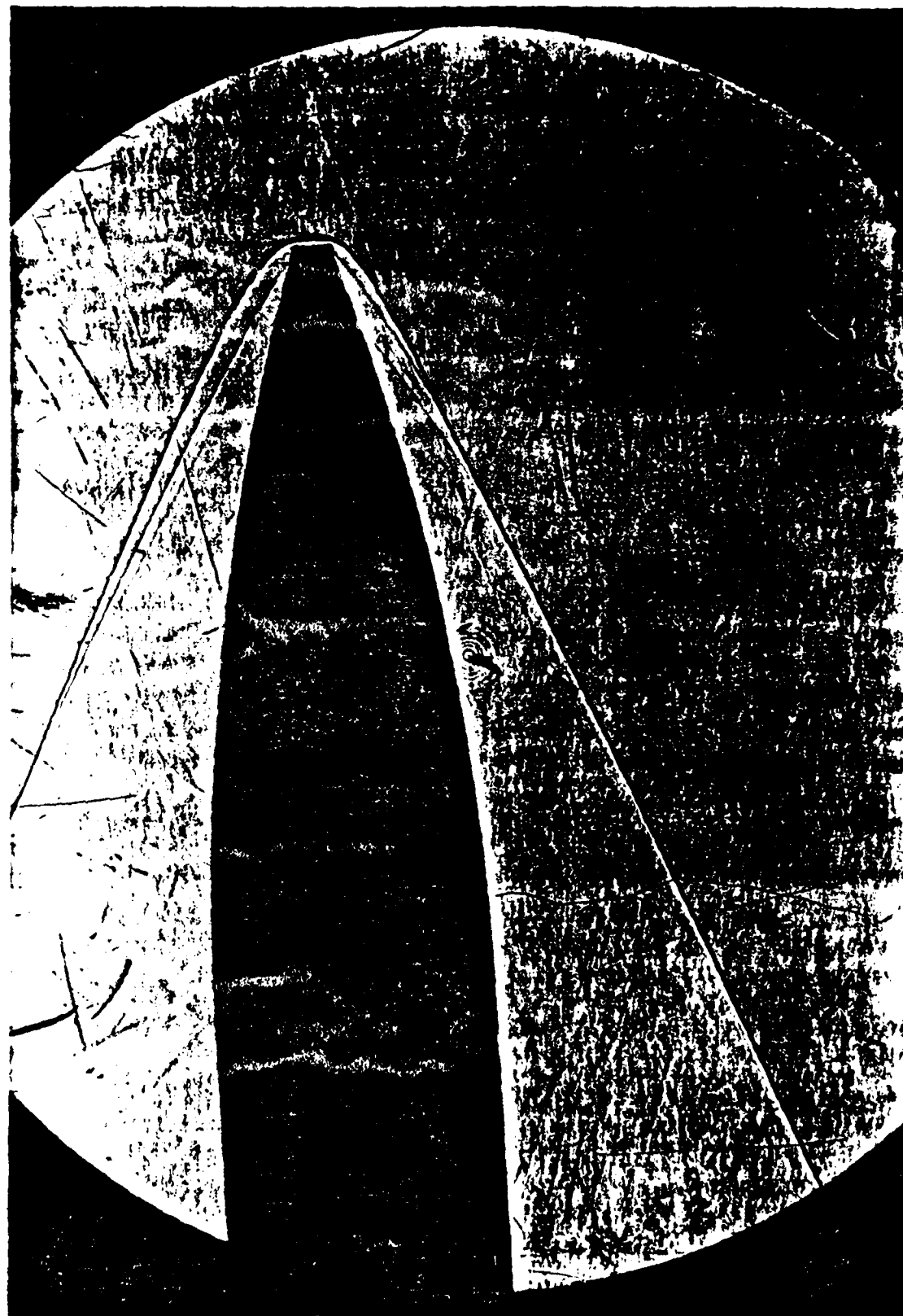
Photograph A10: Tip R2,  $\alpha = 2.9^\circ$ .



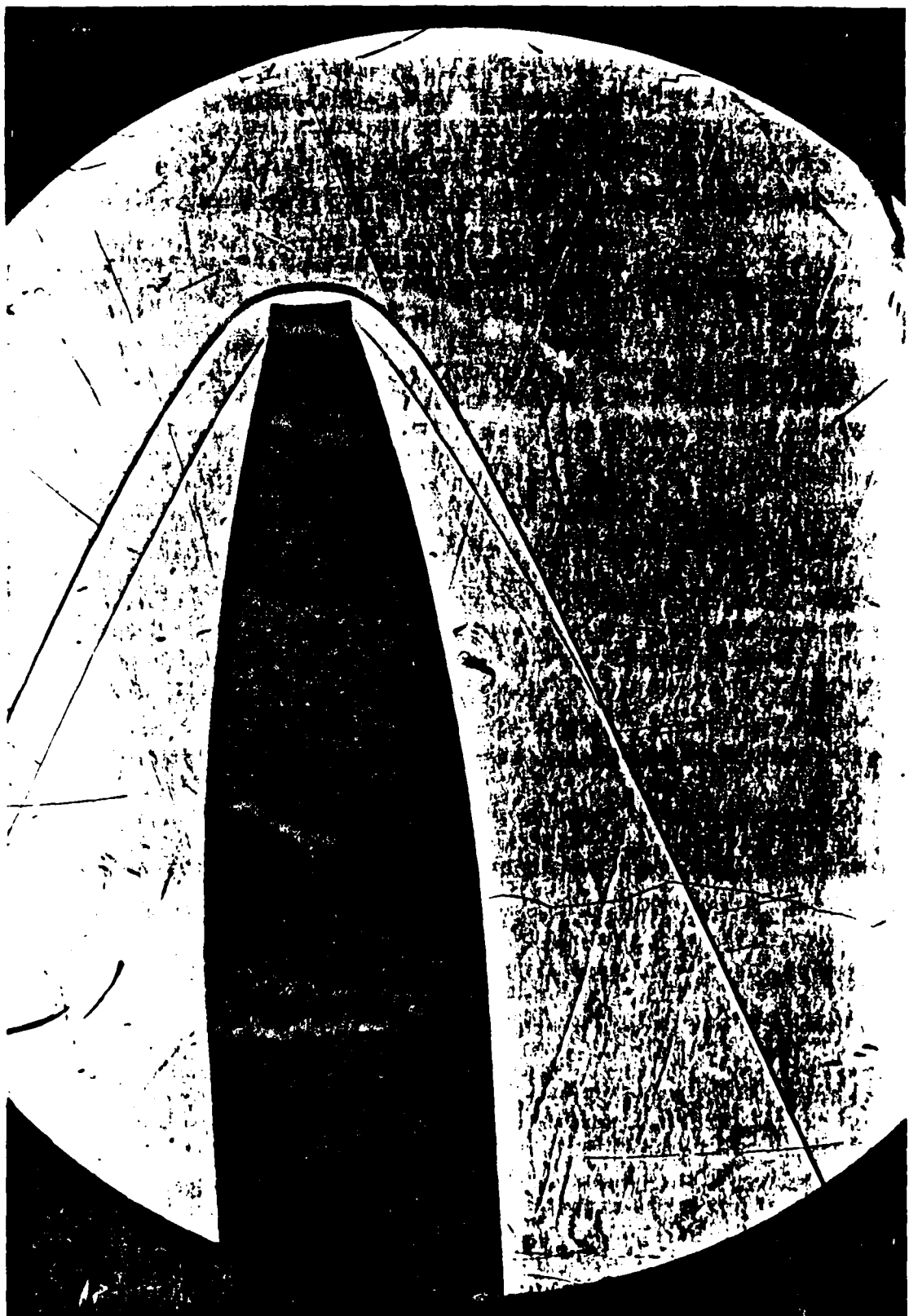
Photograph A11: Tip R3,  $\alpha = 2.9^\circ$ .



Photograph A12: Tip F1,  $\alpha = 2.9^\circ$ .



Photograph A13: Tip F2,  $\alpha = 2.9^\circ$ .



Photograph A14: Tip F3,  $\alpha = 2.9^\circ$ .

## APPENDIX B Velocity Profile Comparisons

<u>Figure</u>	<u>Subject</u>
B1	$X/D = 3.175 \alpha = 0^\circ$
B2	$X/D = 4.925 \alpha = 0^\circ$
B3	$X/D = 6.175 \alpha = 0^\circ$
B4	$X/D = 3.175 \alpha = 2.9^\circ \phi = 0^\circ$
B5	$X/D = 4.925 \alpha = 2.9^\circ \phi = 0^\circ$
B6	$X/D = 6.175 \alpha = 2.9^\circ \phi = 0^\circ$
B7	$X/D = 3.175 \alpha = 2.9^\circ \phi = 180^\circ$
B8	$X/D = 4.925 \alpha = 2.9^\circ \phi = 180^\circ$
B9	$X/D = 6.175 \alpha = 2.9^\circ \phi = 180^\circ$

Note: When the incidence is given as  $2.9^\circ$  the plot is for the windside ( $\phi = 0^\circ$ ) and when the incidence is given as  $-2.9^\circ$  the plot is for the leeside ( $\phi = 180^\circ$ ).

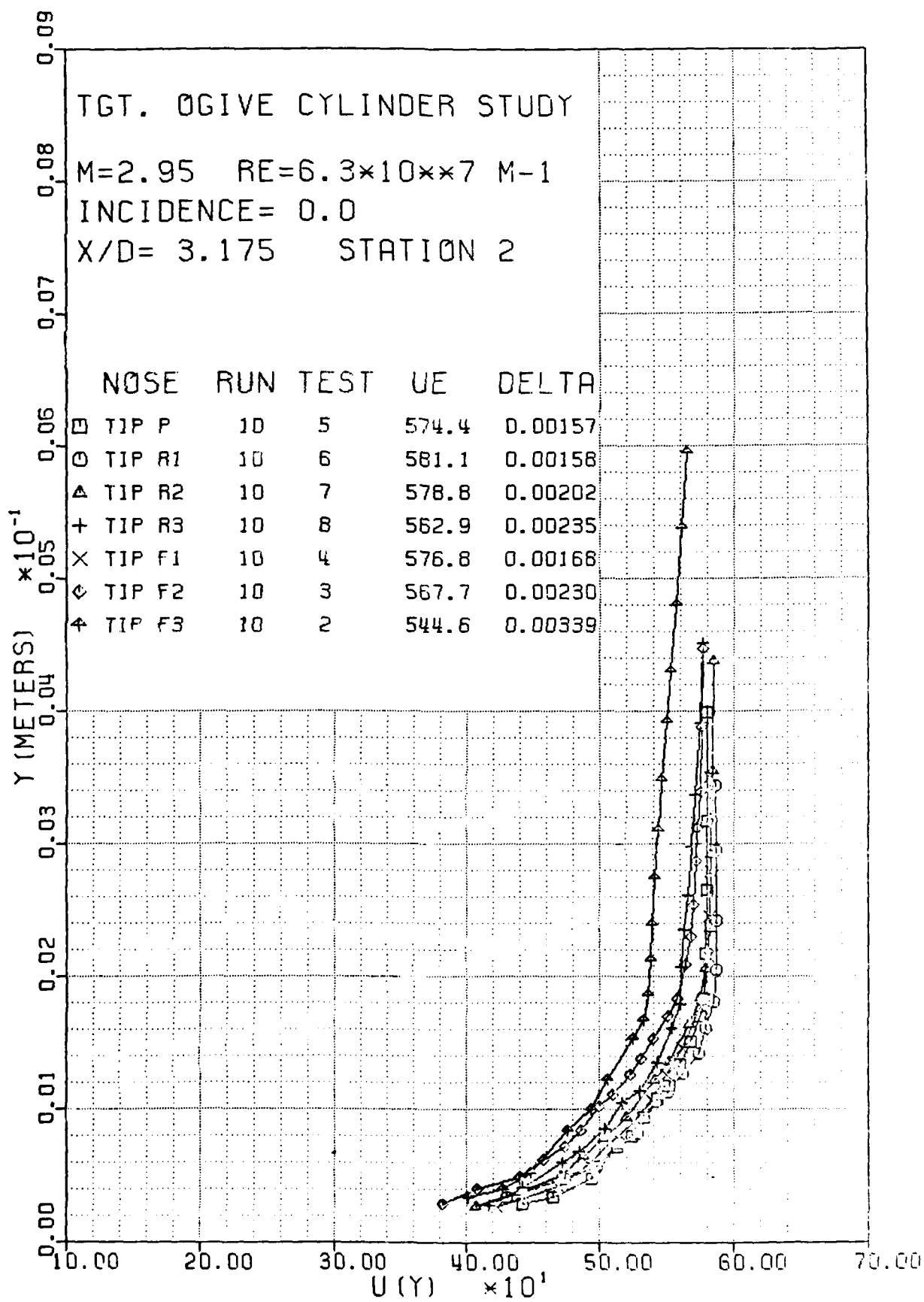


Figure B1. Velocity Profiles,  $X/D = 3.175$ ,  $\alpha = 0^\circ$ .

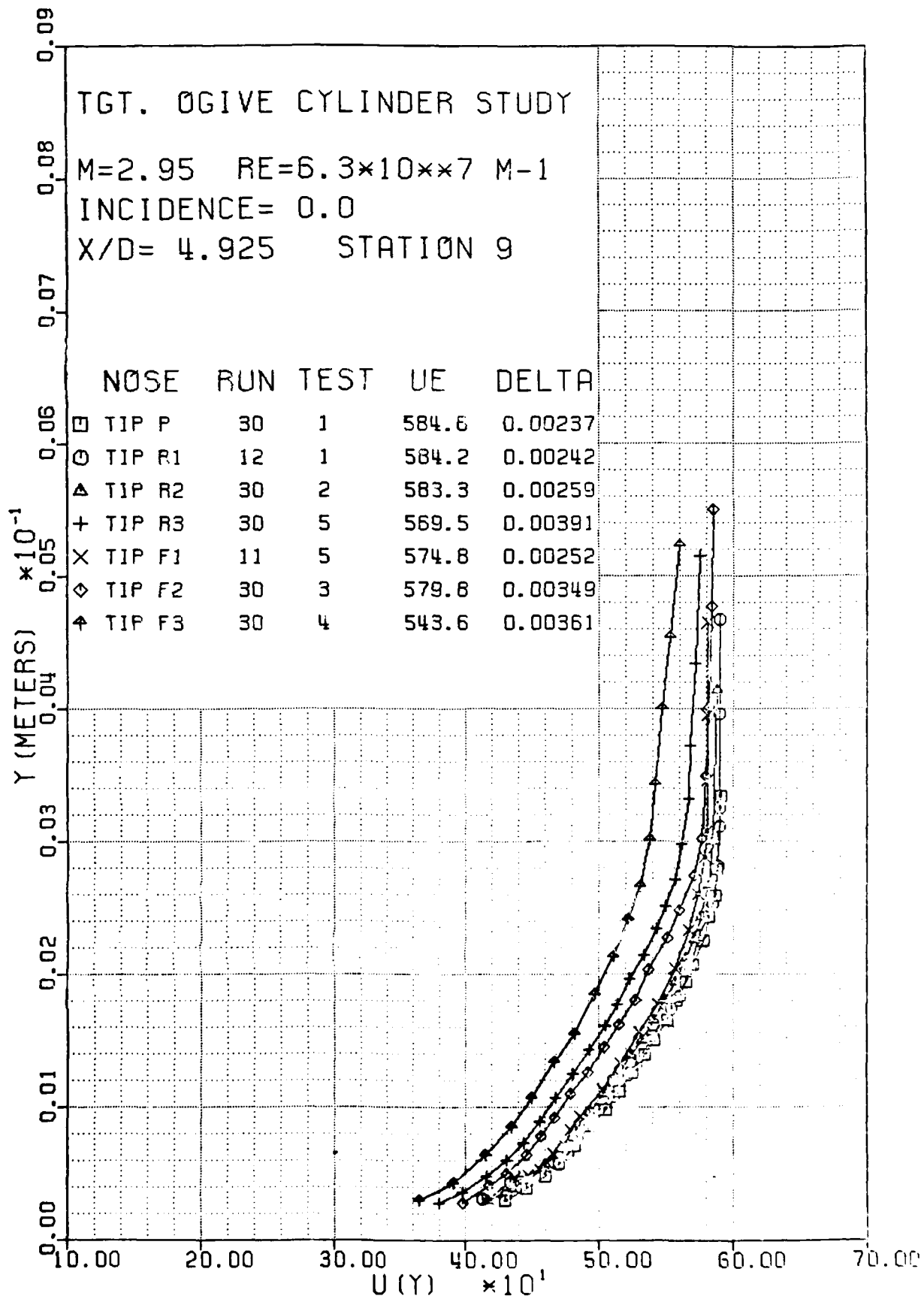


Figure B2. Velocity Profiles,  $X/D = 4.925$ ,  $\alpha = 0^\circ$ .

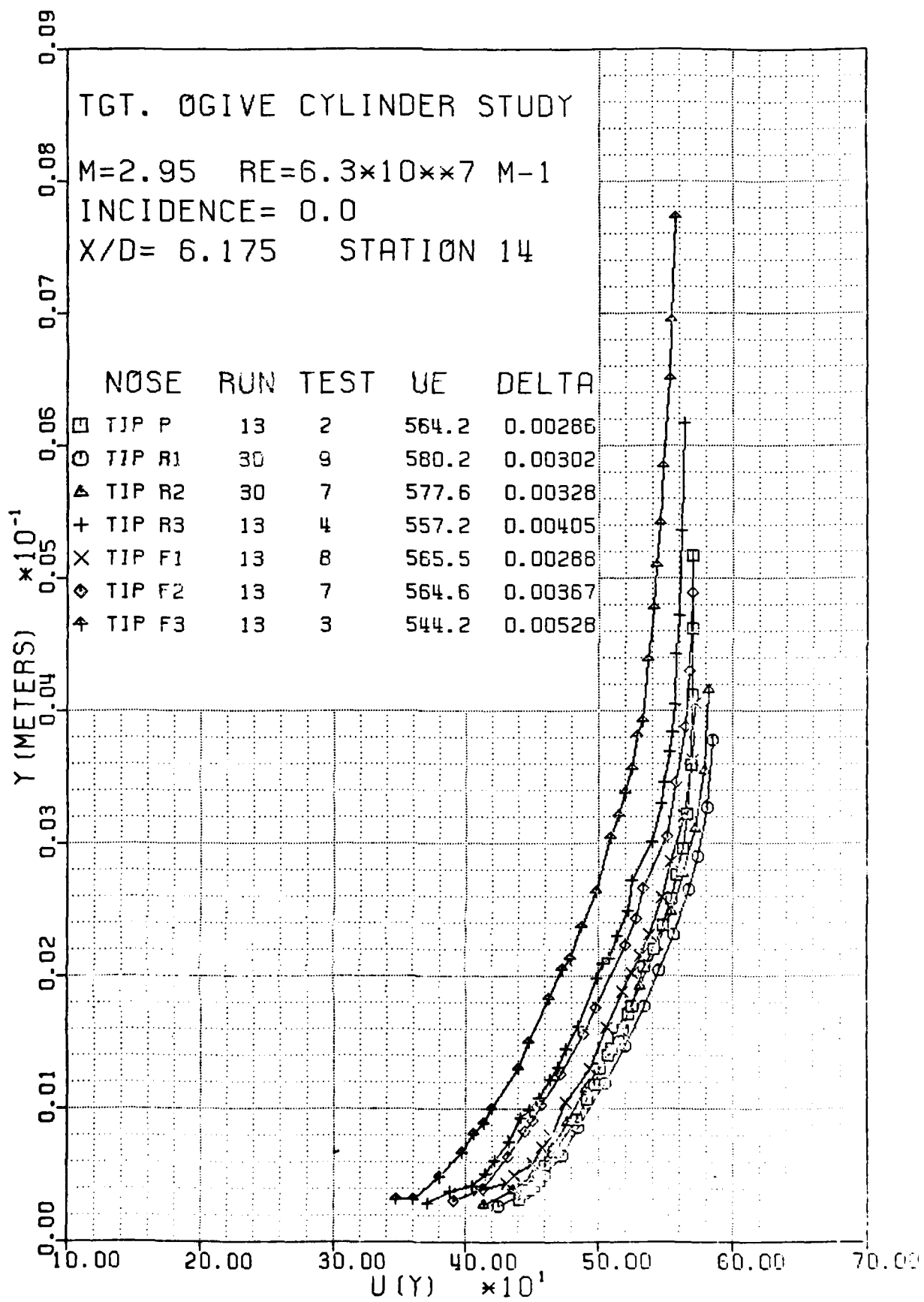


Figure B3. Velocity Profiles, X/D = 6.175,  $\alpha = 0^\circ$ .

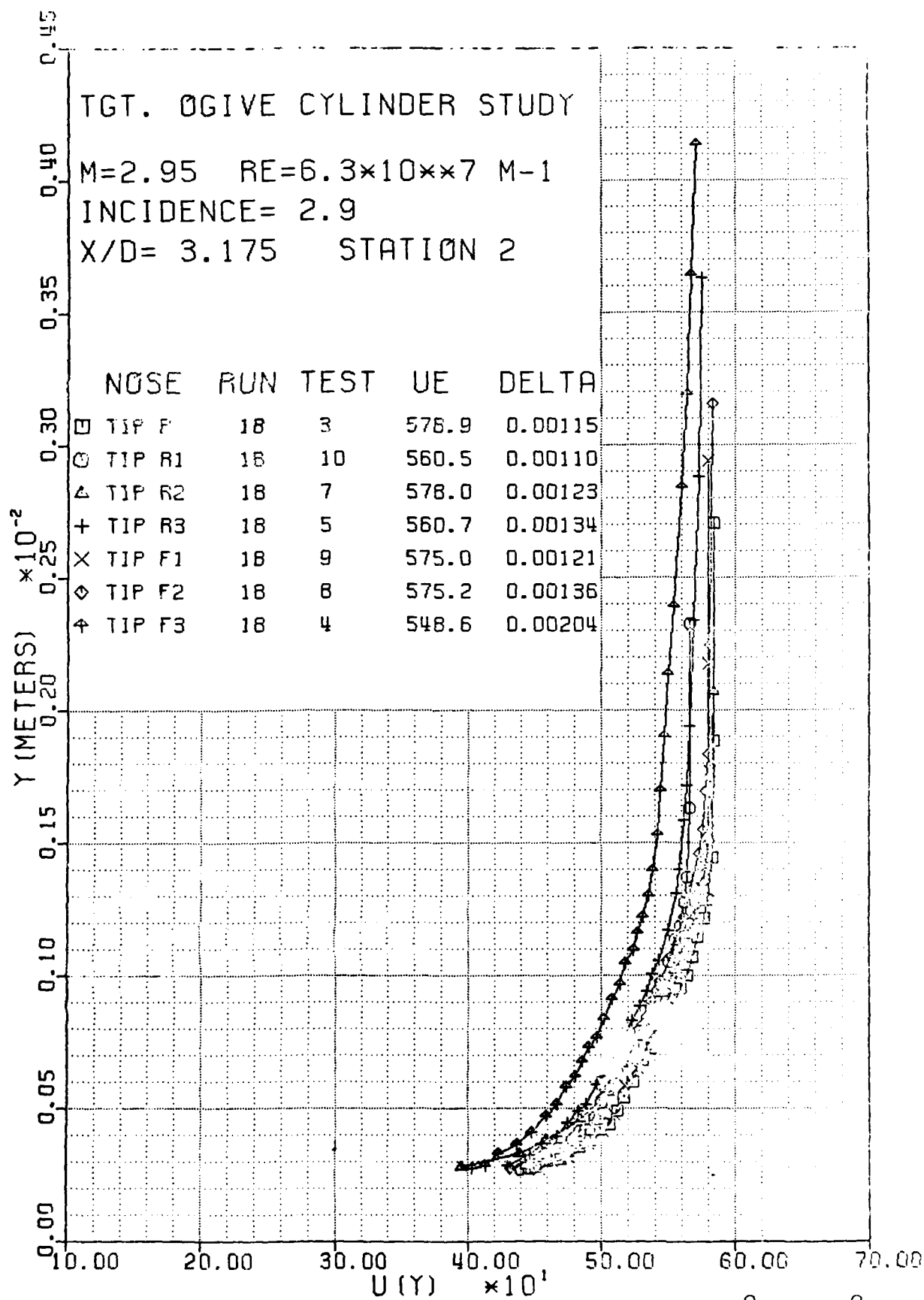


Figure B4. Velocity Profiles,  $X/D = 3.175$ ,  $\alpha = 2.9^\circ$ ,  $t = 0^\circ$ .

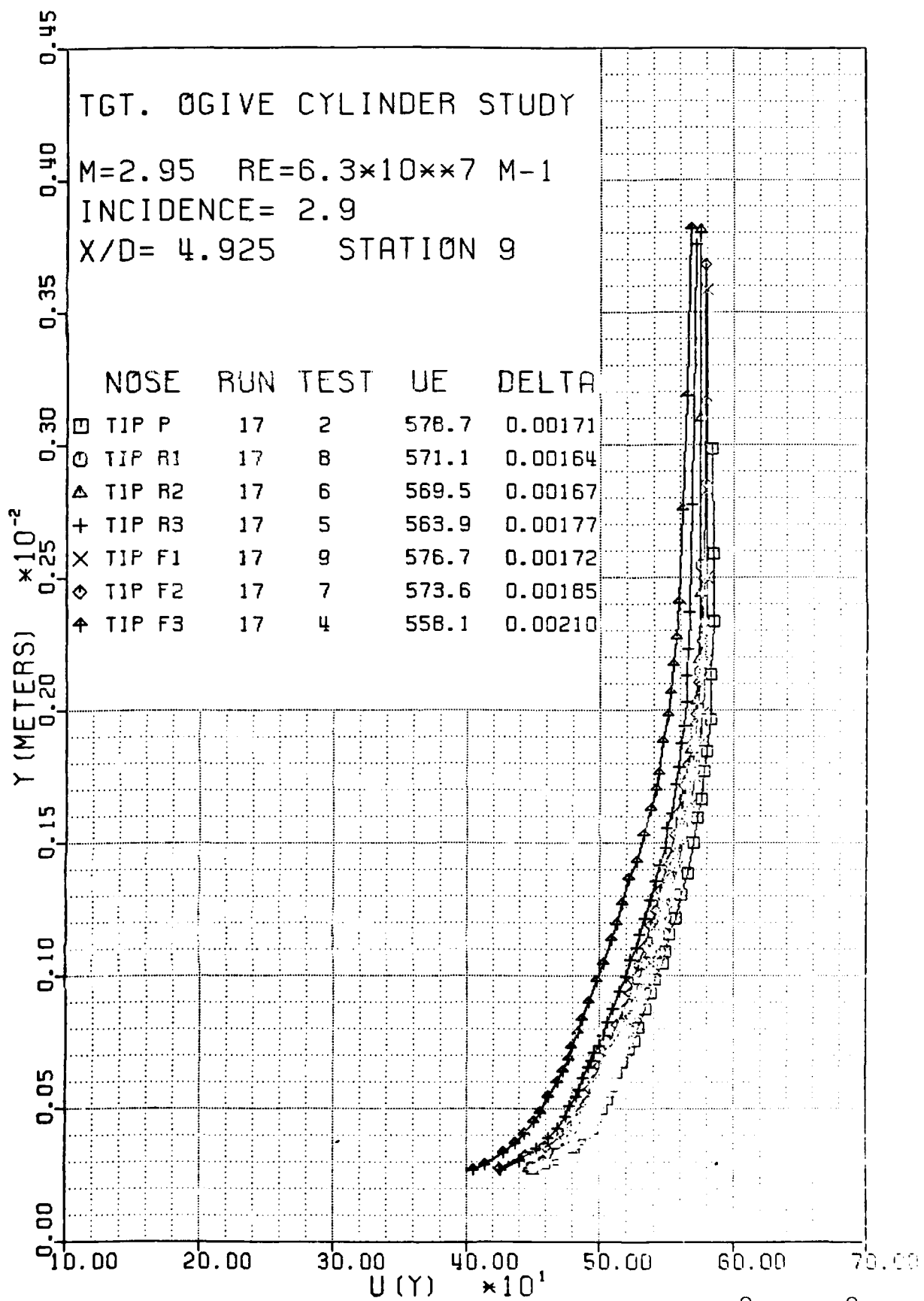


Figure B5. Velocity Profiles,  $X/D = 4.925$ ,  $\alpha = 2.9^\circ$ ,  $\phi = 0^\circ$ .

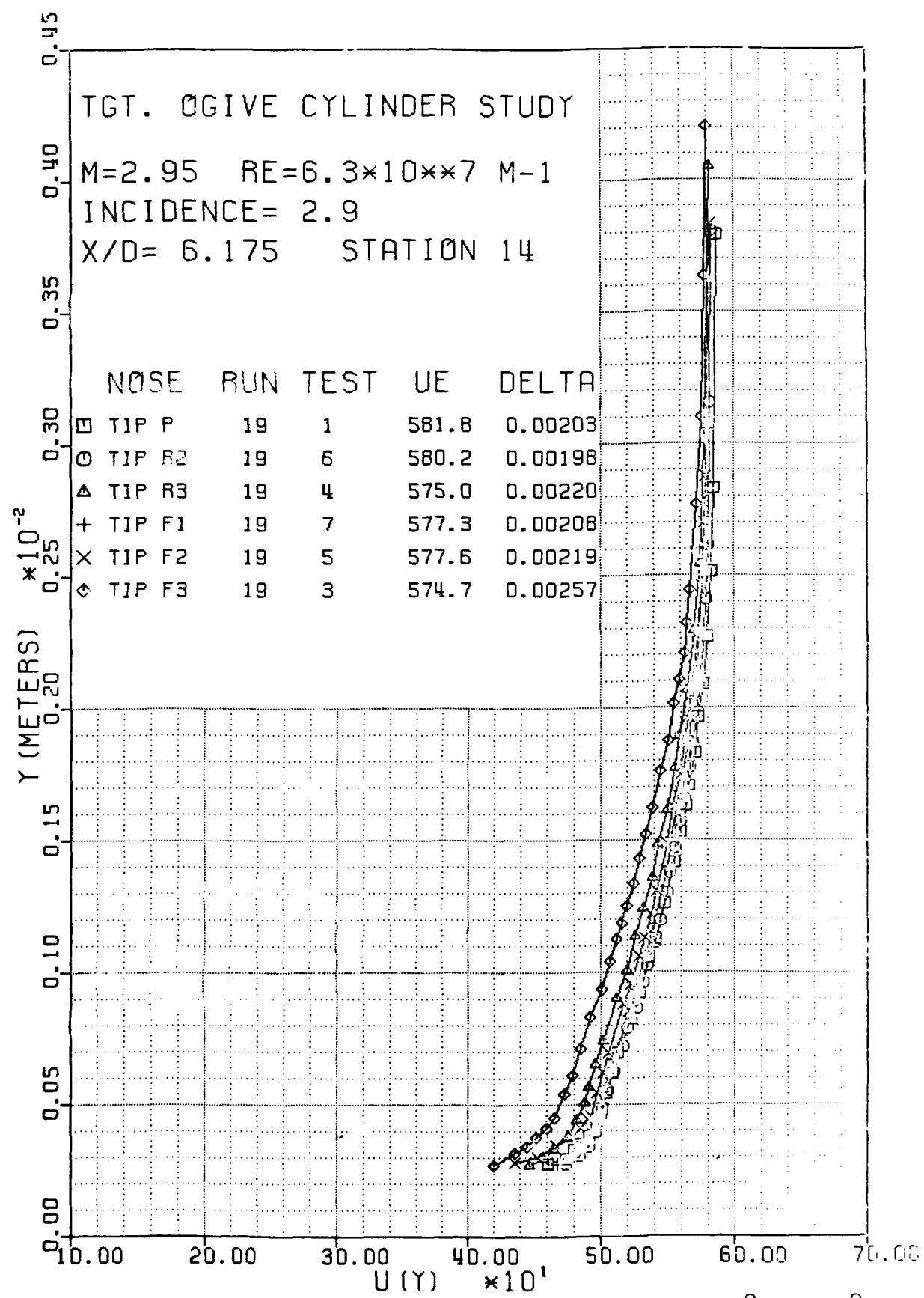


Figure B6. Velocity Profiles,  $X/D = 6.175$ ,  $\alpha = 2.9^\circ$ ,  $\phi = 0^\circ$ .

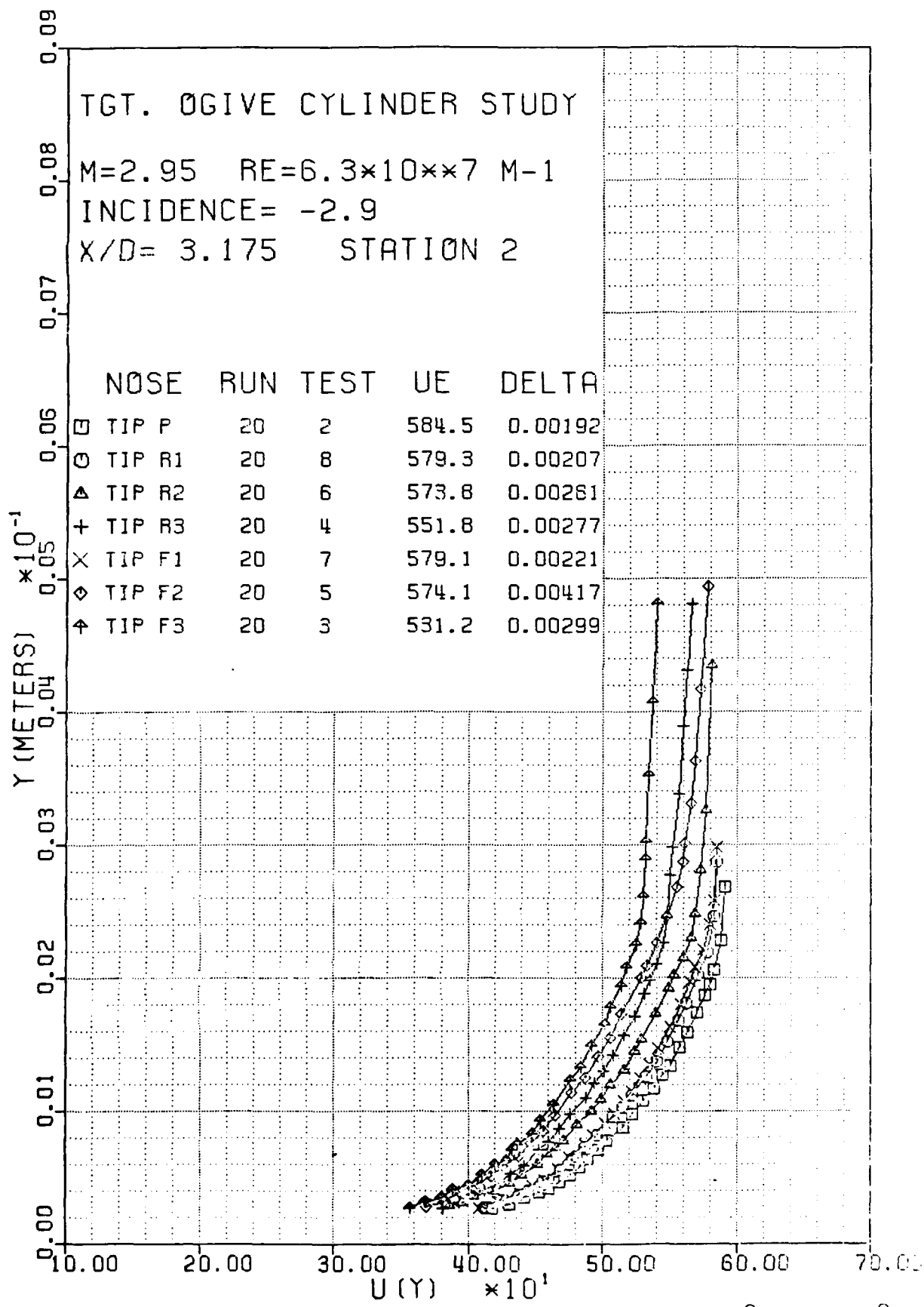


Figure B7. Velocity Profiles,  $X/D = 3.175$ ,  $\alpha = 2.9^\circ$ ,  $\delta = 180^\circ$ .

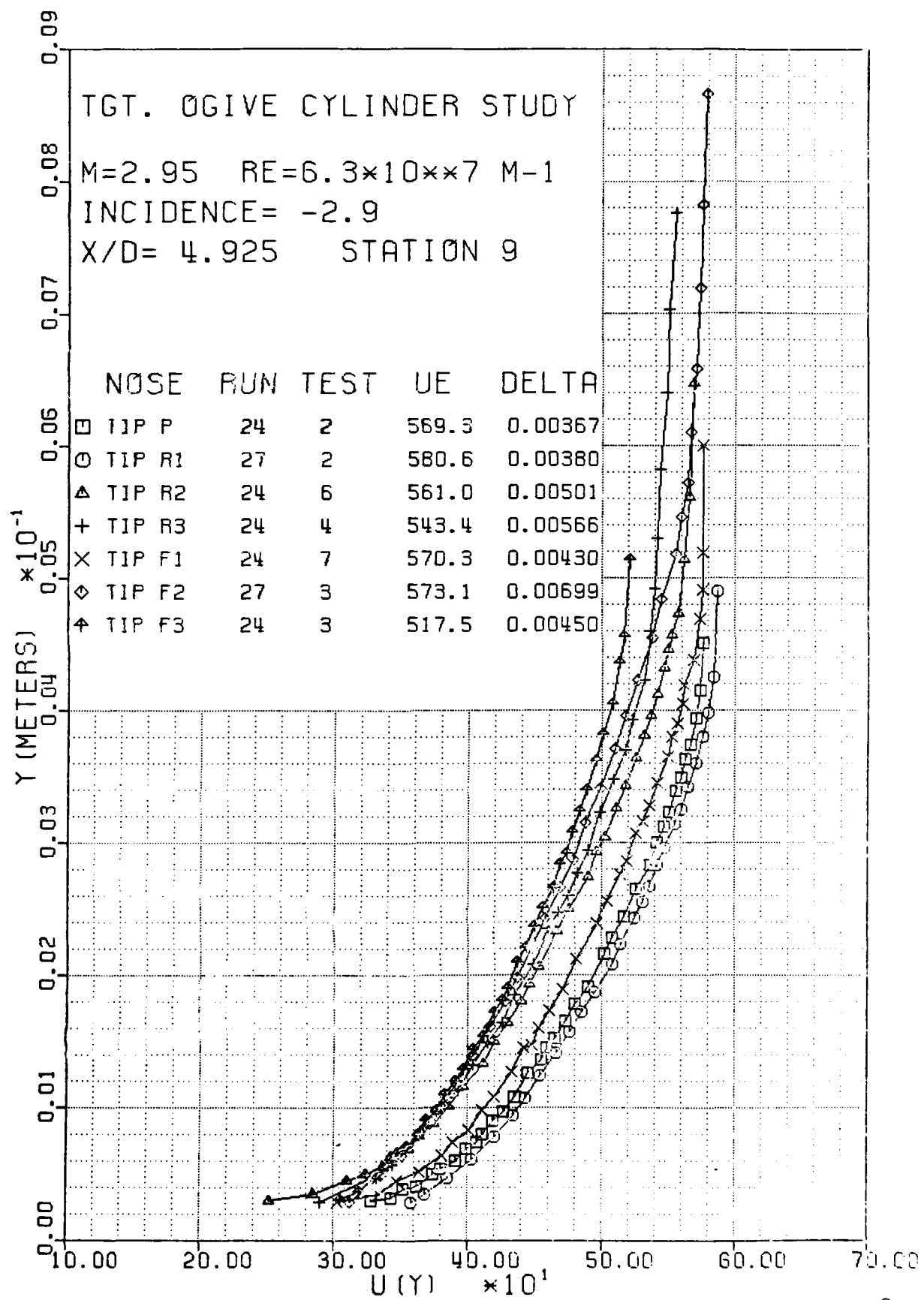


Figure B8. Velocity Profiles,  $X/D = 4.925$ ,  $\alpha = 2.9^\circ$ ,  $\psi = 180^\circ$ .

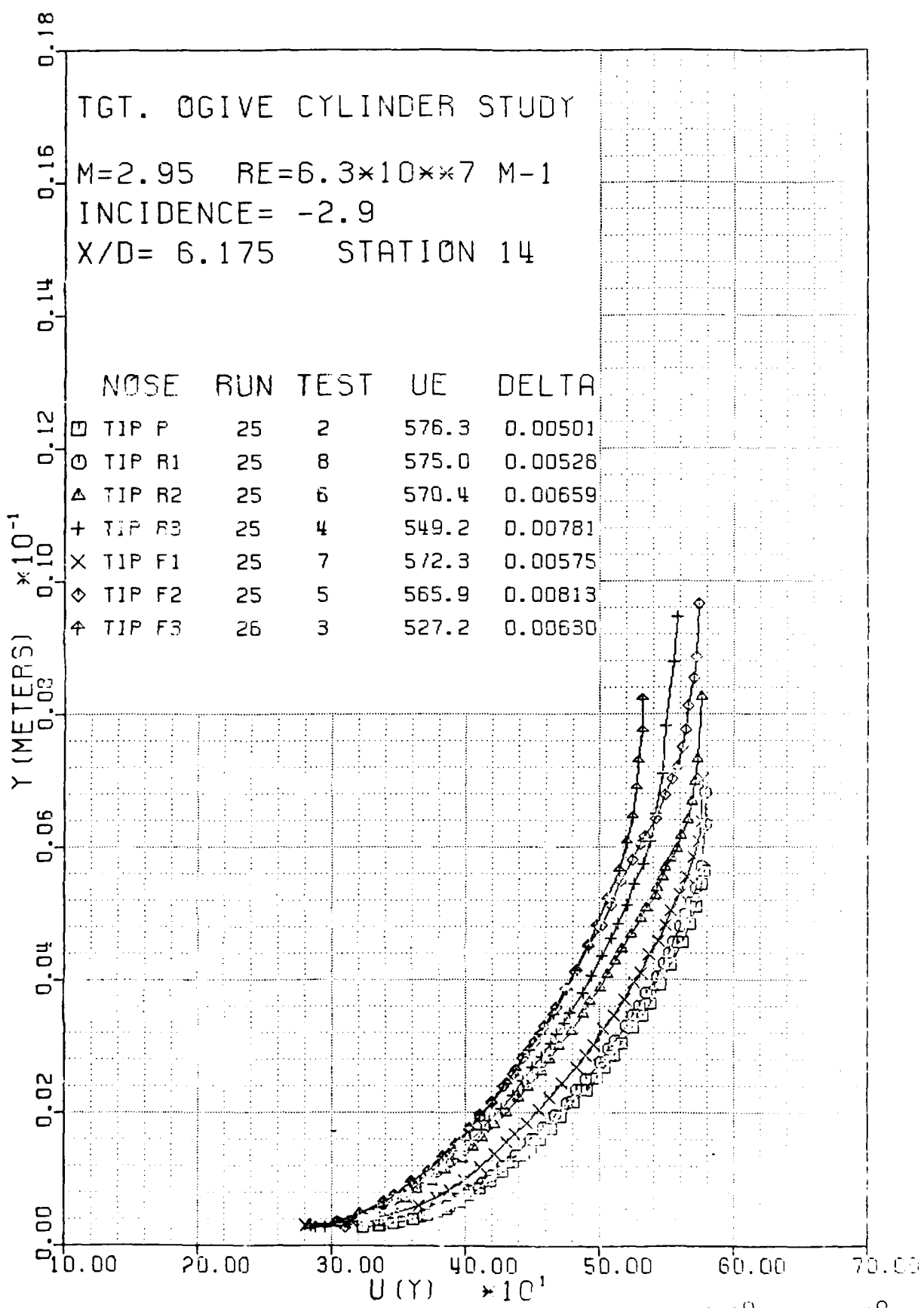


Figure B3. Velocity Profiles,  $X/D = 6.175$ ,  $\alpha = 2.9^\circ$ ,  $\delta = 180^\circ$ .

## APPENDIX C Boundary Layer Parameter Tables

<u>Table</u>	<u>Subject</u>
C1	Displacement thickness, $\delta^*$
C2	Momentum thickness, $\theta$
C3	Form Factor, $H$
C4	Power law exponent, $n$
C5	Wake strength parameter, $\pi$
C6	Skin friction coefficient, $C_f$
C7	Reynolds number based on momentum thickness, $Re_\theta$

Table C1

Quantity: Displacement thickness,  $\delta^*$ Units:  $m \times 10^{-3}$ 

Source: Wall-Wake Fitted Velocity Profile Analysis

Estimated Accuracy:  $\pm 0.05 m \times 10^{-3}$  $\alpha=0^\circ$ 

Tip X/D	Tip P	Tip R1	Tip R2	Tip R3	Tip F1	Tip F2	Tip F3
3.175	0.568	0.613	0.682	0.558	0.645	0.752	0.551
4.925	0.920	0.948	0.960	1.102	0.977	1.165	1.015
6.175	1.056	1.109	1.232	1.350	1.185	1.393	1.525

 $\alpha=2.9^\circ \phi=0^\circ$ 

Tip X/D	Tip P	Tip R1	Tip R2	Tip R3	Tip F1	Tip F2	Tip F3
3.175	0.446	0.442	0.506	0.449	0.458	0.527	0.460
4.925	0.574	0.576	0.607	0.601	0.597	0.665	0.712
6.175	0.680	---	0.664	0.744	0.679	0.727	0.846

 $\alpha=2.9^\circ \phi=15^\circ$ 

Tip X/D	Tip P	Tip R1	Tip R2	Tip R3	Tip F1	Tip F2	Tip F3
3.175	0.797	0.832	0.931	0.784	0.879	1.128	0.764
4.925	1.648	1.678	2.128	1.769	1.930	2.503	1.599
6.175	2.110	2.246	2.919	2.462	2.508	3.497	2.210

Table C2

Quantity: Momentum thickness,  $\theta$

Units:  $m \times 10^{-3}$

Source: Wall-Wake Fitted Velocity Profile Analysis

Estimated Accuracy:  $\pm 0.01 m \times 10^{-3}$

$\alpha=0^\circ$

Tip X/D	Tip P	Tip R1	Tip R2	Tip R3	Tip F1	Tip F2	Tip F3
3.175	0.108	0.114	0.132	0.124	0.119	0.149	0.136
4.925	0.177	0.180	0.187	0.233	0.187	0.228	0.244
6.175	0.208	0.219	0.242	0.282	0.233	0.275	0.345

$\alpha=2.9^\circ \phi=0^\circ$

Tip X/D	Tip P	Tip R1	Tip R2	Tip R3	Tip F1	Tip F2	Tip F3
3.175	0.082	0.082	0.093	0.094	0.086	0.100	0.106
4.925	0.112	0.114	0.118	0.124	0.117	0.130	0.152
6.175	0.134	---	0.129	0.149	0.134	0.143	0.173

$\alpha=2.9^\circ \phi=18^\circ$

Tip X/D	Tip P	Tip R1	Tip R2	Tip R3	Tip F1	Tip F2	Tip F3
3.175	0.141	0.153	0.181	0.179	0.162	0.229	0.192
4.925	0.301	0.307	0.400	0.393	0.351	0.484	0.401
6.175	0.392	0.416	0.548	0.540	0.462	0.670	0.557

Table C3

Quantity: Form factor, H

Units: Nondimensional

Source: Wall-Wake Fitted Velocity Profile Analysis

Estimated Accuracy:  $\pm 0.01$  $\alpha=0^\circ$ 

Tip X/D	Tip P	Tip R1	Tip R2	Tip R3	Tip F1	Tip F2	Tip F3
3.175	5.255	5.376	5.162	4.511	5.395	5.112	4.051
4.925	5.213	5.263	5.126	4.724	5.223	5.111	4.164
6.175	5.084	5.070	5.089	4.797	5.080	5.063	4.427

 $\alpha=2.9^\circ \phi=0^\circ$ 

Tip X/D	Tip P	Tip F1	Tip R2	Tip R3	Tip F1	Tip F2	Tip F3
3.175	5.375	5.413	5.410	4.757	5.296	5.290	4.242
4.925	5.134	5.062	5.141	4.837	5.122	5.126	4.679
6.175	5.088	---	5.150	4.977	5.075	5.087	4.893

 $\alpha=2.9^\circ \phi=18^\circ$ 

Tip X/D	Tip P	Tip R1	Tip R2	Tip R3	Tip F1	Tip F2	Tip F3
3.175	5.658	5.443	5.141	4.373	5.428	4.916	3.984
4.925	5.466	5.472	5.316	4.502	5.491	5.124	3.986
6.175	5.379	5.399	5.330	4.556	5.433	5.222	3.965

Table C4

Quantity: Power law exponent,  $n$ 

Units: Nondimensional

Source: Power Law Analysis

Estimated Accuracy:  $\pm 0.15$  $\alpha=0^\circ$ 

Tip X/D	Tip P	Tip R1	Tip R2	Tip R3	Tip F1	Tip F2	Tip F3
3.175	6.66	6.08	6.12	6.58	6.63	5.88	6.80
4.925	6.07	5.91	5.90	5.65	6.16	5.56	6.03
6.175	7.46	7.34	6.64	6.10	6.84	6.26	5.85

 $\alpha=2.9^\circ \phi=0^\circ$ 

Tip X/D	Tip P	Tip R1	Tip R2	Tip R3	Tip F1	Tip F2	Tip F3
3.175	6.80	6.61	5.94	7.45	7.39	6.83	7.14
4.925	8.04	8.11	7.99	7.34	8.17	7.67	7.63
6.175	8.82	---	9.24	8.34	9.32	8.85	7.52

 $\alpha=2.9^\circ \phi=18^\circ$ 

Tip X/D	Tip P	Tip R1	Tip R2	Tip R3	Tip F1	Tip F2	Tip F3
3.175	6.24	6.09	5.85	6.38	6.19	6.03	6.06
4.925	4.70	4.79	4.10	4.34	4.55	4.40	4.73
6.175	5.28	5.23	4.54	4.91	4.86	4.70	4.96

Table C5

Quantity: Wake strength parameter,

Units: Nondimensional

Source: Wall-Wake Velocity Profile Curve Fit

Estimated Accuracy:  $\pm 0.01$  $\alpha=0^\circ$ 

Tip X/D	Tip P	Tip R1	Tip R2	Tip R3	Tip F1	Tip F2	Tip F3
3.175	0.55	0.67	0.66	0.61	0.57	0.79	0.51
4.925	0.77	0.85	0.82	0.92	0.78	0.98	0.82
6.175	0.57	0.60	0.76	0.88	0.71	0.89	0.97

 $\alpha=2.9^\circ \phi=0^\circ$ 

Tip X/D	Tip P	Tip R1	Tip R2	Tip R3	Tip F1	Tip F2	Tip F3
3.175	0.50	0.54	0.70	0.48	0.40	0.51	0.44
4.925	0.35	0.32	0.35	0.43	0.33	0.41	0.54
6.175	0.27	---	0.23	0.34	0.22	0.28	0.44

 $\alpha=2.9^\circ \phi=18^\circ$ 

Tip X/D	Tip P	Tip R1	Tip R2	Tip R3	Tip F1	Tip F2	Tip F3
3.175	0.68	0.71	0.79	0.62	0.69	0.84	0.67
4.925	1.50	1.43	1.97	1.63	1.66	1.91	1.38
6.175	1.42	1.45	1.88	1.59	1.65	1.94	1.42

Table C6

Quantity: Skin friction coefficient,  $c_f$ Units: Nondimensional  $\times 1000$ 

Source: Wall-Wake Velocity Profile Analysis

Estimated Accuracy:  $\pm 0.5 \times 10^{-3}$  $\alpha=0^\circ$ 

Tip X/D	Tip P	Tip R1	Tip R2	Tip R3	Tip F1	Tip F2	Tip F3
3.175	1.69	1.61	1.61	1.87	1.59	1.58	2.03
4.925	1.46	1.42	1.45	1.46	1.42	1.36	1.66
6.175	1.42	1.42	1.35	1.37	1.37	1.29	1.37

 $\alpha=2.9^\circ \phi=0^\circ$ 

Tip X/D	Tip P	Tip R1	Tip R2	Tip R3	Tip F1	Tip F2	Tip F3
3.175	1.74	1.69	1.64	1.90	1.77	1.69	2.07
4.925	1.72	1.72	1.67	1.74	1.70	1.64	1.70
6.175	1.62	---	1.66	1.64	1.67	1.63	1.59

 $\alpha=2.9^\circ \phi=180^\circ$ 

Tip X/D	Tip P	Tip R1	Tip R2	Tip R3	Tip F1	Tip F2	Tip F3
3.175	1.49	1.50	1.51	1.80	1.49	1.48	1.91
4.925	1.11	1.13	1.01	1.22	1.05	1.02	1.41
6.175	1.07	1.04	0.95	1.13	0.99	0.92	1.31

Table C7

Quantity: Reynolds number based on momentum thickness,  $Re_\theta$

Units:  $m^{-1} \times 10^{-3}$

Source: Wall-Wake Velocity Profile Analysis

Estimated Accuracy:  $\pm 5\%$

$\alpha=0^\circ$

Tip X/D	Tip P	Tip R1	Tip R2	Tip R3	Tip F1	Tip F2	Tip F3
3.175	5.85	6.29	6.77	4.82	6.95	7.17	4.50
4.925	9.64	9.97	9.96	10.58	10.85	11.99	8.79
6.175	12.74	12.72	14.14	14.24	13.92	16.06	15.50

$\alpha=2.9^\circ \phi=0^\circ$

Tip X/D	Tip P	Tip R1	Tip R2	Tip R3	Tip F1	Tip F2	Tip F3
3.175	4.91	5.41	5.53	4.41	5.06	5.76	4.12
4.925	6.38	6.55	7.07	6.45	6.79	7.52	7.21
6.175	7.62	---	7.72	8.26	7.85	8.33	8.91

$\alpha=2.9^\circ \phi=180^\circ$

Tip X/D	Tip P	Tip R1	Tip R2	Tip R3	Tip F1	Tip F2	Tip F3
3.175	7.76	8.09	8.48	6.17	8.53	9.85	5.64
4.925	18.19	17.84	22.22	16.13	21.22	24.11	12.97
6.175	23.74	25.43	31.36	23.57	28.22	36.31	17.66

